Schweizerische Eidgenossenschaft
Confédération suisse
Confederazione Svizzera
Confederaziun svizra

Federal Department of the Environment, Transport, Energy and Communications DETEC

Swiss Federal Office of Energy SFOE
Energy Research and Cleantech Division

Final report dated 22.07.2025

HydroLEAP

Modernisation du Parc Hydroélectrique Suisse pour une Stratégie Énergétique 2050 réussie

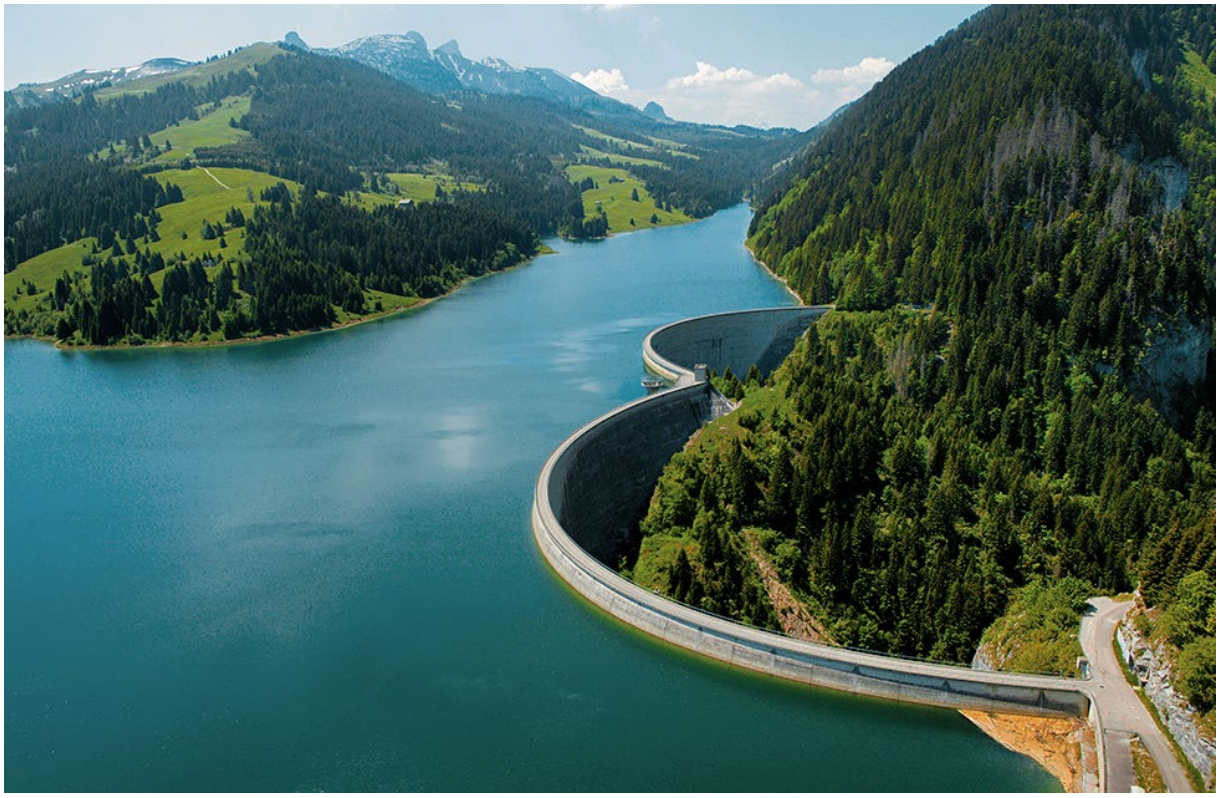

Source: Hongrin Dam, FMHL









Date: 22.07.2025

Location: Bern

Publisher:
Swiss Federal Office of Energy SFOE
Energy Research and Cleantech
CH-3003 Bern
www.bfe.admin.ch

Subsidy recipients:
Ecole polytechnique fédérale de Lausanne,
Plateforme Technologique en Machines Hydrauliques
Avenue de Cour 33 bis,
1007 Lausanne

ALPIQ SA
Chemin de Mornex 10
CP 570
1001 Lausanne

Forces Motrices Hongrin-Léman SA
Chemin de Mornex 10
c/o CP 570
1001 Lausanne

FMVSA
Rue de la Dixence 9
CP 506
1951 Sion

MBRSA
c/o FMV SA
Rue de la Dixence 9
CP 506
1951 Sion

HYDRO Exploitation SA

Rue de l'industrie 10
CP 750
1951 Sion

Power Vision Engineering Sàrl
Rue des Jordils 40
1025 St-Sulpice VD

HES-SO Valais-Wallis
Rte du Rawyl 47
CP 2134
1950 Sion

ETH Zürich
Versuchsanstalt für Wasserbau, Hydrologie und Glaziologie VAW,
Hônggerbergring 26
8093 Zürich

Authors:
Elena Vagnoni, elena.vagnoni@epfl.ch; Aldo Leonardo Alerci, Monica Suarez, Philippe Cerrutti (EPFL);
Martin Boden (ALPIQ)
Ismail Albayrak, Robert Boes (ETH)
Jean-Noël Saugy, Caroline Roduit (FMV)
Jean Decaix; Maxime Chiarelli, Cécile Münch (HESSO)
Alexandre Bircher (HEX)
Christian Landry, Christophe Nicolet (PVE)

SFOE project coordinator:
Klaus Jorde, klaus.jorde@kjconsult.net, Michael Moser, michael.moser@bfe.admin.ch, Karin Soederstroem, Karin.Soederstroem@bfe.admin.ch

SFOE contract number: SI/502106-01

Résumé

Le secteur hydroélectrique suisse fait actuellement face à des importants défis. La Stratégie énergétique 2050 prévoit une augmentation très ambitieuse de la production annuelle d'ici 2035 et 2050. Dans ce même contexte, les services de régulation du réseau deviennent de plus en plus importants avec l'intégration massive de sources d'énergie renouvelable intermittentes. Enfin, un grand nombre de concessions en exploitation arriveront à expiration au cours des trois prochaines décennies, entraînant d'importants besoins de rénovation. Pour faire face à ces enjeux, HydroLEAP rassemble les principaux acteurs de l'hydroélectricité suisse dans un projet dont les résultats représentent un saut qualitatif vers la réussite de la transition énergétique.

Plus précisément, les développements technologiques nécessaires pour atteindre les niveaux de production hydroélectrique fixés sont appliqués à un ensemble représentatif de centrales hydroélectriques, dans le but de démontrer de manière vérifiable leur impact sur l'amélioration des performances, la réduction des coûts d'exploitation et la minimisation de l'impact environnemental.

Au démonstrateur de pompage-turbinage FMHL, l'optimisation du fonctionnement en court-circuit hydraulique permet une augmentation significative des capacités de régulation du réseau, tout en améliorant le rendement global de la centrale grâce au remplacement des roues Pelton de l'ancienne centrale. De plus, le cycle de maintenance est optimisé par la détermination expérimentale et numérique du véritable coût d'un démarrage d'un groupe hydroélectrique, intégré aux algorithmes existants d'optimisation de la gestion des actifs (Maintenance 4.0). Cette approche est également mise en œuvre au démonstrateur de turbine Francis au fil de l'eau de KW Ernen, en parallèle à la détermination du choix optimal de rénovation dans le cadre d'une nouvelle demande de concession, et à la simulation, le dimensionnement et les essais d'une batterie installée en configuration hybride pour améliorer les services de régulation. Par ailleurs, la manière de minimiser l'impact environnemental d'une nouvelle centrale au fil de l'eau à faible chute et fort débit est illustrée sur le démonstrateur de turbine bulbe Massongex-Bex-Rhône (MBR), où des recommandations sont également formulées sur la manière d'aborder la présence de fortes concentrations de particules abrasives dans les phases de planification et d'appel d'offres.

Enfin, HydroLEAP répond également au besoin d'infrastructures expérimentales de pointe, non seulement pour vérifier indépendamment les gains de performance et les optimisations sur les trois démonstrateurs, mais aussi pour réaliser les mesures complexes indispensables au développement d'algorithmes de maintenance prédictive avancés, pour faire progresser la compréhension des mécanismes physiques en jeu, et, enfin, pour former une nouvelle génération de professionnels de l'hydroélectricité. De telles infrastructures expérimentales présentent une importance majeure pour l'industrie, car elles permettent de valider et de réduire les risques liés à des concepts innovants dans des conditions contrôlées et reproductibles – conditions qui ne peuvent être atteintes dans les centrales commerciales, en raison de contraintes opérationnelles et économiques. Le fait d'implanter cette infrastructure au sein d'un établissement public de recherche garantit la neutralité, un accès à long terme et la possibilité de partager les résultats avec l'ensemble du secteur, plutôt que de les limiter à un seul acteur industriel. Cela favorise la collaboration précompétitive et accélère le transfert de technologies vers l'ensemble des exploitants hydroélectriques. À l'avenir, cette infrastructure servira de plateforme nationale de référence pour tester de nouveaux composants hydrauliques, des systèmes de surveillance numérique et des stratégies d'exploitation hybrides, en soutenant à la fois les projets de R&D industriels et la recherche académique. Cela revêt une importance particulière pour la Suisse, où l'hydroélectricité constitue la colonne vertébrale de la production d'électricité et de la fourniture de flexibilité. Maintenir une position de leader technologique et une excellence opérationnelle dans ce domaine est essentiel pour garantir un système énergétique sûr, durable et compétitif – notamment face à l'intégration croissante des énergies renouvelables variables et à la nécessité accrue de solutions de stockage flexibles. Cette mesure essentielle pour un transfert de connaissances durable garantit que les résultats principaux du projet puissent être reproduits et appliqués à l'ensemble du parc hydroélectrique suisse d'ici 2050. Concrètement, ces résultats sont : la définition des choix de

rénovation idéaux pour augmenter le rendement et la production annuelle, l'identification et l'optimisation du potentiel de fonctionnement en court-circuit hydraulique pour la régulation de fréquence dans les stations de pompage-turbinage, l'optimisation des services auxiliaires par hybridation avec des batteries, la réduction des coûts d'exploitation grâce à des algorithmes avancés de maintenance prédictive, ainsi que la minimisation de l'impact environnemental des nouvelles centrales au fil de l'eau.

Zusammenfassung

Die Schweizer Wasserkraftbranche steht derzeit vor enormen Herausforderungen. Die Energiestrategie 2050 sieht bis 2035 und 2050 einen sehr ambitionierten Anstieg der jährlichen Stromproduktion vor. Gleichzeitig gewinnen Netzdienstleistungen im Zuge der massiven Integration intermittierender erneuerbarer Energiequellen zunehmend an Bedeutung. Schließlich laufen in den nächsten drei Jahrzehnten zahlreiche bestehende Konzessionen aus, was umfangreiche Modernisierungen notwendig macht. Um all dem zu begegnen, bringt HydroLEAP die zentralen Akteure der Schweizer Wasserkraftbranche in einem Projekt zusammen, dessen Ergebnisse einen entscheidenden Schritt in Richtung Energiewende darstellen.

Konkret werden die technologischen Entwicklungen, die notwendig sind, um das angestrebte Produktionsniveau der Wasserkraft zu erreichen, auf eine repräsentative Auswahl an Kraftwerken angewendet – mit dem Ziel, deren Einfluss auf eine gesteigerte Leistung, niedrigere Betriebskosten und eine geringere Umweltbelastung nachweislich zu demonstrieren.

Beim Pumpspeicherkraftwerk FMHL wird durch die Optimierung des hydraulischen Kurzschlussbetriebs die Netzregelkapazität erheblich gesteigert, während gleichzeitig der Gesamtwirkungsgrad der Anlage durch den Austausch der Pelton-Laufräder im alten Kraftwerk verbessert wird. Zudem wird der Wartungszyklus durch die experimentelle und numerische Bestimmung der tatsächlichen Kosten eines Starts eines Aggregats optimiert. Diese werden in bestehende Algorithmen zur Anlagenbewirtschaftung integriert (Maintenance 4.0). Diese Maßnahmen werden auch am Demonstrator KW Ernen (Laufwasserkraftwerk mit Francis-Turbine) durchgeführt – dort zusätzlich mit der Bestimmung der optimalen Erneuerungsoption im Rahmen eines neuen Konzessionsantrags sowie der Simulation, Auslegung und Erprobung einer Batterie in hybrider Konfiguration zur Verbesserung der Netzregelung. Wie sich die Umweltwirkungen eines neuen Niederdruckkraftwerks mit hoher Abflussmenge minimieren lassen, wird am Laufwasserkraftwerks-Demonstrator Massongex-Bex-Rhône (MBR) mit Bulb-Turbinen gezeigt. Dort wird auch beraten, wie mit hohen Konzentrationen erosiver Schwebstoffe in der Planungs- und Ausschreibungsphase umgegangen werden sollte.

Darüber hinaus adressiert HydroLEAP den Bedarf an hochmodernen Versuchsinfrastrukturen – nicht nur zur unabhängigen Verifizierung der Leistungssteigerungen und Optimierungen bei den drei Demonstratoren, sondern auch zur Durchführung komplexer Messungen, die für die Entwicklung fortschrittlicher prädiktiver Wartungsalgorithmen unerlässlich sind. Diese dienen auch dazu, die physikalischen Mechanismen besser zu verstehen und nicht zuletzt eine neue Generation von Wasserkraftfachleuten auszubilden. Solche Versuchsinfrastrukturen sind für die Industrie von grosser Bedeutung, da sie die Validierung und Risikominimierung innovativer Konzepte unter kontrollierten und reproduzierbaren Bedingungen ermöglichen – Bedingungen, die in kommerziellen Kraftwerken aufgrund betrieblicher und wirtschaftlicher Einschränkungen nicht realisierbar sind. Die Ansiedlung dieser Infrastruktur an einer öffentlichen Forschungseinrichtung gewährleistet Neutralität, langfristige Zugänglichkeit und die Möglichkeit, Ergebnisse sektorenübergreifend zu teilen, anstatt sie auf einzelne industrielle Akteure zu beschränken. Dies fördert die vorkompetitive Zusammenarbeit und beschleunigt den Technologietransfer in die gesamte Wasserkraftbranche. Künftig wird die Infrastruktur als nationale Referenzplattform für die Erprobung neuartiger hydraulischer Komponenten, digitaler Überwachungssysteme und hybrider Betriebsstrategien dienen und sowohl industriegetriebene F&E-Projekte als auch akademische Forschung unterstützen. Dies ist insbesondere für die Schweiz von zentraler Bedeutung, da die Wasserkraft das Rückgrat der Stromproduktion und der Bereitstellung von

Flexibilität bildet. Die Aufrechterhaltung der technologischen Führungsposition und der betrieblichen Exzellenz in diesem Bereich ist entscheidend, um ein sicheres, nachhaltiges und wettbewerbsfähiges Energiesystem zu gewährleisten – insbesondere im Hinblick auf die zunehmende Integration fluktuierender erneuerbarer Energien und den wachsenden Bedarf an flexiblen Speicherlösungen. Diese wichtige Massnahme für einen nachhaltigen Wissenstransfer stellt sicher, dass die zentralen Projektergebnisse bis 2050 auf den gesamten Schweizer Kraftwerkspark übertragbar und multiplizierbar sind. Konkret umfasst dies: die Bestimmung idealer Erneuerungsmassnahmen zur Effizienz- und Produktionssteigerung, die Identifikation und Optimierung des hydraulischen Kurzschlussbetriebs für die Frequenzregelung in Pumpspeicherkraftwerken, die Optimierung von Systemdienstleistungen durch Batterie-Hybridisierung, die Reduktion der Betriebskosten durch fortschrittliche Wartungsalgorithmen sowie die Minimierung der Umweltwirkungen neuer Laufwasserkraftwerke.

Summary

The Swiss hydroelectricity sector is currently facing important challenges. The Energy Strategy 2050 is prescribing a very ambitious rise in annual production until 2035 and 2050. In the same context, grid regulation services are increasingly important in the course of a massive integration of intermittent renewable energy sources. Finally, a vast number of operating concessions will expire over the next three decades, leading to extensive refurbishment needs. To cope with all of this, HydroLEAP brings together key stakeholders from the Swiss hydropower industry, in a project whose outcomes represent a significant leap towards achieving the energy transition.

More specifically, the technological developments necessary to bring the hydroelectric generation to the targeted levels are applied to a representative set of hydropower plants, in a goal of verifiably demonstrating their effect on increasing performance, decreasing the operating costs and minimizing the environmental impact.

At the FMHL pumped storage demonstrator, the optimization of the hydraulic short-circuit operation leads to a significant expansion of the grid regulation capacities, while increasing the round-trip efficiency of the plant with a replacement of the Pelton runners at the old power house. Moreover, the maintenance cycle is improved by determining experimentally and numerically the true cost of a hydro unit's start-up sequence, and by integrating it into existing asset management optimization algorithms (Maintenance 4.0). The latter is also performed at the KW Ernen run-of-river Francis turbine demonstrator, besides determining the optimal refurbishment choice in the application process for a new concession, and in parallel to simulating, sizing and testing a battery to be installed in a hybrid configuration for enhanced grid regulation services. Furthermore, the way in which the environmental impact of a new low-head, high-discharge power station can be minimized is illustrated on the Massongex-Bex-Rhône run-of-river bulb turbine demonstrator, where it is also advised how the presence of high concentrations of erosive silt particles should be approached in the planning and equipment tendering phases.

Finally, HydroLEAP also addresses the need for state-of-the-art experimental infrastructures; not only for independently verifying the performance increase/optimization on all of the three demonstrators, but to perform the complex measurements which are instrumental to the development of advanced predictive maintenance algorithms, pushing the boundaries of our understanding of the involved physical mechanisms, and, last but not least, the education of a new generation of hydropower professionals. Such experimental infrastructure is of high significance for the industry, as it enables the validation and de-risking of innovative concepts under controlled and repeatable conditions that cannot be achieved in commercial power plants, where operational and economic constraints limit experimentation. Locating this infrastructure at a public research facility ensures neutrality, long-term accessibility, and the possibility to share results across the entire sector, rather than restricting them to a single industrial stakeholder. This fosters pre-competitive collaboration and accelerates technology

transfer to all hydropower operators. In the future, the infrastructure will serve as a world reference platform for testing novel hydraulic components, digital monitoring systems, and hybrid operation strategies, supporting both industry-driven R&D projects and academic research. This is particularly key for Switzerland, where hydropower represents the backbone of electricity production and flexibility provision. Maintaining technological leadership and operational excellence in this field is essential for ensuring a secure, sustainable, and competitive energy system, especially in light of the increasing integration of variable renewable sources and the growing need for flexible, low-carbon storage solutions. This important measure for a sustainable knowledge transfer ensures that the main outcomes of the project are multipliable and applicable to the entire Swiss hydropower fleet until 2050. Namely, these outcomes are the determination of the ideal refurbishment choices for an efficiency and annual production increase, the identification and optimization of hydraulic short-circuit operation potential for frequency regulation in pumped storage power plants, the optimization of ancillary services provision through battery hybridization, the reduction of operating costs through advanced predictive maintenance algorithms, as well as the minimization of the environmental impact of new run-of-river power plants.

Contents

1 Introduction

1.1 Background information and current situation

The electricity production from hydropower, as prescribed by law (EnG; SR 730.0), is to reach 37'400 GWh by 2035 and 38'600 GWh by 2050[1] (compared to the reference value of 35'350 GWh in 2011). An additional concern of particular importance is caused by the concessions granted to the owners and operators of power stations by the public hand. As illustrated in Figure 1, for many sites representing a large part of the annual hydroelectric production, matters are pressing. Over the coming 30 years, hydraulic concessions worth 23 TWh (or 65% of the annual hydro generation) will expire. The administrational and legal aspects of the renewal procedure, which have to comply, among others, with the Federal Act on the Protection of Waters (Waters Protection Act, WPA), prove to be very complex. On top of these hurdles, the entire technical setup and operational strategy have to be reviewed in detail for each case.

Hydropower is a cornerstone of Switzerland's renewable energy system, yet existing plants face increasing operational, technological, and environmental challenges. Traditional hydroelectric units are often constrained in flexibility, efficiency, and ecological performance, while refurbishment and modernization of a vast number of hydraulic concessions demand cost-effective and reliable solutions. Additionally, the energy transition requires hydropower to actively provide grid ancillary services, increasing demands on dynamic operation and system responsiveness.

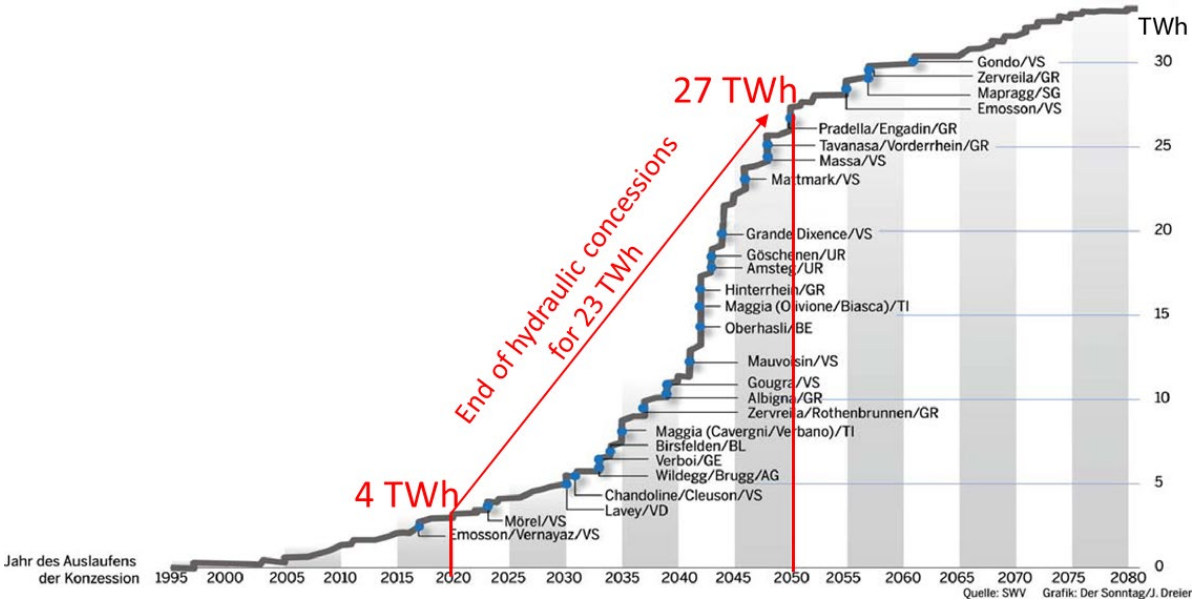

Figure 1 Production annuelle en TWh contre année de fin des concessions hydrauliques.

The hydropower sector is experiencing a paradigm shift as its operation is more and more stressed by variable loads, requests for grid regulation, and compliance with sustainability standards. Hydropower plants have long provided flexibility to the power system and will continue to be a key player in the future energy landscape. Identifying their flexibility potential is crucial: it requires understanding how flexibility

[1] Office fédérale de l'énergie OFEN : Potentiel hydroélectrique de la Suisse. Évaluation du potentiel de développement de la force hydraulique dans le cadre de la Stratégie énergétique 2050 (août 2019).

impacts plant elements and predicting flow phenomena within hydraulic systems for which interdisciplinary approaches using experiments and simulation models are necessary. New methods are needed to consider long-term flexibility services, necessitating accurate vision and potentially smart algorithms for real-time adjustments of the operation. Additionally, smart algorithms for real-time control are required to fully exploit the potential of innovative technologies, such as variable speed and hybridization with batteries, achievable with increased digitalization.

With focus on the hydroelectric units, when hydraulic machines operate in conditions for which they were not designed, they experience an abrupt decrease in efficiency and other severe issues such as vibrations leading to damage of the mechanical components, failures and power swing. These threats are mainly related to flow phenomena and fluid-structure interactions causing pressure fluctuations and instabilities in the hydraulic machine. Another matter for hydraulic machines is the erosion of the components surface due to the collision of sediments in the water flow and leading to wear, premature aging, and impacting on the machine performance. Abundant research activities and industrial developments have been addressing these matters. However, enhancing hydraulic machines performance, flexibility, and surpassing their limitations without impacting on their lifetime poses numerous challenges that current practices and cutting-edge methods cannot efficiently address.

Another threat is about the mitigation of environmental impact for enhanced sustainability. Hydropower potential for sustainability is recognized, yet its environmental impact remains a concern. Despite technological advancements, research gaps persist, hindering efforts to enhance sustainability. Compliance with the Water Directive framework is essential for responsible water management and protecting aquatic ecosystems in hydropower projects. Hydropower operators must adopt best practices for water intake and discharge, implement efficient water recycling systems, and monitor water quality to align with the objectives outlined in the Water Directive. Research is needed to assess the effectiveness of these measures in different contexts and develop new technologies to reduce the impact on the aquatic species, such as development of fish-friendly turbines, and innovative control methods which include water management and the impact on the eco-system, such as hydropeaking.

1.2 Purpose of the project

HydroLEAP presents the current state of hydropower generation, identifies the specific technical challenges and obstacles to achieving a significant production increase, and, most importantly, demonstrates how these challenges can be overcome through a joint effort between industry and academia at three strategically important Swiss hydropower plants. The achievements also contribute decisively to advancing the state of the art in their respective fields.

The project consolidates existing knowledge, develops important aspects of specific relevance to the Swiss market environment. It simultaneously guarantees the long-term existence of a top-level research infrastructure, which is instrumental to sustainably mastering the today and future challenges of the hydropower sector. The innovative core of HydroLEAP lies in the development, testing, and validation of new technologies and operational concepts that enable highly flexible, efficient, and environmentally compatible hydropower. Several new concepts are examined, developed and demonstrated during the four years. The following list contains the main innovations brought forward by the project.

- Flexible operational strategies for existing Pumped Storage Power Plants (PSPP), such as hydraulic short-circuit (HSC) modes and optimized start-stop sequences to enhance grid support while reducing mechanical stress.
- Digitalization and predictive maintenance tools, including the Hydro-Clone digital twin, vibration-based virtual sensors, and machine-learning algorithms for real-time monitoring, performance optimization, and life-cycle management including fatigue, cavitation and erosion issues.
- Battery hybridization for grid regulation to absorb parts of power regulation, prolong mechanical component lifetime and reduce the maintenance costs of the power plant. To the authors

knowledge this has so far not been achieved in Switzerland, making HydroLEAP a unique blueprint for the simulation, sizing and testing of such systems.

- Eco-hydraulic innovations, such as curved-bar racks, foiled bypass geometries, and suspended sediment monitoring, designed to minimize environmental impact while maintaining hydraulic efficiency.
- Novel reduced scale model test procedures. EPFL is home to the world's leading laboratory for the independent testing of reduced scale physical models of turbines, pumps and pump-turbines. The facilities are not only in high demand for contractual model acceptance tests, but an essential tool for basic and applied research as well as an important instrument for the education of tomorrow's engineers. HydroLEAP satisfied the vital need for these installations to be up-to date, in order to develop and investigate the latest technical advances according to modern power system needs.

The project follows a pilot-oriented methodology, structured in four key steps:

- Identifying challenges: HydroLEAP evaluates the operational and environmental limitations of current hydropower plants through advanced simulations, full-scale measurements, and dynamic analysis of flows, transients, and mechanical stresses.
- Designing innovative solutions: Based on these insights, new operational strategies, hybridization concepts, predictive maintenance approaches, and eco-hydraulic designs are developed to overcome existing limitations and enable the next generation of hydropower operation.
- Building laboratory testing infrastructure: The comprehensive modernization of the EPFL Technology Platform for Hydraulic Machines provides a world-class laboratory environment for high-fidelity, reduced-scale testing of turbines, pumps, transient operation, and hybrid energy configurations. This infrastructure allows rapid, safe, and controlled experimentation, bridging the gap between theoretical concepts and field implementation.
- Empirical validation in the lab and field: Innovations are first optimized in the lab under realistic conditions and then validated at three representative Swiss power stations: the 420 MW Forces Motrices Hongrin-Léman (FMHL) pumped-storage plant, the 32 MW KW Ernen run-of-river plant, and the 15.6 MW Massongex-Bex-Rhône low-head facility. These full-scale demonstrations confirm the feasibility, safety, and performance of the proposed solutions, providing proof of concept for broad application.

By combining advanced laboratory infrastructure, innovative operational strategies, digital tools, and field validation, HydroLEAP establishes a pilot framework for modernizing Swiss hydropower. The project demonstrates how flexibility, efficiency, and ecological compatibility can be simultaneously enhanced, providing a model for large-scale deployment and future-proofing of hydropower assets.

1.3 Objectives

HydroLEAP seeks to demonstrate how Switzerland's annual hydroelectric production can be increased and the use of existing capacity modernized and optimized by implementing strategic technological development. The project combines research, laboratory experimentation, and full-scale demonstrations at three representative Swiss power plants to achieve its objectives.

1. Maximize hydroelectric production through optimal refurbishment. HydroLEAP defines best practices for selecting turbine and pump upgrades using advanced decision-making tools. New designs are validated through reduced-scale model testing and numerical simulations, ensuring that performance gains are accurately quantified and providing critical input for the refurbishment of remaining units.
2. Enhance grid flexibility and resilience. The project develops innovative operational strategies, such as hydraulic short-circuit operation at the FMHL pumped-storage plant and hybrid battery-

hydropower configurations at KW Ernen. These strategies are experimentally validated to quantify and extend the provision of ancillary services, enabling safe, efficient, and market-optimized operation.

3. Reduce operational costs through predictive maintenance. HydroLEAP integrates mechanical stress analysis from transient operations into advanced asset management models. Reduced-scale experiments, Computational Fluid Dynamics (CFD) and Finite Element Methods (FEM) allow the estimation of start-and-stop costs and the optimization of maintenance cycles, providing empirical validation for predictive maintenance tools and supporting more efficient life-cycle management.
4. Minimize environmental impact of new low-head hydropower plants. Eco-hydraulic solutions for fish protection, including curved-bar racks and optimized bypass geometries, are developed and tested. Laboratory flumes and numerical modeling are used to evaluate their effectiveness, establishing best practices for environmentally sustainable plant design and operation.
5. Anticipate and mitigate sediment-related issues. HydroLEAP investigates suspended sediment characteristics and turbine erosion potential, particularly at low-head sites such as the Massogex-Bex-Rhone hydropower plant. The findings guide turbine design and operational strategies to enhance sustainability, reduce maintenance needs, and preserve efficiency in sediment-rich rivers.
6. Experimentally validate project outcomes. Laboratory and field experiments provide rigorous validation of simulations, operational strategies, and eco-design solutions, linking innovation to full-scale demonstration, supporting industrial adoption, and training the next generation of hydropower engineers.

Through these objectives, HydroLEAP establishes a pilot framework for modernizing Swiss hydropower, providing empirical evidence of feasibility, efficiency, flexibility, and environmental performance, and setting the foundation for scalable implementation across the national hydropower fleet.

2 Description of facility

2.1 EPFL Technology Platform for Hydraulic Machines

Modernizing hydraulic machinery technology to enhance hydropower resilience against complex system dynamics and evolving flow conditions is a major challenge driven by the energy transition and the need for climate adaptation. Reduced-scale model testing remains essential for addressing these challenges, as it enables high-fidelity replication of full-scale operating conditions.

Within HydroLEAP, this need was addressed through a threefold upgrade of the EPFL Technology Platform for Hydraulic Machines (PTMH)—a facility that, since its establishment in 1969, has been recognized worldwide as a reference center for research in hydraulic machinery and systems. PTMH has long played a pioneering role in performance characterization and flow dynamics assessment across all types of hydraulic machines, combining advanced experimental measurements with numerical simulations. The modernization carried out under HydroLEAP thus represents a major step forward, strengthening PTMH's capacity to support cutting-edge research and innovation in hydropower technology.

The first upgrade focused on Test Rig 1, which was successfully adapted to enable comprehensive investigations of high-head hydropower plants equipped with Pelton turbines. This upgraded facility now allows precise measurements of transient operating modes—including start-up, idle operations, and emergency shut-downs—while offering the flexibility to conduct tests at variable speeds across a broad operating range. HydroLEAP achieved the commissioning of Switzerland's only independent IEC compatible Pelton testing facility, which is a major asset given the critical importance of this turbine type in our energy landscape.

The second major upgrade involved Test Rig 3, representing a pivotal advancement for the study of next-generation hydropower systems. By integrating a Battery Energy Storage System (BESS) and an electrical subsystem capable of emulating realistic grid connections, this facility now provides a unique experimental platform for validating and quantifying the benefits of hybridizing hydraulic units with battery storage. The incorporation of variable-speed technology further enhances the versatility and representativeness of experimental testing.
Finally, the third upgrade was implemented on Platform 2, which underwent modernization of the generator and control systems. This enhancement enables the detailed investigation of transient operations across all types of hydraulic machines, completing the integrated experimental capabilities of PTMH.
Collectively, these developments position PTMH at the forefront of experimental hydropower research, offering unparalleled capabilities to explore and validate innovative technologies supporting the sustainable evolution of the hydropower sector. The successful implementation of Platform 1 for reduced-scale Pelton turbine model testing, Platform 2 for transient operation studies, and Platform 3 for hybrid battery-hydraulic experiments ensures that all experimental objectives of HydroLEAP have been achieved. These advancements not only reinforce the effectiveness of the PTMH experimental platforms but also secure their long-term role in facilitating advanced investigations and training future generations of hydropower professionals.
Beyond the direct outcomes of HydroLEAP, this modernization holds strategic relevance for Switzerland, where hydropower remains the backbone of the national electricity system. The enhanced PTMH infrastructure strengthens the country's ability to address challenges linked to grid flexibility, climate-resilient operation, and digitalization of hydropower assets. It opens new frontiers for research on hybrid energy systems, variable-speed fast ramping, transient operation, advanced monitoring, and model-based control strategies, reinforcing EPFL and Switzerland's position as a global leader in hydropower innovation and as a key contributor to Europe's energy transition.

Upgrade for testing of Pelton turbines

The successful modernization of the independent test rig 1 for testing Pelton turbines, conforming to the IEC60193 standard, represents a noteworthy accomplishment within the Technology Platform for Hydraulic Machines. The hydraulic circuit, neatly designed to align with the current test rig 1, incorporates valves, a tailrace channel with adaptable overflow, and hydraulic instrumentation (flowmeter, sensors, etc) with a nominal pressure capacity of up to 37 bar, making this test-rig suitable for testing Pelton runner under Froude similarity. The previous direct current generator has been replaced with a robust 435 kW asynchronous machine featuring a 4-quadrant full-size frequency converter, enabling reliable transient and variable speed operation.
To generate specific hydraulic energy, four pumps, each with a power rating of 230 kW, operate in parallel, capable of achieving a maximum test head of up to 370 m and a maximum discharge of 0.3 $m^3 s^{-1}$. These pumps have been successfully installed and commissioned. Additionally, a new laser system has been integrated to measure the calibration tank's level, improving accuracy from 1.220 mm with the limnometric method to 0.1601 mm using the laser system. This hydraulic setup has been installed, validated, and commissioned, as shown in Figure 2 and Figure 3. The control system has been also fully updated to perform transient operations and test start-up sequences. It has been exploited to perform the experimental tests of the reduced scale model of the Pelton turbines at FMHL.

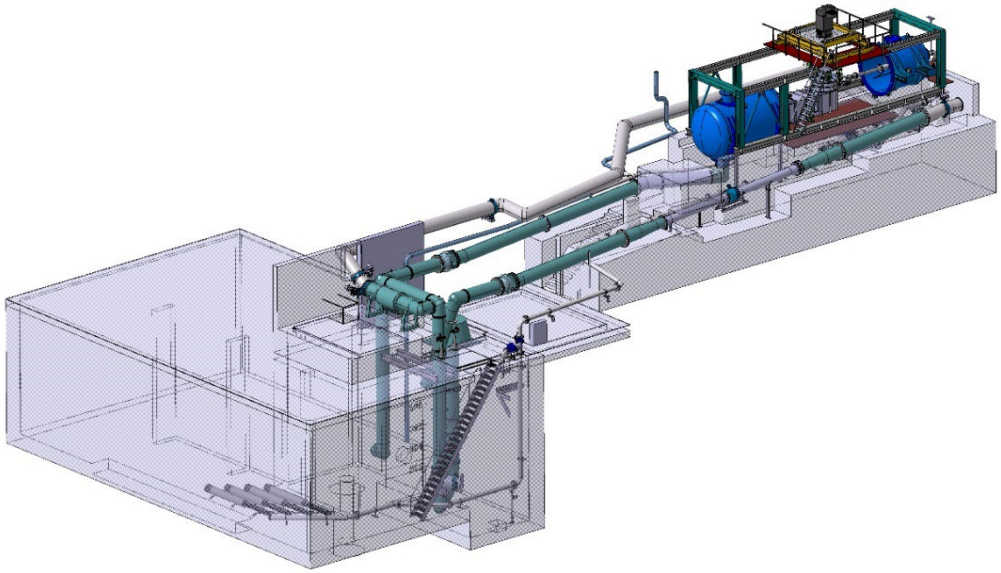

Figure 2: Hydraulic Circuit PF1

Figure 3: Picture of the upgraded PF1+.

Upgrade for versatile transient testing of pumps, turbines and pump-turbines

The upgrade of test-rig 2 has been successfully accomplished, involving the modification of the electrical machine's supporting structure, the installation of advanced instrumentation for measuring main torque and friction torque and the development of a control system to test different transient operations. Furthermore, maintenance activities have been carried out, including the cleaning and painting of the downstream tank, upkeep of the discharge valve, and installation of a new joint. To enhance data acquisition capabilities, a new pressure pulsation acquisition system has been procured. This system enables real-time display of the pressure pulsation signal concurrently with the acquisition of other parameters. Additionally, a monovar valve has been integrated to facilitate online flow calibration at high pressures. It has been exploited to perform the experimental tests of the reduced scale model of the multistage pump at FMHL. A picture of the installation is given in Figure 4.

Figure 4: Front view of the PTMH PF2 test-rig.

Upgrade for battery-hybrid hydroelectric units

The hydraulic test rig 3 has undergone successful modernization, incorporating a BESS and an electrical subsystem capable of simulating a realistic grid connection. A dedicated room has been constructed to house the BESS. Key components, including the grid emulator (REGATRON), the 4-quadrant full-size frequency converter, BESS, and synchronous machine, have been received, installed and commissioned. The carefully connection of these electrical elements has entailed extensive wiring configuration, the installation of safety and security systems, and a control system overhaul. Additionally, a dynamic system for blade opening, in case of testing of Kaplan units, synchronized with the guide vanes opening, has been tested and validated. The test-rig has been firstly validated on a reduced scale model of a Kaplan turbine. An overview of the test-rig additional hardware is illustrated in Figure 5. The experimental campaign of the reduced scale model of the double Francis turbine at Ernen RoR hybridized with a battery energy Storage System was then fully performed.

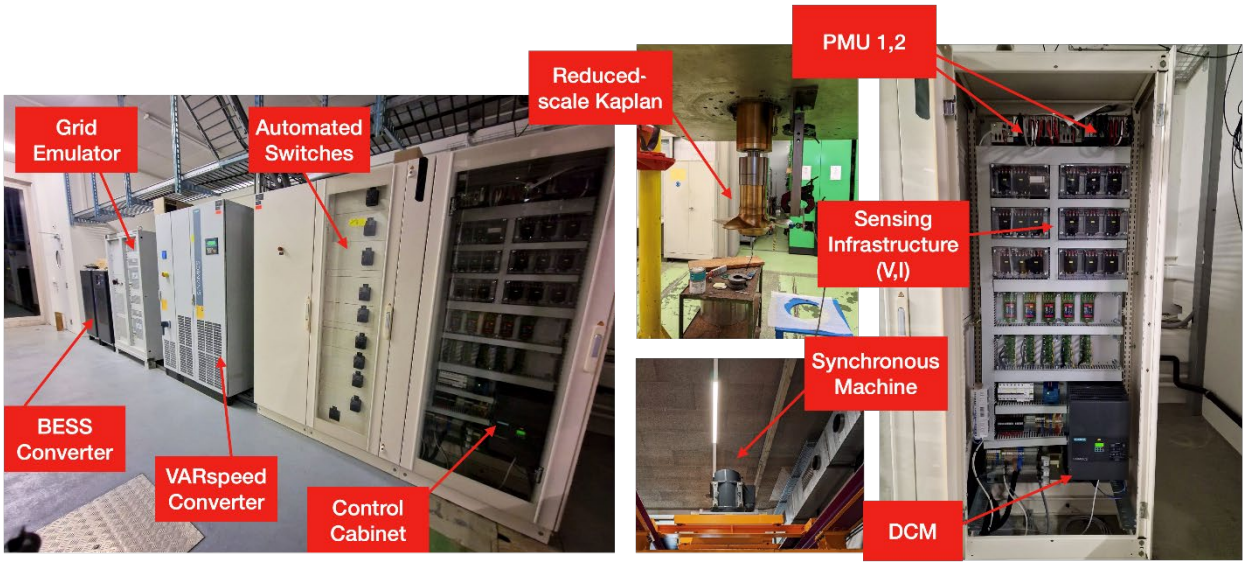

Figure 5: Overview of the hardware allowing for test-rig hybrid operation.

2.2 Forces Motrices Hongrin-Léman (FMHL) Demonstrator

The FMHL hydropower complex represents one of the most advanced pumped-storage installations in Switzerland, located at Veytaux (Canton of Vaud). The demonstrator comprises four 60 MW horizontal units (Units 1–4) commissioned in 1971 and installed in the Veytaux 1 powerhouse, as well as two 120 MW vertical units (Units 5–6) commissioned in 2017 within Veytaux 2. Together, these facilities provide a total capacity of 420 MW, with an additional 60 MW of reserve capacity available at Veytaux 1. Owing to its configuration, broad operating range, and capacity to provide both pumping and generating services, FMHL constitutes an ideal case study for addressing the technical and operational challenges regarding the modernization and flexibility of hydropower assets.

A key aspect of FMHL's operation lies in its provision of primary and secondary frequency regulation services to the Transmission System Operator (TSO). The marketable capacity for ancillary services corresponds to the smallest constantly available capacity in either operating mode—pumping or generating. When operating in pumping mode, these services can only be provided through hydraulic short-circuit operation, which involves the simultaneous operation of pumps and turbines. For safety reasons, this operating mode has historically been restricted to Veytaux 2, and only within the same unit. In this configuration, water pumped from the lower to the upper reservoir partially bypasses the pump outlet and drives the Pelton turbine of the same unit. In theory, this allows each unit to deliver a grid regulation capacity of approximately 85 MW, within a power window ranging from –120 MW to –35 MW (the latter determined by the minimum net discharge through the penstock). However, during transitions between pumping and generating modes, both vertical units at Veytaux 2 must be completely stopped to mechanically decouple or recouple the pumps and turbines, minimizing energy losses during generation. Because hydraulic short-circuit operation between Veytaux 1 and Veytaux 2 is currently not permitted, each mode change results in an approximately one-hour standstill of the entire FMHL facility.

Within HydroLEAP, advanced simulations and experimental investigations were conducted to evaluate and optimize alternative hydraulic short-circuit configurations. The results demonstrate that coupling the hydraulic circuits between Units 5 and 6 of Veytaux 2 would eliminate the need for full plant shutdowns during mode changes. In this configuration, one unit could remain operational in short-circuit mode while the other is being switched, thereby ensuring continuous availability of up to 85 MW of grid regulation capacity over 24 hours. Furthermore, simulations showed that extending short-circuit operation between Veytaux 1 and Veytaux 2 could double the continuously available capacity to about 170 MW, while allowing such operation within Veytaux 1 could further increase regulation capacity up to nearly 300 MW. These configurations, however, depend critically on transient behavior, including pressure fluctuations, surge tank levels, and flow conditions in the station's bifurcations—parameters that were comprehensively assessed during the project.

In parallel, equipment refurbishments at Veytaux 1, such as the replacement of the Pelton runners and the upgrade of the booster pump, have led to measurable improvements in round-trip efficiency and operational stability. Numerical flow simulations and reduced-scale model tests performed at EPFL's PTMH under HydroLEAP provided guidance for the optimal design and operation of these components.

From a system-level perspective, FMHL also served as a testbed for developing data-driven optimization algorithms to enhance operational decision-making. These models integrate not only direct operational costs but also lifetime-related costs associated with transient mechanical loads and component fatigue, offering a more realistic basis for predictive maintenance and flexible operation strategies.

HydroLEAP has achieved the three main objectives in the FMHL Demonstrator:

1. Improving global plant performance through targeted equipment refurbishment;
2. Demonstrating the feasibility and safety of hydraulic short-circuit operation across all possible configurations using advanced numerical tools; and
3. Enhancing operation and maintenance optimization algorithms with data-driven, reliability-informed approaches.

The outcomes demonstrate that FMHL, through both its legacy and upgraded components, remains a strategically important asset for Switzerland's energy transition. Its demonstrated potential for increased flexibility and ancillary service provision highlights new operational frontiers for pumped-storage hydropower—enabling continuous participation in grid regulation markets, improved efficiency, and resilient integration within a renewable-dominated power system.

2.3 KW ERNEN Demonstrator

The KW Ernen (KWE) hydropower plant, located in the Upper Valais, served as the second key demonstrator within HydroLEAP. The facility features two 16 MW horizontal double-Francis units and operates as a run-of-river installation. During HydroLEAP, KWE entered a concession renewal phase, which included a comprehensive refurbishment plan for the entire power plant. This modernization process provided an ideal opportunity to validate HydroLEAP's research outcomes directly within an industrial context.

The KWE installation presents several distinctive characteristics that made it an exemplary demonstrator for hybridization. The plant has been providing primary frequency regulation services for several years, positioning it among the few run-of-river facilities in Switzerland with active participation in grid stabilization. Within HydroLEAP, these services were optimized through the integration of a BESS operating in parallel with the turbines. This hybrid configuration enabled the experimental and numerical assessment of battery-assisted frequency regulation, quantifying the potential performance gains and identifying optimal control strategies. Moreover, KWE is part of a hydraulic cascade, which allowed HydroLEAP to analyse how specific operating patterns and refurbishment strategies at one site influence the performance and flexibility of the adjacent power plants. This system-level perspective proved highly valuable, given that many existing Swiss hydropower plants operate within similar cascaded configurations. The KWE demonstrator therefore provided a representative framework for studying both local and regional effects of flexible operation on flow regulation.

A further element of interest lies in KWE's horizontal double-runner Francis units, each equipped with two draft tubes. This relatively uncommon design was thoroughly analysed to ensure that the findings and optimization strategies derived from HydroLEAP remain generalizable to a wider range of Francis turbine configurations used in Swiss hydropower plants.

Over the course of the project, HydroLEAP successfully achieved the main goals originally set for this demonstrator:

1. Refurbishment planning and validation: Several refurbishment options were assessed through numerical simulations, leading to the identification of the most effective modernization strategy for improving efficiency and operational stability.
2. Hybrid operation with BESS: The feasibility and benefits of battery-supported turbine operation were validated experimentally and numerically. Results confirmed the enhanced frequency regulation capability and reduction of mechanical stress on the turbine during fast response events, establishing best practices for future hybridization projects. Advanced control strategies were developed to minimize environmental impacts while maintaining economic viability.
3. Component lifetime and cost assessment: Detailed monitoring and modelling quantified the specific costs of grid regulation services, both with and without battery support, incorporating mechanical wear, fatigue effects, and expected component lifetime reduction.

In summary, HydroLEAP's work at KW Ernen demonstrated the technical and economic viability of hybrid run-of-river hydropower systems, where conventional turbine-based regulation is enhanced by fast-response battery support. The project established a validated methodology for assessing refurbishment scenarios, quantifying lifetime impacts, and defining operation strategies for hybrid energy systems. These outcomes have direct strategic relevance for Switzerland, offering a replicable model

for upgrading the country's existing fleet of medium-size hydropower plants to meet future flexibility requirements under the evolving energy transition framework.

2.4 Massongex-Bex-Rhone (MBR) Demonstrator

The MBR hydropower plant represents the new-build demonstrator within HydroLEAP demonstrators. The MBR facility is a low-head run-of-river hydropower plant planned on the Rhône River and designed to incorporate the latest innovations in sustainable hydropower development. With an installed capacity of approximately 2 × 7.8 MW, the MBR plant will employ axial bulb turbines specifically designed for high efficiency under variable discharge conditions. The demonstrator's conception within HydroLEAP focused on sustainability, environmental integration, and operational resilience, aiming to establish new design and assessment standards for low-head hydropower projects in Switzerland and beyond.
The scientific work carried out under this work package concentrated on two key areas:

1. Downstream fish protection: Advanced hydraulic and ecological analyses were performed to evaluate and optimize fish-friendly design features, including the layout of bypass systems and intake structures. Numerical simulations and scaled physical model tests were used to quantify flow conditions and fish passage performance, ensuring compliance with emerging environmental regulations.
2. Sediment management and turbine erosion: Particular attention was given to fine-sediment dynamics, which represent a critical issue for low-head schemes on the Rhône. HydroLEAP investigations provided data-driven recommendations for erosion-resistant turbine design, sediment routing strategies, and operational protocols to mitigate wear and efficiency losses over time.

Although the MBR project remained in the pre-construction and approval phase during HydroLEAP, the research activities conducted have produced tangible outcomes for the design and evaluation of future low-head hydropower plants. The methodologies developed for fish protection assessment, sediment management optimization, and environmentally sustainable turbine operation form a transferable framework applicable to many upcoming hydropower licensing processes in Switzerland.
In summary, the MBR demonstrator extends HydroLEAP's scope toward sustainable hydropower expansion, integrating ecological, hydraulic, and technical considerations into the early stages of project design. Its strategic relevance lies in demonstrating that new hydropower capacity can be added responsibly, with minimized environmental impact and maximized long-term operational performance, thus supporting Switzerland's dual goals of energy transition and biodiversity protection.

3 Procedures and Methodology

The methodological framework of the HydroLEAP project was structured to ensure a coherent approach combining experimental, numerical, and field investigations. The work to reach the project goal and objectives was organized by addressing specific technological challenges in pumped-storage, medium-head, and low-head hydropower plants. The overall methodology relied on the integration of advanced hydraulic modelling, real-scale monitoring, digital twin technologies, and laboratory testing, with the aim of improving operational flexibility, efficiency, and environmental sustainability of Swiss hydropower assets.
Across all demonstrators, HydroLEAP adopted a consistent methodological framework based on integration and validation. Numerical simulations were always coupled with laboratory and field measurements to ensure reliability and scalability of results. Digitalization through digital twins and data-driven predictive maintenance enabled continuous improvement and monitoring of hydropower performance and sustainability.

This rigorous multi-layered methodology ensures that the project outcomes are both scientifically robust and directly applicable to the modernization of the Swiss hydropower fleet, supporting the objectives of the Swiss Energy Strategy 2050 and the long-term flexibility of the national power system.

3.1 Performance, flexibility, and lifetime enhancement for existing high head pumped-storage power plants

The FMHL demonstrator served as a large-scale testbed for developing and validating innovative operation strategies in pumped-storage systems including HSC operation. The procedures combined high-fidelity computational modelling, reduced-scale model testing, and field validation under real operating conditions.

- 1D Transient Numerical Simulations: 1D simulations were performed to evaluate dynamic pressure transients, identify potential water hammer phenomena, and optimize valve closure and opening sequences. These results guided the definition of safe operating envelopes and control strategies for HSC transitions to maximize plant flexibility.
- 3D Numerical Modelling: More than 150 steady-state and transient CFD simulations were conducted to analyses internal flow structures, head losses, and flow quality under various operating modes. Advanced turbulence models and multiphase flow representations were used to capture the complex interaction between turbine and pump circuits during simultaneous operation.
- Digital Twin Development and Validation: Parallel to physical testing, a digital twin of the FMHL plant—Hydro-Clone—was deployed. The methodology combined real-time SCADA data acquisition with physics-based simulation models to reproduce plant behavior under dynamic conditions. The twin was calibrated using transient tests and subsequently used to predict system response during HSC operations. The Hydro-Clone framework employs data assimilation algorithms to continuously synchronize simulation results with live measurements, thus enabling real-time monitoring and early anomaly detection. The validated digital twin has become a key component of the plant's predictive maintenance architecture, demonstrating the value of hybrid data–model approaches in asset management.
- On-Site Experimental Validation: Selected configurations were validated through instrumented field campaigns at the FMHL site. High-frequency measurements of pressures, water levels, and vibrations were acquired under controlled HSC operating sequences. The comparison between measured and simulated results confirmed the reliability of the models and the feasibility of both HSC2 and HSC3 configurations for practical implementation.
- Model-Scale Testing for Fatigue Assessment: To evaluate the mechanical response of hydraulic machines during transient operation, dedicated model-scale tests were performed on both Pelton turbines and multistage pumps.
- Full-Scale Dynamic Condition Monitoring: To translate the laboratory findings into full-scale applications, a non-intrusive condition monitoring technique was developed based on FEM simulations to predict the modal properties of the Pelton runner and Experimental Modal Analysis (EMA) coupled to transmissibility tests to validate these results in situ.

3.2 Grid flexibility through hybridization of medium-head run of river power plants

The activities focused on developing, testing, and validating advanced methodologies for the optimization and hybridization of hydroelectric systems, taking the KW Ernen demonstrator as a reference case. The work combined numerical modeling, experimental testing, and data-driven diagnostics to assess performance improvements, mechanical reliability, and environmental effects

under hybrid operation with an integrated BESS. The main procedures and methodologies applied are summarized below:

- Refurbishment Strategy and Modeling: Selection and validation of an optimized 6.14 MW Pelton turbine using the RENOVHydro modeling library, achieving increased energy production, cost-effectiveness, and reduced sediment-induced wear.
- Hybrid System Simulation and experimental validation: Use of Simsen–Python co-simulation and reduced-scale model testing to assess the joint operation of the turbine and a BESS for providing ancillary services such as Frequency Containment Reserve.
- Advanced Control Implementation: Application of Model Predictive Control (MPC) for BESS optimization, leading to improved dynamic response, halved guide vane movements, and reduced pressure fluctuations.
- P Field Testing and Diagnostics: Introduction of a Vibration Content Index and machine learning–based virtual sensors for early detection of damaging patterns and fatigue risks due to cavitation, enabling predictive maintenance and reduced operational costs.
- Environmental and Hydropeaking Analysis: Simulation of hydropeaking behavior and revenue optimization for KW Ernen and KW Mörel, confirming increased energy yield and improved responsiveness with minimal environmental impact.

3.3 Low-Head Hydropower and Environmental Integration

The MBR low-head demonstrator focused on optimizing hydropower design under environmental constraints. The methodological approach integrated 3D numerical simulations, etho-hydraulic experiments, and sediment transport analysis to ensure fish-friendly and sustainable operation.

- Fish Protection and Guidance Systems: Three-dimensional CFD models of Curved-Bar Rack – Bypass Systems (CBR-BS) and Horizontal Bar Rack – Bypass Systems (HBR-BS) were developed to evaluate flow fields, pressure distributions, and fish guidance efficiency. Parametric studies were conducted to assess different rack inclinations, spacing, and bypass positions, optimizing for hydraulic performance, driftwood management, and constructability. Live-fish experiments were carried out using Brown Trout and Common Barbel in an ethohydraulic flume. Passage efficiencies were determined for different bypass inlet designs and flow conditions, providing empirical validation for the numerical models and yielding prototype-scale design recommendations.
- Sediment Management and Erosion Studies: sediment load characterization and turbine erosion assessment were performed. The methodology combined field measurements of suspended sediment concentration (SSC) with empirical and numerical erosion models. Alternative mitigation measures, such as advanced turbine coatings and adaptive operation strategies, were simulated to minimize wear during high-SSC events. Recommendations were formulated for real-time SSC monitoring and operational shutdown thresholds to balance production with long-term asset protection.

4 Activities and results

4.1 Performance, flexibility, and lifetime enhancement for existing high head pumped-storage power plants – the FMHL demonstrator

4.1.1 Stretching flexibility: Definition of hydraulic short-circuit feasible operations

HSC operation refers to configurations in which water circulates between turbines and pumps within a power plant in a way to modulate the net power exchange with the grid. The main advantages of HSC operation are to enable ancillary services in pump mode and improve the overall flexibility of the asset by enabling faster switching between operational modes and increased operating ranges.
Different HSC configurations are possible depending on the asset layout:

- **Intra-unit - HSC1**: between the pump and turbine of a single unit, if the asset is composed of ternary units, (red arrow, Figure 6)
- **Inter-unit - HSC2**: between a unit in pump mode and a unit in turbine mode, within a powerplant (green arrow, Figure 6)
- **Inter-plant - HSC3**: between a plant in pump mode and a plant in turbine mode, if the asset is composed of different plants (blue arrow, Figure 6)

The FMHL asset is composed of 2 plants, Veytaux I and Veytaux II, each composed of respectively 4 and 2 ternary units, which makes all three HSC configurations technically possible.

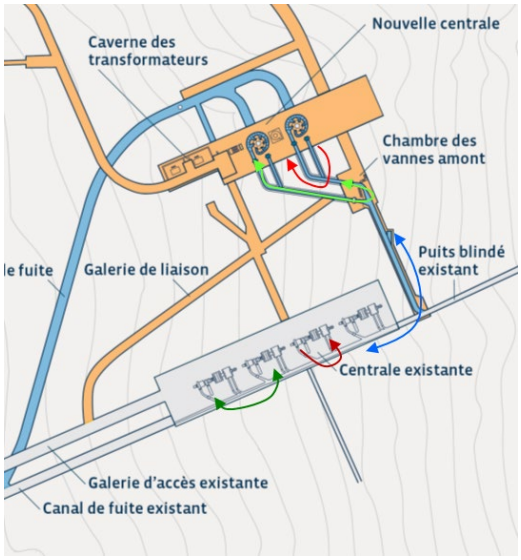

Figure 6 : Illustration of the 3 different Hydraulic Short Circuit (HSC).

Each HSC configuration at FMHL has different operational statuses, expected benefits, and implementation priorities:

HSC1 – Intra-unit short circuit

- Operational status: In Veytaux II, HSC1 is currently operational with restrictions on the operating range due to jet quality limitations. In Veytaux I, this configuration is currently not permitted.
- Benefits: This mode would extend the range of ancillary services that each unit can provide.

- Scope: For Veytaux II, the priority is high, as extending the operating range would be a relatively simple implementation. For Veytaux I, the priority is low, this configuration is not considered in the study.

HSC2 – Inter-unit short circuit

- Operational status: The short circuit between units is currently not permitted in either Veytaux I or Veytaux II.
- Benefits: This mode would increase the range of ancillary services available at FMHL. By enabling concurrent operation of units in pump and turbine modes it also allows for more flexible start/stop sequences and reduced transition times.
- Scope: For Veytaux II, the priority is high, and this mode has been studied in detail. For Veytaux I, the potential is lower; the configuration is only studied for short-term transitions to support faster mode switching.

HSC3 – Inter-plant short circuit

- Operational status: The short circuit between Veytaux I and II is currently not permitted.
- Benefits: This mode would extend the range of ancillary services that FMHL can provide. Furthermore, by allowing one plant to operate in pump mode and the other in turbine mode, it opens the possibility of FMHL operating in islanded mode.
- Scope: The potential is important, and this configuration is studied in detail.

Hydraulic short circuit operation involves multiple units operating in different modes simultaneously, which can introduce several technical challenges:

- Hydraulic transients:
  - Multiple start-ups, shutdowns, or emergency shutdowns from different units operating in pump and turbine modes can combine into sequences that push the waterway into critical states (overpressure, under pressure, or excessive water levels in the surge tank).
  - To prevent these issues, different transient studies are carried out to evaluate the risk of such critical sequences, and, if required, modifications are suggested to mitigate these risks
- Flow quality degradation:
  - Waterway bifurcations are generally designed for unidirectional flow—either all units turbining or all units pumping. HSC operation introduces reversed and complex flow paths, often not originally anticipated in the design, leading to punctual head losses. Additionally, water being turbined may have passed through a pump, potentially carrying disturbances, leading to jet quality degradation (e.g., cavitation, reduced efficiency).
  - To assess these effects, CFD simulations are used to evaluate head losses and flow behaviour under each HSC scenario.
- High frequency phenomena:
  - Transient simulations typically resolve system behaviour up to ~10 Hz, but they do not capture higher frequency effects such as pressure pulsations or vibration modes, which may become critical during HSC operation.
  - To address this, **on-site tests** have been conducted with high-frequency monitoring equipment installed at key locations in the hydraulic circuit, providing insights into phenomena beyond the simulation bandwidth.

4.1.2 1D Transient simulations for HSC feasibility

Transient analysis was carried out for the 3 types of HSC by using the 1D SIMSEN model of FMHL hydropower plant. Different limitations were highlighted.

HSC1 – Intra-unit short circuit

For Veytaux 1, this operating mode is not a priority with a preliminary study revealing a number of limitations.

For Veytaux 2, the current limitation of the operating range is the result of a poor quality of the flow at the turbine inlet and increased temperature due to recirculation. This mode was not further investigated in transient studies, but the jet quality was investigated through CFD and on test sites were carried out to quantify the water heating

HSC2 – Inter-unit short circuit

For Veytaux 1, the transient analysis revealed high static pressure at the bottom of the penstock when a peak of Michaud occurs few seconds after a pump emergency shutdown, see Figure 7. The maximum pressure could be reduced if the number of injectors required to start the turbine were reduced from 4 to 2. This solution needs to be analysed as it has a direct impact on shaft fatigue during the start-up sequence.

For Veytaux 2, no limitations were identified, and on-site tests were carried out to confirm the simulation results.This measurement campaign also enables to check whether any protection measures not modelled with SIMSEN software have been defined in the pumped storage power plant.

HSC3 – Inter-plant short circuit

The transient studies have revealed different limitations (load case B2). In order to reduce the maximum static pressure at the bottom of the penstock, the first slope of the closing time of pump valves P5 and P6 must be increased from 7.2s to 8s, see Figure 8. The operating time of the turbine injectors for Veytaux I need to be increased from 32.0s to 42.5s, see Figure 9. These new closing times have an impact on the responsiveness of the PSPP for ancillary services and Alpiq will have to analyse the advantages and disadvantages of these changes.

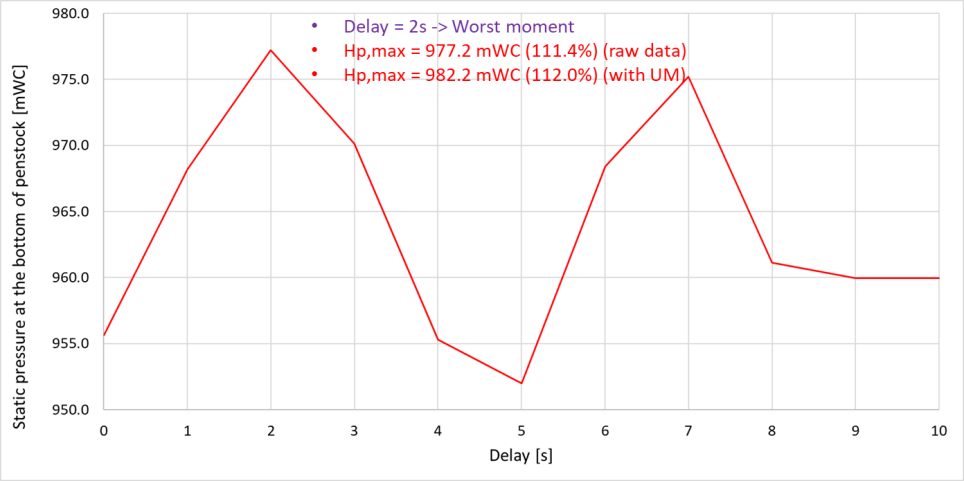

Figure 7: Maximum static pressure at the bottom of the penstock when a peak of Michaud occurs few seconds after a shutdown of a pump.

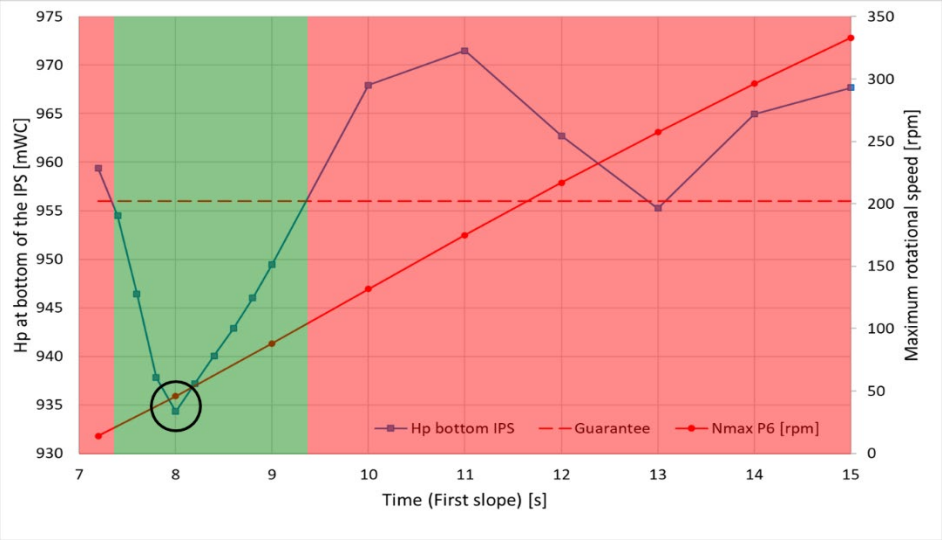

Figure 8: Sensitivity analysis for different closing time of the MIV during an ESD of the 2 pumps P5+P6. The static pressure at the bottom of the penstock is the blue line (left axis) and the maximum rotational speed is the red line (right axis).

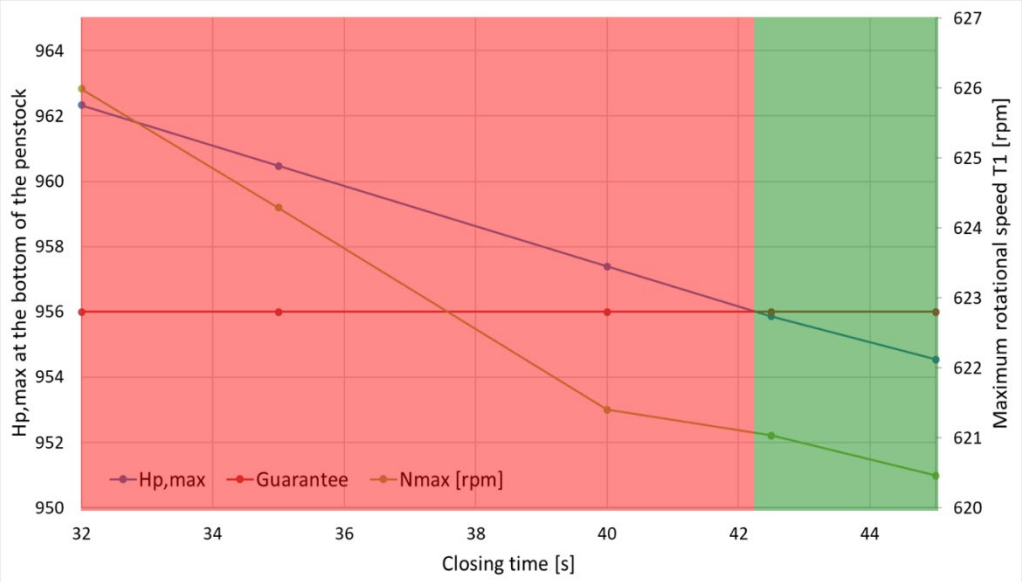

Figure 9: Sensitivity analysis for different closing times of the Pelton turbine at Veytaux I for the load case B2. The static pressure at the bottom of the penstock is the blue line (left axis) and the maximum rotational speed is the red line (right axis).

4.1.3 3D Numerical simulations for HSC feasibility

HSC modes in Veytaux II and HCS3 modes between Veytaux I and Veytaux II

CFD simulations have been conducted for three bifurcations in FMHL: intra-unit and inter-unit in Veytaux II, inter-plant between Veytaux I and Veytaux II. Each HSC mode is investigated at various flow rate corresponding to 0%, 33%, 66% and 100% of pumped flow rate deviated to the turbine:

- 0%: all the discharges are pumped to the upper reservoir of Hongrin,
- 66%: current highest ratio of pumped discharge that can be deviated to the turbine for the HSC2 mode in Veytaux 2, 33% goes to the upper reservoir
- 100%: all the pumped discharge is deviated to the turbine(s) no water goes to the

Table 1 summarises the simulated scenarios, the pumped discharge and the HSC rate. In total around 150 simulations have been performed to embrace all the configurations.

HSC mode configuration	Pumped discharge in $m^3.s^{-1}$	HSC discharge ratio in %
Intragroup	12.4	0 / 33 / 66 / 100
Intergroup: from group 5 to group 6	12.4	0 / 33 / 66 / 100
Intergroup: from group 6 to group 5	12.4	0 / 33 / 66 / 100
Interplant from Veytaux I to Veytaux II	13.4 / 26.8	0 / 33 / 66 / 100
Interplant from Veytaux II to Veytaux I	12.4 / 24.8	0 / 33 / 66 / 100

Table 1: List of HSC mode configurations investigated by CFD at FMHL.

An example of the flow in each of the bifurcations can be seen in Figure 10 where the streamlines are highlighted. For the HSC1 mode in Veytaux 2 (Figure 10a), the streamlines are rolling up in both directions, for the two other cases, this feature is less pronounced or even absent.

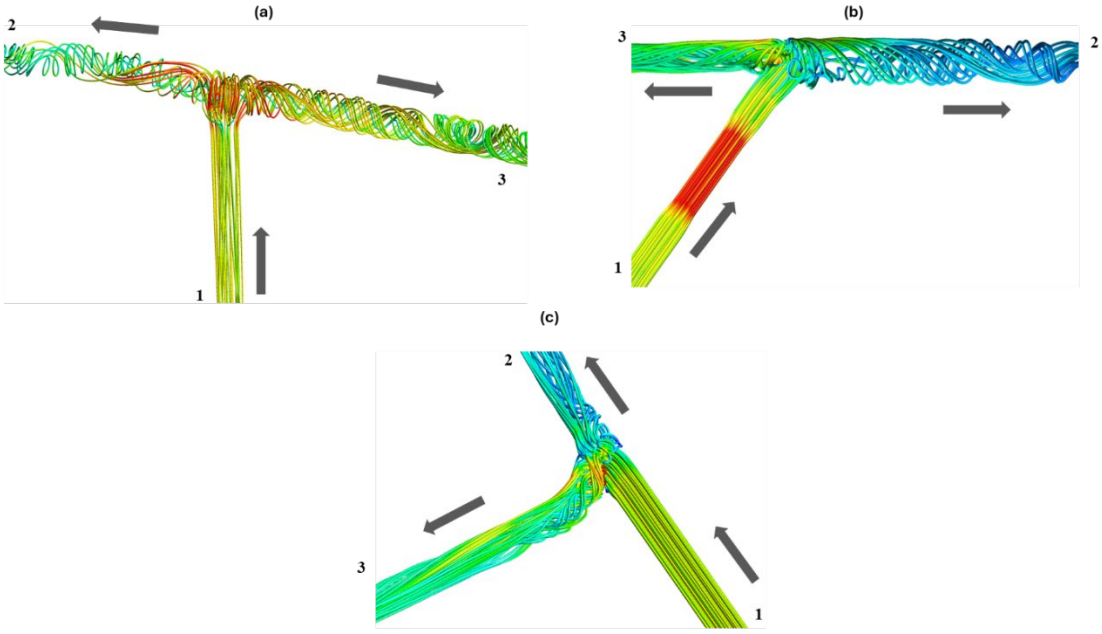

Figure 10: Streamlines coloured by the velocity (blue correspond to zero velocity and red to velocity around 10 $m.s^{-1}$) for the three HSC short circuit modes at a discharge ratio of 66%. (a) HSC1 mode for the u 5 of Veytaux 2. (b) HSC2 mode between the group 5 and 6 of Veytaux 2. (c) HSC3 mode between Veytaux 1 and Veytaux 2. The number 1 refers to the pipe towards the pump, the number 2 to the pipe towards the upper reservoir and the number 3 to the pipe towards the turbine. The grey arrows indicate the direction of the flow.

The head loss coefficient and the helicity in direction of the turbine, the most critical criteria of performance of the HSC, are reported in Table 2 and Table 3 for all the scenarios, allowing to compare their performance. All the results are normalized by the intragroup HSC mode at 66%, which is currently the highest rate of HSC allowed (value set at 100). The head loss coefficients of all the inter-unit and inter-plant HSC configurations are lower than the intra-unit HSC, only the inter-unit HSC56 at 100% the coefficient reaches 95%. All the inter-unit and inter-plant HSC generate less helicity than the intra-unit HSC.

Discharge ratio in %	Intra-unit at Veytaux 2	Inter-unit Veytaux 2		Inter-plant between Veytaux 1 and Veytaux 2			
		Between G5-G6	Between G6-G5	50% of pumped discharge		100% of pumped discharge	
				V1 to V2	V2 to V1	V1 to V2	V2 to V1
33	105	53	47	46	39	44	38
66	**100**	74	50	45	48	43	45
100	118	95	77	70	71	69	68

Table 2: Head losses between the pipe towards the pump and the pipe towards the turbine for each HSC mode investigated by CFD. The head losses for the intragroup HSC mode at Veytaux for a discharge ratio of 66% are arbitrary set to a reference value of 100.

Discharge ratio in %	Intra-unit Veytaux 2	Inter-unit Veytaux 2		Inter-plant between Veytaux 1 and Veytaux 2			
		Between G5-G6	Between G6-G5	50% of pumped discharge		100% of pumped discharge	
				V1 to V2	V2 to V1	V1 to V2	V2 to V1
33	33	4	14	3	1	5	2
66	**100**	17	23	6	5	13	9
100	214	45	82	12	7	43	16

Table 3: Helicity in the pipe toward the turbine for each HSC mode investigated by CFD. The helicity for the intragroup HSC mode at Veytaux for a discharge ratio of 66% is arbitrary, set to a reference value of 100.

Based on these results and compared with the currently HSC configuration permitted, both the inter-unit and the inter-plant HSC configurations could operate without risk. Best performances are expected in terms of head losses and flow disturbance by operating the HSC interplant configuration. The inter-plant HSC seems to be the most interesting mode from a point of view of the intensity of the secondary flow. The HSCI at 100% recirculation shows a 18% increase in head losses and more than 2x intensity of secondary flows. This corroborates the current limit of 66% percent based on jet quality. However, only a prolonged test at higher HSC rates could tell the actual consequences on the turbine.
Detailed analyses are available in Decaix et al. 2022, in Decaix et al. 2023 and in Decaix et al. 2024.

HSC modes at Veytaux I

In Veytaux I, only the HCS2 mode was considered and the study is limited to transient operations allowing for faster switching between operating modes. Consequently, the study was limited to checking the flow quality (unsteadiness) at the inlet of the Pelton manifold for a select number of configurations (between units 2 and 3). It was found that whatever the direction of the flow, the streamlines roll up in the manifold (see Figure 11). However, the flow swirl in the Pelton distributor is weak. Consequently, for a limited operating time, such as the one expected for mode transition, it is not expected that flow disturbances will impact negatively the behaviour of the units.

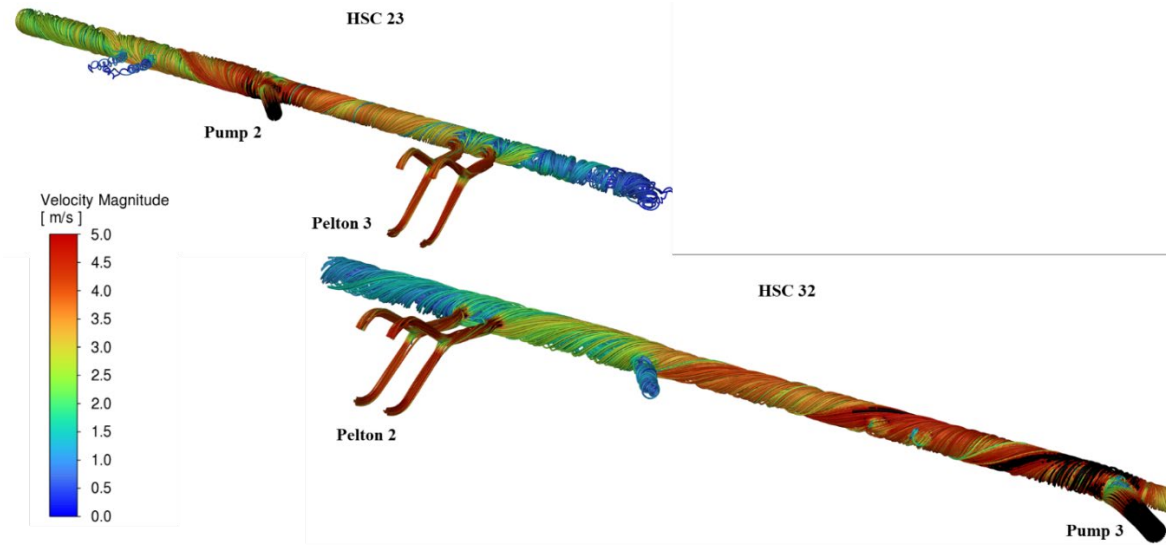

Figure 11: Streamlines coloured by the velocity magnitude for the HSC mode between the group 2 and 3 of Veytaux 1 and vice-versa.

4.1.4 Digital Twin development for real time monitoring

Hydro-Clone is a digital twin of the hydropower plant, based on a soundly calibrated and validated numerical model. This advanced monitoring tool can reproduce any dynamic behaviour of the plant in real time, given the boundary conditions measured in situ. Following a review of the availability of certain signals, 190 signals were finally added to the exchange list between the SCADA and Hydro-Clone. The signal integrity and sampling rate have been verified, as shown in Figure 12, which displays the new surge tank water level and penstock discharge on 1 August 2023 as recorded in the Hydro-Clone database. This digital twin was a very useful digital tool enabling real-time verification of pressures along the waterway and water levels in the upstream surge tank during the on-site tests.

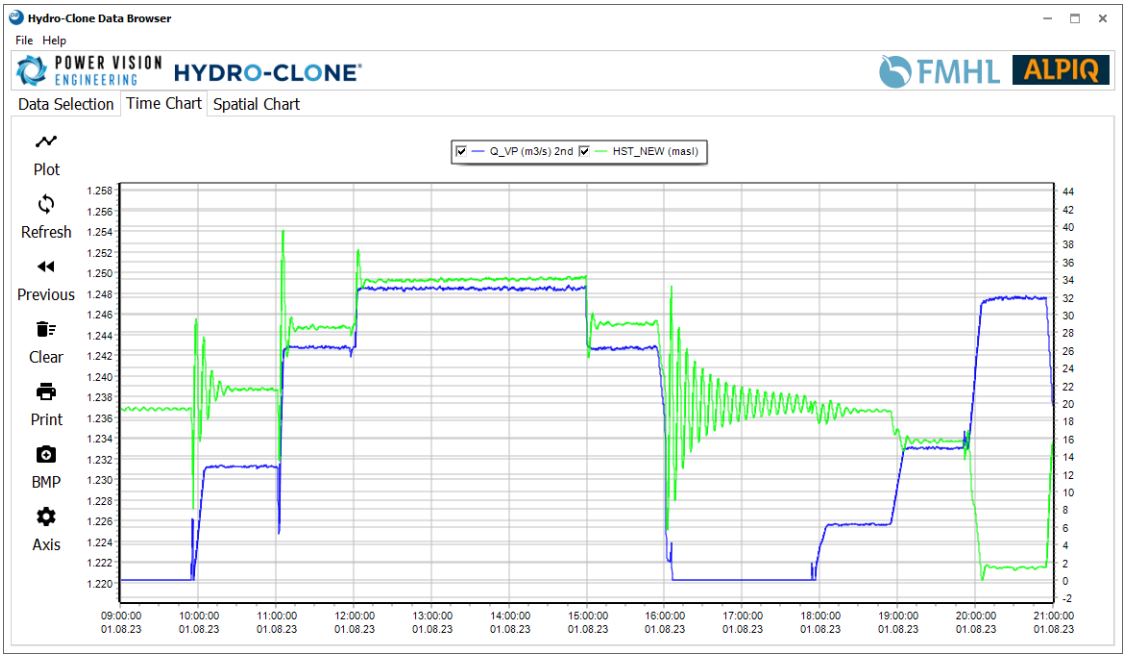

Figure 12. FMHL+ new surge tank water level and penstock discharge on 1 August 2023 as recorded in the Hydro-Clone database.

4.1.5 On-site validation and demonstration of extended flexibility including HSC operation

The aim of the on-site measurement campaign is to analyse the new intra-unit, inter-unit and inter-plant hydraulic short-circuit modes. Vibrations, pressure fluctuations and transients were measured during the test campaign and compared with the current pump and turbine modes. The tests also highlighted whether new protections need to be defined in the control system.
During these tests, the following measurement systems were used:

- The digital-twin Hydro-Clone software was deployed, enabling real-time verification of pressures along the waterway and water levels in the upstream surge tank.
- High frequency data acquisition was deployed on site to record the pressure fluctuations at the main valve of both units.
- High frequency vibration data was extracted from the Vibrosight monitoring system.

HSC2 – Inter-unit short circuit

The following sequences were performed to study the HSC2 hydraulic short circuit, see Figure 13:

1. Loading of the turbine T6 with steps of 10% of power every 5 min. Then, normal shutdown of the unit.
2. Loading of the turbine T6 with steps of 10% of power every 5 min. The pump P5 is in operation during the sequence. Finally, the injectors of unit T5 are closed.
3. Loading of the turbine T6 to rated power. Then, the emergency shutdown of the turbine after 30min. The pump P5 was in operation during the sequence.
4. Normal shutdown of the pump P5 after 30min. Turbine T6 is in operation during the sequence.
5. Emergency shutdown of the pump P5 after 30min. The turbine T6 is in operation during the sequence.
6. Simultaneous emergency shutdown of both units after 30min.

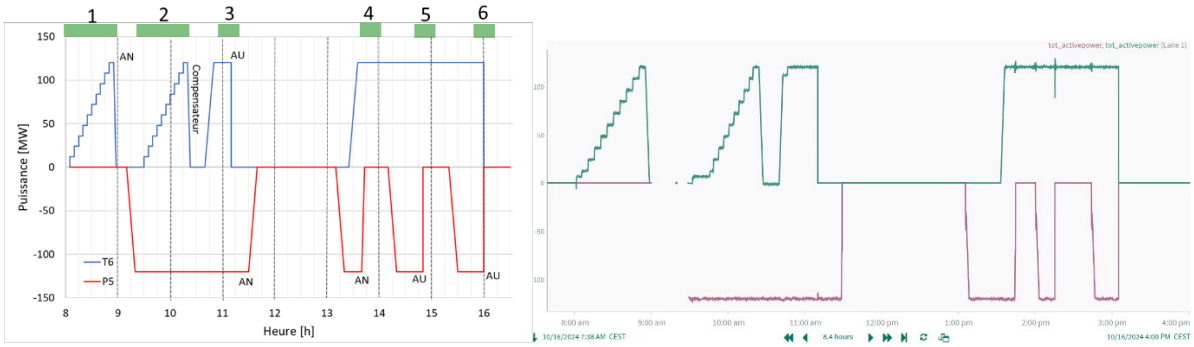

Figure 13: Planned (left) and measured (right) power output from both units of Veytaux 2 during the **HSC2** tests.

HSC1 – Intra-unit short circuit

The following sequences were performed to study the HSC1 hydraulic short circuit, see Figure 14:

1. Loading of the turbine T6 with steps of 15MW every 5 min. The maximum power T6 is 85MW. The turbine T5 is in operation at 120MW. Finally, normal shutdown of the turbine T5.
2. Loading of the turbine T5 with steps of 12MW every 5 min. The maximum power T5 is 120MW. The unit G6 is operated in intra-group at -35MW. Finally, emergency shutdown of the turbine T5 after 60min.
3. The turbine T6 operates at 85MW. Loading of the turbine T6 with steps of 5MW every 5 min. Finally, simultaneous normal shutdown of unit T6/P6.

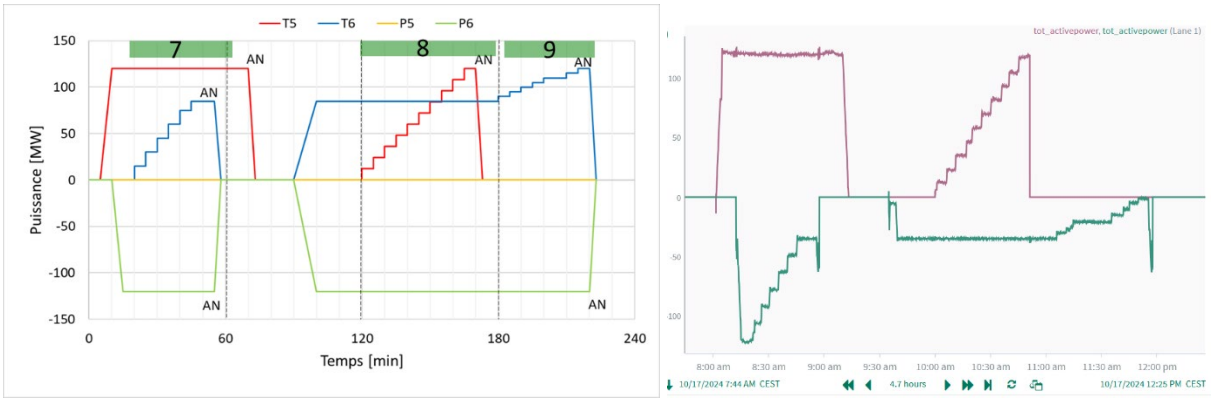

Figure 14: Planned (left) and measured (right) power output from both units of Veytaux 2 during the **HSC2/HSC1** tests on October 17th.

HSC3 – Inter-plant short circuit

The following sequences were performed to study the HSC3 hydraulic short circuit, see Figure 15.

1. The pumps P2-P3-P4 are in operation. The turbine T6 operates at 120MW. Finally, simultaneous emergency shutdown of the 3 pumps P2-P3-P4.
2. The pump P2 is in operation. The turbines T5-T6 are operated at 120MW. Finally, simultaneous emergency shutdown of the 2 turbines T5-T6.
3. The pumps P5-P6 are in operation. The turbine T2 operates at 60MW. Finally, simultaneous emergency shutdown of the 2 pumps P5-P6.
4. The pump P6 is in operation. The turbines T2-T3-T4 are operated at 60MW. Finally, simultaneous emergency shutdown of the 3 turbines T2-T3-T4.

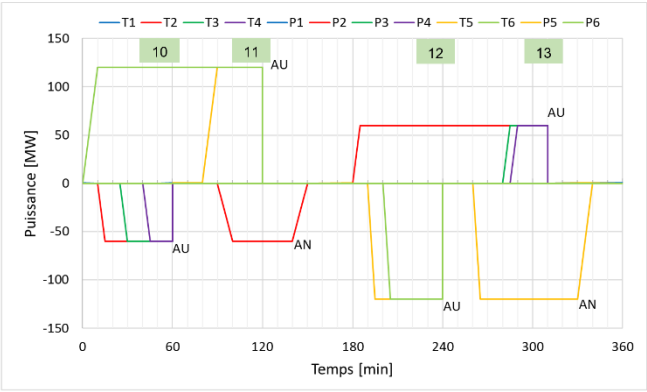

Figure 15: Planned (left) and measured (right) power output from all units of Veytaux 1 + 2 during the **HSC3** tests on May 5th.

The analysis of these two measurement campaigns pointed out that the HSC1, HSC2 and the HSC3 hydraulic short-circuits can be operated on Veytaux 2. The analysis has revealed the following points:

- The emergency shutdown of the pump P5 has a large impact on the turbine T6 (sequence 5). The power of the turbine varies by 44.77MW (37.3% of the rated power) for a few seconds. The static pressure at the spherical valve drops by 187.7mWC, see Figure 16. No protection was activated and the turbine T6 continued production.
- During the sequence 9, the unit G6, operating in intra-group mode, was fixed for 15 minutes at a turbine flow rate equal to the pumped flow rate, in order to analyse changes in water temperature, see Figure 17. The temperature increased by 2.6 degrees in 1 hour and 50 minutes, see Figure 18. However, this increase is probably not linear.

- The emergency shutdown of the pumps P2-P3-P4 has a large impact on the turbine T6 (sequence 10). The power of the turbine varies by 55.45MW (46.2% of the rated power) for a few seconds. The static pressure at the spherical valve drops by 228.3mWC, see Figure 19. No protection was activated and the turbine T6 continued production.

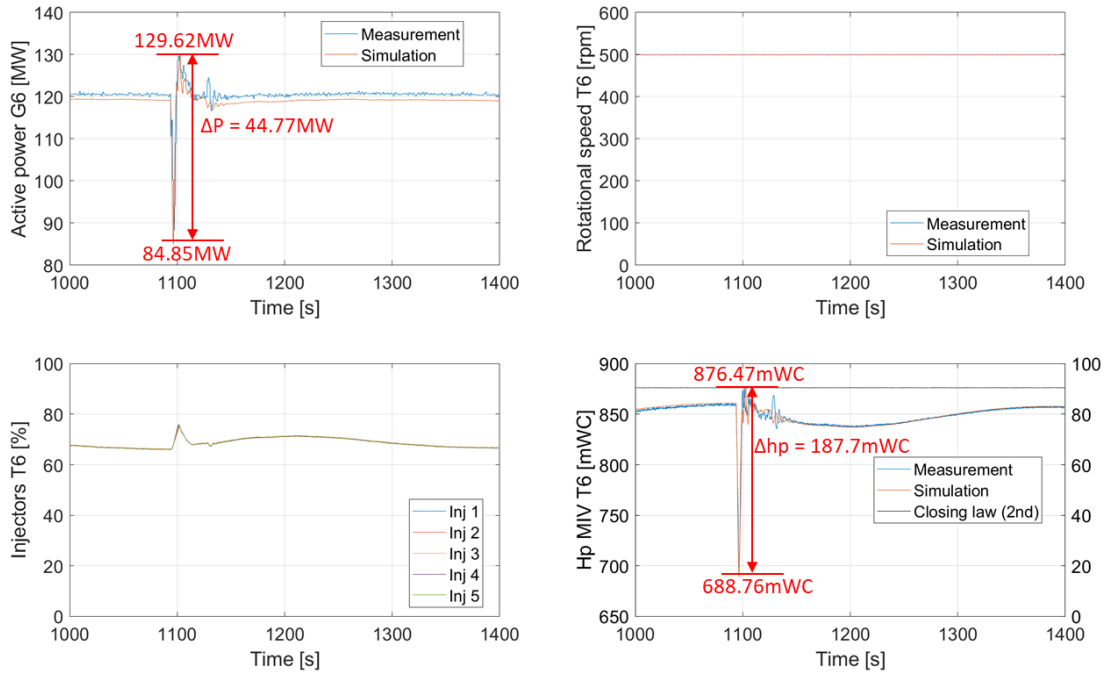

Figure 16: Active power of the unit G6 in MW (top left), Rotational speed of the turbine T6 (top right), Injectors position for the turbine T6 (bottom left) and Static pressure at the spheric valve of the turbine T6 in mWC (bottom right) for the sequence 5.

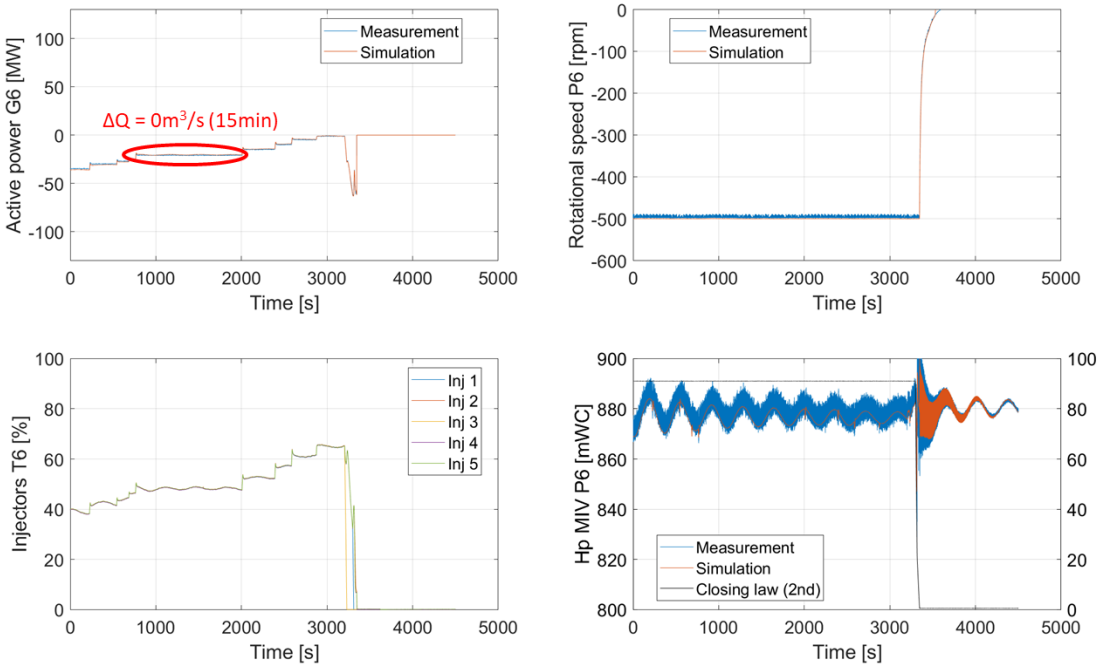

Figure 17: Active power of the unit G6 in MW (top left), Rotational speed of the pump P6 (top right), Injectors position for the turbine T6 (bottom left) and Static pressure at the spheric valve of the pump P6 in mWC (bottom right) for the sequence 9.

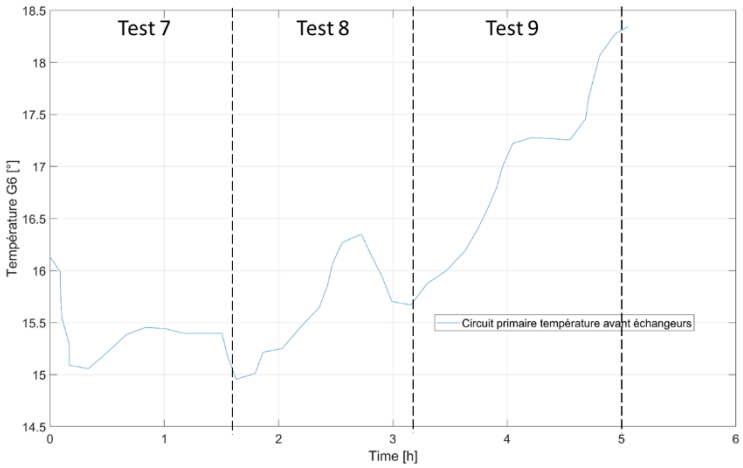

Figure 18: Changes in water temperature during the HSC1 hydraulic short circuit.

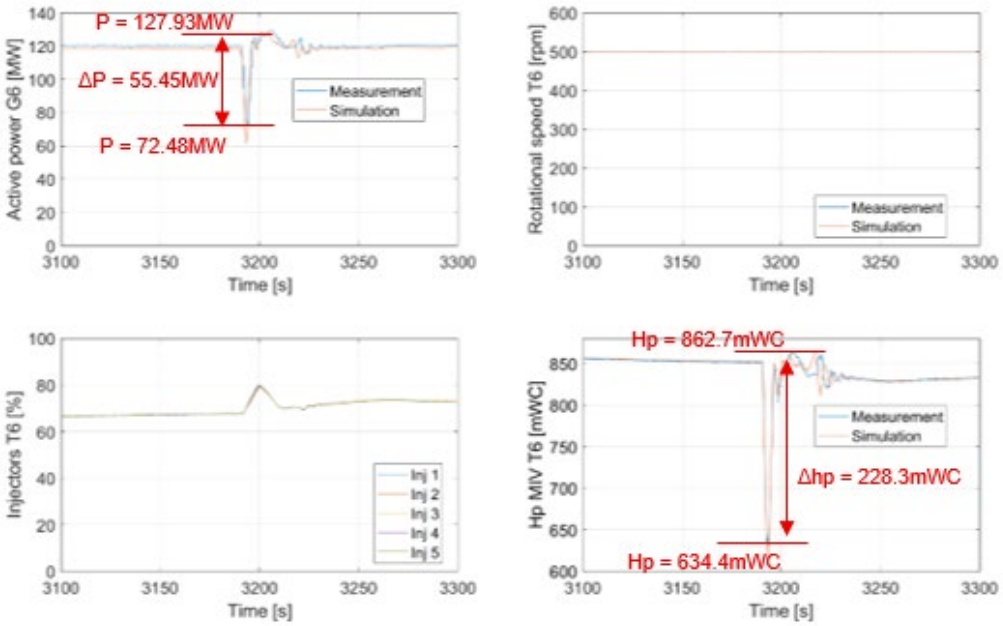

Figure 19: Active power of the unit G6 in MW (top left), Rotational speed of the turbine T6 (top right), Injectors position for the turbine T6 (bottom left) and Static pressure at the spheric valve of the turbine T6 in mWC (bottom right) for the sequence 10.

4.1.6 Fatigue assessment of Pelton buckets and start-ups optimization

During operation, Pelton turbines undergo significant structural dynamic loads that vary with the operating condition. Transient conditions, which are expected to be more frequent due to flexible operation, are acknowledged as particularly damaging with respect to the expected lifetime of the turbines. Given the wide application range of PSPP equipped with ternary units, the study focuses on one of the most critical transient sequence, which is the start-up of the pump driven by the turbine, being thus the primary transient scenario investigated in the project.

Structural load modelling

During the investigation phase concerning the structural assessment research objectives, a preliminary investigation has been carried out to understand the dynamic of the structural damage in Pelton turbines, as well as to identify the critical control parameters that have a significant influence on the optimal operational strategies implemented in ternary units composed by a Pelton turbine and a multistage centrifugal pump. Further details about this study can be retrieved in the research article published in Alerci et al., 2023.

To predict the structural damage occurring in Pelton turbines, a modelling framework is developed to analytically represents the turbine's structural hotspot under dynamic loading. Specifically, the focus is placed on the bucket root, which connects the bucket to the turbine runner. The bucket is modelled as a two-dimensional cantilever beam subjected to excitation from the water jet. Its dynamic behaviour is analysed using Fourier harmonic decomposition to calculate the mechanical stress at the bucket root across the full range of operating conditions. Due to the periodic nature of Fourier analysis, conventional damage quantification methods based on cycle counting are considered unsuitable, particularly at low rotational speeds. Instead, the strain energy density approach is employed to assess structural fatigue. A damage chart is computed by evaluating the strain energy dissipated at the bucket root over a mesh of steady-state conditions, defined by varying rotational speed and injector opening ratio, thus spanning the entire turbine operational interval.

To assess the damage associated with transient behaviour, such as during the start-up of the unit in pumping mode, the analysis adopts a quasi-steady-state approach. The transient sequence is divided into discrete time steps, with the turbine assumed to operate under steady-state conditions at each step. The total strain energy dissipated throughout the transient is computed by summing the damage contributions from each instantaneous operating condition throughout the sequence.

This damage prediction model serves as the input for an optimization algorithm formulated to determine start-up sequences that minimize accumulated structural damage between given initial and final states by adjusting the turbine's control variables. Because the algorithm requires an analytical expression of the objective function, extracted from the strain energy map, and due to the map's complexity, a surface approximation method using Multivariate Adaptive Regression Splines (MARS) is applied. Given the inherently non-convex nature of the resulting Polynomial Optimization Problem (POP), which is known to be NP-hard, a specific solution technique is needed. To this end, the problem is relaxed using a semidefinite programming (SDP) formulation, allowing the identification of globally optimal solutions. The results highlight a strong sensitivity of the optimal start-up trajectories to the admissible opening ramp of the injector, whose opening rate is noted as y_{inj}.

Crack propagation model

As a further step an original fracture mechanics-based framework was developed to compute the propagation of existing cracks in the structure of the turbine as a function of the operating condition. It is important to remark that, since techniques for detecting real cracks were not available, the methodology relies on hypothetical cracks. Indeed, cracks are always present in metallic structures, and their presence are caused by machining or welding processes, as well as by years of operation. This research activity is the subject of a research paper (Alerci et al, 2025). The fracture mechanics-based results are compared with a methodology employed to compute the fatigue-induced damage based on stress-cycles curves (S-N curves) known as Wöhler diagram (further details in Alerci, 2025, Grenoble).

To clarify the logic between the different steps considered when developing the fracture mechanics-based methodology, a schematic representation is presented in Figure 20.

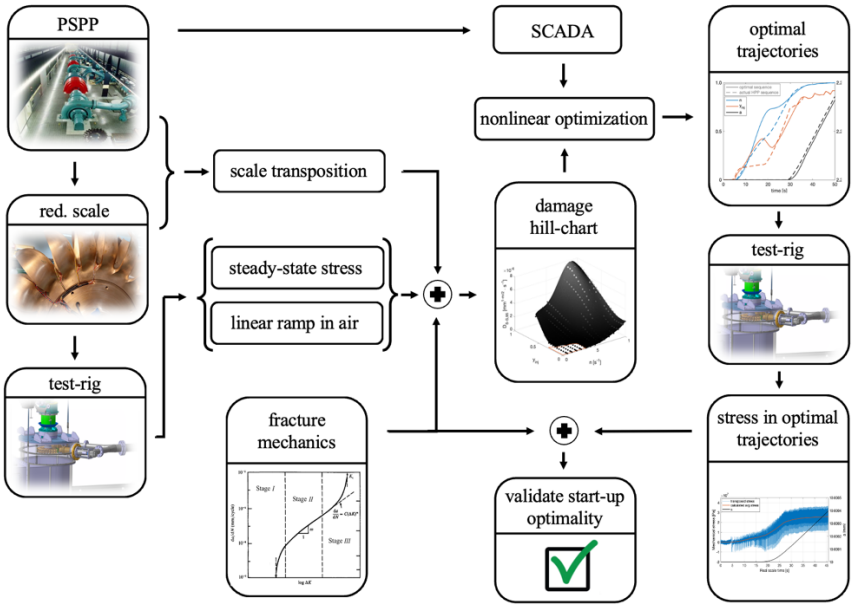

Figure 20 Overview of the fracture mechanics-based methodology.

The propagation of a hypothetical crack at the root of Pelton buckets can be accurately assessed using a linear-elastic fracture mechanics approach, enabling an estimation of the fatigue-induced damage experienced by the runner. While various models exist for estimating crack propagation, the primary objective of this paper is to optimize the operation of Pelton turbines within the context of a daily generation schedule. As such, modelling crack initiation or rare failure events lies beyond the scope of this study. For these reasons, stages I and III of the crack growth diagrams[2] are not considered. Transitions between these stages and stage II are instead handled through threshold values of the crack growth rate. Furthermore, the mean component of the mechanical stress at the bucket root in Pelton turbines is expected to play a significant role in damage evaluation. To meet these modelling needs while maintaining a manageable analytical complexity, the Walker law is adopted as the most appropriate model for describing crack propagation.

In this model, the growth rate of a crack of size a per stress cycle in stage II is given by:

$$\frac{da}{dN} = C_0 \cdot \left(\frac{\Delta K}{(1-R)^{(1-\gamma)}}\right)^{m_a}$$

where C_0, m_a and γ are material-related constants. The stress intensity factor ΔK and the stress ratio R are defined as:

$\Delta K = Y \cdot \Delta\sigma \cdot \sqrt{\pi a}$ and $R = \frac{\sigma_{min}}{\sigma_{max}}$

with Y the crack shape factor. In order to apply Walker's propagation law to the scenario under consideration, certain assumptions must be made regarding the geometry of the crack and the stress distribution. The worst-case scenario, where mechanical stresses result from the combined effects of centrifugal force and bending moment, is represented by a crack located at the outer surface of the bucket root. This crack is assumed to have size a in the tangential direction of the runner and an infinite length in the axial direction. The stress field is assumed to be unidirectional and oriented along the radial direction of the runner. Additionally, as specified by ASTM guidelines (ASTM E647-23), the effects of

[2] Linear elastic fracture mechanics models describe the propagation of cracks in three stages. Stage I models the cracks initiation, stage II models the stable growth of cracks and stage III models the sudden cracks growth leading to rupture (Suresh, 1998).

compressive stresses and those tensile stress amplitudes $\Delta\sigma$ for which $\Delta K \leq \Delta K_{th}$ are considered negligible.

Integrating the crack growth law, it is possible to compute the propagation of a crack that undergoes N stress cycles of amplitude $\Delta\sigma$ in a time interval Δt. Therefore, the crack length $a_{t+\Delta t}$ at the time instant $t + \Delta t$ can be expressed as a function of its state a_t at the time instant t and by regrouping the Walker law parameters and the stress amplitudes in a term that represents the steady-state damage D_{S-S} as:

$$a_{t+\Delta t} = \left(\Delta t \cdot D_{S-S} + {a_t}^{(1-m_a/2)}\right)^{1/(1-m_a/2)}$$

It is crucial to remark that D_{S-S} is function of the operating conditions n, the runner rotating speed, y_{inj} the injector opening rate, and the crack length a.
In contrast to the steady-state damage evaluation, crack propagation during a transient operation sequence does not need to be linked to a fixed operating point characterized by constant n and y_{inj}. Instead, the transient stress signal can be analyzed by summing the contributions of each stress cycle occurring sequentially throughout the entire sequence. This method enables the highest possible resolution in tracking crack growth during transient operation.

Optimization problem

To minimize the crack propagation at the bucket root during start-ups, an optimization problem is formulated to compute optimal trajectories. The objective is to minimize the crack length at the end of the acceleration phase. The synchronization interval is excluded, and only the acceleration stage is considered. The start-up is discretized with a time step $\Delta t = 1$s, where t_k denotes the time at the k-th step (k = 2, ..., T_{start}). The decision variables are the operating points $n(t_k)$ and $y_{inj}(t_k)$. The optimal solutions are evaluated by comparing them to the start-up sequence recorded in the SCADA of the Veytaux 1 HPP.
Constraints ensure consistency with the PSPP dynamics:
i) a bound k_y on the injector opening rate,
ii) acceleration governed by the laws of rotating dynamic,
iii) a final trajectory segment based on SCADA data to avoid interference with synchronization,
iv) initial standstill,
v) closed injectors at start,
vi) crack growth governed by the Walker law,
vii) initial crack length imposed at t_1.

Experimental set-up

The reduced scale models of the old and the newly designed Pelton runners of the power plant Veytaux 1 have been tested on the newly upgraded Pelton test rig at EPFL-PTMH. The test rig can operate either under steady-state conditions, holding operating parameters constant, or follow transient sequences by imposing a rotational speed trajectory and controlling discharge through injector openings y_{inj}. The hydraulic head H is regulated using four service pumps, each rated at 190 kW. Discharge (Q), head (H), and mechanical torque (M_m) are measured using a National Instruments CompactDAQ system, which includes an NI-9220 module for analog voltage and an NI-9203 module for analog current. The CompactDAQ samples signals at 2 kHz.
The reduced-scale Pelton runners are made of tin bronze alloy CuSn12 and equipped with a set of HBM 1-LY61-3/350 resistive strain gauges (gauge factor GF = 2) bonded at the bucket root to monitor structural behavior during operation. Strain gauges are positioned on consecutive bucket roots to guarantee measurement reliability and repeatability. Figure 21 and Figure 22 illustrate the PTMH test-rig and the reduced scale runner of the old Pelton turbine, instrumented with strain gauges.

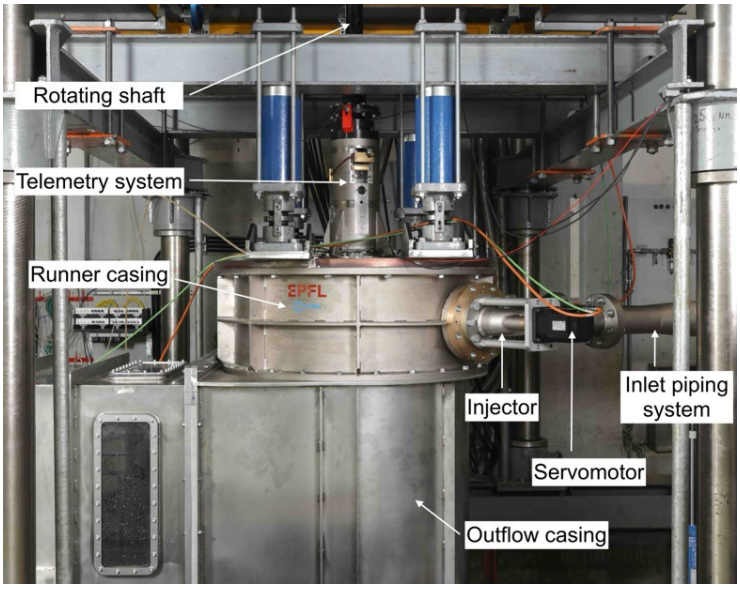

Figure 21 Pelton test-rig.

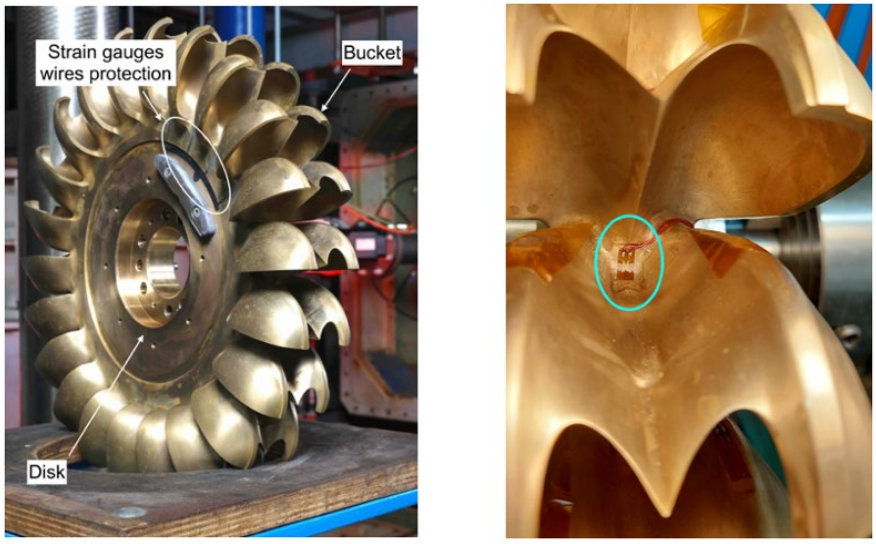

Figure 22 Runner instrumentation.

Strain measurements on the runner are acquired using a telemetry system that transmits signals from the rotating frame to a multi-channel amplifier. The system supports a bandwidth of 0 to 40 kHz (-3 dB). Amplified signals are captured by an NI-4472 data acquisition device, sampling at 20 kHz. For steady-state conditions, 5-second strain measurement windows are recorded. Strain-to-stress conversion assumes elastic deformations only.

The reduced-scale runner replicates the geometry of the full-scale turbine with a geometric scale ratio $\lambda = \frac{D_P}{D_M} = 5.07$, where P and M stand for Prototype and Model, respectively. Kinematic similarity is ensured by matching dimensionless speed and flow factors according to IEC standards. The computation of the crack propagation on the real scale turbine from reduced scale stress measurements requires a dedicated transposition framework to define a stress scaling factor $\lambda_\sigma = \frac{\sigma_P}{\sigma_M}$. Further details of the methodology can be found in (Alerci et al., 2025).

Steady-state damage

The damage $D_{S-S}(n, y_{inj}, \mathrm{a})$ is computed over the full range of n and y_{inj} to generate the damage hill-chart. In Figure 23, the comparison between the damage hill-chart at $H_P = 845$ m considering a crack length $a = 10.0$mm for the old and the newly designed runners is presented.

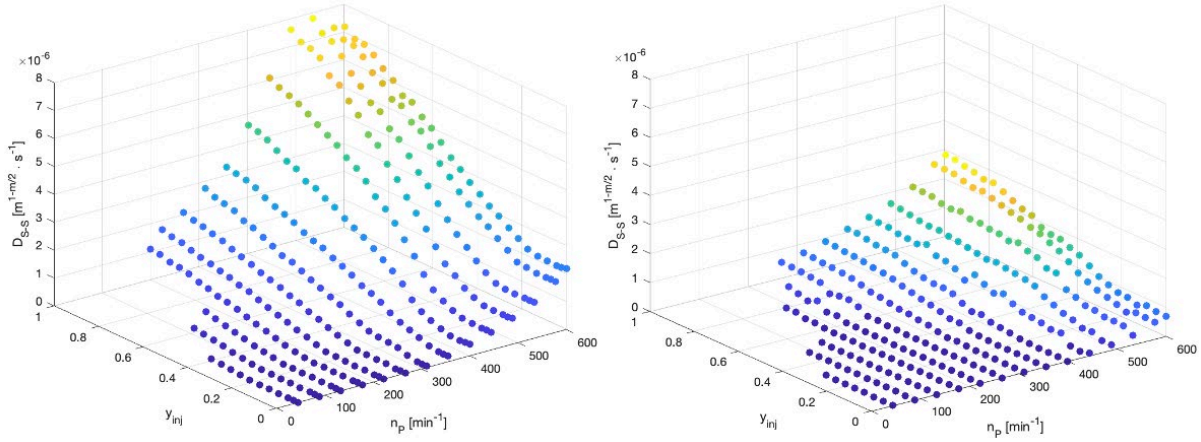

Figure 23 Damage hill-chart. Fracture mechanics approach. Old (left) and new (right) Pelton runners.

It is interesting to remark that, despite the trend of the damage is similar between the two runners, the magnitude is significantly lower for the newly designed runner. The main factor that influences this divergence is the lower average stress values experienced by the bucket root of the new runner. By contrast, the peak-to-peak stress oscillations magnitude are similar in magnitude, with less than 20% difference. Due to this difference in the damage hill-chart, crack propagation is expected to initiate for cracks of larger sizes in the new Pelton runner compared to the old runner.

Optimal start-up sequences validation

The transient tests are conducted under two different net head conditions. The first represents standard operation, with the headwater reservoir at its average level, leading to a model-scale net head:

$H_M = \frac{H_P}{\lambda_D} = \frac{845m}{5.07} \approx 167$m

The second simulates the highest possible pressure at the injectors, with the reservoir at maximum level and both FMHL powerhouses in pumping mode, resulting in:

$H_M = \frac{H_P}{\lambda_D} = \frac{910m}{5.06} \approx 179$m

For the old runner, the optimization algorithm considers the crack length range $a = [1.7{:}\,0.1{:}\,2.5,\ 2.9, 3.2, 10.0]$ mm. The reason behind this choice is defined by the fact that, at $H_P = 845$ m, no propagation is shown for crack length values $a < 1.7$ mm, and the trend of the hill-chart presents negligible variations for $a > 3.2$ mm. With the same logic, the analysis on the newly designed runner considers the crack length range $a = [4.5, 5.0, 6.0, 8.0, 10.0]$ mm. Recalling that the optimal start-sequences are evaluated by comparing them to the start-up sequence recorded in the SCADA of the Veytaux 1 HPP, Figure 24 shows an example of the stress signals, already transposed at the full-scale, as well as the test-rig parameters Q, H and n at the reduced scale. An example at $H_P = 845$ m is presented, namely the case with $a = 10.0$ mm for the old runner.

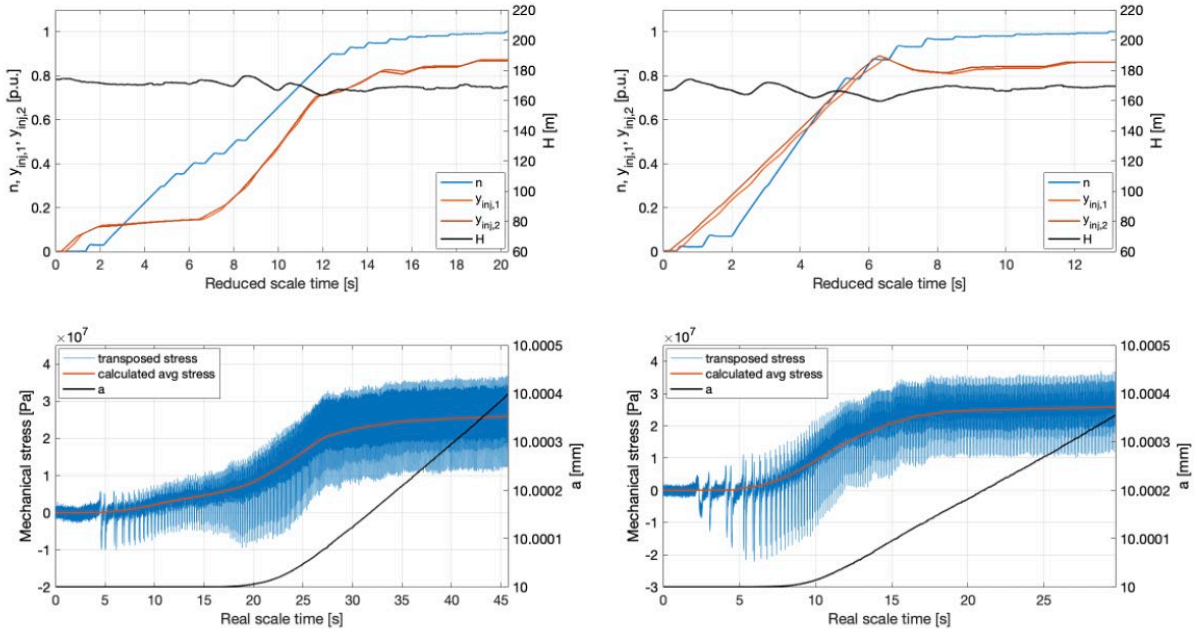

Figure 24 Acquisition during start-up sequences. Baseline case of the Veytaux HPP (left) and optimal case (right). Old runner, $H_P = 845$m.

The summary of the improvement provided by the experimentally validated optimal sequences is presented in Figure 25 and Figure 26. The optimization strategy is effective for the vast majority of the sequences. In particular, only scenarios with the smallest crack sizes do not ensure a systematic improvement, probably due to the very small increase of the crack, that leads to high sensitivity to single stress cycles in the propagation calculation.

Crack length	Bas. case	Optimal	Rel. improv.
1.7 mm	+0.096 nm	+0.149 nm	+ 54.4%
1.8 mm	+0.511 nm	+0.618 nm	+ 21.0%
1.9 mm	+2.665 nm	+3.823 nm	+ 43.5%
2.0 mm	+11.88 nm	+11.06 nm	- 6.9%
2.1 mm	+19.24 nm	+17.03 nm	- 11.5%
2.2 mm	+22.81 nm	+21.52 nm	- 5.7%
2.3 mm	+25.07 nm	+23.99 nm	- 4.3%
2.4 mm	+27.03 nm	+24.01 nm	- 11.2%
2.5 mm	+29.12 nm	+26.95 nm	- 7.5%
2.6 mm	+30.97 nm	+28.42 nm	- 8.2%
2.9 mm	+37.08 nm	+33.55 nm	- 9.5%
3.2 mm	+43.23 nm	+39.81 nm	- 7.9%
10.0 mm	+398.7 nm	+355.1 nm	- 10.9%

Crack length	Bas. case	Optimal	Rel. improv.
1.7 mm	+0.258 nm	+0.196 nm	- 23.9%
1.8 mm	+0.695 nm	+1.237 nm	+ 77.9%
1.9 mm	+5.553 nm	+5.911 nm	+ 6.4%
2.0 mm	+15.05 nm	+14.63 nm	- 2.8%
2.1 mm	+20.43 nm	+19.21 nm	- 6.0%
2.2 mm	+23.46 nm	+22.97 nm	- 2.1%
2.3 mm	+26.01 nm	+23.81 nm	- 8.4%
2.4 mm	+28.12 nm	+25.71 nm	- 8.6%
2.5 mm	+29.98 nm	+28.13 nm	- 6.2%
2.6 mm	+31.88 nm	+30.14 nm	- 5.5%
2.9 mm	+38.14 nm	+36.35 nm	- 4.7%
3.2 mm	+44.89 nm	+42.12 nm	- 6.2%
10.0 mm	+417.3 nm	+356.6 nm	- 14.5%

Figure 25 Experimental validation of optimization. Old Pelton runner

Crack length	Bas. case	Optimal	Rel. improv.
4.5 mm	+28.49 nm	+31.04 nm	+ 8.9%
5.0 mm	+45.97 nm	+42.54 nm	- 7.5%
6.0 mm	+69.25 nm	+62.47 nm	- 9.8%
8.0 mm	+110.40 nm	+98.07 nm	- 11.2%
10.0 mm	+162.25 nm	+146.17 nm	- 9.9%

Crack length	Bas. case	Optimal	Rel. improv.
4.5 mm	+26.24 nm	+24.51 nm	- 6.6%
5.0 mm	+44.47 nm	+42.27 nm	- 4.9%
6.0 mm	+64.40 nm	+59.97 nm	- 6.9%
8.0 mm	+103.71 nm	+97.40 nm	- 6.1%
10.0 mm	+149.51 nm	+138.08 nm	- 7.6%

Figure 26 Experimental validation of optimization. New Pelton runner.

Comparison with Wöhler diagram-based damage

A comparison with the well-established methodology of fatigue quantification based on Wöhler diagrams has been performed to enable identifying the key differences the developed elastic-fracture mechanics approach. As shown in the conference paper (Alerci et al., 2024), the Palmgren-Miner rule is applied to compute the overall damage *D*. The impact of a non-zero average stress is accounted by considering the Goodman corrective law. The damage hill-chart at the full scale is presented in Figure 27 for the old and the new Pelton runner in the case $H_P = 845$ m. Also in this case, the damage hill-chart reveals lower damage for the new runner.

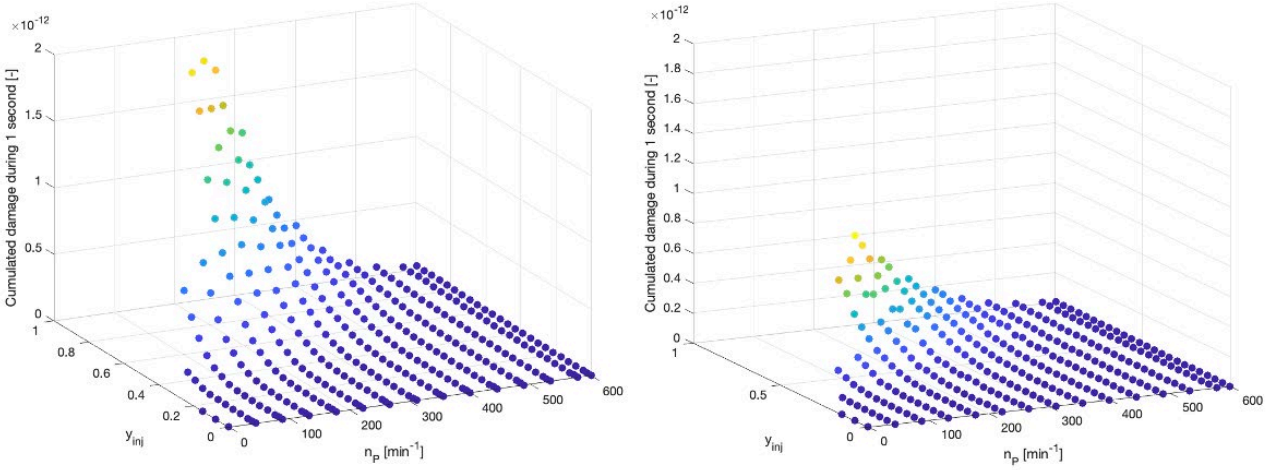

Figure 27 Damage hill-chart. Wöhler diagram approach. Old (left) and new (right) Pelton runners. $H_P = 845$m.

Similarly as performed within the fracture mechanics-based approach, an optimization problem is formulated to compute optimal start-up sequences that minimize the transient-related damage. In the case of the Wöhler diagram methodology, the crack model is not required. Therefore, the algorithm minimizes the damage D, and the constraint vi) of the previously presented problem is excluded.
The optimal sequences is implemented in the test-rig. The stress signal as well as the test-rig data are shown in Figure 28 in case of the old runner. In Figure 29, the comparison between the SCADA-extracted start-up (dashed line) and the optimal start-up (solid line) can be observed. A reduction of the damage of 14.95% is attained. In the case of the new runner, the optimal sequence reduces the damage of 5.8%. Moreover, it is important to notice that, due to the lower damage suffered by the new runner compared to the old runner, the absolute cumulated damage in case of the optimal sequence for the new runner is 57.9% lower compared to the cumulated damage undergone by the old runner.

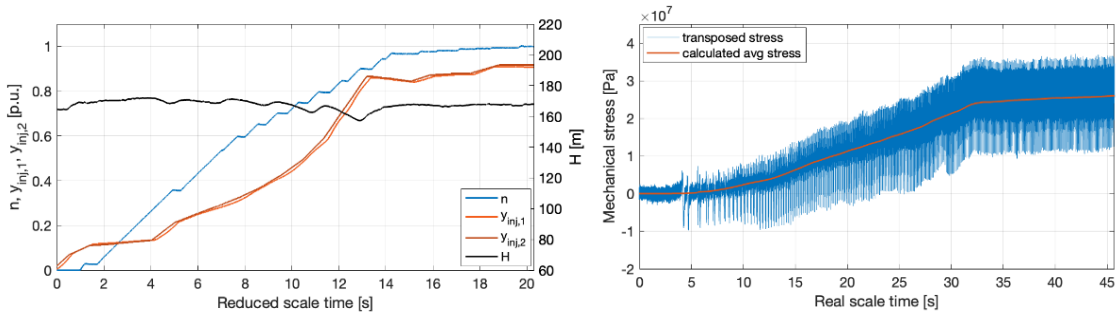

Figure 28 Optimal start-up, old runner, $H_P = 845$m.

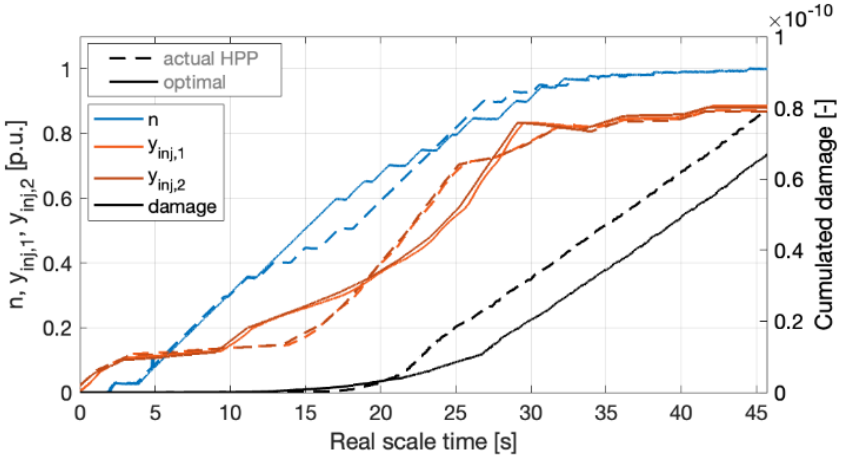

Figure 29 Comparison SCADA vs. optimal start-up. Old runner, $H_P = 845$m.

The results allowed for a deep understanding of fatigue mechanism in Pelton turbines in operation, and provided a methodology to quantify and reduce the fatigue-related impact of transient sequences, with focus on the particular case of the ternary unit start-up in pumping mode performed with the Pelton turbine.

When modernizing, from a fatigue perspective, new design, that features a bucket centre of mass closer to the disk, reduces the impact of average stress: reduced tensile stress which results in reduced fatigue impact. The study also highlighted the main divergences between fracture mechanics-based approach and Wöhler diagram-based approach:

- Fracture mechanics method:
    - Compressive stresses neglected
    - Significant impact of the average stress in the instantaneous damage
    - fast accelerations reducing the time spent during start-up is usually the optimal strategy.
- Stress-life method:
    - Compressive stresses considered
    - Limited impact of the average stress in the instantaneous damage by Goodman corrective law

- fast acceleration is optimal only in the second half of the acceleration; during the first half, it is optimal to reduce the maximal amplitude (tensile + compressive) of the stresses.

4.1.7 Booster pump improvements

Persistent vibrations observed on the booster pumps (PSA) of Veytaux I were known as limiting factor for an efficient and flexible operation of the plant. Therefore, their mitigation has been addressed through dedicated numerical simulations and field tests. These vibrations, occurring at 32 Hz, caused axial oscillations on the pump shaft exceeding 30 mm/s. A CFD investigation conducted prior to the HydroLEAP project identified a cavitating vortex at the pump inlet as the root cause of the phenomenon. That study also evaluated several mitigation strategies, including geometric modifications of the suction chamber and the installation of a turbulence-inducing grid. Among the options considered, the grid was selected for its ability to suppress the vortex without requiring pump modifications or extensive civil works (see Figure 30). Additionally, the grid is fully removable, making it compatible with maintenance requirements and adaptable in case the operational results diverge from simulation predictions.

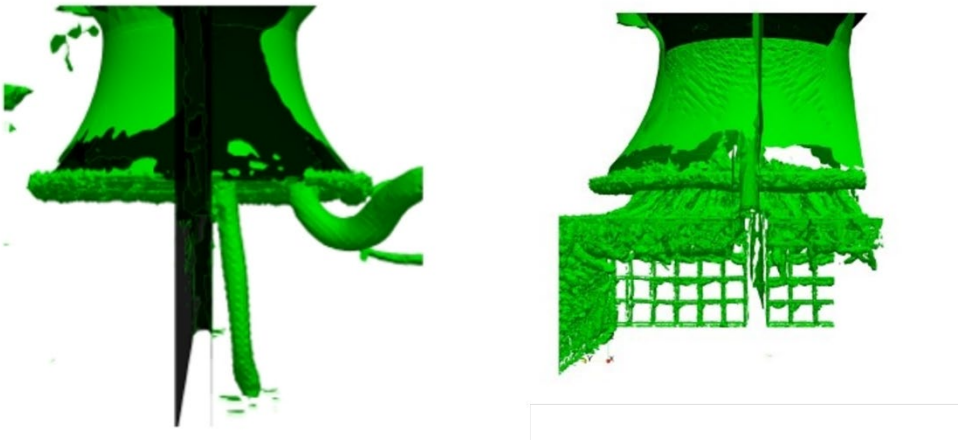

Figure 30: Iso-surface of the Q-criterion before and after the grid installation. The presence of the cavitation vortex before the grid installation is clearly visible.

The grid has been installed on unit 2 of Veytaux 1 at the end of the year 2024 (see Figure 31). Subsequent on-site tests show a decrease in the longitudinal vibrations by a factor of 5 with maximum values reduced to around 6 mm/s. The success of this implementation supports extending the solution to the remaining groups at Veytaux I. Furthermore, this approach may be applicable to other facilities experiencing similar vortex-induced vibration issues. The results of this work have been published in the journal *Wasser Energie Luft* (Decaix et al., 2025).

Figure 31: The grid installed on site underneath the booster pump bell.

4.1.8 Fatigue assessment of the multistage pump runner

As for Pelton turbines, centrifugal pumps may also undergo significant structural dynamic loads that vary with the operating condition. In particular, transient conditions are acknowledged as particularly damaging with respect to the expected lifetime of the machines. Therefore, the structural impact of transients' scenarios was experimentally evaluated by investigating the mechanical behaviour of multistage centrifugal pumps. The study focuses on one of the most critical transient sequence, which is the start-up of the pump driven by the turbine, being thus the primary transient scenario investigated in the project. The reduced scale models of the multistage centrifugal pump of the power plant Veytaux 1 have been tested on the newly upgraded test-rig at the EPFL-PTMH, allowing for transient operations. The last stage of the impeller has been equipped with strain gauges to investigate the dynamic response. The extracted data have been used as input for analytical models developed to predict the ageing of the pump structure.
The methodology to quantify the fatigue-related impact on the pump impeller relies on the same fracture mechanics theory applied to the Pelton turbine, i.e. by considering pre-existing cracks within the pump, that are governed by the Walker law, and that grow as a function of the measured mechanical stresses.

Experimental set-up

The stresses on the impeller blades during start-up sequences are evaluated through an experimental campaign conducted at PTMH test-rig, which complies with IEC-60193 standards. The reduced-scale pump is installed in a closed-loop piping system designed to withstand pressures up to 10 bar, and is driven by a 300 kW vertical-axis motor/generator. The hydraulic power delivered by the pump is dissipated via a valve, which also regulates the flow rate.
The reduced-scale model is a three-stage pump made of EN AW 5083 aluminium alloy, with a stage unit specific speed of $n_{q,s} = 31.3$ min $m^{0.75}$ $s^{-0.5}$. Two blades of the outlet stage are instrumented with four piezo-resistive strain gauges each (Kyowa KSPB-1-350-E4, GF = 160), positioned along the blade-crown intersection. The strain gauges are located on the suction side of the first blade and on the pressure side of the second blade, as shown in Figure 32, in order to capture the hydrodynamic behaviour within a single inter-blade channel. To increase their durability during operation, the sensors are covered with a thin layer of ceramic-reinforced ARC 855 coating. A picture of the test-rig and of the strain gauges before applying the protective layer are shown in Figure 33. During the experimental

campaign, strain gauges 'a', 'd', and 'g' failed; thus, the results presented rely on the remaining five sensors. The strain signals are transmitted from the rotating impeller to a multi-channel amplifier via the telemetry system previously described.

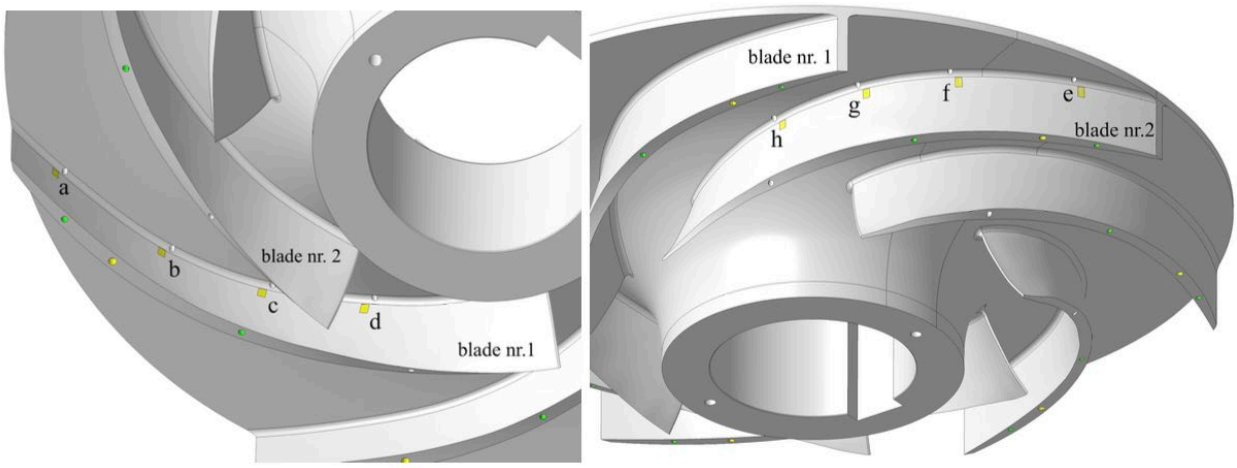

Figure 32 CAD view of the strain gauges location.

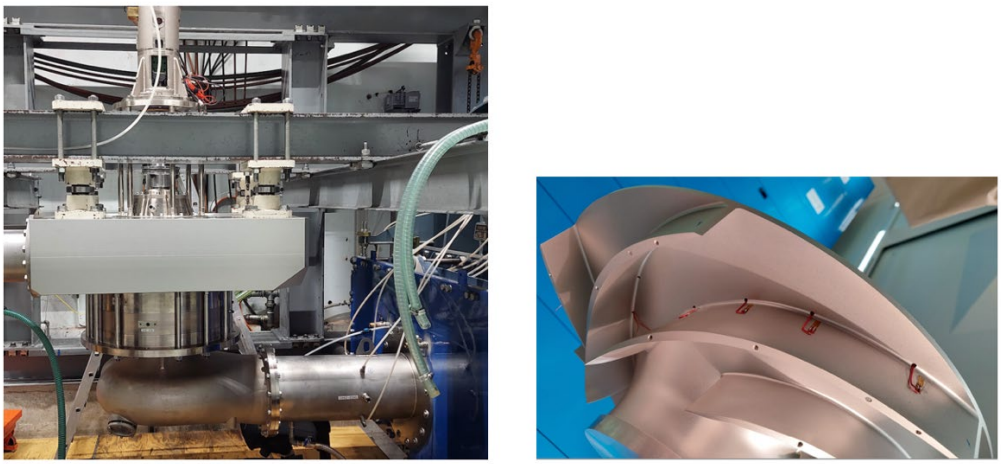

Figure 33 Implementation in the test-rig (left), and view of strain gauges 'e-h' on the reduced scale impeller (right).

Scaling laws

The reduced-scale pump is built according to the geometry of the full-scale machine. The geometric scale ratio is $\lambda = \frac{D_P}{D_M} = 3.96$, where the subscripts P and M refer to the Prototype (i.e., full-scale at the PSPP) and the Model scale, respectively.

To accurately reproduce the hydrodynamic behaviour of the full-scale pump, the model must operate under similarity of velocity triangles. This condition is ensured by applying the IEC-defined dimensionless speed and discharge factors, ensuring that the specific speed and discharge factors are equal for both prototype and model. Due to pressure limitations of the test rig, the speed scale ratio used in this study is $\frac{n_P}{n_M} = 0.75$.

Furthermore, to account for the potential formation of cavitating multiphase structures at the inlet stage, the Thoma number $\sigma_C = \frac{NPSH}{H}$ must be matched between prototype and model. In the test rig, the net positive suction head (NPSH) is controlled by a vacuum pump operating on the upstream tank, which

adjusts the pressure at the pump inlet. To estimate the mechanical stresses on the full-scale impeller, a scaling factor $\lambda_\sigma = \frac{\sigma_P}{\sigma_M}$ is applied to transpose the measurements from the reduced-scale model. Further details of the methodology can be found on the research paper Alerci et al, 2025.

Due to the laboratory implementation constraints and to avoid an excessively large geometric scale ratio, the reduced scale model is designed with three stages: an inlet stage, an outlet stage, and one intermediate stage. Since the hydraulic design of the intermediate stages is identical, the flow conditions entering the final stage of the model reliably replicate those of the full-scale machine, ensuring the measured dynamic response is representative of real plant behaviour [Florjancic, 1967, Sulzer report]. Each stage has 7 blades, while the diffuser consists of 15 stay vanes in both the inlet and intermediate stages, and 12 vanes in the outlet stage.

At FMHL, an auxiliary pump pressurizes the inlet flow to mitigate cavitation, providing about 2.5 bar of additional pressure. Given the average gross head of the PSPP ($H_{HPP} = 853$ m), this results in a Thoma number per stage of approximately $\sigma_{C,S} = \frac{NPSH}{H_S} \approx \frac{\frac{p_{inlet}}{\rho_W \cdot g}}{\frac{853}{5}} = 0.21$. To replicate this value at model scale, the inlet flow would need to be depressurized to $p_{depr} = -0.60$ bar. However, such low-pressure levels led to instability in the test rig before the start of the acceleration sequences. A steady inlet condition was maintained for depressurization up to $p_{depr} = -0.45$ bar, corresponding to a Thoma number $\sigma_{C,S} = 0.29$. This value was therefore selected for the experimental campaign.

Definition of start-up trajectories

Start-up sequences are defined by modelling the dynamics of a ternary unit equipped with a Pelton turbine and a pump. The sequences are selected based on the optimization framework achieved for the Pelton runner damage minimization. For most of the machine's operating life, the turbine-side optimal start-up corresponds to the shortest possible sequence, achieved by applying the maximum permitted acceleration. Thus, the label "seq.1: opt. Pelton" refers to the steepest acceleration sequence, while "seq.2" to "seq.8" correspond to more gradual trajectories. The sequence implemented in the Veytaux I ternary units, extracted from the SCADA and used in this study is labelled "actualHPP". An overview of the tested acceleration trajectories and their names is shown in Figure 34.

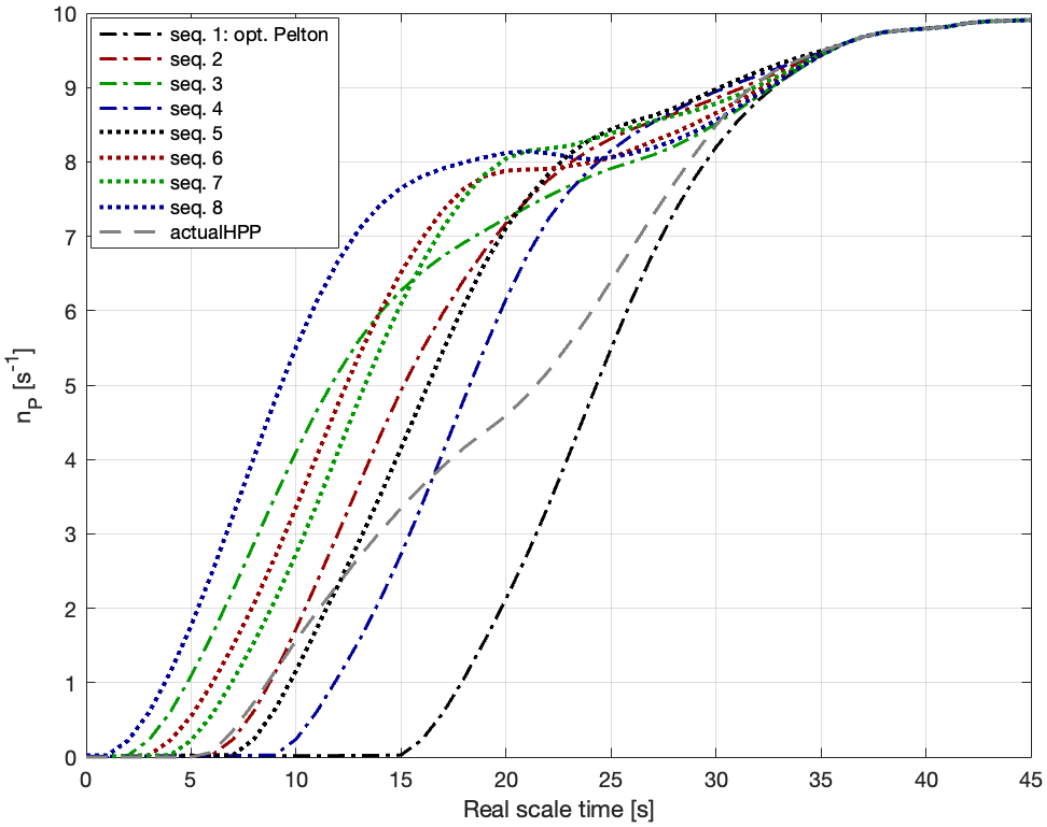

Figure 34 Acceleration phase of the start-up sequences.

Steady-state operating conditions – stress measurements and damage assessment

To assess the impact of start-up sequences and identify key damage drivers, it is essential to understand the hydrodynamic phenomena that cause significant vibrations. This requires observing pump behavior across its operating range. Since start-up occurs with the valve closed, steady transitions from standstill to nominal speed at zero flow, and from the best efficiency point (BEP) to zero flow at full speed, are illustrated in Figure 35.

Stress cycles are recorded over 8-second windows at steady-state conditions, defined by pump speed (n_P) and flow rate (Q_P). Two operating ranges are tested: steady conditions from 0 to 10 s^{-1} at zero flow, and flow variation from 0 to 9 m^3/s at constant speed (10 s^{-1}). Figure 35 shows the corresponding stress amplitudes. As observed, zero-flow conditions clearly result in much higher stress: amplitudes are up to five times greater than at BEP for most strain gauges, and about twice as high for the gauge located at the blade leading edge. This observation shows how operating at closed valve, as in the case of pump start-up, implies significant stress levels, with consequently important fatigue-related impact. From these stress amplitudes, crack growth rates are computed as a function of pump speed for zero-flow conditions. Only strain gauges ‘b’ and ‘c’ detect tensile stress cycles and are used for crack propagation analysis. The growth rate, calculated using the Walker law over each 8-second window and shown in Figure 36, increases with speed. Below 7 s^{-1}, crack growth is prevented by the stress intensity threshold. Gauge ‘c’ shows growth rates about three times higher than gauge ‘b’, partly due to higher mean stress.

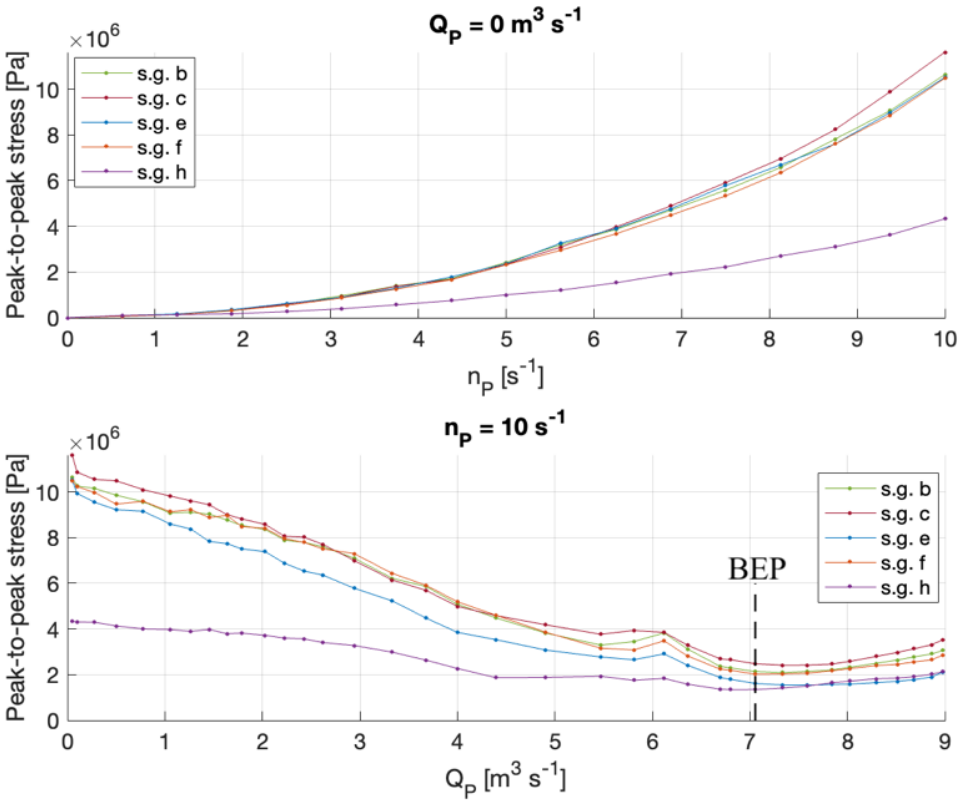

Figure 35 Peak-to-peak stress against closed valve (upper Fig.) and across the Q_P range (lower Fig.) at real scale.

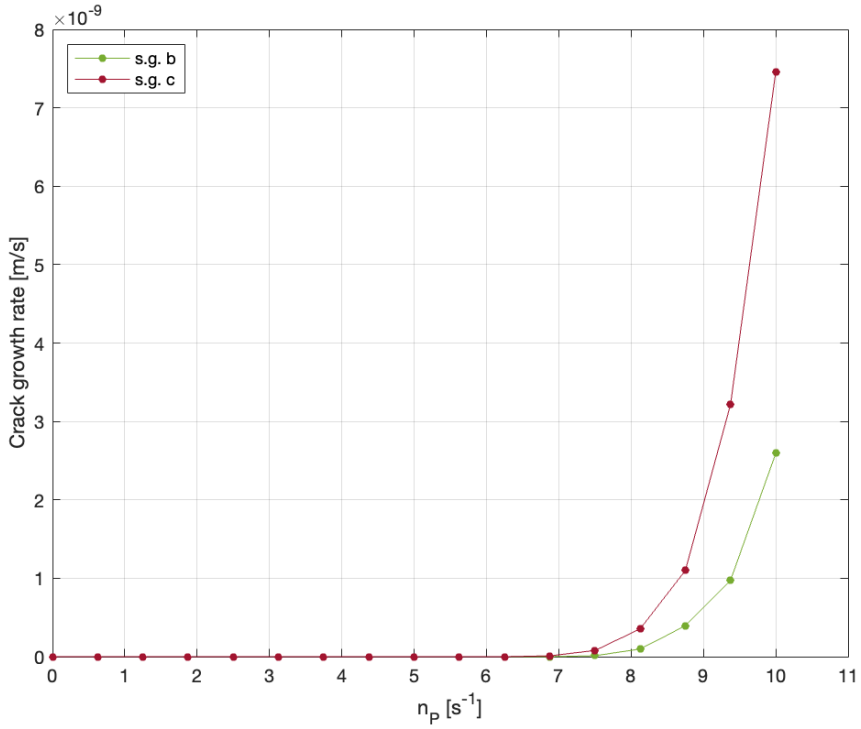

Figure 36 Average crack growth rate operating against closed valve.

Spectrograms in Figure 37 and Figure 39 show the frequency content of stress signals at various flow rates at fixed synchronous speed. At zero flow, strong peaks appear in the ranges $f = [0.2, 0.4] \cdot f_n$ and at $f = [1; 8; 12] \cdot f_n$. Frequencies below $0.5 \cdot f_n$ are often linked to turbulence, separation, or rotating stall. The latter, though poorly documented at low flows, has been shown to rotate at 60-70% of impeller speed at zero flow (Lennemann, 1970), which may be detected as $f = [0.3, 0.4] \cdot f_n$ in the rotating frame. By contrast, the vane-passing frequency at $12 \cdot f_n$ is clearly visible as the main RSI component, while the peak at $8 \cdot f_n$ likely results from pressure field modulation due to interactions between rotating and stationary elements.

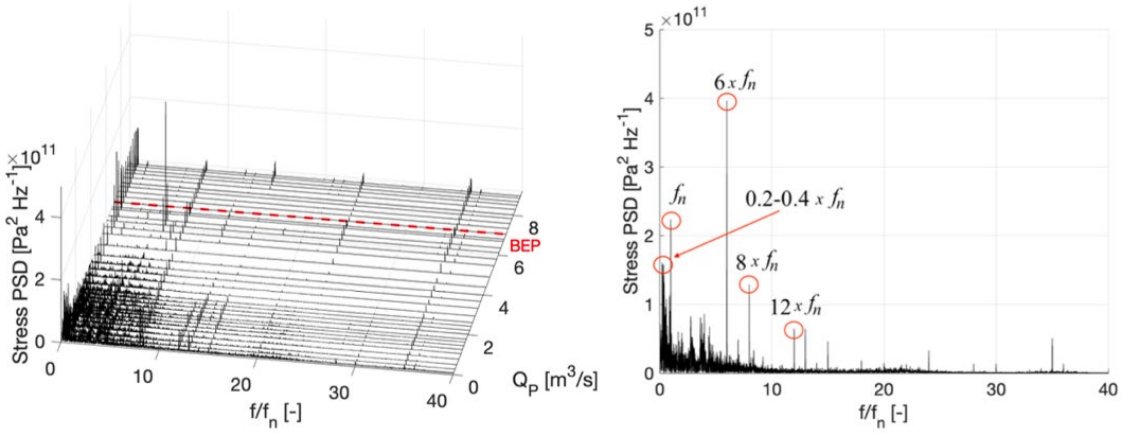

Figure 37 Spectrogram of steady-state stress signals along the flow rate range QP at synchronous speed. Strain gauge 'b'.

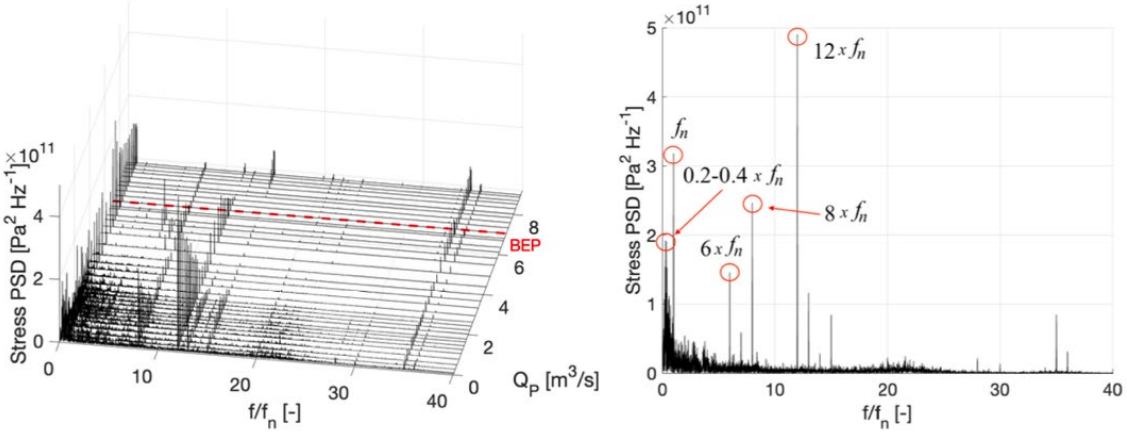

Figure 38 Spectrogram of steady-state stress signals along the flow rate range QP at synchronous speed. Strain gauge 'c'.

Start-up sequences

Once the pump's structural behaviour is characterized, its dynamic response during start-up can be assessed. Nine different acceleration trajectories are tested on the rig, with stress signals recorded throughout the ramp-up phase until synchronous speed is reached. The sequence durations range from 34.6 seconds for the fastest case ("seq.1: opt. Pelton") to 48.7 seconds for the slowest ("seq.8"), corresponding respectively to 25.9 s and 36.5 s at reduced scale.

Transient operating conditions – stress measurements and damage assessment

Figure 39 displays the stress signals in the time domain and their spectrograms, in the case of the "actualHPP" sequence taken as example. As previously observed, strain gauges 'b', 'c', 'e', and 'f' show

comparable stress amplitudes, while gauge 'h' records significantly lower values. The power spectral density (PSD) is computed using 3-second Hann windows with 50% overlap. Dominant frequencies appear in the sub-synchronous and RSI ranges. Additionally, a spectral peak at $f = 15 \cdot f_n$ is seen in all gauges except 'e' (located at the trailing edge), suggesting a rotor-stator interaction in the intermediate stage (15 stay vanes) that propagates downstream.

To investigate the effect of different trajectories, propagation is analyzed for an initial crack of 15 mm. Figure 40 shows the crack growth over time for each sequence. The most damaging case results in 21.3% and 19.6% more propagation than the least damaging one, for strain gauges 'b' and 'c', respectively. All curves show slow initial growth, followed by a steep increase. Final crack length doesn't directly depend on total duration, but time spent at high rotational speed significantly increases damage. For example, for gauge 'c', the crack growth rate jumps from less than 1e-9 m/s to around 6e-9 m/s as the pump speed crosses 90–93% of nominal speed.

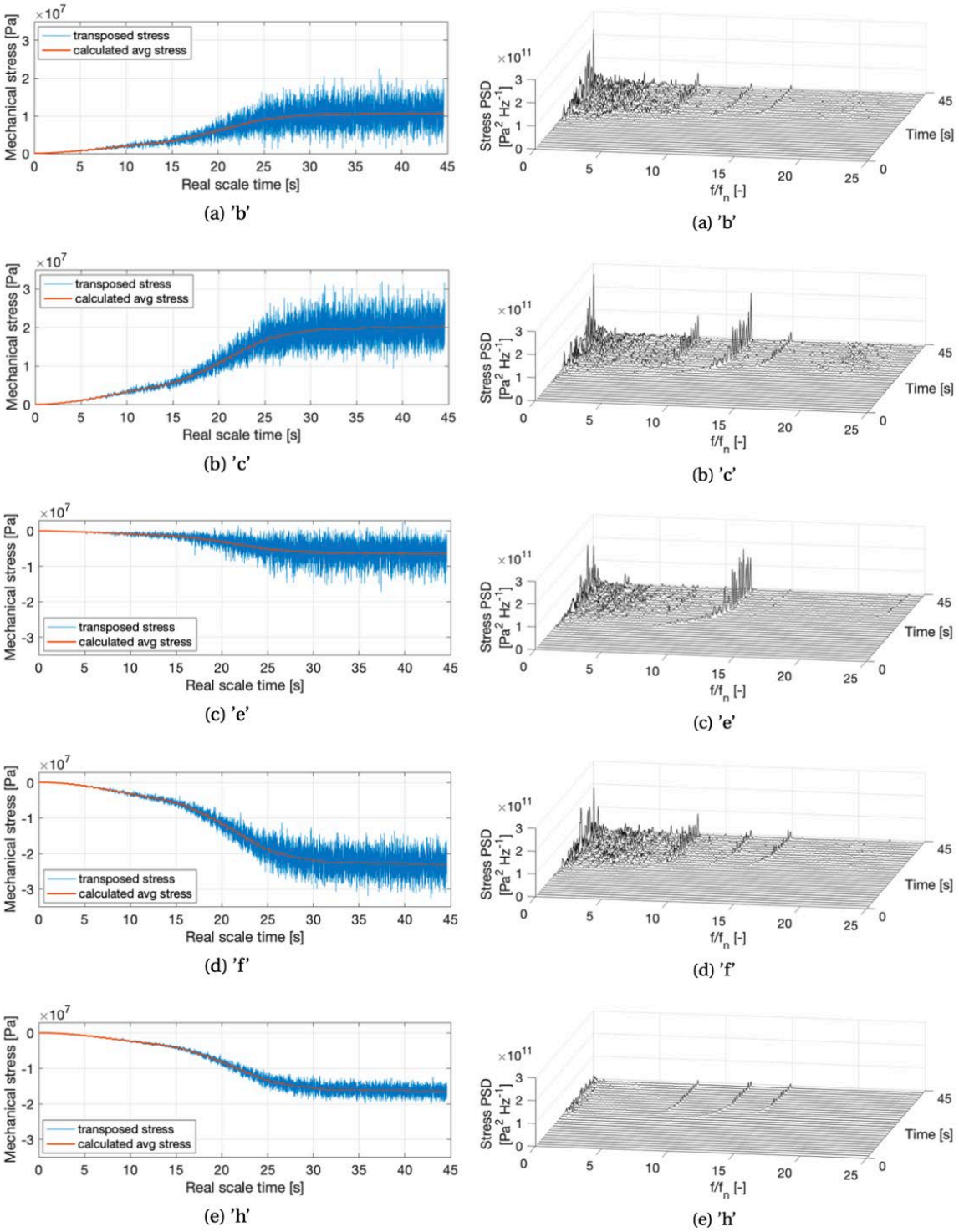

Figure 39 Spectrogram of stress measurements during "actualHPP" start-up. Five strain gauges.

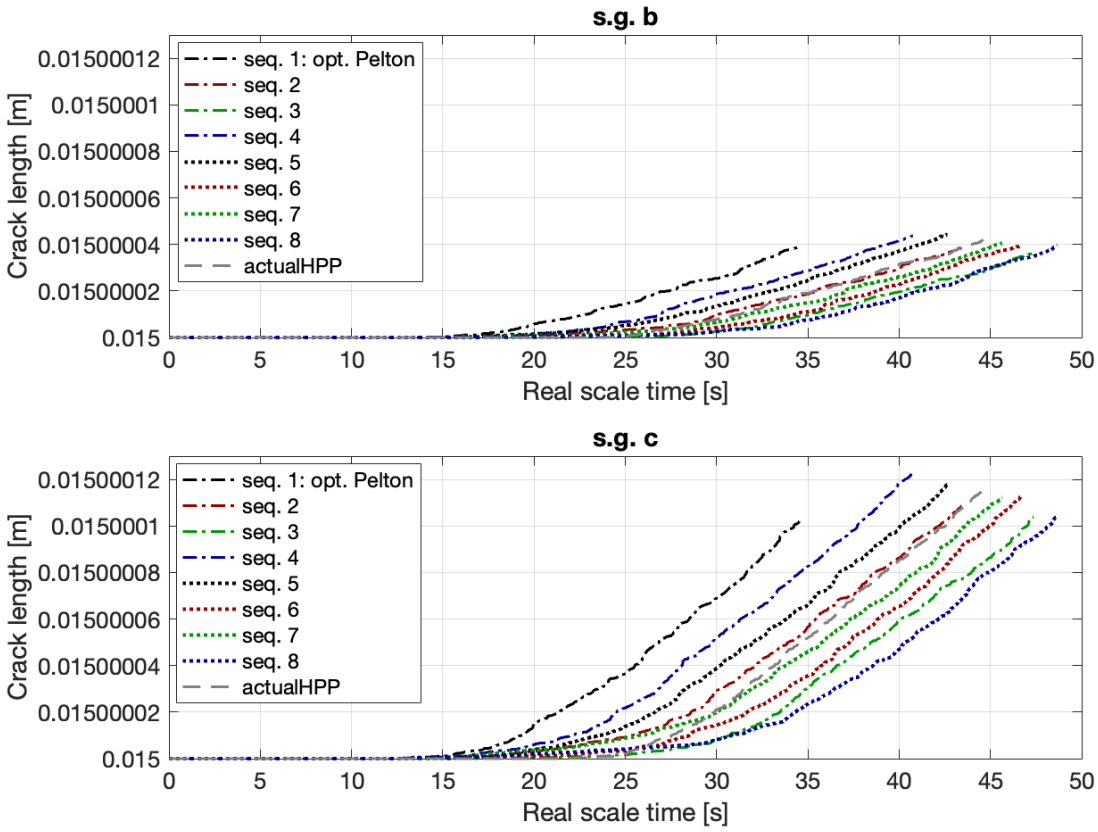

Figure 40 15 mm crack propagation induced by the tested sequences against time. Strain gauge 'b' (upper Fig.) and 'c' (lower Fig.).

To quantify the influence of high-speed operation, propagation is plotted against the time spent above a speed threshold ($n_{th} = 550$ rpm). Figure 41 shows a clear trend: sequences spending more time at high speed lead to greater damage. Notably, sequences with minimal crack propagation either accelerate quickly (e.g., "seq.1") or slowly through early stages but speed up significantly near nominal speed (e.g., "seq.3" and "seq.8"). In contrast, the most damaging cases ("seq.4" and "seq.5") slow down around 80-95% of nominal speed, extending time spent at damaging speeds.

Still, time above the threshold alone doesn't explain all differences. For instance, "seq.2" and "actualHPP" both spend ~18.2 seconds above n_{th} but show notable differences in final crack length. A more detailed comparison, shown for strain gauge 'c' in Figure 42 and Figure 43, reveals that in "seq.2", the crack grows over a longer period but at a slower rate in the first 10 seconds. Once nominal speed is reached, the stress signals differ in how they influence crack growth. In "seq.2", several drops in the crack growth rate are observed, linked to reductions in stress amplitudes, not seen in "actualHPP".

Examining the frequency content, the power spectral density (PSD) at sub-synchronous frequencies is similar between sequences, with peaks around 1.5e11 Pa²/Hz. However, differences are clear at roto-stator interaction (RSI) frequencies. In "actualHPP", the $12 \cdot f_n$ RSI component stays almost constantly above 5e10 Pa²/Hz, whereas in "seq.2" it is much lower. These variations align with changes in crack growth rates, suggesting a strong dependence between the computed crack propagation and the incipience of strong RSI-related pressure peaks.

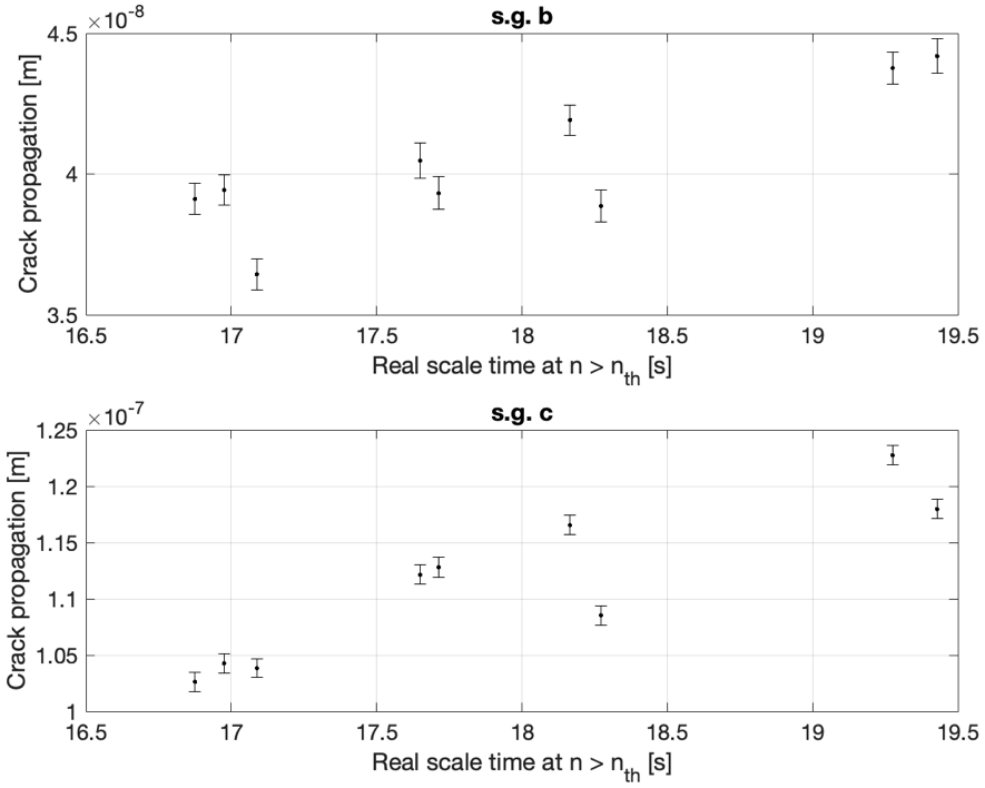

Figure 41 15 mm crack propagation induced by the tested sequences against time spent at high rotational speed. Strain gauge 'b' (upper Fig.) and 'c' (lower Fig.).

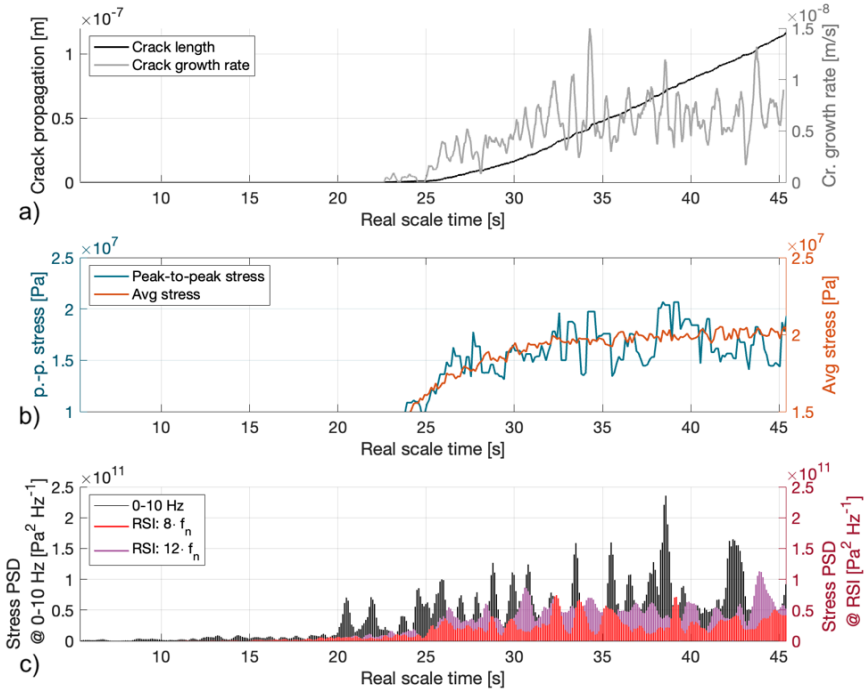

Figure 42 Strain gauge 'c' during "actualHPP". a) crack propagation and growth rate, b) peak-to-peak and average stresses, and c) stress PSD in three frequency ranges.

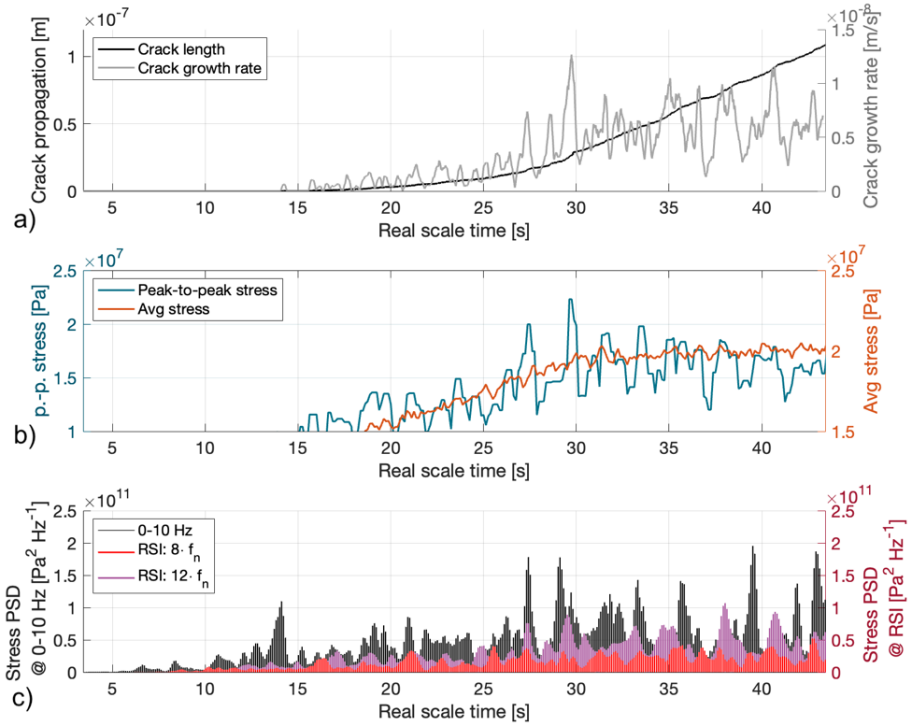

Figure 43 Strain gauge 'c' during "seq.2". a) crack propagation and growth rate, b) peak-to- peak and average stresses, and c) stress PSD in three frequency ranges.

Overall, the results allowed for a deep understanding of fatigue mechanism in multistage centrifugal pumps in operation, and provided a methodology to quantify the fatigue-related impact of transient sequences, with focus on the particular case of the ternary unit start-up in pumping mode performed with the Pelton turbine. Key findings on trajectory impact: among the tested start-up strategies, the shortest and most aggressive trajectory, optimal for Pelton turbines, also results in among the lowest pump damage, suggesting alignment between turbine efficiency and pump reliability. The study highlights the critical role of the final acceleration phase in fatigue damage development, showing that crack propagation is strongly correlated with the time spent at high rotational speed, whereas the early low-speed stages have a limited impact. Moreover, the importance of hydrodynamic phenomena is emphasized, as variations in damage levels, even under comparable high-speed durations, are associated with flow-related effects such as rotor–stator interaction (RSI), stall, recirculation, and flow separation. These findings underline the necessity of dynamic analyses that go beyond simple duration-based criteria. Finally, the proposed methodology establishes a foundation for data-driven predictive maintenance and joint turbine–pump optimization, paving the way for advanced asset management strategies that balance operational performance with degradation costs.

4.1.9 3D numerical simulations of the multistage pump

A refined unsteady simulation of the pump has been performed using a mesh with more than 50 million elements. Since on the experimental test rig, the nominal velocity is limited to 800 min^{-1} instead of the 1'000 min^{-1} used in the computation, only the dimensionless discharge factor Q_{ED}, speed factor n_{ED}, torque factor T_{ED} and power factor P_{ED} are compared. Two experimental operating points are considered for the comparison that surrounds the simulation operating point. Figure 44 is a bar chart that compares the experimental results with the simulation. Regarding the speed factor, the discrepancy is less than 1%. The simulated discharge factor is between the two experimental values. The torque and power

factors are underestimated by the simulation by approximately 10%. Therefore, the simulated operating point is in accordance with the experimental measurements. The efficiency predicted by the simulation is close to 87%, whereas the experimental efficiency is less than 83% and the prototype efficiency is higher than 91%. Figure 45 shows the streamlines computed using the time-averaged velocity and projected on the mid-plane located between the first and second stages of the pump. Several large recirculation zones are observed in the channels between the two runner stages as if the channels were not designed to match the flow angle at the outlet of the runner. This feature is observed in all stages of the pump.

While the CFD results revealed flow features and efficiency levels inconsistent with prototype measurements, further investigation has shown that uncertainty remains regarding the exact runner geometry used in the simulations. Although 3D scans of the pump body confirmed consistency with the model and prototype, no equivalent verification was possible for the runner. Nevertheless, the numerical work carried out during the HydroLEAP project remains valuable in highlighting the sensitivity of the results to geometric fidelity and in preparing a robust workflow for future studies. This experience underscores the importance of systematically acquiring high-quality 3D scans as a foundational step for any numerical investigation.

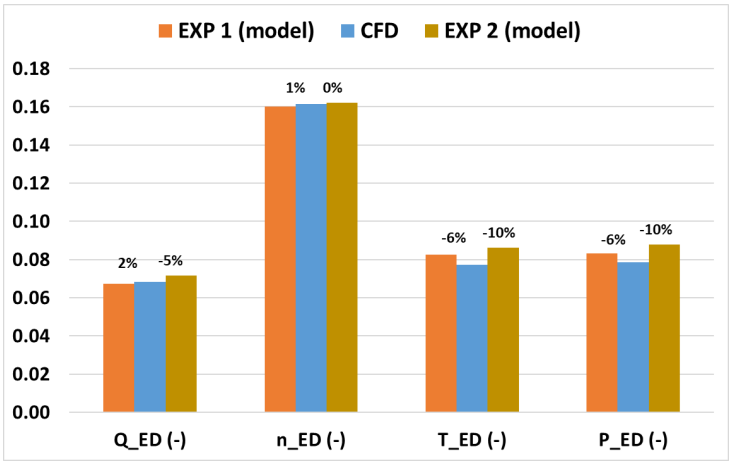

Figure 44: Comparison of the discharge, speed, torque and power factors between the experiment (EXP1 and EXP2) and the simulation (CFD).

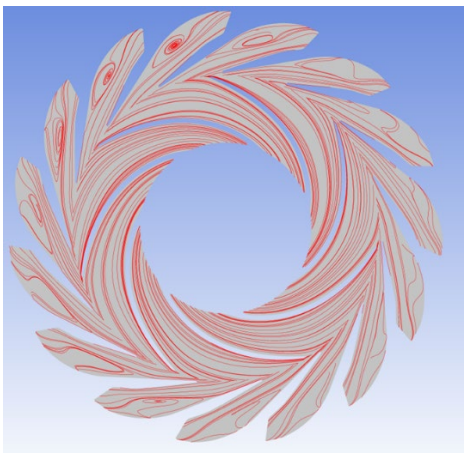

Figure 45: Computed streamlines

4.1.10 Cost of flexible operation

The cost associated with start-stop cycles of hydraulic machines—particularly pumps— was performed and integrated into into Alpiq's optimization and asset management models to assess their influence on operational strategies. In particular, a comparative study of two complementary methodologies for estimating and integrating start-stop costs was performed.

The first approach is a detailed bottom-up estimation which drew upon maintenance records, expected mechanical strains, and design-specific parameters. This method is grounded in existing literature, notably the framework developed by Abdi, adapted and extended to Alpiq's hydropower fleet. It breaks down start-stop costs into several contributing categories, including labor, water losses, failure risk, main inlet valve wear, generator degradation, pump and turbine-related impacts. To operationalize the method, a Python-based Tkinter application was developed, enabling interactive cost calculations based on unit-specific parameters and time-dependent maintenance histories. This tool provides transparency and usability for plant engineers and planners and represents a concrete deliverable of the project.

In parallel, a top-down modelling approach is used to investigate the system-wide impact of start-up costs on asset operations. This was done by integrating a range of hypothetical start-up cost values into Alpiq's production optimization tool and studying their effect on both the number of start-ups and the overall objective function. A series of simulations across multiple years and cost levels revealed a clear trade-off: higher start-up costs reduce the frequency of start-ups but also slightly reduce the model's economic performance. A Pareto analysis helped to visualize the balance between equipment preservation and revenue maximization (Figure 46).

Together, these two perspectives provide valuable insight into the role and practical estimation of start-stop costs. Although the data from the model tests could not be directly used due to geometric inconsistencies with the actual pumps, the comparative analysis between approaches proved instructive and sets the stage for more refined future studies.

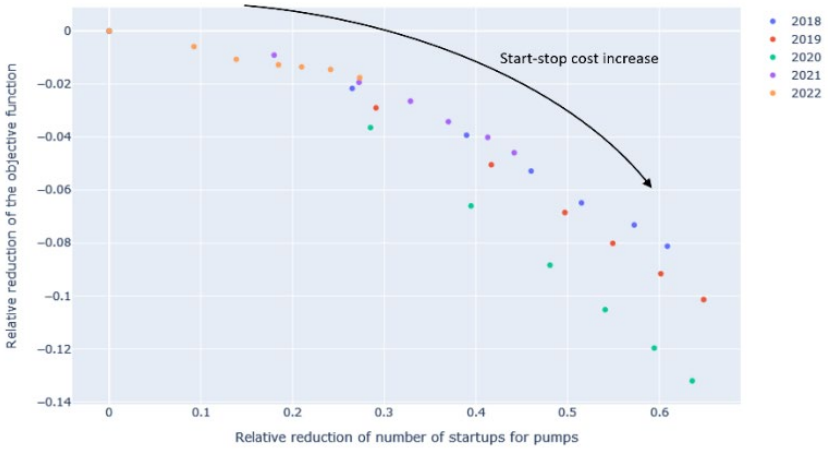

Figure 46: Relative reduction of objective function versus relative reduction of number of start-stops with varying start-stop costs.

4.1.11 Predictive maintenance

Fatigue cracks and hydro-abrasive erosion are currently the main challenges affecting Pelton runners. At the FMHL, the water in both the upper (Hongrin) and lower (Léman) reservoirs is free of abrasive sediment. As a result, Pelton runners at this site are not subject to erosion. Nevertheless, in 2017, a fatigue crack approximately 100 mm long was detected at the root of a bucket on one of the original runners. Since 2022, all the original cast Pelton runners of Veytaux 1 have been replaced with fully forged monobloc runners, significantly reducing the likelihood of similar failures in the future.

To support the implementation of a condition-monitoring strategy for the early detection of damage in Pelton runners, an approach based on identifying changes in the dynamic behaviour of Pelton runners in the presence of incipient damage was employed. Although erosion is not an issue at Veytaux 1, the site offers an excellent test case due to the presence of both original and newly installed runners—eight of each—throughout the project. At the start of the project, the ternary units were still operating with the original runners. The new runners were installed roughly one year later. This transition provided a valuable opportunity to measure and compare the dynamic response of the units equipped with both runner types. The methodology relied on comprehensive Finite Element Analysis (FEA) numerical simulations and an experimental modal analysis on the full-scale machine. For comprehensive technical descriptions, the reader is referred to the relevant published articles on the subject (Chiarelli et al. 2022, Chiarelli et al. 2023, Chiarelli et al. 2025a, Chiarelli et al. 2025b).

Experimental campaigns on the full-scale machines were conducted by following the timeline in Figure 47. In September 2021, a vibration fingerprint was performed on Gr3, which was still operating with the original runners. This fingerprint involved measuring the vibration response of the power unit under both steady-state and transient operating conditions, across various power outputs. To carry out the test, several accelerometers were installed on the unit's bearings, and data from the permanent vibration sensors were also recorded. In 2022, the runners of Gr3 were replaced. An EMA was then conducted on one of the original runners after it had been removed from the unit. Following the installation of the new runners, a second vibration fingerprint was performed, using the same instrumentation setup and test procedure as the initial campaign. In 2023, a transmissibility experiment was carried out on Gr2, which was still equipped with the original runners. This experiment aimed to characterize the attenuation of vibration transmission from the runner to the bearings. The objective was to assess the feasibility of detecting runner-originating vibrations via bearing-mounted sensors, thereby reducing the need for intrusive instrumentation on the runner itself. The final two experimental campaigns were conducted in April 2024. These included an EMA on a new runner suspended by a sling, and a repetition of the transmissibility experiment on Gr3—this time with the new runners installed.

In parallel with the experimental campaigns, several FEM modal simulations were performed to characterize the dynamic behaviour of the original runners. Additionally, a FEM modal simulation of the new runner was carried out by ANDRITZ, the manufacturer, to supplement the experimental measurements. These simulations enabled a rapid assessment of how boundary conditions influence the dynamic response of the runners. Furthermore, a series of simulations with modified hub and bucket geometries was conducted to evaluate the effects of geometric changes on the runners' modal parameters.

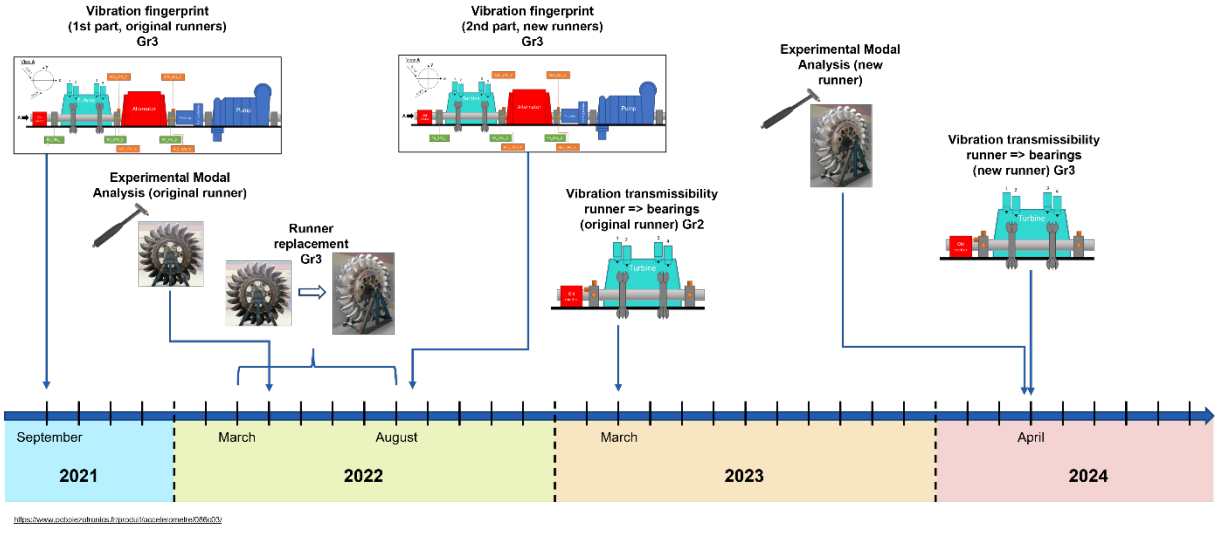

Figure 47: Timeline of experimental campaigns at the FMHL demonstrator.

Dynamic behaviour of the original runners

The first six vibration modes of a single bucket were computed using FEM modal simulations and are shown in Figure 48. These six bucket modes correspond to the first six mode families observed on the complete runner. Since the runner comprises 22 buckets, a variety of vibration modes can be classified according to their mode family and the number of nodal diameters (NDs). NDs are imaginary lines along which a phase shift occurs in the vibration pattern. For the 22-bucket runners of Veytaux 1, the maximum number of NDs is 11, as illustrated in Figure 49. The classification of the runner modes into the first six mode families is presented in Figure 50. The grey area highlights the disk modes with fewer than four NDs. These modes involve significant deformation of the hub, as shown in Figure 49, and are more representative of global runner deformation, as a disk, rather than isolated bucket deformation. In contrast, modes with a higher number of NDs exhibit minimal hub deformation and more pronounced bucket deformation. These modes are therefore more sensitive to changes in bucket geometry and less influenced by the runner's boundary conditions.

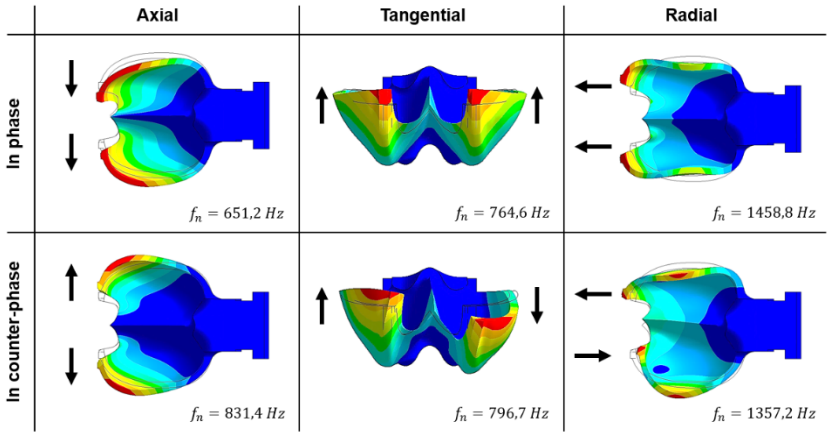

Figure 48: First six bucket modes reproduced from Chiarelli et al. 2025b.

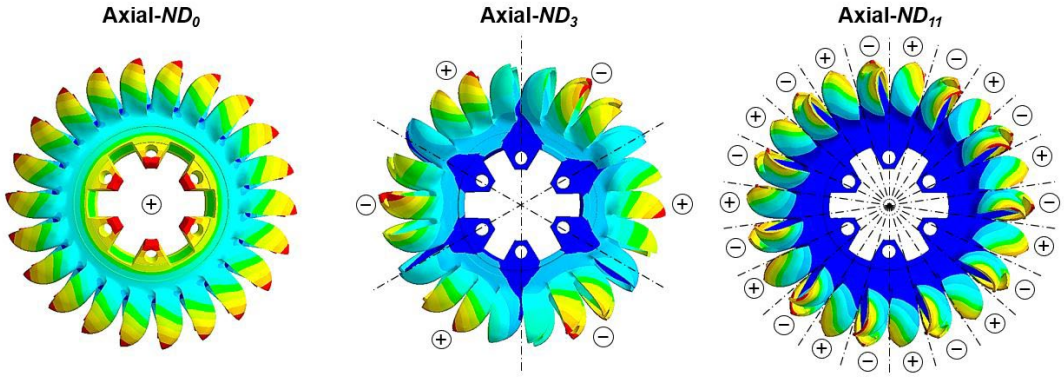

Figure 49: Runner vibration modes of the Axial mode family counting 0, 3, and 11 nodal diameters. Figure reproduced from Chiarelli et al. 2025b.

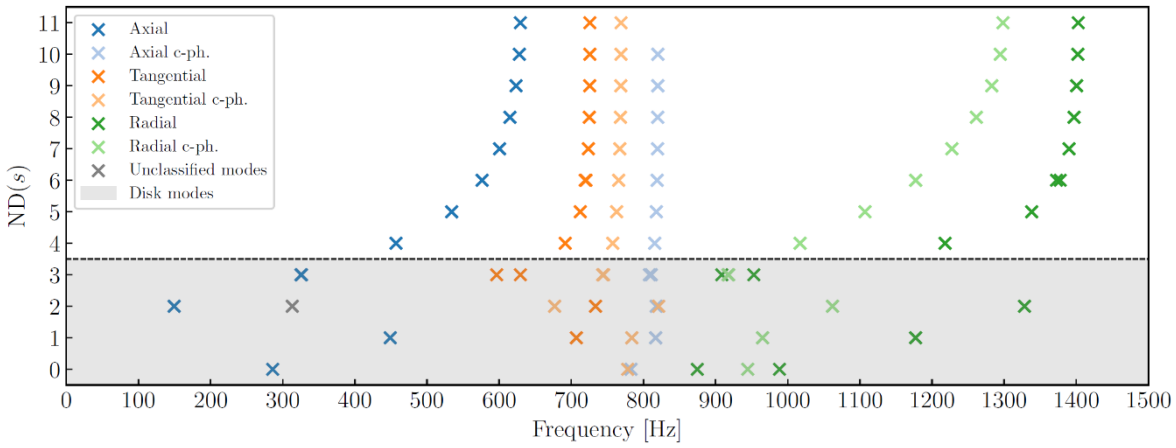

Figure 50: Runners modes for the first six mode families. The modes are classified according to the mode family and the number of NDs. Figure reproduced from Chiarelli et al. 2025b.

These numerical results were validated through EMA conducted on three different original runners. *EMA-1* was performed on a runner mounted on a metallic support typically used for maintenance activities. *EMA-2* and *EMA-3* were carried out on runners attached to the turbine shaft inside the turbine housing. The results of the three EMAs, along with the FEM simulations of the original runners, are summarized in Figure 51.

The three numerical simulations are labelled as follows: *FEM: free-BC*, representing free boundary conditions; *FEM: 3-BC*, where three out of six hub bores are constrained; and *FEM: 6-BC*, where all six hub bores are constrained, simulating a runner fixed to the shaft. Results are normalized to the Axial–ND_{11} mode in the left graph, while the right graph highlights frequency shifts, using the *FEM: free-BC* simulation as the reference.

Since *EMA-1* was used to calibrate the numerical simulations, a good correspondence is observed between the *FEM: free-BC* simulation and *EMA-1* results, particularly for modes with higher NDs. However, for *EMA-2* and *EMA-3*, consistent frequency shifts are observed in modes with NDs greater than 4. These discrepancies may indicate slight geometric differences among the tested runners. Given that all three runners were commissioned in 1971, such variations could be attributed to the cumulative effects of maintenance operations over the years. Furthermore, as the runners were originally cast, some degree of geometric variability is expected due to the inherent limitations of the manufacturing process.

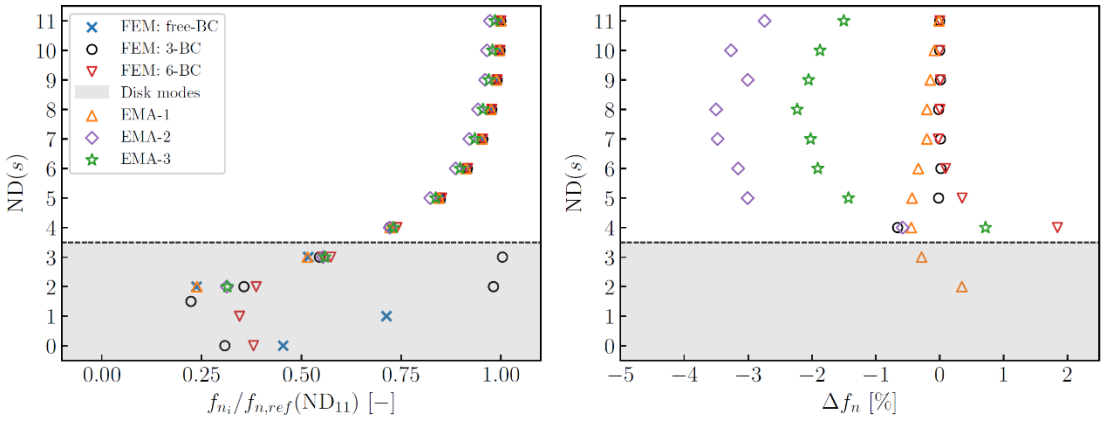

Figure 51: Axial modes for the three EMA and the numerical simulations performed with different boundary conditions. Figure reproduced from Chiarelli et al. 2025b.

Dynamic behaviour of the new runners

The new runners installed at Veytaux 1 share similar hydraulic characteristics with the original runners. The hub geometry remained unchanged, while the primary difference lies in the hydraulic design of the buckets, as shown in Figure 52.

Figure 52: Geometries of the original runner (left) and new runner (right).

The EMA conducted on the new runner enabled the identification of each mode with its corresponding natural frequency and mode shape. This makes a full comparison with the FEM simulation possible for the first six mode families. The results presented in Figure 53 show excellent agreement between the EMA and FEM across the entire frequency range, indicating a well-calibrated numerical model and validating the experimental procedure. However, some high-ND modes could not be resolved by the EMA due to its limited frequency resolution. When successive modes have a frequency spacing close to the resolution limit, they appear as a single peak, making individual modes indistinguishable.

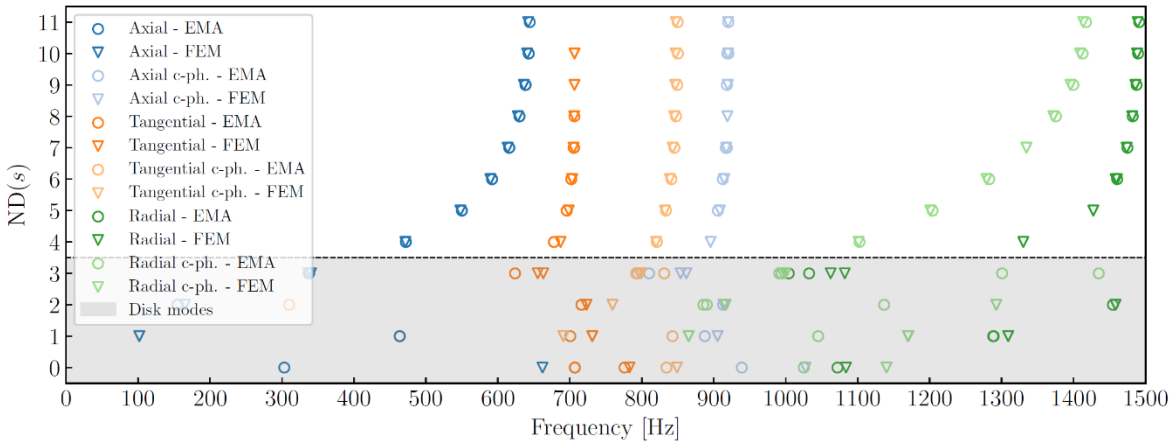

Figure 53: Comparison of the numerical (FEM) and experimental (EMA) results on the new runner.

A comparison of the FEM modal simulations performed on the original and new runners reveals significant differences in their respective dynamic behaviour. In Figure 54, the vibration modes of the original runner are indicated by cross markers, while the corresponding modes of the new runner are represented by inverted triangles. All mode families of the new runner exhibit higher natural frequencies, except for the Tangential mode family. While the frequency shift within the axial mode family is limited to a few hertz, the difference in natural frequencies between the two runner geometries increases with frequency. This trend highlights the growing divergence in dynamic behaviour between the original and new runners across higher-frequency mode families. However, the order of appearance of the mode families is preserved across both runner types.

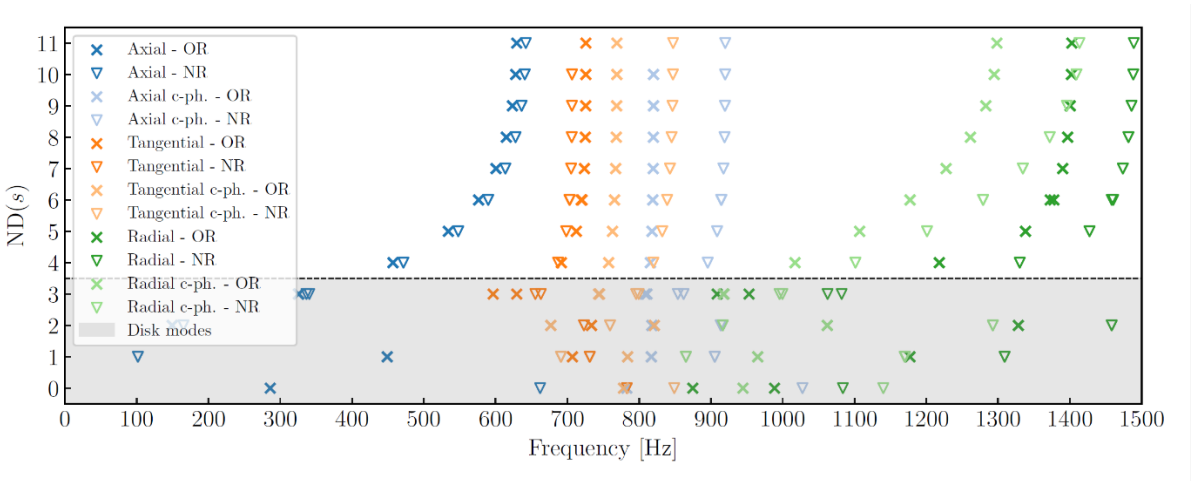

Figure 54: Vibration modes for the first six mode families for the original runner "OR" and the new "NR". The modes have been computed through numerical FEM modal simulations with a free BC.

The differences in the dynamic behaviour of the two runner geometries are attributed to variations in the bucket design, which have been shown to dominate the modes with high NDs within a given mode family. Therefore, although the hydraulic characteristics, such as pitch diameter and bucket width, remain unchanged, the significant differences in bucket geometry result in substantial changes in the overall dynamic behaviour of the runners.

Transmissibility experiments– original and new runners.

The experimental setup for the transmissibility tests is shown in Figure 55. While the original runners are visible in the central image, the same setup was used for the transmissibility experiment conducted with the new runners. The measurement consists of impacting the runner with an instrumented hammer and recording the response at both the runner and the two bearings. The hammer is equipped with a force sensor, allowing one force signal to be recorded for each impact, along with eight acceleration signals (one per accelerometer). A frequency response function (FRF) is then computed for each force–acceleration pair. The FRF represents the transfer function between the acceleration measured at a specific location and the applied force. Peaks in the FRF indicate resonances, i.e., vibration modes, while the amplitude of the response reflects the level of attenuation of the vibration signal between the point of impact and the measurement location.

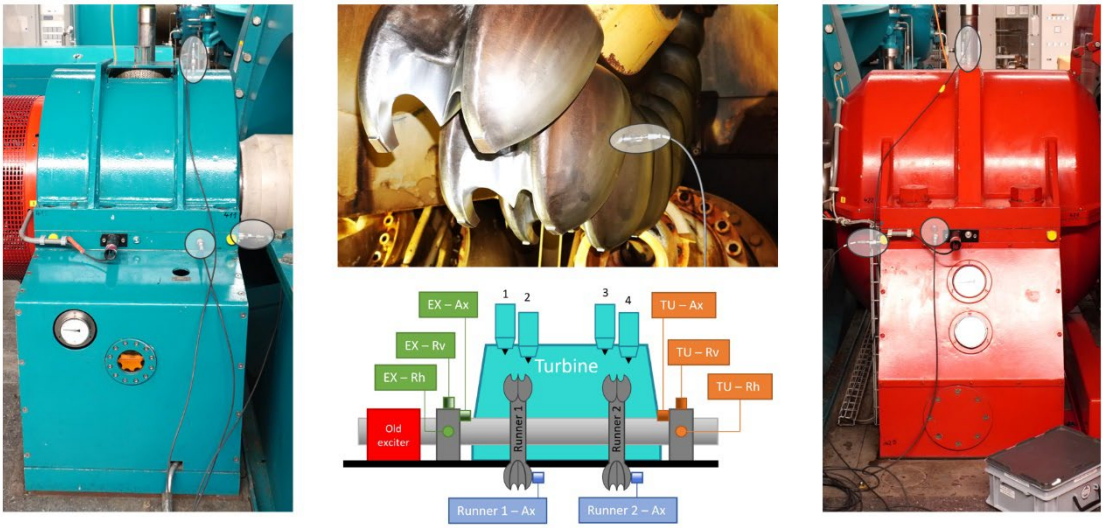

Figure 55: Experimental setup of the transmissibility experiment conducted with the original runners. The light blue exciter bearing (EX) and the red turbine (TU) bearing are instrumented with three accelerometers each.

Both graphs in Figure 56 highlight the attenuation of vibration from the runner to the bearings. The black curves, which represent the FRFs measured directly on the impacted runner, show amplitudes that are, on average, two orders of magnitude higher than those measured at the bearings, represented by the orange and blue curves. This attenuation is attributed to the transmission path: vibrations travel from the runner through the shaft and are transmitted to the bearings via the narrow contact lines of the journal bearings. It is important to note that the bearings are hydrodynamic, and during the measurements, no oil film was present between the shaft and the bearings. Despite the significant attenuation, nearly all of the runner's natural frequencies can still be detected at the bearings. The Axial modes, in particular, are visible as sharp and well-defined peaks. However, in the 650–850 Hz range, the FRFs become noisier, making it more difficult to clearly isolate all natural frequencies. Additionally, the transmissibility from runner 1 to the turbine bearing (blue curve in the top graph of Figure 56) is noticeably lower than that to the exciter bearing, particularly for the axial modes. In contrast, when runner 2 is impacted (bottom graph), both bearings show FRFs of similar amplitude across the entire frequency range, indicating that both bearings detect the natural frequencies of runner 2 equally well. This discrepancy could be due to the asymmetry of the shaft: the two bearings are subject to different loading conditions, with the old exciter on the left side and the alternator on the right. However, this hypothesis could not be confirmed experimentally.

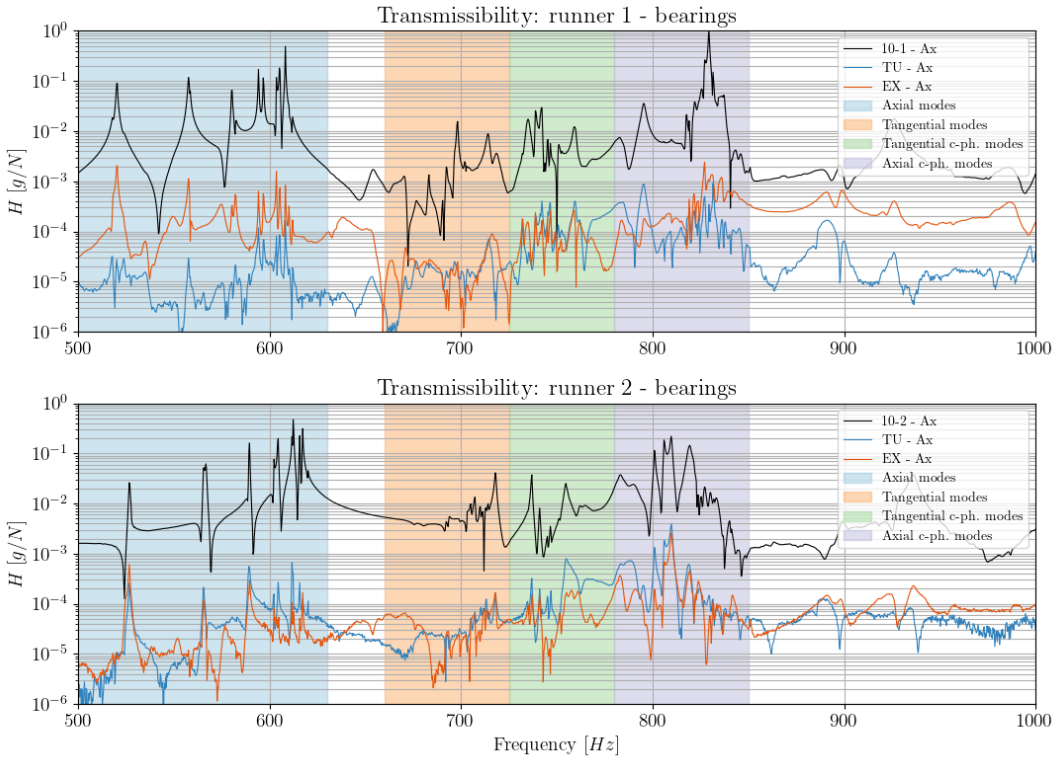

Figure 56: Transmissibility experiment from the runners to the bearings. The black lines represent the FRFs on buckets n°10 of each runner, while the orange and blue lines depict the FRFs between the runners and the accelerometers positioned in the axial direction on the exciter (EX) and on the turbine (TU) bearings, respectively. The top graph corresponds to the impact on runner 1, while the bottom graph to runner 2. Figure reproduced from Chiarelli et al. 2023.

To evaluate the influence of accelerometer positioning on the bearing, the three FRFs measured on the turbine bearing during impacts on runner 2 are compared in Figure 57. All three positions effectively capture the axial modes, displaying similar amplitudes in their respective FRFs. However, the radial-horizontal (Rh) position shows greater sensitivity in the 700–850 Hz frequency range compared to the other two positions. For this reason, the Rh position is given particular emphasis in the analysis of the startup transients.

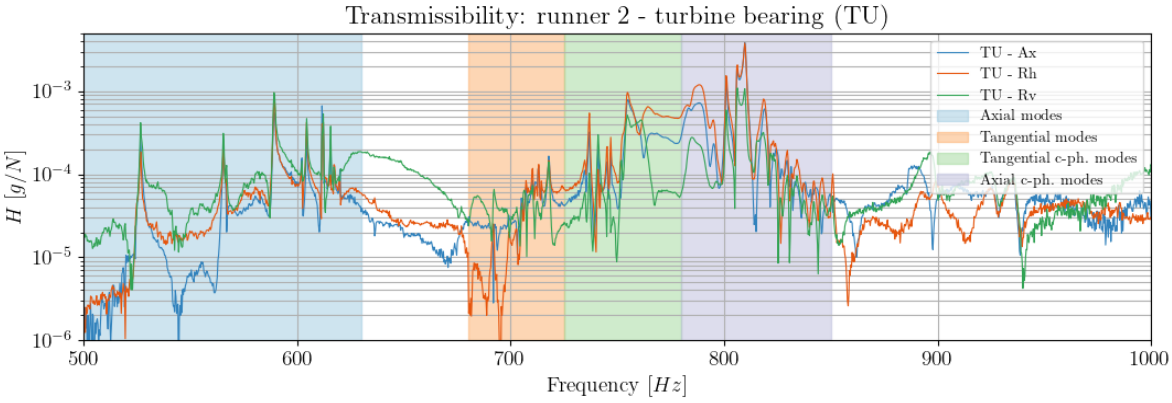

Figure 57: FRFs measured on the turbine (TU) bearing when impacting runner 2. The FRFs for the three accelerometer positions are represented: axial (Ax), radial-horizontal (Rh), and radial-vertical (Rv). Figure reproduced from Chiarelli et al. 2023.

Real-time condition monitoring during start-up

Start-up transients were recorded to take advantage of the strong broadband excitation that occurs when the injectors first open. In this early phase, the water jets strike the stationary runner buckets with significant force, acting similarly to an impact hammer and exciting a broad frequency range. The underlying hypothesis is that this phase enables the identification of runner natural frequencies that are otherwise difficult to detect during steady-state operation. Previous studies have shown that startup transients are particularly effective for detecting runner-associated natural frequencies from the bearings. Therefore, during the two vibration fingerprints performed with the original and new runners, several startup transients were recorded and analysed.

The signal from the accelerometer mounted on the turbine bearing in the radial-horizontal direction was analysed in both the time and frequency domains. The top graph of Figure 58 shows the accelerometer signal over the first 40 seconds of the three recorded startups. Although startup transients are inherently non-repetitive, the graph reveals that the vibration amplitudes follow a consistent and predictable pattern throughout the transient phase. A similar trend is observed for the three startups recorded with the new runners during the second fingerprint campaign, as shown in the top graph of Figure 59. Moreover, regardless of the runner type, the peak vibration amplitudes consistently fall within a similar range of ±1.2 g.

The lower graphs in Figure 58 and Figure 59 present the ensemble average of the power spectral density (PSD), computed over a two-second window starting two seconds after the initial water jet impact. This time interval is highlighted by the grey band in the upper graphs. In the first fingerprint campaign with the original runners, the startup transients consistently excite frequencies with significantly higher amplitudes in the 680–780 Hz range. This frequency band corresponds to the tangential and tangential in counter-phase (c.-ph.) modes of the original runners, suggesting that these natural frequencies are reliably excited during startup. However, it must be noted that, in the absence of onboard instrumentation directly on the runner, the possibility that these frequencies originate from other turbine components cannot be entirely excluded.

In the second fingerprint campaign, conducted with the new runners, the highest excitation levels during startup are observed in the 740–890 Hz range, as shown in the bottom graph of Figure 59. This band corresponds to the tangential in c.-ph. and axial in c.-ph. natural frequencies of the new runners, as predicted by FEM modal simulations.

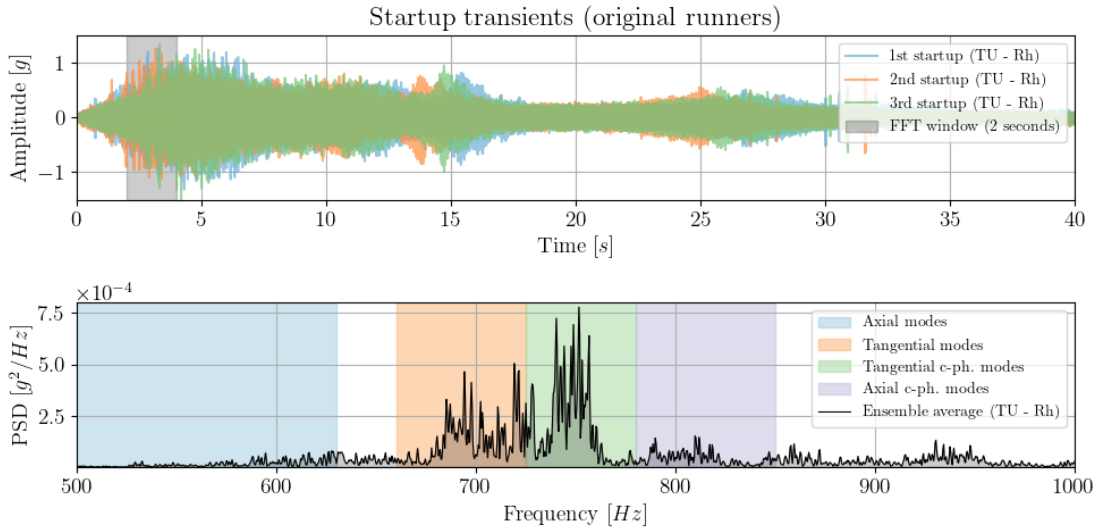

Figure 58: Three start-up transients measured during the first fingerprint (top graph). The unit is operated with the original runners. Ensemble average of the power spectral density (PSD) computed two seconds after the first impact, with a FFT window width of 2 seconds (bottom graph). Figure reproduced from Chiarelli et al. 2023.

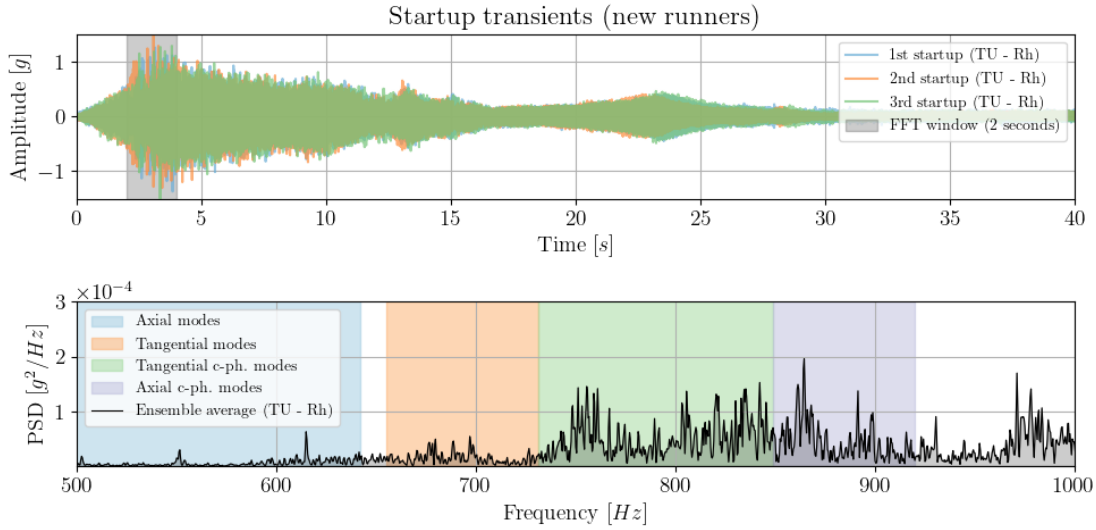

Figure 59: Three startup transients measured during the second fingerprint (top graph). The unit is operated with the new runners. Ensemble average of the power spectral density (PSD) computed two seconds after the first impact, with a FFT window width of 2 seconds (bottom graph).

Change in dynamic behaviour of the runners due to abrasive erosion.

Even though abrasive erosion is not a concern for the FMHL demonstrator, its impact becomes significant when considering the broader Swiss hydropower fleet, particularly for Pelton runners, where erosion can notably alter surface conditions and runner efficiency over time. Therefore, the study on the dynamic behaviour of the Pelton runner was extended to include scenarios in which material removal occurs due to abrasive erosion. This extension aims to evaluate the robustness and applicability of the developed methodology for real-time condition monitoring and predictive maintenance, even under

conditions of substantial erosion rates. By incorporating erosion-induced changes into the analysis, the study enhances the practical relevance of the proposed approach, ensuring its effectiveness in capturing performance degradation and supporting maintenance planning across a wider range of operating and environmental conditions.

FEM modal analyses were conducted to evaluate the effect of localized erosion on the dynamic behaviour of the original Pelton runners. Four simplified erosion scenarios were examined, each involving uniform material removal according to realistic erosion patterns documented for uncoated Pelton runners. The analysis focused solely on the bucket, as its natural frequencies are close to those of the full runner with 11 NDs, and changes in bucket geometry significantly affect the runner's vibration modes, especially at higher NDs, as demonstrated earlier. The erosion scenarios and the results are presented in Figure 60.

In the first scenario, erosion of the main splitter was simulated by uniformly removing material along its entire length. The erosion level was quantified by the *b/B* ratio, defined as the width of the eroded main splitter (*b*) relative to the inner width of the bucket (*B*). The scenarios ranged from an intact splitter (*b/B* = 0.27%) to a severe erosion case with *b/B* = 5.55%, equivalent to a splitter width of about 40 mm. The results showed that the main splitter erosion led to small shifts in natural frequencies: the Radial c-ph. frequency increased slightly due to mass reduction, while the tangential mode decreased as the local stiffness was reduced. Other modes showed only minor changes.

The second scenario investigated uniform thickness loss within the intrados, using elliptic-shaped erosion patches positioned in high-curvature regions where sediment impacts are most severe. This reflects the typical hydro-abrasive wear pattern where sediment particles deviate from the flow and strike the intrados surface. The erosion depth was specified by the *t/B* ratio, with (*t*) being the eroded thickness. Thickness losses from 0.5 mm to 3 mm were simulated, corresponding to t/B ratios up to about 1.5%. The simulations revealed a consistent and more pronounced reduction in natural frequencies for all modes as erosion depth increased, with the Radial mode showing the largest shift (up to -49 Hz). These results highlight that the intrados region plays a key role in maintaining bucket stiffness and that its erosion affects the structural rigidity of the bucket.

The third scenario combined the first two scenarios to evaluate their combined effect. The results showed that the frequency shifts from each pattern were largely additive, demonstrating that spatially separate erosion regions influence the modal response independently when they do not overlap.

A fourth scenario simulated a more extensive and realistic intrados erosion pattern based on field measurements from a Pelton turbine operating under high sediment loads. Here too, the erosion depth was expressed by t/B ratios corresponding to erosion thickness of 1, 2, and 3 mm. Although this resulted in the highest overall material loss, the frequency shifts were partly offset by the balancing effect of mass removal counteracting stiffness loss for some modes. Notably, the Radial and Radial c-ph.modes were still strongly affected, highlighting the role of specific bucket regions in maintaining overall stiffness.

Finally, the erosion of the bucket cutout was also assessed by removing material uniformly along its length. This region showed limited influence on most modes in comparison to the other scenarios.

Overall, these simulations demonstrate that localized erosion can alter the natural frequencies of Pelton buckets in different ways depending on the erosion location and depth. Understanding these effects is essential for predicting shifts in the dynamic response of runners operating under severe hydro-abrasive conditions.

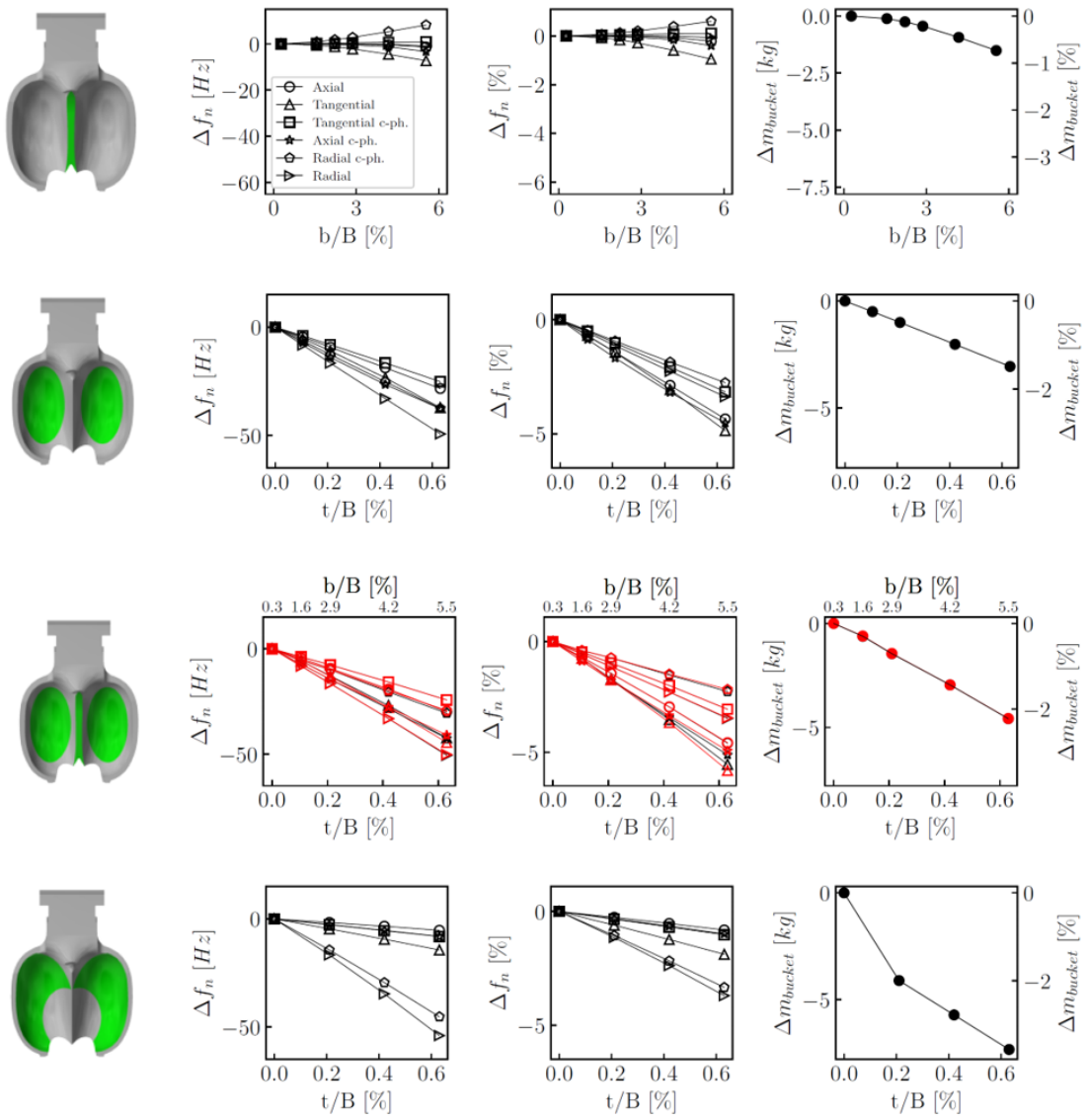

Figure 60: Erosion scenarios, from top to bottom: Scenario 1 - Main splitter only; Scenario 2 - Elliptic patterns; Scenario 3 – combination of Scenario 1 and 2; Scenario 4 – realistic erosion pattern. Figure reproduced from Chiarelli et al. 2025b.

4.2 Grid flexibility through battery hybridization of medium- head run-of-river power plants – The KW Ernen demonstrator

4.2.1 Increased annual production and optimal refurbishment choice

The refurbishment strategy for the KWE power plant focused on increasing output capacity and improving operational efficiency. The existing configuration includes two 16 MW Francis turbines operating under a rated head of 270 mWC. The water intakes are collected in the Rhône River at Gluringen through a 3 km long gallery with a free surface and in an upstream reservoir named Zenbinnen through a 4 km long gallery. These two flows are mixed into a surge tank in Wasen characterized by a very small volume. From there, water is conveyed through a 700 m penstock (1.85 m to 1.65 m diameter)

to the powerhouse. A SIMSEN model was developed based on FMV-provided drawings and validated using experimental data from Hydro Exploitation.
The integration of a 6.14 MW Pelton turbine was identified as the optimal refurbishment solution. Two Pelton configurations were compared, one with 4 injectors and another with 6 injectors, but the optimization results show no difference between the two options. The choice of the number of injectors has a significant impact on the life of the Pelton turbine. The configurations with 4 injectors and 6 injectors were compared by assessing the mechanical and economic advantages. From an energy point of view, there is no difference between 4 injectors and 6 injectors because the efficiency curves are very close. The new Pelton turbine can be used to produce a wide range of power set point and the Francis turbines will be operated around their best efficiency point. This configuration reduces wear and tear on the Francis turbines over all the concession. In terms of electromechanical cost, the prices of the two Pelton are also very close. The choice must be made according to the maintenance, the congestion of the unit in the power plant and the quantity of sediments in the water. In terms of congestion, the volume of the turbine equipped with 6 injectors is 50% higher than the turbine equipped with 4 injectors. However, from an maintenance point of view, the solicitation and erosion of the turbine equipped with 4 injectors are reduce by 47% compared to the 6 injectors.
An additional step for this optimal refurbishment has been to better consider the Zenbinnen reservoir in the simulation of the typical year. Indeed, as the water coming from this reservoir is less loaded with sediment, it is interesting to favor the water coming from this source rather than the water coming from Gluringen. This last optimization will make it possible to highlight the storage potential thanks to this dam and to reduce the wear and tear of the different units due to the sediments.
To compare these different final options, the RENOVHydro library (SFOE contract number: SI/501436-01) relies on a systematic assessment of the hydropower plants generation increase of each possible upgrade option using the SIMSEN software as a backbone to identify the most cost-effective civil and electromechanical options. Thus, each hydropower plant upgrade option can be assessed with performance indicators such as annual energy, annual revenue, profitability, by considering hydraulic structure, hydro units and hydropower station interaction with the grid for the provision of ancillary services. To compute these final performance indicators, the optimize annual power output and the maximize annual revenue are provided by the RENOVHydro library. This procedure was applied to the different options by using the electricity market price and the water inflow from Gluringen and Zenbinnen provided by FMV. Although the total annual energy production slightly decreased, the overall revenue increased by 3.4%, due to strategic water use during high peak electricity prices. This shift away from best efficiency operation allowed turbines to operate at full capacity during high-price periods, enhancing economic performance. The final recommendation confirms the proposed integration of the 6.14 MW Pelton turbine, combined with the optimized use of the Zenbinnen reservoir, as the most effective refurbishment strategy for increasing output and reducing sediment-induced wear.

4.2.2 Performance assessment of the existing KWE Francis turbine and in hybrid configuration

Reduced scale model testing of one double-flux Francis turbine unit has been performed at PTMH to assess performance and flexibility potential improvements. Unlike the two units of the KWE power station, the turbine model implemented on the test-rig featured a vertical axis. The experiments have been arranged as follows:

- **Phase 1**: Steady-state characterization on the whole operating range. Tailwater reservoir at atmospheric pressure.
    - Efficiency hill-chart and characteristic curves
    - Pressure fluctuations and torsional torque at the guide vanes axis

- **Phase 2**: Cavitation phenomena characterization at fixed n_{ED} along the whole Q_{ED} range. Tailwater reservoir depressurized at two different level: $\sigma = 0.065$ and $\sigma = 0.04$ (i.e. representative of the σ level on the KWE power plant).
    - Pressure fluctuations and torsional torque at the guide vanes axis
    - High-speed camera videos to depict cavitation incipience and development
- **Phase 3**: Dynamic behavior during frequency containment reserve (FCR) provision and hybridization. At fixed n_{ED}. Tailwater reservoir depressurized at $\sigma = 0.04$ (i.e. representative of the σ level on the KWE power plant). Different dispatch scenarios occurred in 2024 at KWE, time duration of 4-hours each. Occasional sequences (5-7 minutes pre-defined time lapse) of pressure fluctuations and torsional torque at the guide vanes axis measurements.
    - Constant power setpoint, at part load.
        - No BESS
        - Hybrid, with BESS: “deadband governor” (not optimized BESS control) and MPC (optimized BESS control)
    - Variable power setpoint, closer to BEP.
        - No BESS
        - Hybrid, with BESS: “deadband governor” (not optimized BESS control) and MPC (optimized BESS control)

Experimental set-up

To assess the impact of fatigue on the lifespan of hydraulic machines, a well-established methodology involves evaluating the mechanical stresses experienced by the runner during operation and correlating these stresses with material failures documented in relevant databases. However, applying strain gauges to the turbine has not been possible due to the need for sufficient space between the runner blades. Since for a Francis turbine the primary structural loads arise from hydrodynamic phenomena that occurs at known locations, such as the rotor-stator interaction (RSI) in the vaneless gap, the incipience of inter-blades cavitation and the cavitation structures in the low-pressure side (i.e. elbows and draft tubes), the amplitude of these phenomena can be determined through pressure measurements on the static frame of the hydraulic circuit. Consequently, this study uses pressure fluctuation measurements from various locations on the installation's static frame to depict the damaging effects of different operating conditions. Hereafter, the 95% confidence interval for the peak-to-peak amplitude of pressure fluctuations is considered as an indicator of the damage trend. In Figure 61, a summary of the implemented instrumentation is provided. For each investigated steady-state operating condition, the measured voltage signals are amplified using an amplifier and recorded by a NI4472 data acquisition system. Sensor signals are sampled at 5 kHz rate over a duration of 10 seconds. The conversion from volts to pascals is achieved through the calibration of the pressure sensors conducted before the tests. The 3D CAD model of the reduced scale model is presented in Figure 62, while two different views of the test-rig are shown in Figure 63.

The tests are conducted while ensuring both kinematic similarity and cavitation similarity. These criteria are used to guarantee that the velocity triangles and cavitation inception conditions are similar between the reduced scale model and the full-scale runners. To meet these requirements, the dimensionless speed and discharge IEC Machine Factors, n_{ED} and Q_{ED}, along with the Thoma number σ, are considered, as defined in the IEC 60193 standard.

INPUT SIGNAL			AMPLIFIER	AMPL. CH	PXI CARD	PXI CH
PCB	7480	UPPER DRAFT TUBE - FRONT	PCB 1	1	2	0
PCB	7481	UPPER DRAFT TUBE - DOWN	PCB 1	2	2	1
PCB	6893	UPPER DRAFT TUBE - BACK	PCB 1	3	2	2
PCB	35954	LOWER DRAFT TUBE - FRONT	PCB 1	4	2	3
PCB	7488	LOWER DRAFT TUBE - UP	PCB 1	5	2	4
PCB	6907	LOWER DRAFT TUBE - BACK	PCB 1	6	2	5
PCB	7451	UPPER ELBOW - FRONT	PCB 2	1	3	0
PCB	6908	UPPER ELBOW - BACK	PCB 2	2	3	1
PCB	40079	LOWER ELBOW - FRONT	PCB 2	3	3	2
PCB	6905	LOWER ELBOW - BACK	PCB 2	4	3	3
PCB	6891	SPIRAL CASE - INLET	PCB 2	5	3	4
PCB	7849	SPIRAL CASE	PCB 2	6	3	5
KYOWA	P1	VANELESS SPACE	OLD	1	4	0
KYOWA	P2	VANELESS SPACE	OLD	2	4	1
KYOWA	P3	VANELESS SPACE	OLD	3	4	2
TORSION TORQUE	LABEL A	GV TORQUE 1	OLD	9	4	3
TORSION TORQUE	LABEL B	GV TORQUE 7	OLD	10	4	4
TORSION TORQUE	LABEL C	GV TORQUE 15	OLD	11	4	5
TORSION TORQUE	LABEL D	GV TORQUE 16	OLD	12	4	6

Figure 61 Summary of the PF3 test-rig instrumentation

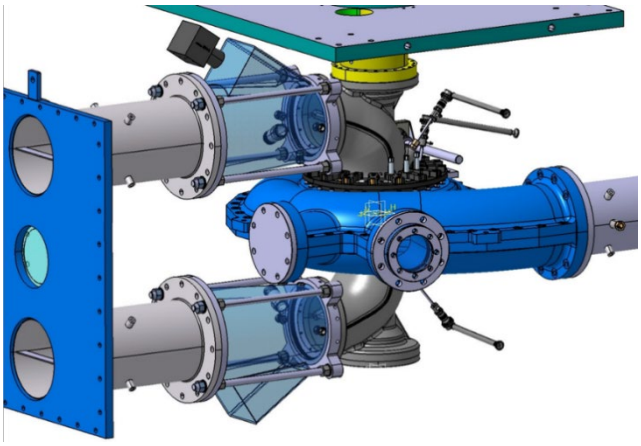

Figure 62 Reduced scale model CAD

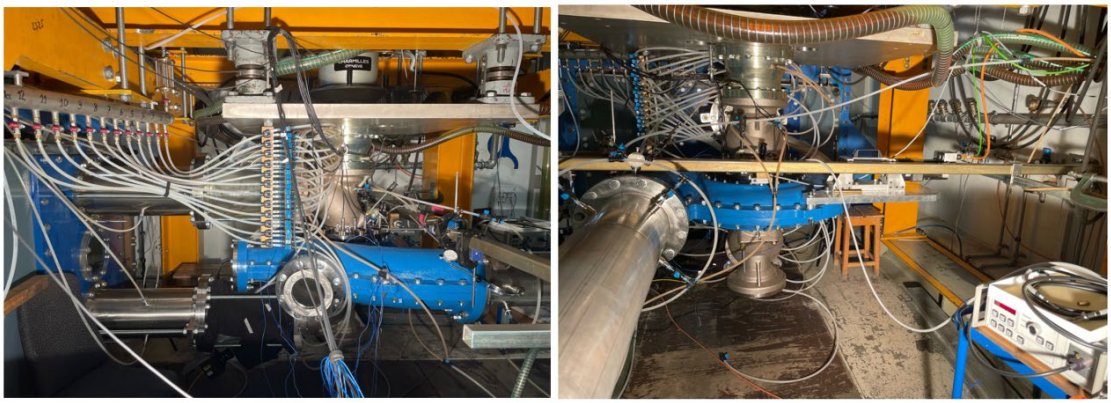

Figure 63 Instrumented PF3 test-rig. View coplanar (left) and perpendicular (right) to the spiral case inlet and the draft tubes.

Phase 1: Steady-state characterization

Figure 64 presents the efficiency hill chart of the turbine in the $n_{ED} - Q_{ED}$ plane. The axes are normalized by their respective values at BEP ${n_{ED}}^* = 1, {Q_{ED}}^* = 1$ and ${\eta}^* = 1$.

Experimental data points are shown as black dots, the BEP as a white dot, with efficiency contours overlaid on the diagram. The BEP is measured at $\eta = 0.898$ for a guide vane opening (GVO) of 15.4°. The efficiency decreases more rapidly as n_{ED} exceeds its nominal value compared to its decline at lower n_{ED}.

There is a sharp increase in efficiency until ${Q_{ED}}^* < 0.3$, after which the efficiency remains relatively constant for ${Q_{ED}}^* > 0.3$. Implementing the step-up procedure to compute the efficiency at full scale, the BEP translates in $\eta = 0.917$ for an equivalent mechanical power $P_m = 14.4$ MW. In Figure 65, a comparison with full scale data for a constant value of $n_{ED} = 0.24$ (i.e. nominal speed and head H = 270m) is presented.

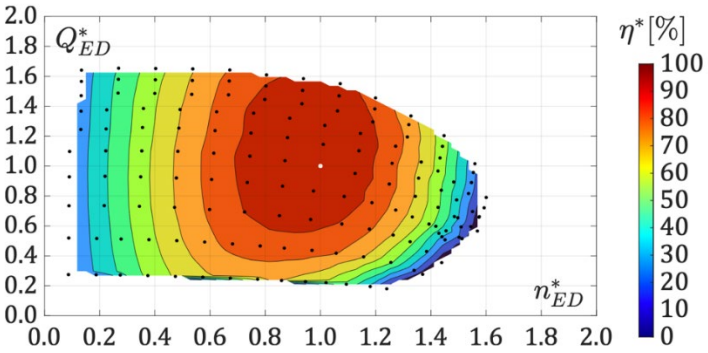

Figure 64 Reduced scale model efficiency hill-chart

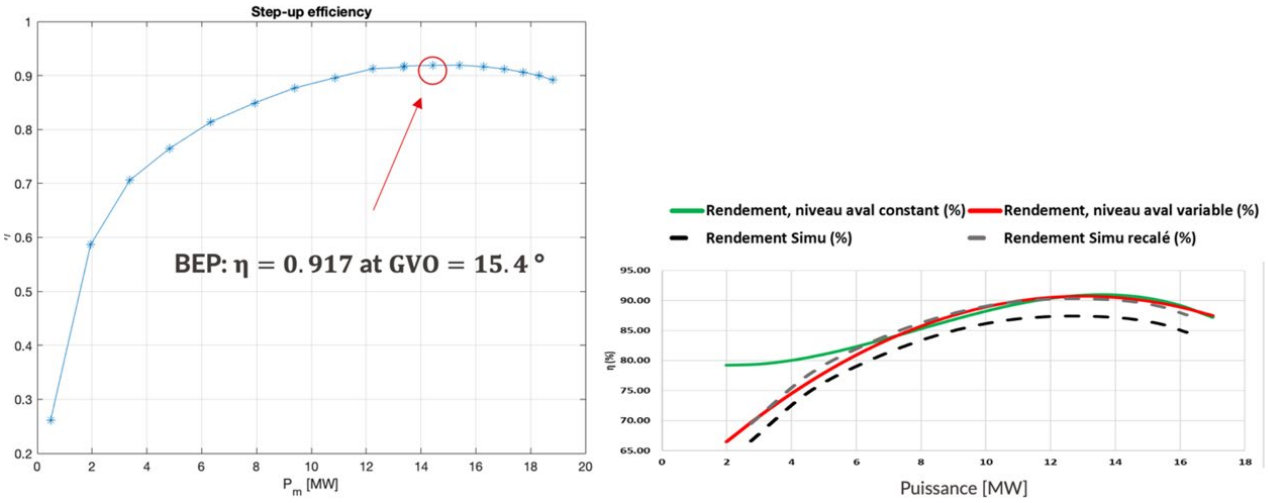

Figure 65 Full-scale hill chart at $n_{ED} = 0.24$

Phase 2: Cavitation phenomena

A comparison between the draft tube and elbows pressure sensors is performed for different values of Thoma number σ to investigate the cavitation incipience. The pressure sensors used to illustrate such behavior are selected in reason of the related hydrodynamic phenomena, i.e. the swirling flow at the machine outlet (elbows and draft tubes) that involve a cavitating vortex rope in case of low Thoma values σ, and the rotor-stator interaction observed in the vaneless gap between the guide vanes outlet and the blades leading edge. The speed factor n_{ED} is set to the nominal value. Concerning the elbows, minor differences in peak-to-peak values are found in elbows when changing σ. This is probably due to the minor impact that cavitating structures have given that the traversing shaft prevent the development of such structures. For both draft tubes, the three curves overlap in the BEP range. The curve with σ equivalent to KWE diverges from the one with intermediate σ value earlier than it does from the curve with σ equivalent to atmospheric pressure. At lower values of $Q_{ED}{}^{*}$ the curve with σ atmospheric remains relatively flat, while the other two curves show approximately three times higher peak-to-peak values, indicating a stronger cavitation regime. Furthermore, the curve with the lowest σ demonstrates a sharper increase in peak-to-peak values at higher $Q_{ED}{}^{*}$, suggesting that cavitation begins to develop in this region as well.

Phase 3: Dynamic behaviour during frequency containment reserve (FCR) provision and hybridization

The quantification of the operating parameters at reduced scale for hybrid operation has been achieved as follows:

- Real-scale HPP - current capacity:
    - 20 MW rated power
    - 2.67% permanent droop: 15MW/Hz
- Reduced scale model: scale ratio $\lambda = 3.7$
    - 0.405% power scale ratio: 60.75kW/Hz droop
- BESS: aim to double the droop
    - Replace 95% of the GV movements: cover $\pm$40 mHz during FCR
    - Doubled droop: $\pm$ 1.2 MW on real HPP -> $\pm$5kW on reduced scale model

The size of the BESS has been estimated based on the stochastic character of frequency deviations handled during FCR provision. As a reference, it has been considered a size such that the 95% of the frequency deviations could be managed by the BESS, allowing the hydraulic unit to operate at a constant power output. The comparison between the operation with and without BESS is performed using the peak-to-peak amplitude and the number of guide vanes movements as reference for fatigue damage and wear and tear damage. In this report, the comparison of the variable setpoint scenario is presented for the optimized BESS control. In Figure 66 we illustrate the measurements of the GVO with and without BESS operating in parallel to the hydraulic unit, as well as the reference grid frequency sequence and the active power decomposition between the hydraulic machine and the BESS, already scaled at full-scale. The absolute number of GV movements has been reduced by about 40%. Concerning pressure fluctuations and torque at the GV axis, different 5 or 7 minutes long sequences have been recorded. Two sequences of 5 minutes are employed as an example, and are recorded during the time lapse indicated by the vertical dashed line in Figure 66. In both sequences, 17 sensors out of 19 showed a decrease in the peak-to-peak signal amplitudes. The decreases during the first sequence are more consistent compared to the second sequence. This is due to the larger oscillations in the frequency signal of the first sequence, implying a larger impact of the BESS contribution in the mitigation of the damaging pressure and mechanical torque fluctuations.

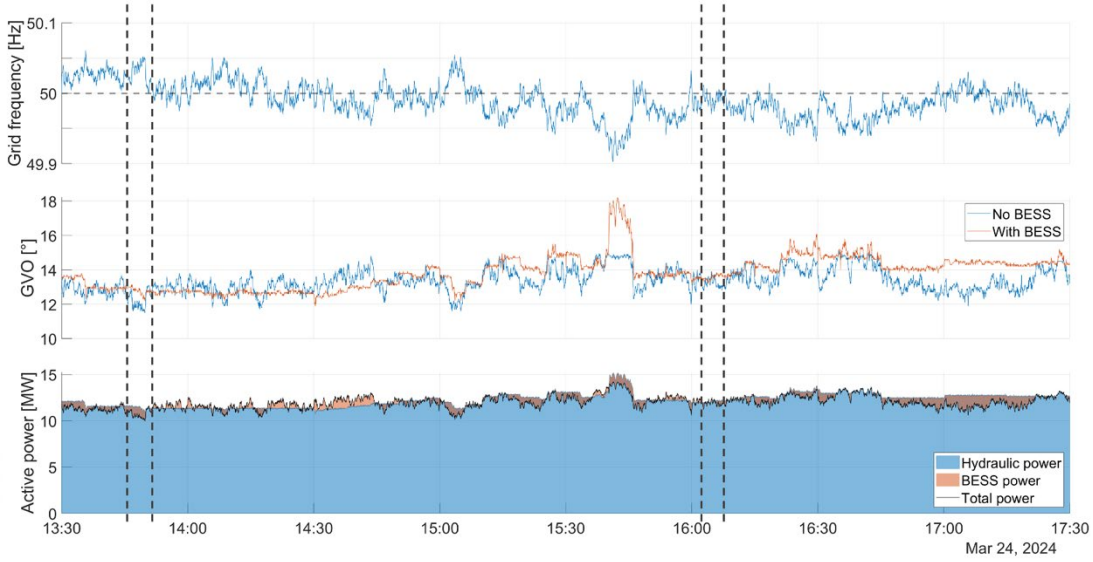

Figure 66 4-hours of variable power setpoint scenario. Power at full scale.

4.2.3 Transient behaviour and real-time monitoring of the KWE power station

Following the validation of the Simsen model, the newly selected Pelton turbine was integrated into the model, and various critical load cases were analyzed to assess the maximum pressure at the bottom of the penstock and the maximum transient overspeed. The highest pressure at the penstock occurred during the “Peak of Michaud” load case. The resulting pressure reached 117% of the rated head, remaining within the 120% design limit. The maximum overspeed was observed at 126% and respects the guarantee fixed at 170% of the nominal speed. This simulation assumed a 10-second injector closing time. Extending this closing time could provide a greater safety margin, but at the same time reduce responsiveness to ancillary services.

In 2022, the Hydro-Clone system was successfully implemented, with high-frequency pressure sensors installed on both the high- and low-pressure sides. The Hydro-Clone system supervised experimental tests, enabling real-time monitoring of transient behavior during these tests. In 2023, the Simsen model was further fine-tuned using data collected from these measurement campaigns conduct by HES-SO. The final step was to update the Francis turbine's 4-quadrant characteristic with measurements from the

EPFL-PTMH reduced-scale model test, in order to finalize the implementation of the Hydro-Clone system.
During the calibration and validation phase of the SIMSEN model for the Ernen power plant, a critical aspect emerged regarding the behavior of the Pressure Relief Valves (PRV) installed on the Francis turbines. These valves play a key role in limiting overpressure and overspeed during hydraulic transients. A combined modeling approach, integrating 1D optimization hydraulic simulations with SIMSEN and 3D CFD analysis, was applied to better understand the dynamic behavior of the PRV system. These additional studies helped explain discrepancies observed during on-site tests, particularly concerning irregular discharge behavior of the PRV.
The PRV original reference discharge characteristic curve no longer represents the actual behavior of the system. Although the 1D model was optimized to reproduce the hydraulic transients with improved accuracy, questions remained regarding the influence of the valve geometry on the discharge curve and the potential occurrence of cavitation. To address these limitations and gain deeper insight into the internal flow phenomena, a detailed CFD analysis was initiated. This approach aimed to investigate how geometric features affect the discharge behavior and to identify potential cavitation zones and their impact on the valve's performance.
Initial incompressible and steady-state simulations without a cavitation model were performed to provide initial conditions for subsequent transient computations, including cavitation effects. These preliminary simulations enabled the reconstruction of the discharge characteristic curve of the PRV by imposing a fixed head across the valve for various stroke positions. They also helped evaluate the impact of the flow-limiting section within the PRV, which contributes to the saturation observed in the discharge curve. Figure 67 shows the mesh of the PRV geometry along with the resulting velocity magnitude field from the steady-state incompressible simulation. Regions where local pressure falls below the saturation pressure (Psat = 2300 Pa) were identified, indicating potential zones of cavitation inception.

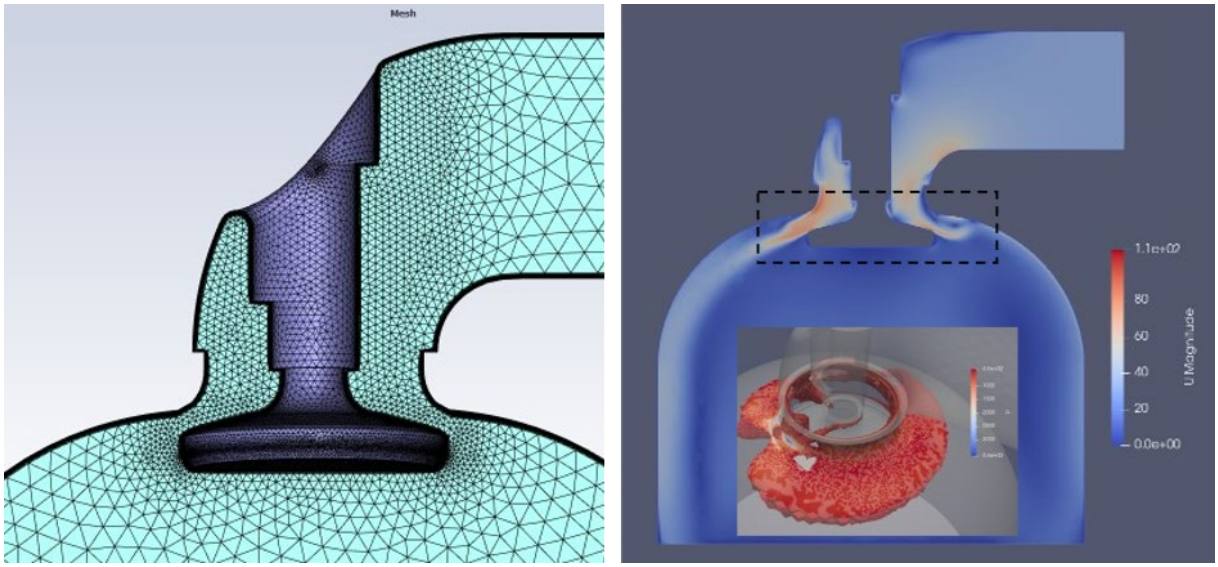

Figure 67: Representation of the mesh of the PRV geometry (left) and a steady-state incompressible simulation at the maximum valve opening showing the velocity magnitudes.

Figure 68 summarizes all the results obtained from both 1D and 3D simulations, compared against the original reference discharge curve. The steady-state incompressible CFD simulations successfully reproduced the discharge behavior predicted by the optimized 1D model. The flow rate curve was accurately captured by CFD up to approximately 80% valve opening, demonstrating strong consistency

with the 1D results and confirming the validity of the simplified modeling approach. However, as expected from a solver that does not account for cavitation effects, the flow rate drop observed near 85% opening in the reference data was not captured.
To further investigate this phenomenon, compressible two-phase flow simulations were performed to model vapor formation during cavitation events. These advanced CFD calculations revealed a premature drop in the dimensionless flow rate (Q11), beginning around a normalized valve stroke of 0.6, instead of 0.8 as expected. This earlier onset is likely due to cavitation inception occurring sooner than predicted by simplified models. The results indicate a high sensitivity to the cavitation number setup, and potential improvements could include a calibration of the cavitation model parameters to better match the experimental data. However, these results clearly illustrate the hypothesized presence of cavitation in the PRV system.

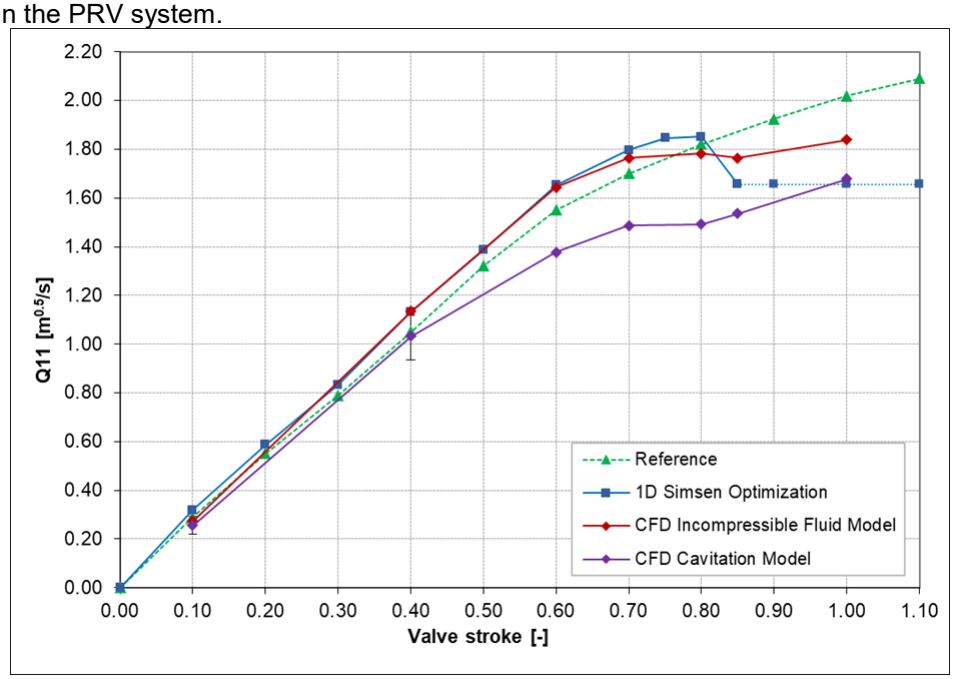

Figure 68: Results of the simulations compared to the reference data.

In conclusion, CFD analysis provided valuable insights into the complex hydraulic behavior of the PRV under transient conditions. It confirmed the presence of cavitation as a limiting factor for flow rate at large openings and demonstrated the importance of combining 1D and 3D approaches to capture both global trends and local flow phenomena.

4.2.4 Battery sizing, electrical layout design and simulations

The battery sizing and integration was accomplished through a co-simulation framework which was established to enable interaction between SIMSEN and EPFL's Python-based control model for hydropower and BESS. The SIMSEN model of the plant was expanded by modelling and calibrating the turbine governor for the Ernen units based on Swissgrid primary control data. A simplified version of the control model was also implemented to operate the co-simulation for battery sizing purpose. The co-simulation framework allowed for simulating the behaviour of the Ernen HPP during scenarios of primary frequency provision by considering different sizes of BESS.

Control for BESS-hybrid system

The control framework implemented to perform the co-simulations is based on a Double-Layer Model Predictive Control (DLMPC) architecture, developed by Gerini et al. (Gerini et al., 2024) specifically

designed for BESS hybridized HPPs providing frequency containment reserve (FCR). It comprises two hierarchically organized MPC layers: an upper layer that handles long-term energy management and a lower layer responsible for real-time power allocation and tracking. The upper layer MPC (ULMPC) operates on an hourly timescale and manages the State of Charge (SOC) of the BESS. It leverages a forecast of the hourly regulating energy demand to compute a constant power offset. This offset modifies the dispatch plan of the HPP and ensures the BESS SOC remains within its operational limits. To ensure realistic operation, the SOC is constrained to remain within the 10–90% range. Its initial condition is set a 50%. The lower layer MPC (LLMPC) runs in real time with a one-second control interval and a 30-second prediction horizon. It allocates the instantaneous FCR power setpoint between the HPP and BESS by solving a constrained optimization problem. The cost function minimizes a weighted combination of the FCR tracking error and the variation in hydropower setpoints, the latter being a proxy for servomechanism wear. The turbine control, that determines the Guide Vanes Opening (GVO) at each simulation step, includes a ramp rate limiter to model the turbine's physical ramping constraint, set to 100% of nominal power in 60 seconds.

Simulated scenarios and results

The 4-hours scenario implemented in the co-simulation corresponds to the "Variable power setpoint" scenario for wich reduced scale model tests were performed. This corresponds to the real grid data extracted from the Ernen HPP SCADA in March 24th, 2024, covering the period between 13:30 and 17:30. An overview of the power setpoint as well as the grid frequency during the 4 hours is provided in Figure 69 and Figure 70.

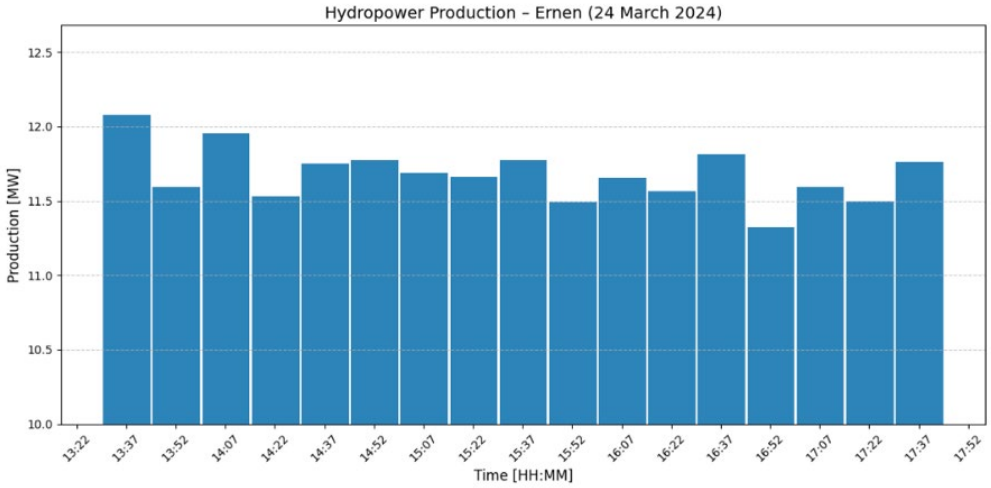

Figure 69 Production of the Ernen HPP on the 24th March 2024 between 13.30 and 17.30.

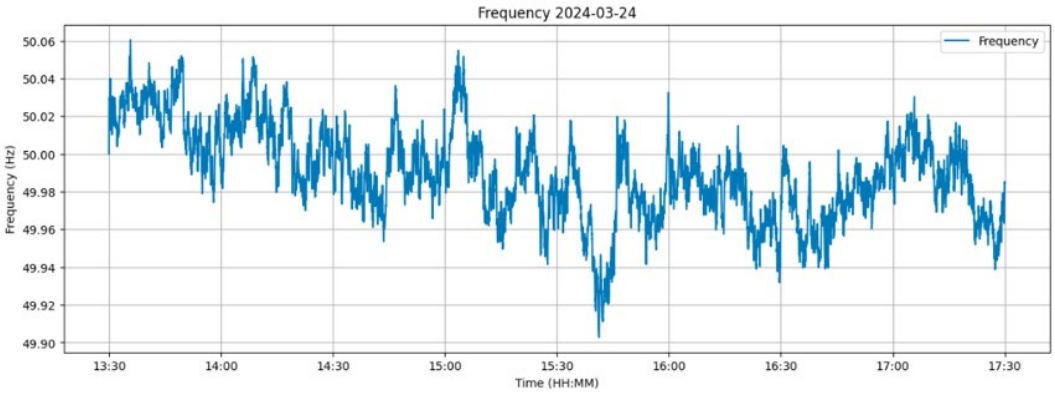

Figure 70 Grid frequency measured on the 24th March 2024 between 13.30 and 17.30

The considered BESS sizes are the following:

- 10% of the HPP active power: 1.645 MW (and 1.645 MWh)
- Size to cover up to 40 mHz of frequency deviation with a 30MW/Hz droop: 1.2 MW (and 1.2 MWh)
- 2 MW and 2 MWh

The considered droop values are the following:

- Current droop (2.67 %): 15 MW/Hz
- Doubled droop: 30 MW/Hz

No BESS – current droop

The co-simulation is initially carried out without implementing the MPC optimization, using instead fixed hydropower setpoints calculated to match the power demand while providing FCR. This approach serves as a baseline for comparison, representing the current operational configuration of the power plant without a BESS.

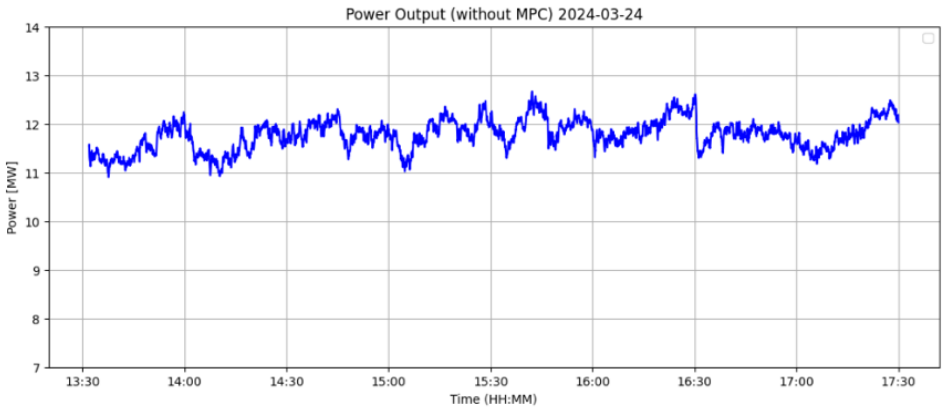

Figure 71 Power output without BESS and with droop of 15MW/Hz.

Figure 72 GVO without BESS and with droop of 15MW/Hz.

The simulation results, presented in Figure 71 and Figure 72, reveal frequent fluctuations in both power output and Guide Vanes Opening (GVO), underscoring the mechanical strain imposed on the turbine regulation system.

1.645 MW BESS – doubled droop

The first simulated BESS scenario considers a BESS with a power rating of 1.645 MW, corresponding to 10% of the plant's nominal capacity, and an energy capacity of 1.645 MWh. This setup allows the battery to be fully charged or discharged within one hour. The resulting profiles for power output, BESS SOC, and GVOs are presented in Figure 73, Figure 74 and Figure 75.

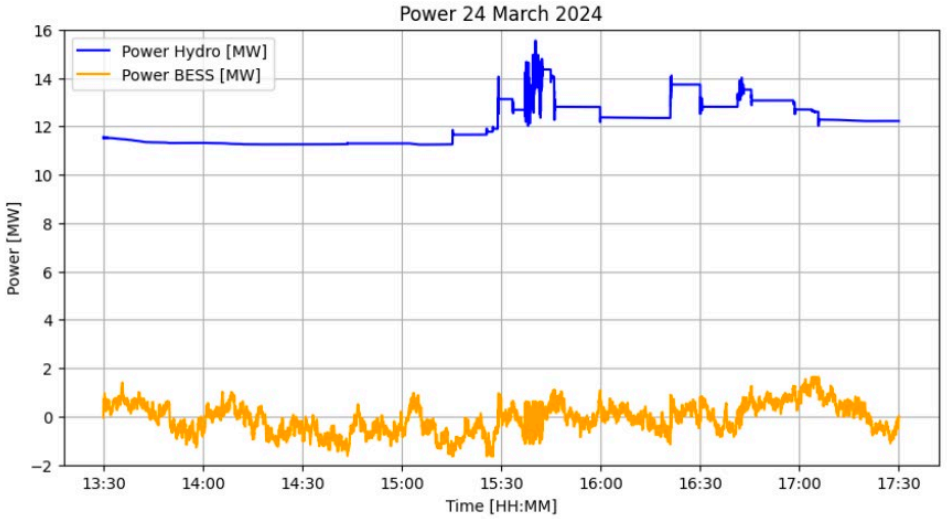

Figure 73 Power delivered by the turbine and exchanged by the BESS, with 30MW/Hz droop and 1.645 MW BESS.

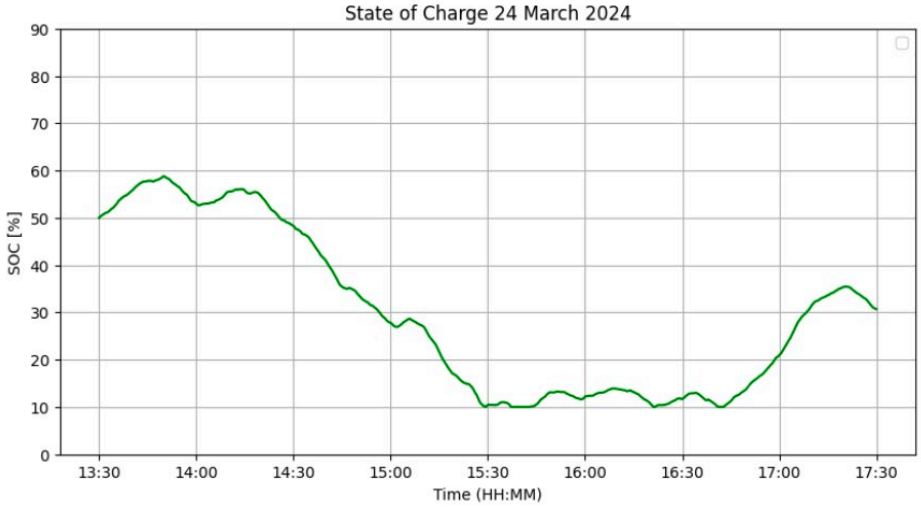

Figure 74 SOC of the 1.645 MW BESS, 30MW/Hz droop. Note the 10% SOC lower bound.

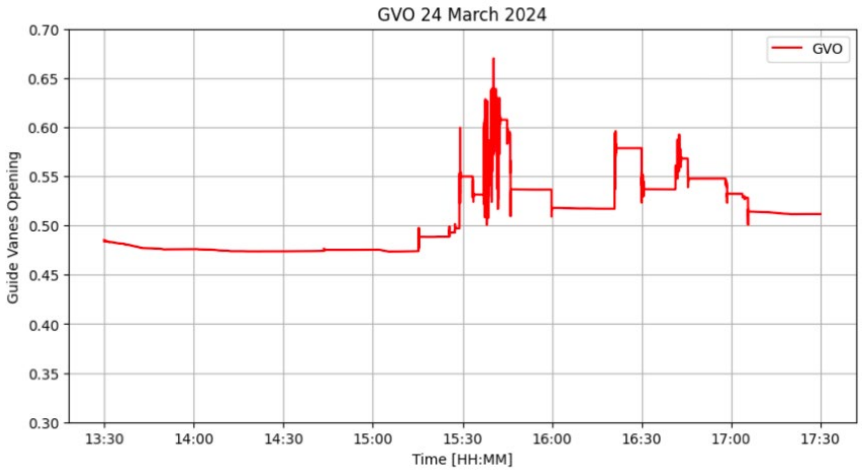

Figure 75 GVOs of the 1.645 MW BESS, 30MW/Hz droop.

As shown, the guide vanes remain mostly static for almost the half of the simulation period, while the BESS alternates between charging and discharging. The turbine's guide vanes activate when the BESS alone cannot meet the demand. The BESS is discharged until it reaches the minimum SOC allowed of 10%.

1.2 MW BESS – doubled droop

From the results shown in Figure 76, Figure 77 and Figure 78, it is evident that reducing the battery size leads to more frequent variations in turbine power output compared to the 1.645 MW BESS simulated previously. It is important to note how, with such tested grid scenario, the BESS reduces its contribution, remaining for at the lowest admissible SOC (10%) for about one hour. During this time frame, the turbine provides an important fraction of the regulation power required by the frequency deviations, leading to a significant amount of GVO movements between 16:00 and 17:00. However, the fluctuations remain globally significantly lower compared to the case without BESS.

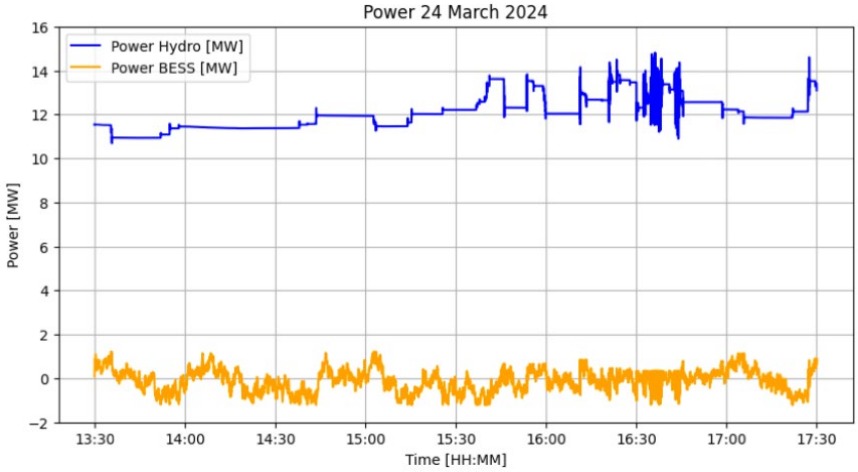

Figure 76 Power delivered by the turbine and exchanged by the BESS, with 30MW/Hz droop and 1.2 MW BESS.

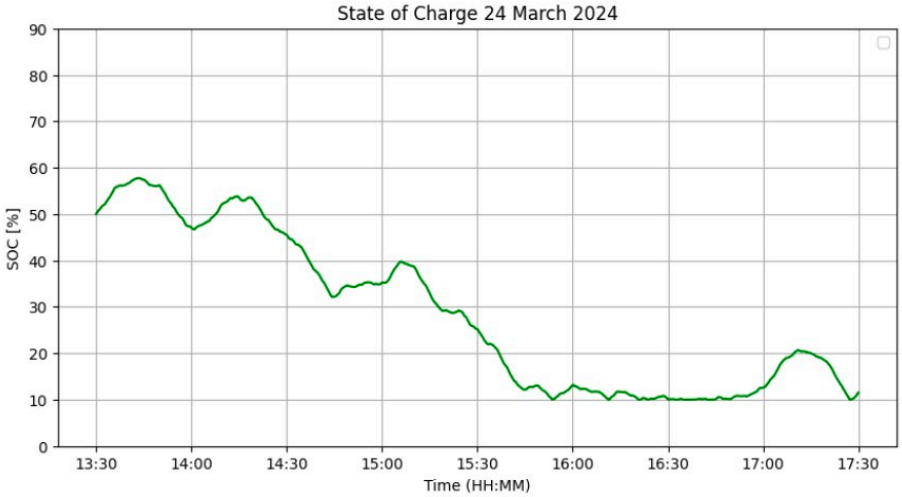

Figure 77 SOC of the 1.2 MW BESS, 30MW/Hz droop. Note the 10% SOC lower bound.

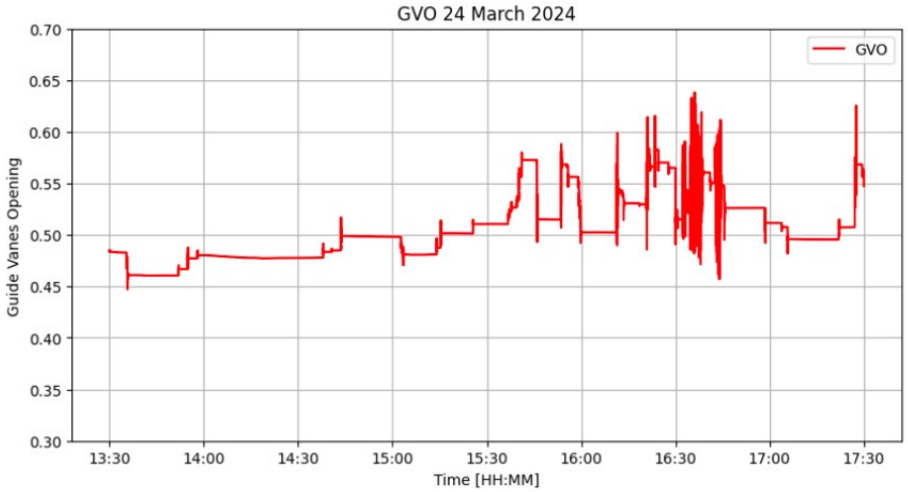

Figure 78 GVOs of the 1.2 MW BESS, 30MW/Hz droop.

2 MW BESS – doubled droop

Increasing the battery size results in smaller variations in turbine power output for both droop settings and significantly reduces the need for guide vane movement, as show in Figure 79, Figure 80 and Figure 81.

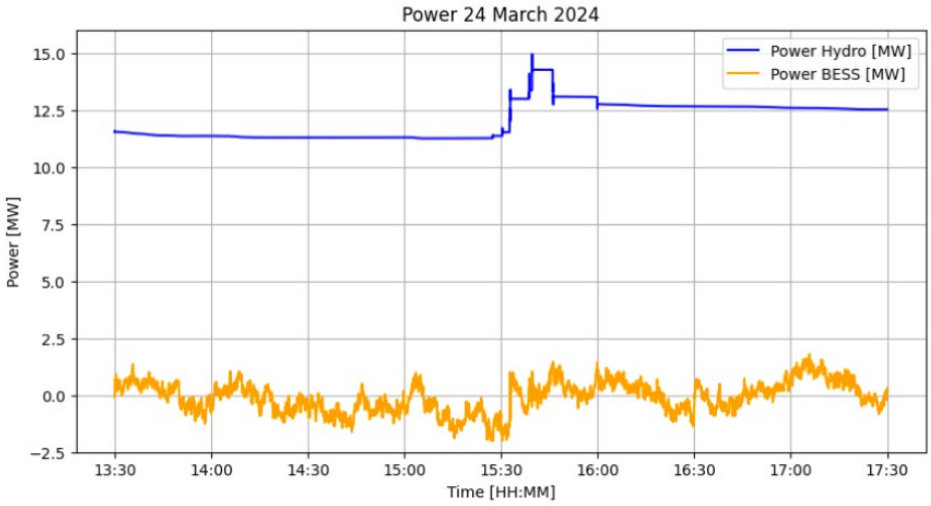

Figure 79 Power delivered by the turbine and exchanged by the BESS, with 30MW/Hz droop and 2 MW BESS.

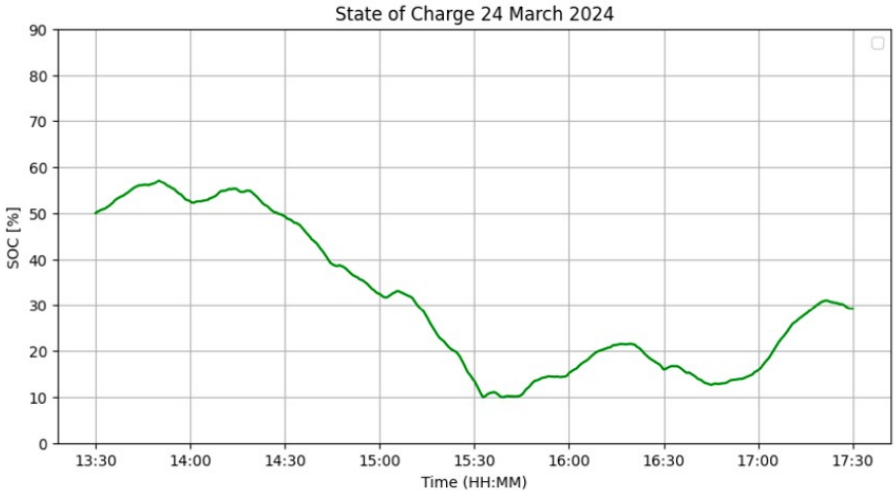

Figure 80 SOC of the 2 MW BESS, 30MW/Hz droop. Note the 10% SOC lower bound.

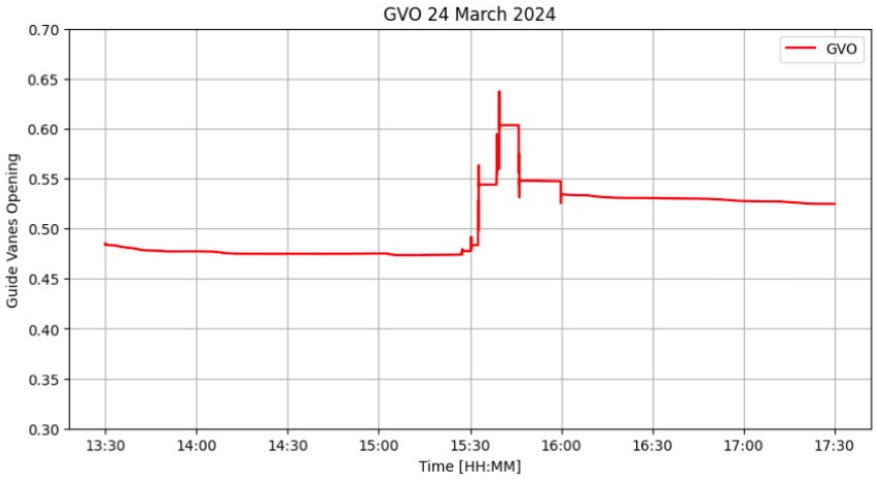

Figure 81 GVOs of the 2 MW BESS, 30MW/Hz droop.

In all scenarios, the SOC follows a similar trend: it decreases until approximately the midpoint of the simulation, which coincides with a change in turbine output power across all cases. This shift occurs due to the battery reaching its limit and no longer being able to supply additional power. After this point, the MPC provides with a power offset that allows the BESS to recharge, following distinct patterns depending on the specific simulation.

To assess the benefits of installing a BESS, the different scenarios have been compared using two indicators: the number of sign changes in the GVO and the normalized stroke of the servomotor. These metrics serve as proxies for mechanical wear and tear of the servomotor system, providing insight into how effectively the BESS reduces mechanical stress and extends component lifespan. The sign change count measures how often the direction of the GVO movement reverses over the course of the simulation, reflecting the frequency of servomotor actuation. The normalized stroke, computed as shown in the following equation, is defined as the cumulative sum of the absolute changes in the GVO angle, normalized over its full operating range, where 0 corresponds to fully closed and 1 to fully open. This value quantifies the total movement of the guide vanes providing a measure of the mechanical workload imposed on the servomotor.

$$Norm.stroke = \sum_{i=1s}^{14400} |GVO_i - GVO_{i-1}|$$

However, in these simulations, excessive amplitudes of power and GVO oscillations were observed following setpoint changes on SIMSEN. These transient oscillations, probably due to the responsiveness of the model, are also captured in the normalized stroke, which results in abnormally high values, particularly when the droop is doubled. Therefore, while both indicators are useful, the number of sign changes is a more reliable and meaningful metric for comparing different operating conditions in this context.

BESS size	Droop	Sign changes	Normalized stroke
No BESS	15MW/Hz	6979	7.668
No BESS	30MW/Hz	6207	15.680
1.645 MW	15MW/Hz	76	0.317
1.645 MW	30MW/Hz	624	8.100
1.2 MW	15MW/Hz	117	0.704
1.2 MW	30MW/Hz	1100	18.159
2 MW	15MW/Hz	39	0.303
12 MW	30MW/Hz	143	0.837

Table 4 Number of sign changes of the GVO and mileage for the different scenarios.

As shown in Table 4, the scenario without a BESS exhibits the highest number of sign changes in the GVO, indicating more frequent actuator movements. When introducing the BESS, a higher droop value increases GVO activity. However, increasing the BESS size significantly reduces the sign changes. As expected, the fewest movements occur with the largest battery size. This improvement is especially evident in the 30MW/Hz droop case, where sign changes are reduced by up to 98% compared to the scenario without a BESS. Even the smallest battery size provides substantial relief under high demand conditions, achieving an 84% reduction in GVO sign changes with the doubled droop. For the 15MW/Hz droop case, the number of sign changes remains relatively low across all scenarios, with reductions ranging from 98% to 99.4%. When analyzing the normalized stroke, it can be observed that, despite the presence of previously mentioned oscillations, maintaining a lower droop value consistently results in a normalized stroke that is an order of magnitude smaller than in the case without a BESS, even when using the smallest battery. For comparison, an additional simulation was carried out with a doubled droop value and no BESS, in order to benchmark against the cases where a BESS was included. As expected, the normalized stroke in this no-BESS scenario is higher than in the hybrid cases, except for the simulation with the smallest BESS. This exception is likely due to the oscillations in the response from SIMSEN, which inflate the normalized stroke value.
Overall, all scenarios demonstrate the advantages of integrating a BESS in parallel to the turbine, particularly in reducing wear on the servomotors. These trends match the experimental observations, where reduced-scale physical tests confirmed that adding a BESS substantially lowers GV activity. This cross-validation between simulation and experiment supports the reliability of the co-simulation framework and the proposed control strategy.

4.2.5 On-site testing of existing KWE Francis turbines for real-time condition monitoring

A hybrid approach that combines experimental data analysis and machine learning (ML) has been developed to evaluate the flexible operation of the KW Ernen hydropower and enhance its monitoring and diagnostics. Two on-site experimental campaigns have been designed based on a statistical analysis of the plant's production data over a seven-year period. The first campaign was conducted in May 2022 under high inflow conditions, allowing a full "free-run" mode without any pre-defined operating schedule, see Figure 82. These included both steady-state and dynamic regimes, such as fixed power operation, start-ups and shutdowns (emergency, fast, and normal), and ancillary service operations involving variations in discharge, power output, downstream water level, and the operating configuration of the plant's two identical Francis turbines, see Figure 83.

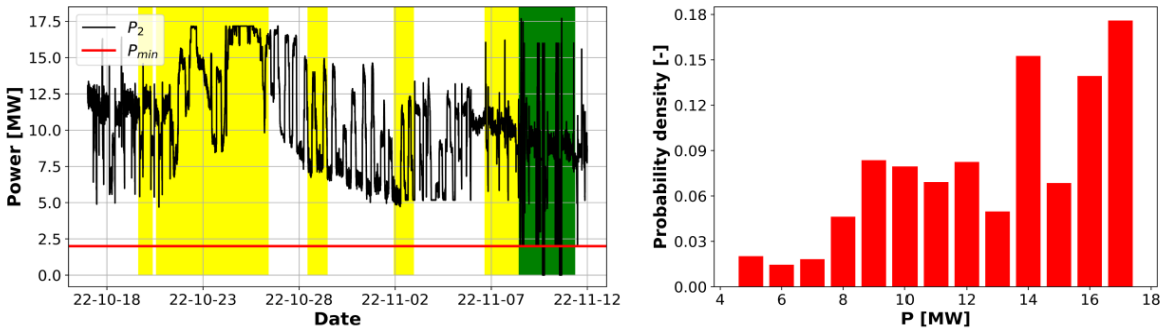

Figure 82: Left) $P2$ variations during the October-November test period with the yellow bands depicting the free-run tests, Right) Normalized histogram of $P2$ for all the free-run tests carried out in May, October, and November 2022. *Source: Amini A. et al. (2025)*

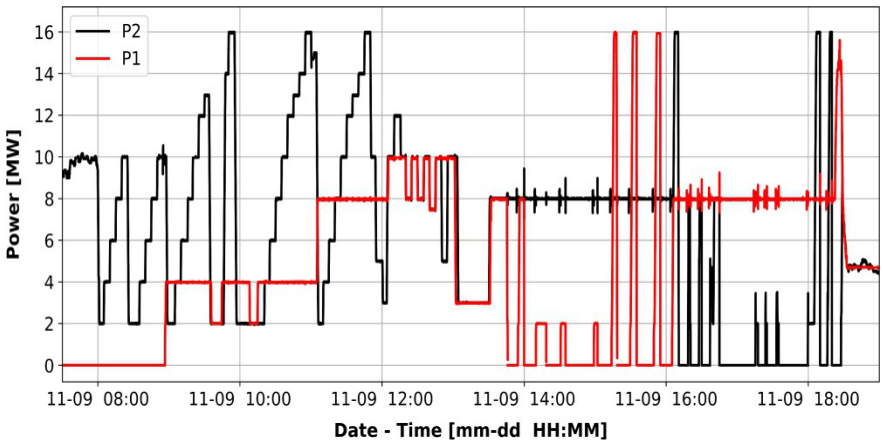

Figure 83: Variations of $P1$ and $P2$ during the second day of the programmed tests in November. *Source: Amini A. et al. (2025)*

In both campaigns, the experimental setup was identical. On one side, standard SCADA signals from the power plant's monitoring system were collected from 47 sensors at an increased frequency of 10 Hz (compared to the usual 1 Hz). On the other side, high-frequency data were acquired from 31 additional sensors connected to two National Instruments CompactDAQ chassis. These signals were sampled at three different rates, depending on the type of physical quantity measured. Process variables—such as turbine discharge and guide vane opening angle—along with selected pre-installed vibration sensors, were recorded at 2 kHz. Other vibration signals and dynamic pressure sensors were sampled at 12.8 kHz, while microphones used forairborne noise measurements were connected to a high-frequency acquisition card operating at 51.2 kHz. A detailed description of the instrumentation setup is provided in Amini et al. (2025).

To evaluate the impact of flexible operations relative to best efficiency conditions, a Vibration Content Index (VCI) was developed based on frequency-domain analysis of various vibration sensors. Although the introduced index cannot be directly related to fatigue, VCI can be considered as a relevant indicator in this regard because higher levels of vibrations are associated with higher stress amplitudes, which in turn increase the risk of fatigue in the component. Figure 84 presents the VCI values across the operating range from 2 MW to 17 MW. The analysis reveals that while the BEP is typically considered the calmest, the lowest vibration levels for this turbine actually occur at 16 MW. In contrast, 10 MW shows the highest vibration levels due to intense part-load cavitation, and a small increase to 17 MW leads to a sharp rise in vibrations caused by self-sustaining vortex rope oscillations. This finding highlights a critical operational threshold between 16 and 17 MW, beyond which further power increase is not advisable.

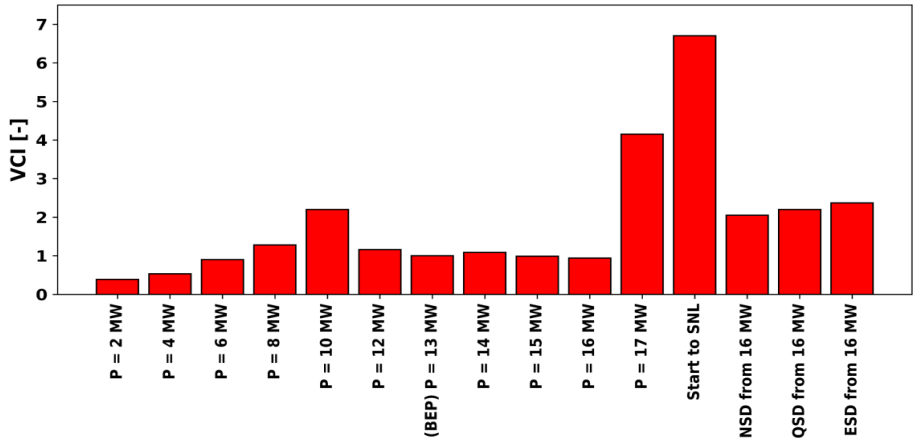

Figure 84: Vibration Content Index (VCI) of various stationary operating points and transient sequences. (SNL: Speed No Load – NSD: Normal Shut Down – QSD: Quick Shut Down – ESD: Emergency Shut Down).

Another key outcome is the development of a method based on dimensionality reduction, enabling a clear overview of the complex dataset—comprising 25,000 samples from 31 sensors, amounting to 7 TB of data collected during the second campaign. Figure 85 illustrates the results obtained using two- and three-dimensional reduction techniques. In these visualizations, data points are color-coded according to turbine power (e.g., P = 13 MW includes all points with P ∈ [12.5, 13.5)). The spatial distance between points in the reduced space reflects their similarity: the closer two points are, the more similar their underlying signals; the farther apart they are, the more different they are. These representations are powerful tools for gaining a global understanding of the machine's behavior across various operating conditions, as they highlight similarities and differences between operating points. For example, the results in Figure 85 indicate that increasing the power from 14 MW to 15 MW leads to only minor changes in machine behavior. In contrast, an equivalent increase from 16 MW to 17 MW results in significant behavioral shifts. This observation aligns well with the findings previously presented in Figure 84. Additionally, this approach can support anomaly detection or wear diagnostics—for instance, if a data point at a given power level falls outside the expected cluster, or if a progressive drift of the cluster is observed over time. Finally, this study also allows to develop the concept of virtual sensor using machine learning model trained to predict high-frequency responses from low-frequency SCADA data, more details can be found in the paper from Amini A. et al. (2025).

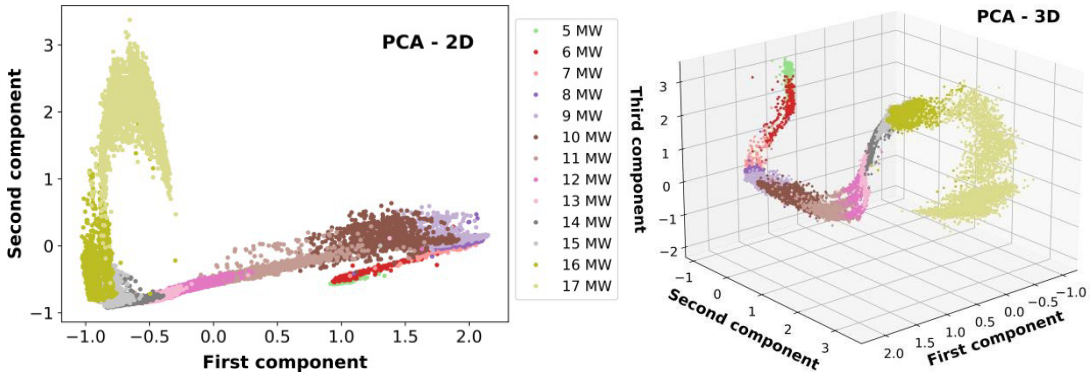

Figure 85: Representation of the turbine vibration response in reduced dimensions creating distinct regions.

4.2.6 Estimation of flexibility associated costs and risks

Following the results of the aforementioned on-site measurement campaign, a CFD investigation of four critical operating points have been performed to understand the cavitation development leading to erosion which is limiting the extension of the operating range of the machine and raising the operational

costs. The four operating points are selected in such a way that they correspond to the deep part load, the part load, the BEP and the full load operating conditions.
For each operating point, an unsteady simulation is performed over 26 runner revolutions while statistics are computed over the last 10 runner revolutions. The time step is set to 1.2° of revolution and second order numerical schemes are used.
The first set of simulations is computed by neglecting cavitation and surface roughness due to erosion (see Figure 86). Then a second set of simulations is performed including cavitation by setting the outlet pressure value in such a way that the pressure measured in the draft tube was in accordance with the measurements (see Figure 87). Finally, a third set of simulations is carried out by considering cavitation and a uniform surface roughness of 0.1 mm on all the solid walls since pictures of the turbine walls clearly show eroded walls.

Figure 86: Pictures of an eroded runner at KW Ernen.

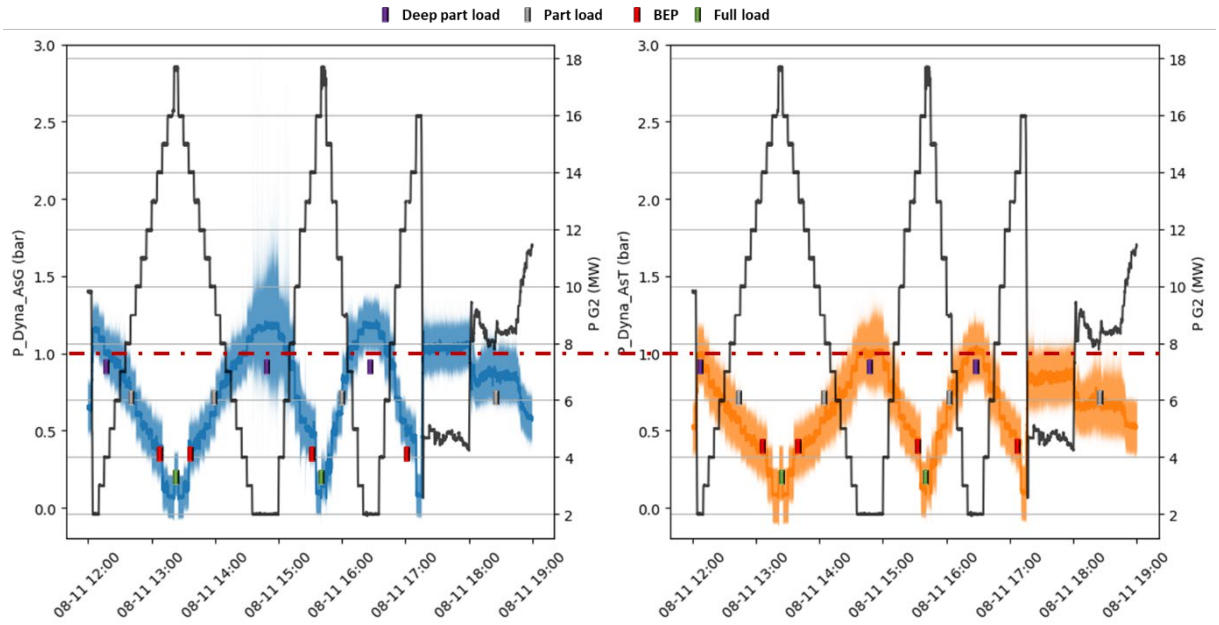

Figure 87: Left graph: blue line is the pressure (left axis) in the draft tube between the generator and the runner, and the black line is the power of the second group (right axis). Right graph: blue line is the pressure (left axis) in the second draft tube and the black line is the power of the second group (right axis), idem as on the left graph. Coloured rectangles refers to the simulated pressure for the four operating points investigated. The dash-dot red line is plotted to put in evidence the pressure imbalance between the two draft tubes observed in the measured data.

The efficiency curve as a function of the mechanical power is shown in Figure 88. Two sets of measurements are available, one with a fixed downstream water level in the tail race channel and one with a variable water level. The latter corresponds to the normal operating condition of the power plant and is associated with a drop in efficiency at deep part load. It is noticeable that by neglecting the roughness, the efficiency is overestimated by the simulation compared to the measurements. Whereas, by considering a wall roughness of 0.1 mm, the efficiency predicted by the simulations matches the measurements with a variable downstream water level.
Regarding the relation between the mechanical power and the discharge (see Figure 89), it can be concluded that the occurrence of cavitation is responsible for lowering the discharge mainly at full load operation.

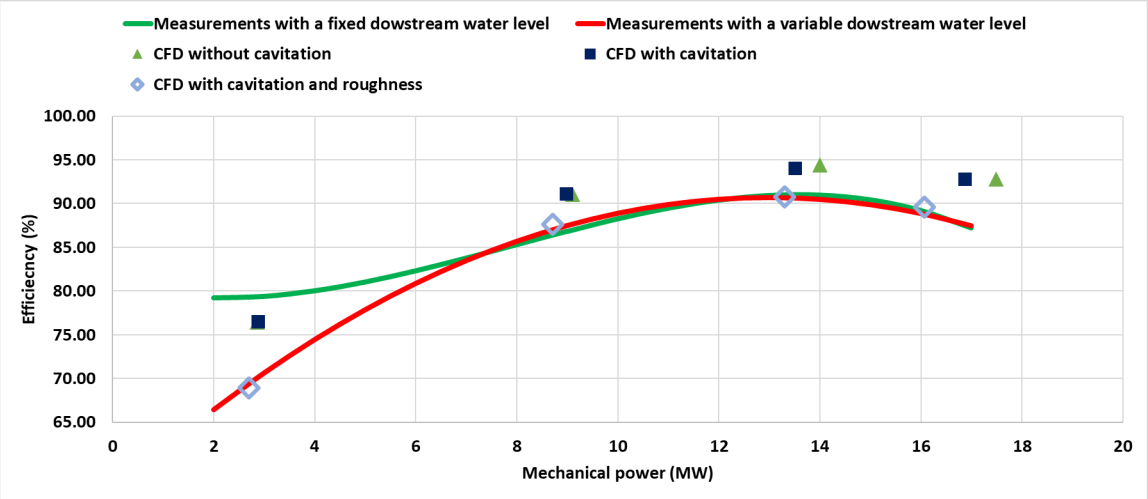

Figure 88: Efficiency as a function of the mechanical power. Comparison between the measures and the CFD.

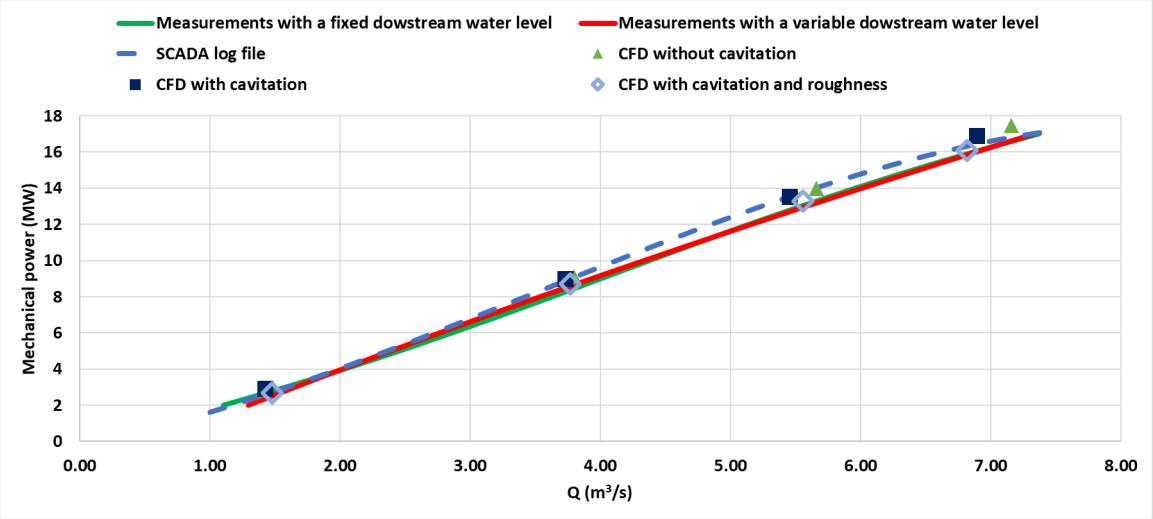

Figure 89: Mechanical power as a function of the discharge. Comparison between the measures and the CFD.

The iso-surface of the cavitation regions shown in Figure 90 for the simulations performed by neglecting the roughness and the air injection clearly put in evidence the presence of cavitation at the runner outlet for all operating conditions. This feature is responsible for a blockage effect that limits the maximum discharge, mainly at full load operation. It is also responsible for the cavitation erosion observed on the runner walls as shown in Figure 86. At part load, the characteristic helicoidal vortex rope is also captured by the simulation and is partially full of vapor.

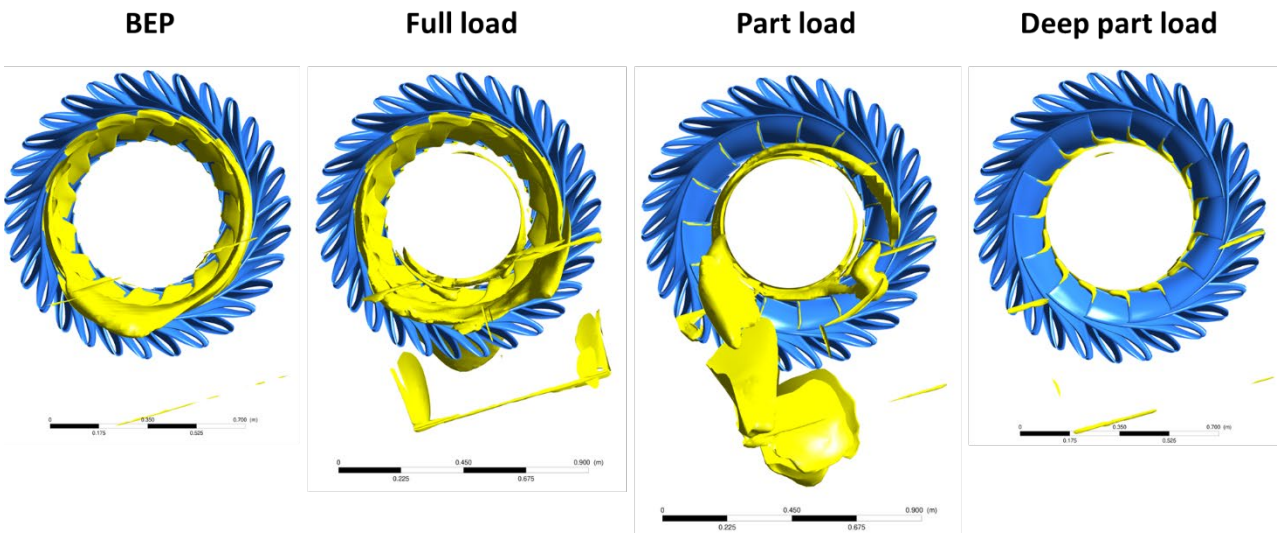

Figure 90: Iso-surface of the liquid volume fraction for a value of 0.9. Cavitation simulations without roughness. Side-view from the draft tube.

It is noticeable that a simulation of the best efficiency point neglecting the surface roughness but including the air injection at the runner outlet and in the draft tube is not able to remove cavitation at the runner outlet (see Figure 91). Nevertheless, this result should be taken with caution since there are no models to accurately capture the air/cavitation interaction.

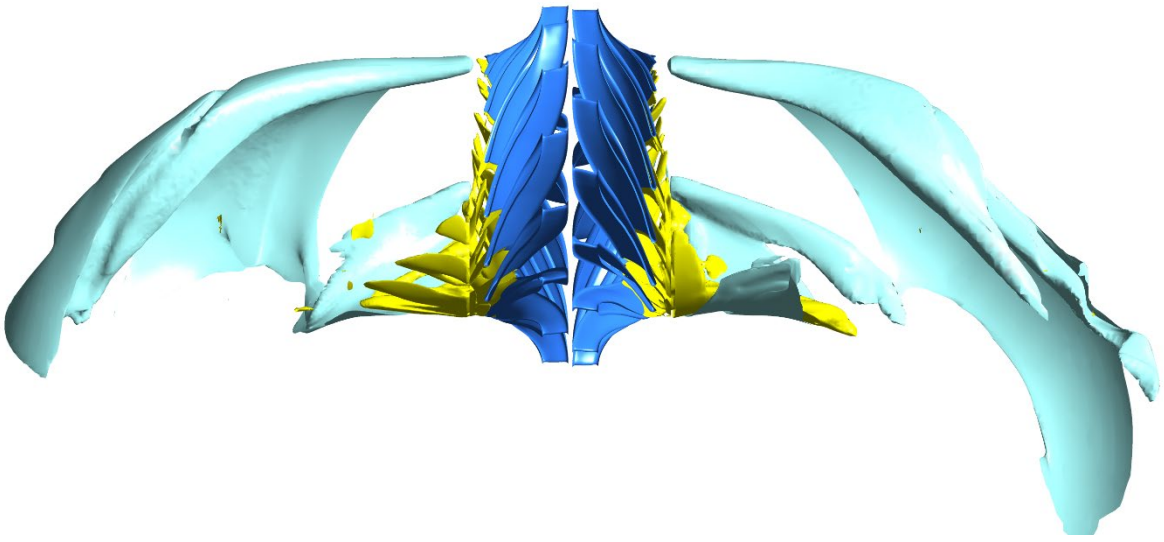

Figure 91: Time-average iso-surface of the air volume fraction (light blue) and the vapour volume fraction (yellow) for a volume fraction of 0.5. Best efficiency point computed by neglecting the surface roughness.

The standard deviation of ten parameters have been considered for comparison with the vibration index. The parameters are the two runner torques, the head at the outlet of the draft tubes, the hydraulic power, the mechanical power, the axial force on the runner, the total pressure and the static pressure in both draft tubes. Figure 92 displayed the dimensionless values of the standard deviation for each parameter and each simulated operating point. The reference value use for making the parameter dimensionless is the maximum standard value for this parameter among the four operating points simulated. For 7 parameters among the 10, the standard deviation at the part load operating condition is at least twice

the value for the other operating conditions. This is particularly true for the axial force on the runner and the pressure in the draft tube. This observation is in line with the vibration index derived from the measurements. The reason for such high standard deviations could be the cavitating helicoidal vortex observed for this operating point. Regarding the outlet head and the hydraulic and mechanical powers, the full load operating condition shows the largest standard deviation, which are assumed due to the large amount of cavitation at the runner outlet. Once again, this feature is in accordance with the large value of the vibration index derived from the measurements (Decaix et al. 2025b).

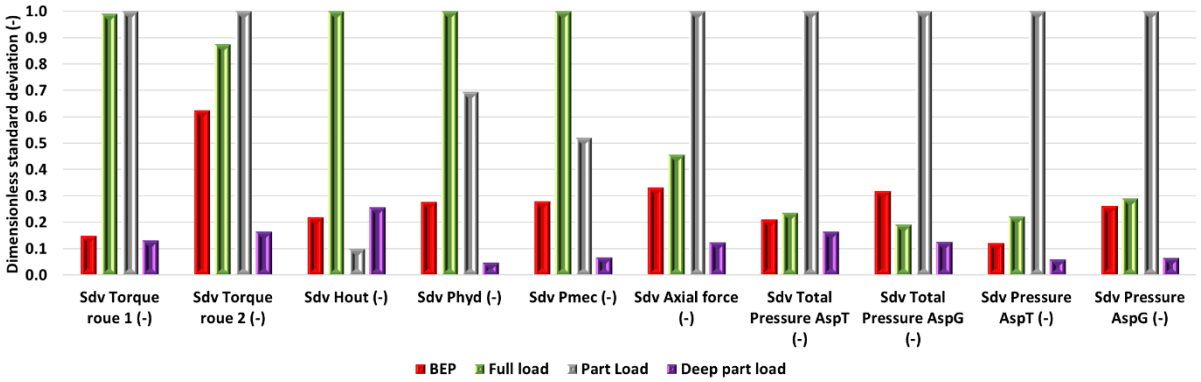

Figure 92: Dimensionless standard deviation for various variables. For each variable, the reference value is the maximum value among the four operating points.

In parallel to the flow simulations, experimental and numerical modal analyses have been carried out. The experimental modal analysis has been performed by Hydro Exploitation on a suspended runner. Figure 93 compares the frequency of the fourteen first modes between the simulation based on a FEM and the EMA. Qualitatively all the modes agree. However, some frequencies are overestimated by the FEM. This mismatch is explained by the absence of the calibration of the material properties, which is not necessary because, based on the on-site measurement, no excitation of a runner frequency is expected.

Figure 94 shows the deformation corresponding to the first mode as computed by the FEM and as extracted from the EMA. It is a flexion mode with two nodal diameters in both cases.

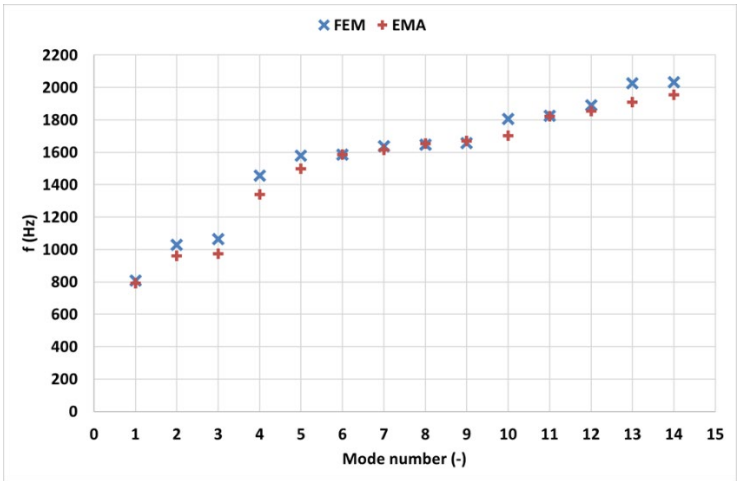

Figure 93: Comparison of the frequency of the fourteen first modes between the FEM and EMA.

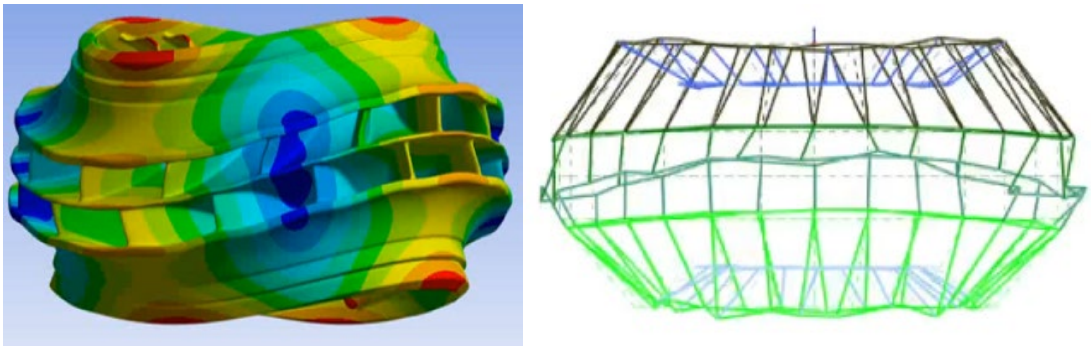

Figure 94: Illustration of the deformation corresponding to the first mode of the runner. Left: FEM analysis; right: EMA.

The numerical investigation strengthens the conclusions drawn from the on-site measurements. Furthermore, the simulations provide explanations on the harmful operating conditions for the turbine:

- Cavitation at the outlet of the runner and along the trailing edge of the runner blades are observed for all the operating conditions. Despite the air injection, cavitation is responsible of the erosion at the blades trailing edges and at the runner walls.
- The erosion due to cavitation is responsible of a change in geometry. In the simulation, a wall roughness 0.1 mm of the walls leads to a loss in efficiency compared to a non-eroded runner in agreement with the measurements.
- At part load, cavitation occurs also in the vortex rope, which is responsible for large pressure fluctuations in the draft tube and for fluctuations of the axial force on the runner. The latter seems in agreement with the observations performed by the operators.
- At full load, the volume of vapour at the runner outlet is the largest, which is responsible for a blockage effect limiting the maximum discharge through the turbine. Moreover, it causes large power fluctuations, which agrees with the vibrations observed experimentally.

Therefore, the part load and full load operating points should be limited to increase the lifetime of the turbine. To improve the operating conditions, the influence of the air injection should be considered more in detail since air injection does not seem to attenuate the effect of cavitation and on the contrary seems to amplify the unsteady behaviour of the flow.

4.2.7 Cascade power plant operation optimization for hydropeaking mitigation

KW Ernen is connected to the upper Rhône cascade of hydropower plants. The outlet discharge from KW Ernen combines with the Fiesch and Alte Binna tributaries before flowing into KW Mörel. The resulting outlet discharge flows into the Rhône, where it feeds into other hydropower plants downstream. Hydropeaking simulations of a typical year for KW Ernen as well as KW Mörel where performed by using a Matlab code. These simulations were based on hydraulic performance tables generated from the SIMSEN model, input discharge measurements and electricity price data series. The objective of the code is to optimize the engagement of the units in order to maximize the revenue, according to the RenovHydro approach (SFOE Grant SI/501436-01).
First, the hydropeaking simulation was carried out for KW Ernen, with and without the new Pelton unit. The electricity spot price for 2019 and the mean inflow over the period 2014-2017 were used as inputs into the simulation – see Figure 95.

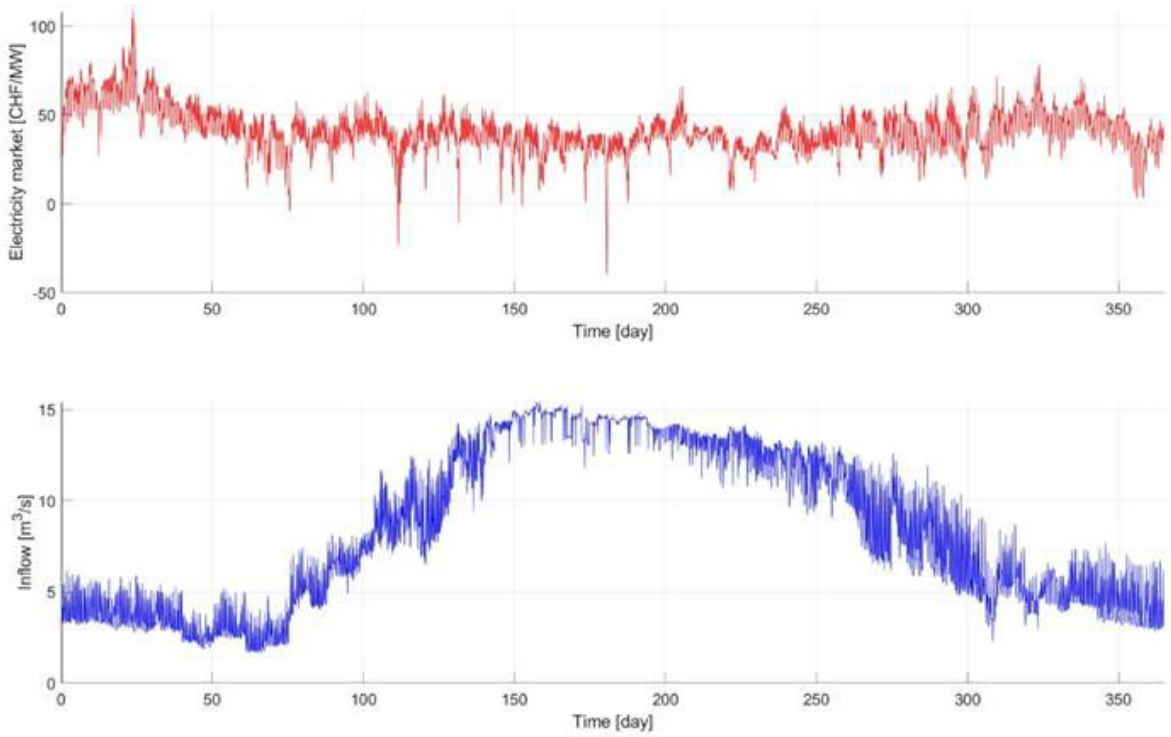

Figure 95: Electricity market (spot price 2019) and inflow into KW Ernen (mean value over the period 2014-2017).

Without the Pelton, the calculation returns an annual energy of 169.3 GWh and an annual revenue of 6.87 MCHF. The addition of the Pelton turbine leads to an increase of the annual energy produced by the plant of 1.1%, and an increase of the annual revenue of 1.9%, while the total turbined volume stays the same, as summarized in Figure 96.

KW Ernen	2 Francis	2 Francis + 1 Pelton
Annual energy [GWh]	169.3	171.2 (1.1%)
Annual revenue [MCHF]	6.87	7.01 (1.9%)
Average unit revenue [CHF/MWh]	40.6	40.9 (0.8%)
Turbined volume [Mm^3]	264.0	264.0

Figure 96: Main results of the hydropeaking simulation for KW Ernen.

Figure 97 illustrates the resulting engagement of the units with and without the Pelton turbine. Without the Pelton turbine, the Francis turbines operate principally at either 100% or 0% of the power set point. When the Pelton turbine is added, the two Francis turbines operate less at 100% of the power set point, and prioritize operating at 90%. The Pelton turbine, on the other hand, operates most of the time at 100% of the power.

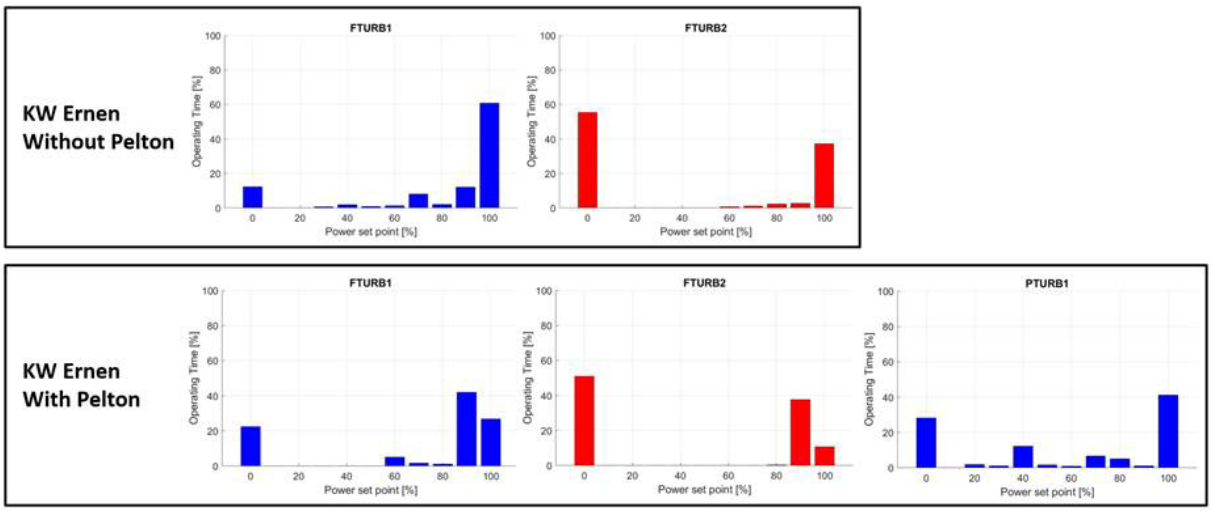

Figure 97: Units engagement for KW Ernen.

Secondly, the hydropeaking simulation was carried out for KW Mörel. The inlet discharge into Mörel consists of a combination of flows from KW Ernen, Fiesch and Alte Binna. Calculations were carried out with three different sources for this inlet discharge:

- The three discharges are given by measurements.
- Discharges from Fiesch and Alte Binna are given by measurements, while the discharge from KW Ernen comes from the hydropeaking calculation, without the Pelton turbine.
- Discharges from Fiesch and Alte Binna are given by measurements, while the discharge from KW Ernen comes from the hydropeaking calculation, including the Pelton turbine.

For the two cases where the operation of KW Ernen was optimized, the total volume turbined by KW Mörel is 0.8% larger than the total turbined volume obtained when measurements of the inlet discharges are imposed. When the discharge from KW Ernen results from the optimization without the Pelton turbine, KW Mörel produces 289.2 GWh annually and makes 12.28 MCHF of revenue. That is 0.15% more energy and 1.3% more revenue than with the non-optimized flow from KW Ernen. When the flow from KW Ernen takes into account the Pelton turbine, the annual energy of KW Mörel decreases by 0.2% and the revenue increases by 0.21% compared to the calculation without the Pelton turbine. For this case, the revenue increases, even though the energy decreases. The optimization of the unit engagement with respect to the market price is notable, as illustrated in Figure 98.

KW Mörel	Qout Ernen from measurements	Qout Ernen from Matlab, without Pelton	Qout Ernen from Matlab, with Pelton
Annual energy [GWh]	288.8	289.2 (0.15%)	288.7 (-0.06%)
Annual revenue [MCHF]	12.12	12.28 (1.3%)	12.31 (1.6%)
Average unit revenue [CHF/MWh]	42.0	42.5 (1.2%)	42.6 (1.6%)
Turbined volume [Mm^3]	447.8	451.4	451.4

Figure 98: Main results of the hydropeaking simulation for KW Mörel.

The graphs below show the outlet discharge over a year, averaged per day, for KW Ernen and KW Mörel. The grey curve in the graph on the left corresponds to the measurement of discharge exiting Ernen. The blue and orange curves are the result of the optimizations, with and without the Pelton turbine. The variation of the outlet discharge reflects the more reactive behaviour of the powerplants in

order to optimize the revenue. The optimized discharges variate with an amplitude of approximately 5 m^3/s around the current discharge. For both KW Ernen and KW Mörel, the addition of the Pelton turbine leads to more variation of the discharge during the beginning of summer. This variation, which represents approximately 30% and 20% of the maximum discharge for Ernen and Mörel respectively, should not significantly impact the environment. In the case of Mörel, a 5 m^3/s variation would probably not be too impactful since the outlet discharge flows into the Rhône river. These results are available as inputs for a specialized environmental impact study.

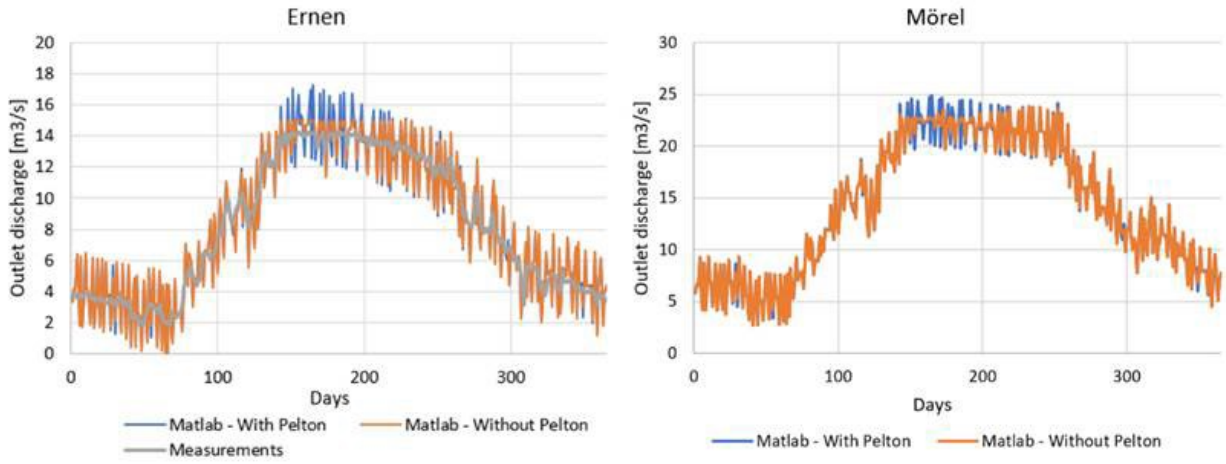

Figure 99: Daily outlet discharges for KW Ernen and KW Mörel.

4.3 Increasing the sustainability of new low-head hydropower plants – The MBR demonstrator

4.3.1 Downstream fish protection

Run-of-river hydropower plants (HPP) pose an obstacle to the longitudinal connectivity of rivers and thus impede the movement of fluvial organisms such as fish and increase mortality through delay and physical damage inflicted during the passage of turbines and other structures (Larinier & Travade, 2002; Silva et al., 2018). One approach of mitigating the detrimental effects of HPP on downstream movement is the installation of a fish guidance rack (FGR) with a bypass system (BS). The FGR-BS consists of a bar rack positioned at an angle in plain view of the approach flow guiding the fish towards the subsequent bypass. For the MBR demonstrator, both a horizontal bar rack and a vertical curved-bar rack are being considered for fish protection and guidance. The main focus is on the Curved-Bar Rack – Bypass System (CBR-BS) newly developed at VAW (Beck, 2020, Beck et al., 2020a, b and c, Beck et al., 2021).

Modelling Concept

The core tool used for the analysis is a 3D CFD model of the headrace channel and powerhouse based on the geometry of the planned HPP layout. This model is further referred to as *powerplant model* (“Kraftwerksmodell”). For the evaluation of possible FGR positions, normal and tangential velocities in the plane of potential FGR positions are extracted and assessed. For the analysis of the effect of the FGR on the flow conditions and the turbine admission flow, a distinction is made between horizontal and vertical-curved bar racks. For the horizontal bar rack, it is assumed that the effect of the rack on the flow condition is negligible (Meister, 2020; Meister et al., 2020, 2021a, b). This does not hold for the CBR as the flow is deflected by the curved bars. An additional representation of the CBR is included in the model to capture these effects.

In addition to the powerplant model, two supportive CFD models are used to ensure the efficiency and quality of the simulations. The first, called *approach flow model*, simulates the inflow conditions upstream of the powerplant model considering the right-hand and left-hand bends. Thus, a flow profile at the inlet of the powerplant model can be extracted and used as an upstream boundary condition.

The last model, called *detail model*, is a small-scale model for the analysis of the CBR. Here, a section of the CBR is modelled in detail. This allows an in-depth assessment of the effects of the bars on the flow conditions upstream and downstream of the rack and also a comparison of different configurations, e.g. of different bar shapes or rack angles. Based on these simulation results, an inner boundary condition called *bar rack baffle (BRB)* can be calibrated. The BRB is then used within the powerplant model to introduce the effect of the bar rack on the flow conditions without the need to represent the individual bars. This nested approach has been used in similar projects and ensures the efficiency of the simulations. For all models, the open source software OpenFOAM® was used (www.openfoam.com).

The general layout of a FGR-BS is shown in Figure 100. It functions on the principle of guiding the fish along the rack out of the main channel and towards the bypass. The FGR acts either as a physical barrier (Horizontal Bar Rack and/or for large fish) or as a mechanical behavioral barrier (Vertical Bar Rack) by creating flow patterns that trigger an avoidance reaction from the fish.

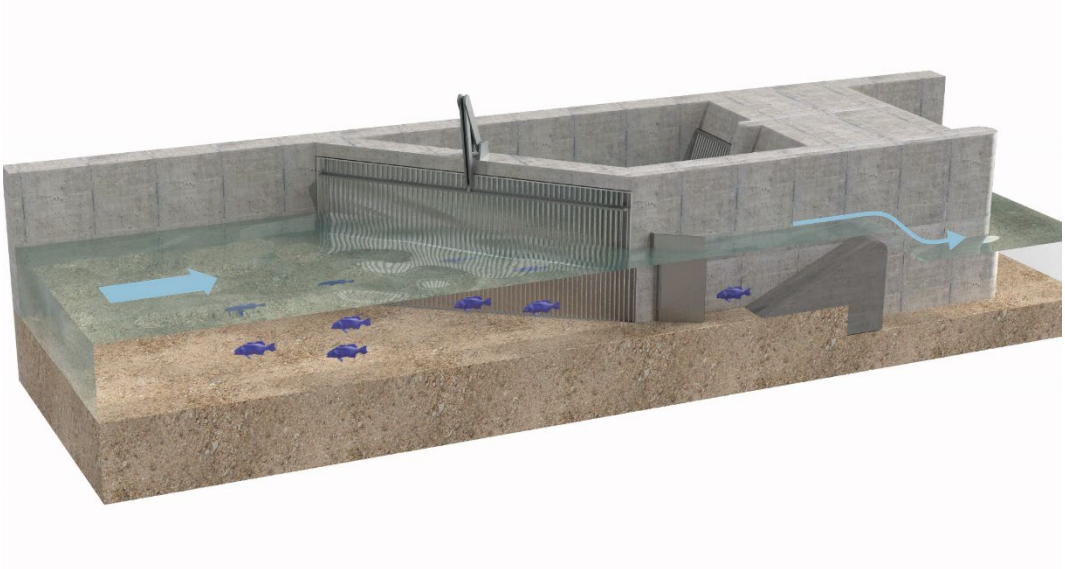

Figure 100 General layout of a fish guidance rack and subsequent bypass system (© VAW of ETH Zurich)

Approach Flow Model

The approach flow model was set up using a constant discharge corresponding to the load case at the inlet and a fixed water level at the outlet. The water surface elevation was set at the headwater level of the MBR powerplant. The flow profile of the approach flow model which was subsequently used as inlet for the powerplant model, shows a flow concentration towards the left-hand bank due to the upstream right-hand bend as shown in Figure 101.

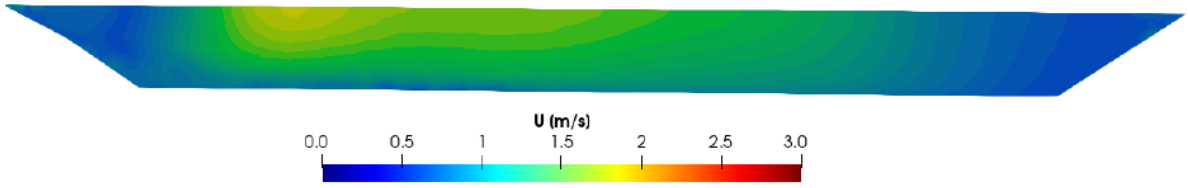

Figure 101 Flow distribution at outlet approach flow model / inlet powerplant model at design discharge of Qd = 220 m³/s

For the powerplant model, a rigid lid approach was chosen. With this, the model ends at a fixed water surface and only the water phase is modelled and computational time is improved. This was possible since the powerplant model was located within the backwater area of the powerplant. The model mesh comprises the thusly defined water body. A top view of the mesh is shown in Figure 102. The mesh resolution was chosen with respect to optimizing computational effort while still representing all the important flow features accurately enough. In Figure 102, the different mesh zones and their resolutions are specified. The base resolution of the main channel is 1.5 m in *x*- and *y*-direction and 1 m in *z*-direction. The mesh is refined by a factor of 0.5 at the channel bed and within the headrace channel. At the structures of interest, i.e. the bed load diversion sill, the bar rack and the bypass, the mesh is refined further.

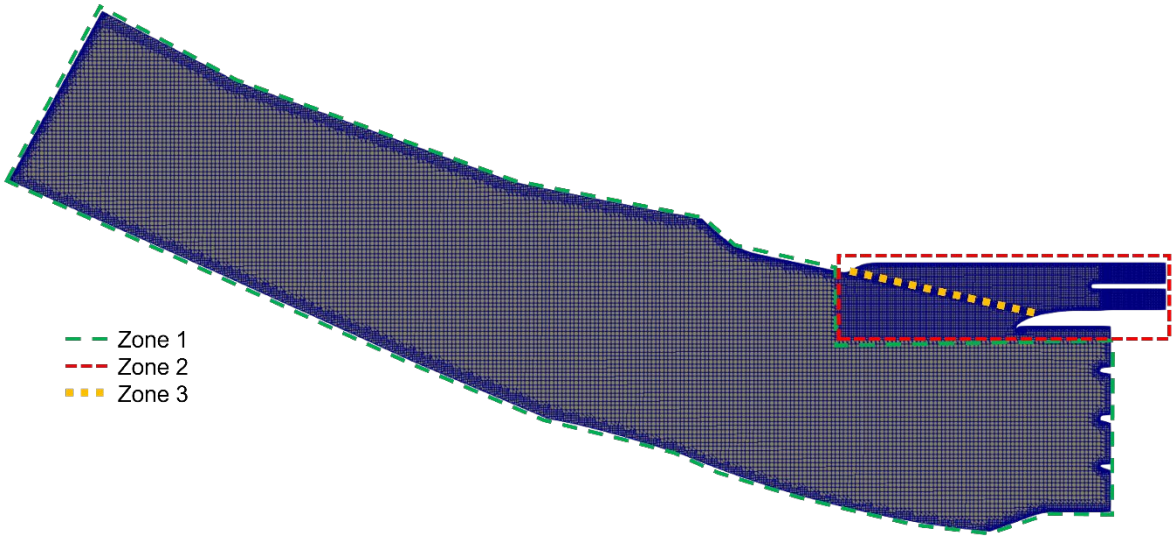

Figure 102 Overview mesh and mesh resolution

At the model inlet, a constant discharge corresponding to the respective load case is set. The flow distribution over the cross-section is mapped from the approach flow model and is exemplarily shown in Figure 101 for the design discharge Q_d = 220 m³/s. The flow distribution is similar for all load cases, albeit with different velocities. At the outlet, a constant relative pressure is applied with the outflow matching the inflow. For simulations with weir discharge, a constant discharge was defined at the weir outlet. The roughness was set in correspondence to that used for the numerical model of the MBR powerplant by Sahraei et.al (2021). The roughness used was 0.443 m for the bed of the Rhone and 0.003 m for the concrete elements. The *RNG* (Re-Normalized Group) *k-ε* turbulence model was used for the powerplant model and approach flow model simulations and the *k-ω* turbulence model for the detail model.

To find the optimal position for the fish guidance rack in terms of fish guidance efficiency but also considering technical feasibility and monetary aspects, several possible rack positions were evaluated. In a first step, a base geometry with none of the additional structures such as the bed load diversion sill, the bypass or the bar rack itself was used in order to separate the effects of the different elements on the flow conditions.

The ratio of normal and tangential velocity components was extracted and evaluated at the different rack positions. The two best performing rack positions were then analysed in more detail and by adding the necessary structures both with and without the *bar rack baffle*. The flow field without the bar rack baffle corresponds to a horizontal bar rack, the flow field with bar rack baffle to the one with a vertical bar rack.

Due to the upstream right-hand bend of the Rhone, the flow approaching the MBR demonstrator is concentrated on the left half of the river bed. Without the HPP, the main flow would shift to the right side in the proximate left-hand bend. However, due to the positioning of the powerhouse on the left-hand side, the current is pulled back to the left again while in front of the weir a large right turning vortex is formed (Figure 103). The magnitude of flow entering the headrace channel is closer to the dividing pier.

In Figure 103, the evaluated rack positions are indicated in a top view figure of the velocity field upstream of the powerplant for the design discharge (Table 3). Position *R01* (θ = -12°) corresponds to the initially proposed rack position. For positions *R02* and *R03*, the rack angle θ is decrease to -30° and -45° respectively. The increased angle results in shorter racks, reducing both the cost for the rack and the effort for the cleaning of the rack. These three positions impose that the bypass is located within the dividing pier.

In contrast, for positions *R04*, *R07* to *R09* the bypass entrance is located in the left wall of the headrace channel. Thus, for these positions the orientation of the rack is reversed. In position *R04* the rack angle θ is 45° for the layout with original pier (variant V-0). For the other positions *R07* to *R09* the original pier is too short for positioning of longer racks and thus the dividing pier has to be elongated (variant V-LT, Figure 103 on the right). The rack angles θ are 30° for *R07*, 35° for *R08* and 45° for *R09*.

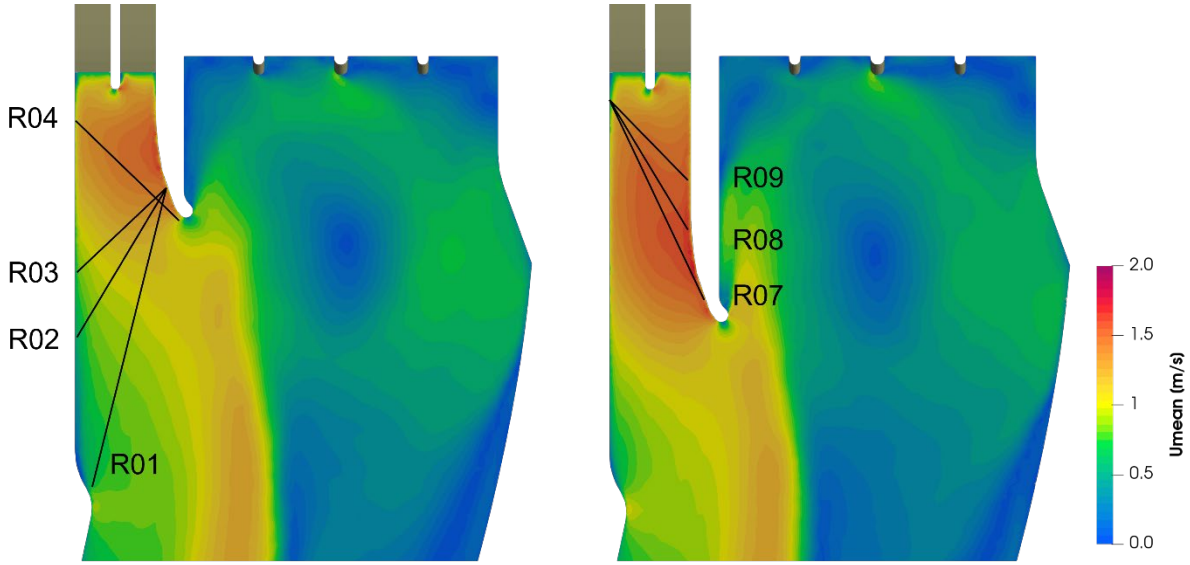

Figure 103: Rack positions for the original design V-0 (left) and design with elongated pier V-LT (right) without bed load diversion sill.

To illustrate the effect of the rack angle and the rack orientation on the flow field in front of the bar rack, the velocity ratio v_t/v_n in front of the rack is shown for the initial four rack positions in Figure 104. in Figure 104a, the development with increasing rack angle is shown: for *R01*, the ratio is above 1 for the most part of the rack area with only a comparatively small area at the bottom of the rack on the right-hand

side with high normal velocities. This area increases considerably with the increase of the rack angle, resulting in majority of area with a ratio below 1 for *R03*.When comparing *R03* and *R04* (Figure 104b), the picture is almost reversed for racks with an angle of 45° but opposite orientations and *R04* shows the more favorable velocity field.

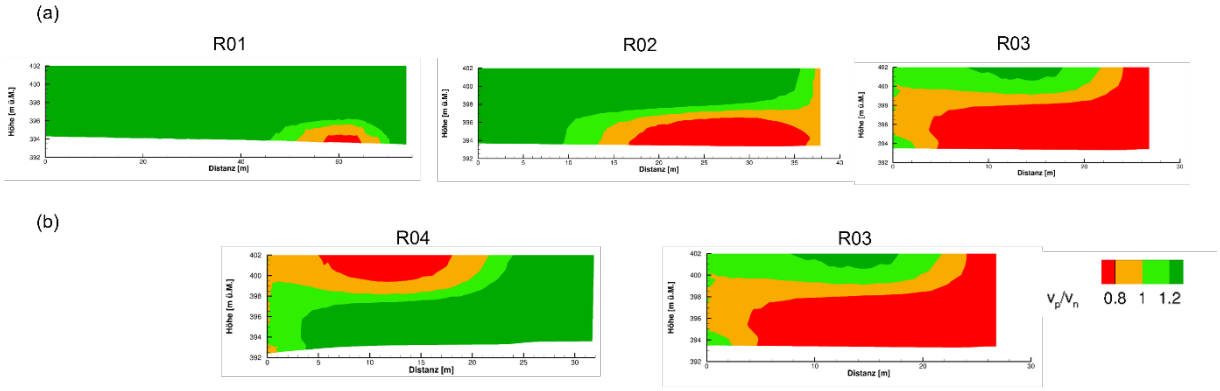

Figure 104: (a) Velocity ratio for R01 to R03 representing a negative increase of the rack angle and (b) velocity ratio for R03 and R04 representing the same rack angle (45°) with opposite orientation, both for variant V-0.

The results of this initial investigation into the optimal rack position can be summarized into two trends: Firstly, flow conditions in terms of fish guidance improve with decreasing rack angle. This corresponds with previous findings of Kriewitz (2015) and Beck (2020). Secondly, flow conditions for racks starting at the dividing pier and ending at a bypass on the left-hand side are more favorable than those for racks starting at the left bank and ending at a bypass located in the dividing pier for the same rack angle. This is true only for the specific flow conditions at the MBR demonstrator. The reason for this is the specific direction of the approach flow to the headrace channel. The best performing rack positions for each rack orientation, *R01* and *R07*, were subsequently analyzed in more depth.The geometries of the variants V-0 and V-LT including positions *R01* and *R07* of the FGR are shown in Figure 105. *R01* corresponds to the originally proposed layout of the powerplant. *R07* has a longer dividing pier to provide sufficient space for the FGR inside the headrace channel. The bed load diversion sill is positioned across the headrace channel inlet to guide the bed load towards the weir. The resulting FGR is shorter but higher than the one of *R01*. The greater rack angle of *R07* leads to about half rack length compared to *R01*. However, the vertical extend is almost doubled because the rack is not positioned on top of the bed load diversion sill. Both effects mostly cancel each other out in terms of total rack area. These comparative measures of the two variants are summarized in Table 5.

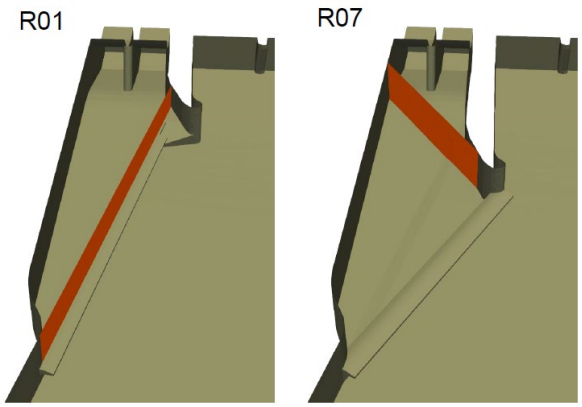

Figure 105 Geometry and position for positions R01 and R07

Table 5 Comparison of rack dimensions for R01 and R07

	R01	R07
Rack area*	ca. 380 m^2	ca. 350 m^2
Rack length	76.8 m	40.9 m
Mean rack height*	5 m	8.6 m
Length of bed load diversion sill / (top overlay)	76.8 m	48.8 m
Depth bypass*	5 m	9 m

** all measures consider only the immerged section of the bar rack with the water surface level at 402 m a.s.l.*

In Figure 106, the flow field in front of the FGR position is depicted for both *R01* and *R07*. In the top figure, the normal velocities are shown in contour and the tangential velocities with vectors. For *R01* the flow field is strongly concentrated at the end of the FGR near the bypass entrance at the bottom of the rack. In the last quarter of the rack, there are high normal velocities of up to 1.5 m/s. These high normal velocities negatively affect the fish guidance efficiency, which is also illustrated by the velocity ratio in the bottom figure. There, a large area at the bottom and towards the right exists with normal velocities greater (v_n) than tangential velocities (v_p). Both the velocity ratio (v_p/v_n) and the high velocities are adverse factors for fish guidance and protection. Furthermore, the area of negative effect is both close to the bypass and to the bottom of the rack, where most fish are likely to pass. In case of the *R07*, the flow and subsequently the velocity is more evenly distributed over the rack area. In the wake of the bed load diversion sill, a horizontal, counter-clockwise vortex develops. After detaching from the sill, it follows along the right-hand side of the headrace channel. It causes the disturbance in flow visible on the right side of the figure of *R07* and the velocity concentration at the bottom. The highest normal velocities at the FGR are around 1.2 m/s. The area with an unfavorable velocity ratio is much smaller than for *R01*. It is located on the far side from the bypass and therefore likely to affect a smaller percentage of fish and to not disturb the critical area of the bypass entrance.

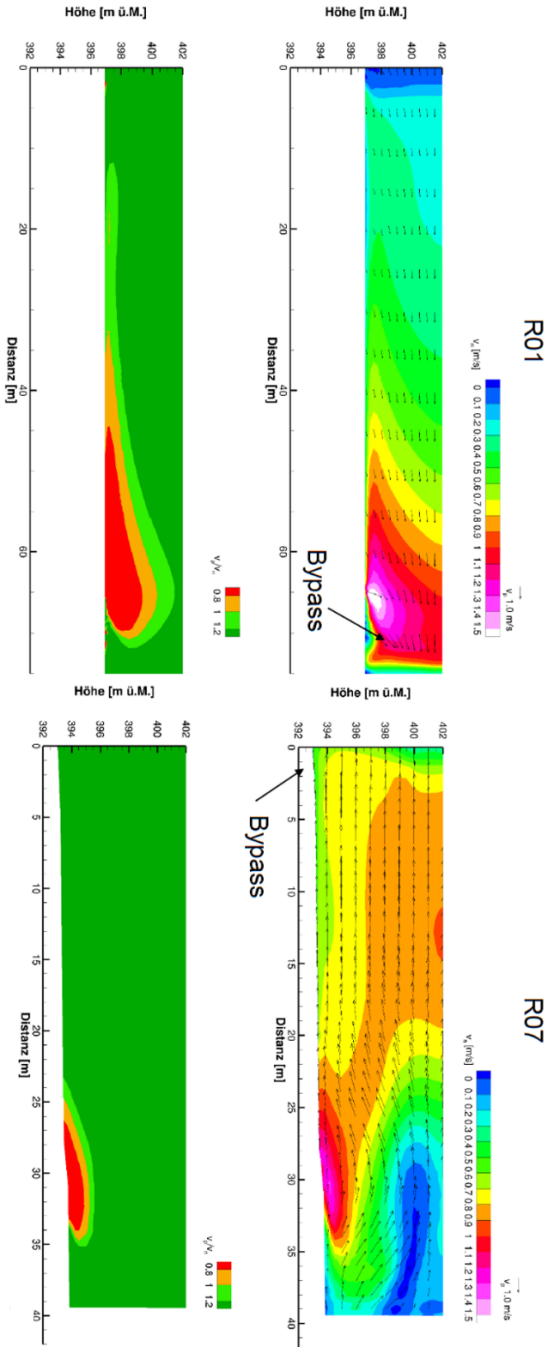

Figure 106 Flow field in front of the FGR position for R01 and R07; top: normal velocities (contours) and tangential velocities (vectors); bottom: velocity ratio v_p/v_n.

Detail Model

The detail model is a horizontal 2D model of an open channel flume with resolved bars. It corresponds to the set-up of a physical laboratory model where head loss and velocity measurements were conducted for various configurations of the modified bar rack and the curved bar rack at VAW (Kriewitz, 2015; Beck, 2020). This numerical model set-up has successfully been used in previous analyses and could be validated with measurements from the physical model of the modified bar rack and the curved bar rack. It is used to calibrate the *Bar Rack Baffle* necessary for the implementation of

the flow deflection caused by the CBR in the powerplant model. The channel is 10 m long for the 30°-rack (standard case) and 12.5 m for the 12°-rack. The increase in length in the latter case was chosen to have a comparable distance downstream of the rack end for the analysis of the downstream flow conditions. The rack is positioned with its upstream end at 4.5 m downstream of the inlet. The approach flow velocity U_o was 0.5 m/s. For an accurate representation of the bars, the mesh resolution was set to 0.25 cm in both x and y direction and refined to 0.125 cm around the bars. The rack parameters are defined in Table 6.

Table 6 Overview Rack Parameters

Parameter			Magnitude
Rack angle	α	[°]	12 / 30
u/s bar angle	β	[°]	45
d/s bar angle	δ	[°]	27
Bar spacing	b	[mm]	50
Bar thickness	s	[mm]	12
Bar depth	l	[mm]	80

The hydraulic losses (Δh) in the numerical model are obtained through the pressure loss (Δp) over the length of the domain after reaching quasi-stationary conditions. The head losses for the different bar shapes are shown in Figure 107. For the MBR and CBR also results from the empirical formula and physical model study in the laboratory are included for reference. This was used to validate the numerical approach as a means to analyse the different bar shapes and rack configurations. The figure illustrates how the CBR and m-CBR drastically reduce head loss compared to the MBR configuration. The head loss coefficient for the m-CBR, which is used here, is about 1.1.

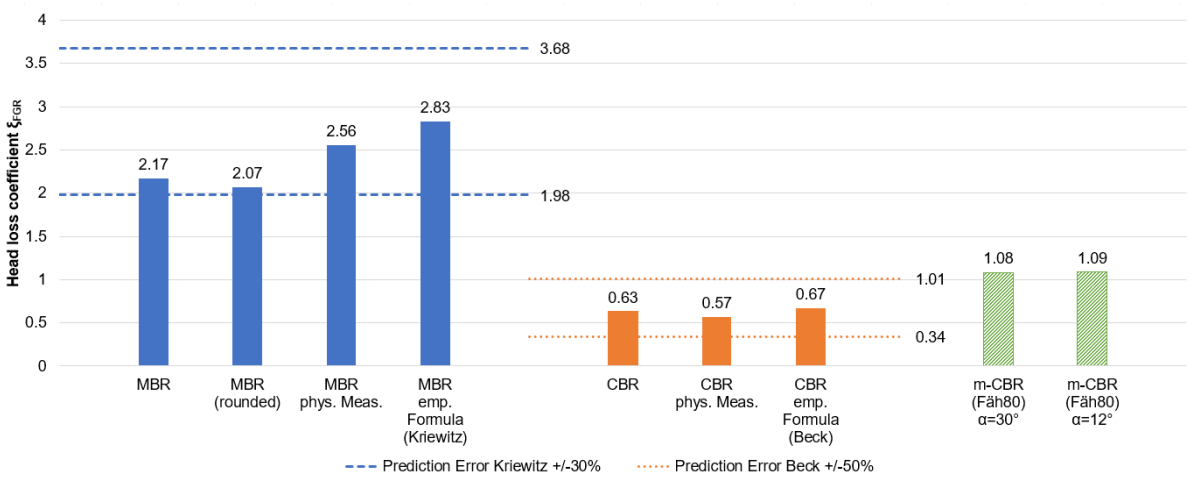

Figure 107 Head loss coefficients of the numerical simulations, the physical model study in the laboratory and the empirical formulas incl. prediction error of the latter for MBR and CBR (rack angle α = 30°, bar spacing b = 50 mm) as well as the head loss coefficient of the numerical simulation for the m-CBR (rack angle α = 30° and 12°, bar spacing b = 50 mm)

The inclination of the bars (expressed with the bar angle β) as well as the declination of the rack as a whole (rack angle α/θ) with respect to the approach flow leads to two main effects: Firstly, the flow is accelerated along the length of the bar rack. This acceleration is important for the fish guidance and the bypass acceptance. Secondly, the flow downstream of the rack is deflected away from the rack. The magnitude of this deflection influences the flow distribution to the turbines and therefore their overall efficiency. Both effects need to be adequately represented in the powerplant model by the *bar rack baffle* (BRB) that substitutes the implementation of the actual bars in the model.

The BRB is calibrated with the detail model. It can represent the flow deflection both by the angle of the deflection and through the percentage of the flow being deflected. Both parameters combined reproduce the overall effect on the flow caused by the FGR. In Figure 108, a comparison of the flow field with resolved bars and with the calibrated BRB is shown for (a) a rack angle of 30° which corresponds to the one of *R07* and (b) a rack angle of 12° which corresponds to the one of *R01*. For *R01*, an angle of deflection of 45° was used and a percentage of defected flow of 40%. For *R07*, the angle of deflection was 45° and the defected flow 50%.

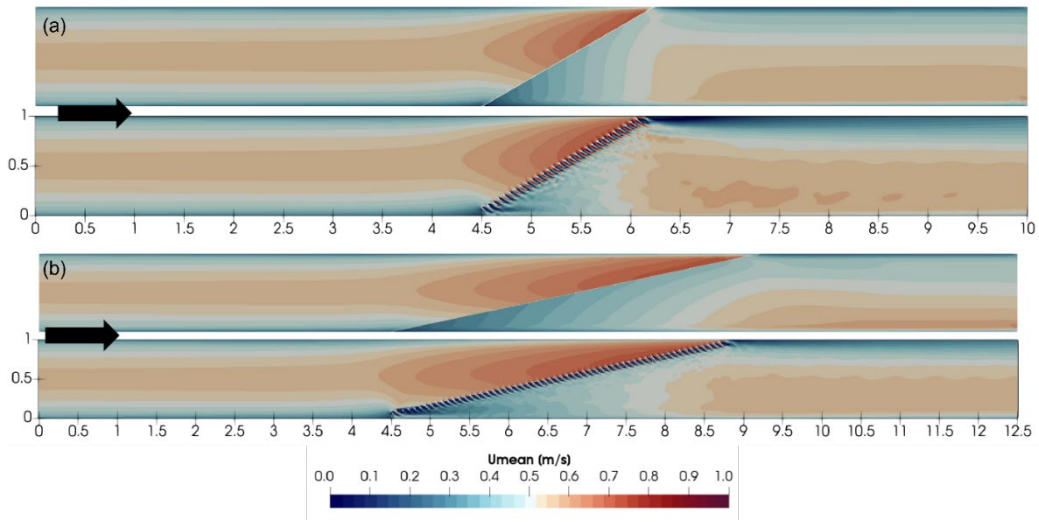

Figure 108 Flow field for resolved m-CBR (bottom) and Bar Rack Baffle (top) in the detail model: (a) a rack angle of 30°, corresponding to R07 and (b) a rack angle of 12°, corresponding to R01

Fish Guidance Rack in Powerplant Model

A direct representation of the FGR in the powerplant model is not convenient due to the comparatively small dimensions of the bars. To resolve the bars, a mesh of a great number of very small cells would be necessary that would cause very high simulation times. Instead of a direct simulation of the FGR, its effects on the flow field are implemented into the model by means of an inner boundary condition called *Bar Rack Baffle* (BRB). The BRB was calibrated to the specific FGR configuration using the model. The CBR concentrates the flow towards the end of the rack. In the case of *R01*, this further increases the tendency already present without the CBR. Consequently, the area of high normal velocities in the last quarter of the rack increases whereas the velocities at the start of the rack decrease. This acceleration along the rack is also palpable for *R07*. The effect is less pronounced than for *R01* as it is counteracting existing flow concentration resulting in lower peak normal velocities. The flow along the rack also reduces the effect of the sill-vortex and improves the overall velocity ratio compared to the situation without the CBR. The acceleration along the rack is smaller and more evenly distributed along the length of the rack for *R07*, indicating that the fish guidance is better for this variant.

In Figure 109 (left), the turbine approach flow for the design discharge Q_d = 220 m³/s is shown in the case (a) without CBR and in the case (b) with CBR. The *admission per quadrant* criterion is fulfilled for both scenarios. For the right turbine, the flow is more evenly distributed with the CBR. The flow distribution between the two turbines is almost identical in both cases. The left turbine receives 52.3% and 52.2%, the right turbine 47.7% and 47.8% respectively. The CBR therefore does not influence the turbine admission flow significantly for the *R01* variant.

Figure 109 (right)shows the turbine admission flow for *R07* with design discharge. Subfigure (a) represents the scenario without CBR and subfigure (b) the one with CBR. Here, the effect of the rack is more apparent. The flow is deflected towards the right side of the headrace channel, leading from an uneven distribution of flow of 53.1% on the left turbine and 46.9% on the right turbine without the rack

to an almost even distribution of 49.4% on the left turbine and 50.6% on the right turbine when the rack is in place. The *admission per quadrant* criterion is exceeded in the latter scenario on the left turbine.

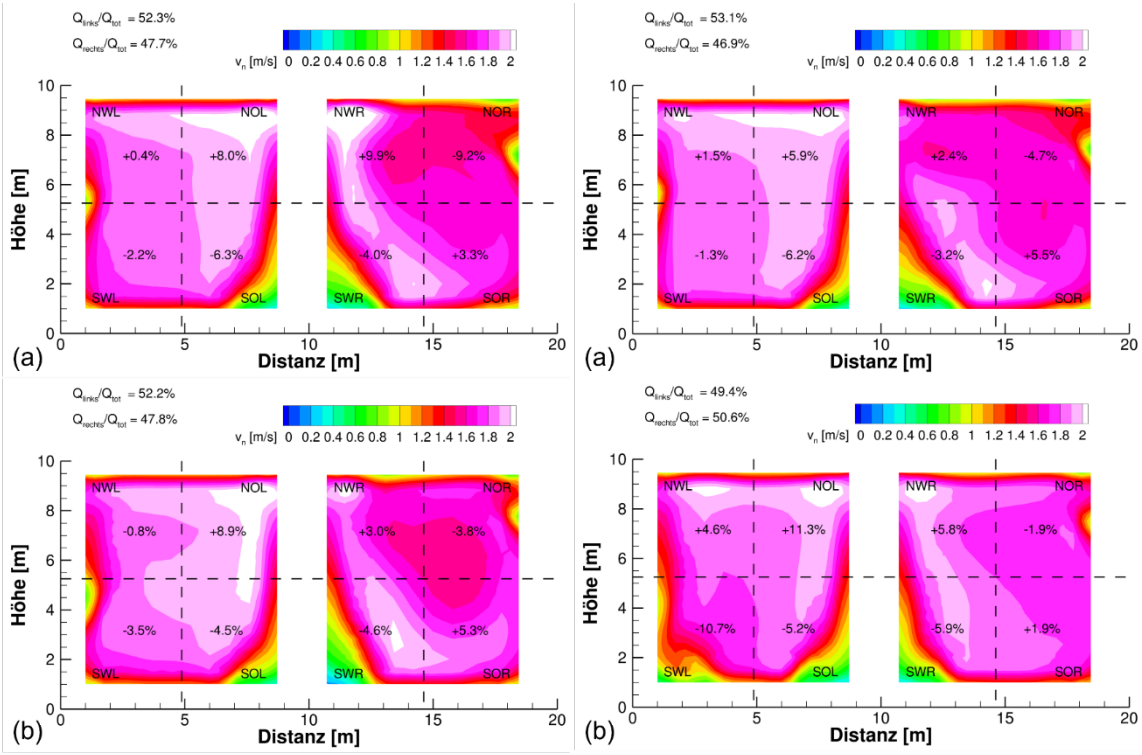

Figure 109 Turbine approach flow for R01 (left) and R07 (right): (a) without CBR and (b) with CBR at design discharge Q_d = 220 m³/s

The other load cases show that the admission per quadrant criterion is not fulfilled in most cases with one-sided turbine operation both in the reference state and with CBR for both variants. This effect is more pronounced for smaller discharges (Q_{330}).

A comparison of *R01* and *R07* shows that the CBR is counteracting the vortex development in the wake of the bed load diversion sill. Its effect is still recognizable at the turbine inlet for *R01* where the rack is located on top of the sill and is almost eliminated for *R07* where the rack is located after the sill. The flow distribution between the turbines is improved by the CBR for *R07*. Here, the natural flow field and the effects of the rack cancel each other out, resulting in a very even distribution. Within the cross-sections (quadrant criterion), the flow is more evenly distributed for *R07* in case without CBR and for *R01* with the CBR. In *R01*, driftwood is prevented from entering the headrace channel by the FGR and diverted along the rack towards the area on front of the weir. Using the FGR for this purpose in *R07*, however, would lead to chocking of the upstream part of the headrace channel with driftwood that would be stuck there and need to be removed manually. To prevent this, an additional top overlay parallel to the bed load diversion sill is needed to guide the wood towards the weir. The top overlay pushes the flow including the sill-vortex further towards the left channel side increasing the velocity in the last third of the rack. The velocity ratio stays predominantly above 1 and is even slightly improved in the area of the vortex close to the bottom of the rack.

Because the analysis so far showed very promising results for *R07*, constructional aspects of the bypass were considered for this variant. The same constructional aspects were already studied for *R01* as this variant was the one originally proposed including the layout of the bypass. The rack and the bypass entrance in *R01* are located on top of the bed load diversion sill, resulting in 5 m of water depth to be overcome within the bypass and for the steel gate regulating the bypass entrance to operate in. In *R07*, the FGR is positioned downstream of the bed load diversion sill and therefore covers the entire 9 m flow

depth of the headrace channel. Such large height would be very challenging for steel gate construction. Furthermore, a bypass of such depth would need a lot of discharge to maintain a sufficiently high bypass flow velocity. Furthermore, the fish would have to overcome 9 m of flow depth and a related long distance within the bypass before the point of no return at the flap gate would be reached.

On this basis, 9 m of rack height was judged to be unfeasible. An alternative design was investigated where the elevated height of the top of the bed load diversion sill was maintained further along the headrace channel bottom up to the position of the FGR. The elevation of the channel bottom was limited by the need to overcome the height difference to the turbines within the restricted space between the FGR and the powerhouse and to retain a sufficiently large flow cross-section. The resulting rack height and corresponding bypass depth was 6 m. In both variants, deep rack and the shallow rack, a top overlay for driftwood deflection is included. The velocity ratio for the shallow variant is improved compared to original deep variant. This is mainly because there is no vortex structure in the wake of the sill as the bottom elevation is maintained. The velocities at the rack, however, are significantly larger due to the reduced flow cross-section available. There is a considerable area with normal velocities of around and above 1.5 m/s.

In addition, thought was given to several other operational aspects of the FGR-BS:

- One-sided turbine operation: Operation of the turbine on the side of the bypass will help to flush floating debris while operation of the turbine on the side of the fishpass for upstream migration will help with the attraction flow. *R07* combines both aspects as both up and downstream migration take place on the left-hand shore. *R01* can support only one of the two effects.
- Trash rack and safety: For the *R01* variant, an additional trash rack at the turbine inlet is needed. With *R07*, a concrete covering of the headrace channel downstream of the FGR could be considered instead of a second rack.
- Rack cleaning: The rack of *R07* has longer bars but the length of the rack is shorter than for the *R01* variant. The benefits of either would need to be checked with the supplier of the rack cleaning machine.
- Rack vibration: *R07* has longer bars whereas the velocities occurring at *R01* are higher. Both factors contribute to vibrations. The relative importance of both would need to be checked with a hydraulic steel construction expert.
- Sediment transport: Transport of bed load towards the weir is better supported in case of *R07* compared to *R01*. For the latter, there is a bend between the bed load diversion sill and the pier head (at the ramp to the bypass) that could act as a sediment trap, whereas the bed load diversion sill in *R07* ends seamlessly at the pier head. Fine sediments could be deposited at the upstream end behind the deflection sill in the headrace channel due to low flow velocities. This is similar for both variants.

In terms of fish guidance, bypass acceptance and flow distribution on the turbines, the base variant of *R07* shows better overall flow characteristics than *R01*. The design of *R01* on the other hand already covers additional aspects such as driftwood or bypass depth and operation. For *R07*, further measures are needed to consider these aspects, and consequent measures change the flow conditions for the worse by increasing flow velocities especially towards the end of the rack. The deciding aspect was the shallow headrace channel. The resulting velocities are very high and there are too many uncertainties related to fish behavior at such velocities because there is no experimental data available. Therefore, variant *R01* was chosen for fish protection and guidance at the MBR demonstrator.

Bypass Optimization

Even though *R07* showed the better general flow characteristics, it proved to be unfeasible and *R01* was chosen. Therefore, different approaches to optimize flow conditions at the FGR and especially the bypass entrance are investigated to improve fish guidance efficiency. In the original layout of *R01*, there is a gap between the cantilever of the bed load diversion sill and a ramp connecting the river bottom to

the bypass entrance. This causes a flow disturbance at this critical point where flow velocities were already unfavorably high. In Figure 110 on the left, vertical velocities within this gap are shown as well as normal velocities in the rack plane. The vertical velocities close to the rack are very high (peaking at over 1.5 m/s) and are judged to further adversely affect fish guidance and bypass efficiency. To counteract this effect, the bed load diversion sill was gradually broadened along its length so that the face along the bottom would match up with the tip of the dividing pier. This essentially eliminates the vertical velocities at the FGR and generally reduces the flow disturbances close to the bypass entrance. The vertical velocities at the lip of the sill cantilever are much smaller than before (cf. Figure 110 on the right).

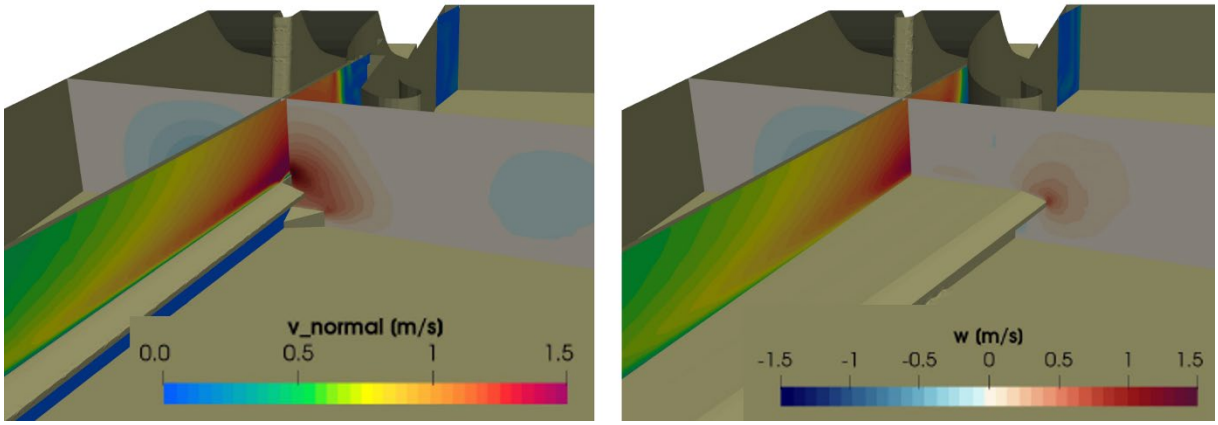

Figure 110 Normal flow velocities along the rack plane and vertical velocities perpendicular to the rack plane for the original bed load diversion sill layout (left) and a broad bed load diversion sill (right).

This layout has an added benefit for bed load diversion. Since the sill here seamlessly connects to the pier, the bed load can be guided on a direct path towards the weir without any chance of getting trapped between the tip of the pier and the end of the sill where the ramp is located in the original design. A drawback of this design is that there is no more direct access from the river bottom to the bypass. Fish travelling close to the bottom have to overcome the cantilever of the bed load diversion sill in order to reach the bypass.

A second starting point for the optimisation of the flow around the bypass entrance is the dividing pier itself. In the original design, the bypass entrance opens right after the upstream tip of the pier at a region where the flow is already likely to detach from being deflected around the pier. Figure 111 (a) illustrates the resulting flow detachment within the bypass entrance. This abrupt deceleration is the opposite of the slowly and gradually accelerating flow optimal for fish guidance.

Figure 111 (b) shows a design in which the pier tip has been elongated in relation to the bypass entrance and been shaped more hydrodynamically to reduce flow detachment at the pier as much as possible. There is still a deceleration at the bypass entrance which is related to the amount of bypass discharge compared to the discharge arriving at this point. However, flow detachment has been much reduced and equally importantly, the acceleration along the end of the rack is much more gradual with slower peak velocities.

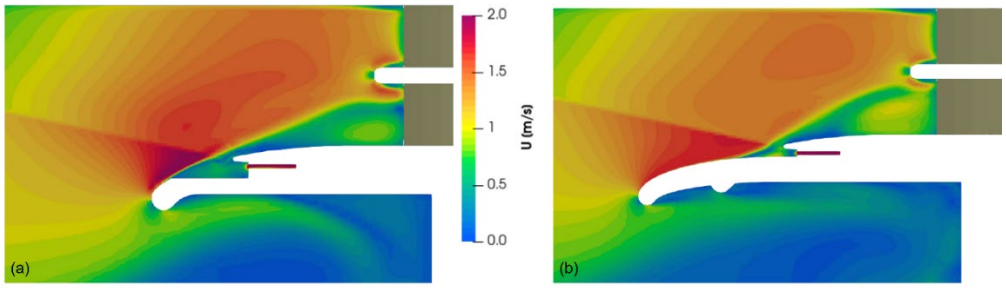

Figure 111 Bypass optimization at the dividing pier: (a) original pier and bypass design and (b) elongated pier and reduced bypass entrance width.

The improved flow conditions by this pier layout are illustrated in Figure 112, too, which shows the flow field in front of the rack. On the left is the situation with the original design and on the right the one with elongated pier. The elongated pier leads to smaller peak normal velocities of about 1.2 m/s and reduces the area with a velocity ratio below 1 significantly.

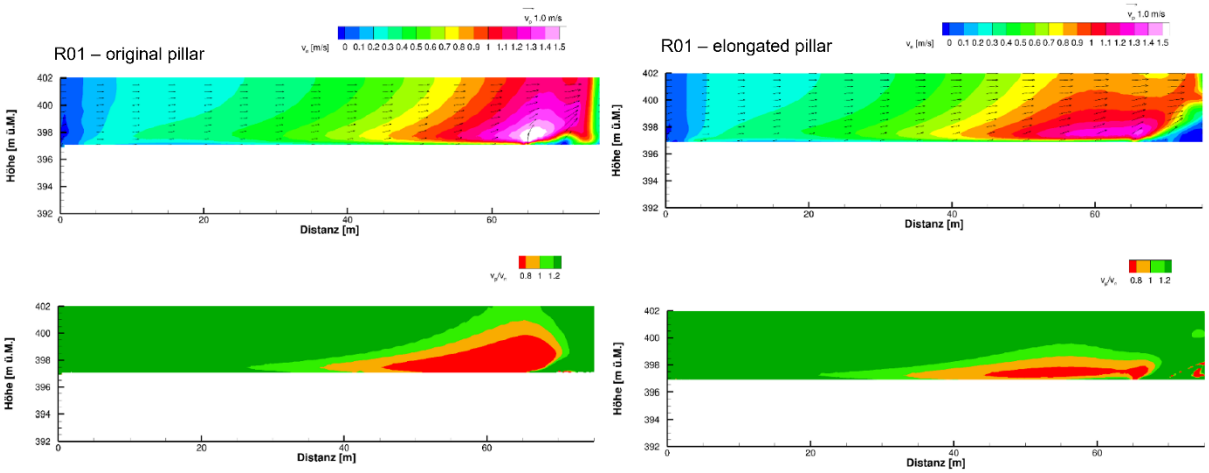

Figure 112 Flow conditions in front of the FGR and velocity ration for the original layout (left) and the layout with elongated pier tip (right).

Elongation of the pier tip increases the area in which driftwood can be trapped and the likelihood of this event happening. This issue will need to be addressed when choosing this approach. Possible solutions are a floating barrier or a top overlay connecting the starting point of the rack with the tip of the pier or a gap within the top part of the pier through which the driftwood can be flushed towards the bypass.

A further approach is the bypass entrance itself. Through reducing its width, the velocities in the bypass can be increased and flow detachment zones reduced. This improves the flow conditions with respect to fish guidance and bypass acceptance. Or, if a certain velocity is going to be maintained, the bypass discharge needed, is reduced. Figure 111 shows the initially 2 m wide bypass entrance on the left side compared to a 1 m wide bypass on the right side. The velocity ratio in front of the rack can also be optimized by adjusting the rack angle θ. A variation of a few degrees can minimize the area in which the normal velocities exceed the tangential velocities.

Discussion

The analysis of the FGR-BS of the MBR demonstrator revealed that in terms of fish migration and turbine operation, a design with the bypass on the left-hand side (*R07*) showed better results but when considering a wider picture and constructional aspects, the best variant was *R01* with the bypass in the dividing pier. The unfavorable flow conditions towards the end of the rack can be extenuated and improved by optimization measures such as a broad bed load diversion sill and a careful design of the

dividing pier. The turbine admission flow for this layout is not significantly affected by the CBR in this case. In contrast to *R07*, the flow distribution between the turbines is also not improved by the CBR. The use of a CBR in comparison to the reference state (which is analogous to the HBR) shows that the flow acceleration along the rack is more pronounced but that the flow conditions otherwise are very little affected. A vertical CBR is therefore recommended due to the large rack area and discharge volume at the MBR demonstrator.

4.3.2 Ethohydraulic tests of the bypass inlet gate for downstream fish passage

For many species, fish guidance racks (FGRs) with adjacent bypass systems (BSs) are effective solutions for safe downstream passage at HPPs. The main function of the bypass is to attract, safely collect, transport, and return fish undamaged to the river downstream of the obstacle. For a successful fish guidance, the design of a bypass is therefore just as important as the design of a FGR. However, to reduce generation loss, bypass discharge is often limited and controlled by adding a vertical axis flap gate with local openings at the bypass inlet, as in the case of MBR. Such gates create high absolute flow velocities and velocity gradients that may cause avoidance reactions of approaching fish. The objectives of this work are to investigate the behaviour of two target fish species, namely brown trout (*Salmo trutta fario*) and common barbel (*Barbus barbus*), at the Curved-Bar Rack-Bypass System (CBR-BS) of MBR based on the numerical study presented in section 4.3.1. For this purpose, a large-scale physical model of the downstream end of the CBR and the adjacent bypass inlet gate was constructed in the ethohydraulic flume at VAW. Inlet gates with a bottom and a top opening were separately investigated for three different approach flow velocities.

Physical model

As described in section 4.3.1, the optimized design of the CBR-BS features foil-shaped bar profiles with a horizontal angle of 12° between the turbine and rack axes and a clear bar spacing of 50 mm. At the downstream end of the CBR, the bypass inlet gate with bottom and top openings is located. The water depth upstream of the bypass inlet is 5.0 m in prototype scale. The physical model was constructed in the 30 m long and 1.5 m wide ethohydraulic flume at VAW. As the maximum water depth in the flume is limited to h_M = 0.9 m, the water column was divided into two parts of h_P = 2.5 m each and the bottom and top opening were investigated separately. For the CBR, the same clear bar spacing of 50 mm as in the prototype was used. As the approach flow of the rack is not parallel to the turbine axis in the prototype, the horizontal rack angle in the model was chosen as 30° based on the determined streamlines in the numerical model. The spaces between bars were covered with a net at the upstream side of the FGR to ensure 100% fish guidance to the bypass, given that the experimental design was focused on determining the acceptance and passage efficiency of the bypass inlet gate. The dimensions of the bypass inlet gate were downscaled by a factor h_P/h_M = 2.78. For the gate with the top opening the resulting maximum flow velocity within the opening is $U_{by,in,max}$ = 1.7 m/s, which is similar to the estimated value of 1.9 m/s for the prototype. For the gate with the bottom opening, the opening height was set to 0.25 m to reach $U_{by,in,max}$ = 2.0 m/s. This value is considerably lower than 3.7 m/s for the prototype, which is due to the limited water column in the model. However, a further reduction of the opening size was refrained from to keep reasonable bypass dimensions with respect to fish size. A full description can be found in Kastinger et al. (2023).

Test program

For each bypass gate type, the live-fish tests were conducted at three different discharges and resulting approach flow velocities. Hence, six configurations were investigated for each fish species. For all experiments, water depths in the approach area and in the bypass downstream of the inlet gate were kept constant at h_o = 0.9 m and h_{by} = 0.5 m, respectively. Hence, only the inflow was varied to reach mean approach flow velocities of U_o = 0.3, 0.4, and 0.5 m/s. Flow velocities within the openings $U_{by,in}$ varied between 0.8 and 1.7 m/s for the top opening and 1.9 and 2.0 m/s for the bottom opening. Compared to previous studies at VAW (e.g., Beck, 2020; Meister, 2020), this resulted in very high flow velocity ratios $U_{by,in,max}/U_o$ between 3.4 and 6.8.

Flow field measurements

Flow fields were mapped by measuring the streamwise, transverse, and vertical velocity components u, v, and w in x, y, and z directions, respectively, with a side-looking Nortek Vectrino+ acoustic Doppler velocimeter (ADV) probe. Measurements were conducted in a grid of 276 points upstream of the FGR-BS, with a reduced grid size in the vicinity of the bypass inlet gate. Sampling duration was 30 s for each measurement point at a sampling rate of 200 Hz for the bottom opening and changed to 100 Hz for the top opening due to technical difficulties. The raw ADV data were despiked according to Goring & Nikora (2002) and Wahl (2003). For filtering, minimum correlation and signal-to-noise ratio were set to 35% and 6 dB, respectively. In addition, the mean streamwise velocity component u was measured with a propeller anemometer within the bypass opening, where ADV measurements were not possible due to geometric constraints close to fixed and solid boundaries.

Live-fish test procedure

Live-fish tests were conducted in July and August 2022 with wild brown trout (*Salmo trutta fario,* total number n_{tot} = 55, mean total length TL_m = 176 mm, standard deviation σ_{TL} = 24 mm) and common barbel (*Barbus barbus,* n_{tot} = 48, TL_m = 158 mm, σ_{TL} = 47 mm) in the ethohydraulic flume for two weeks each. These two species are among the target fish species at MBR and were chosen as they are representatives of two different families, salmonids and cyprinids, respectively. From previous studies it was known that these two species show a considerably different behaviour in ethohydraulic tests. Furthermore, both species are only near threatened in Switzerland and are therefore suitable for animal testing. Fish were caught by electrofishing and had a minimum of 2.5 days to recover from stress before being used for tests.

For each species and configuration, the tests were repeated eight times with groups of three fish each. Hence, 96 tests were conducted in total. Individual fish were used maximum three times for tests. The order of tests was randomized. Water temperature in the holding tanks and experimental flume was regulated to 15 ± 2 °C and 21 ± 2 °C for trout and barbel, respectively. Prior to each test, fish were able to adapt to the approach flow conditions and water temperature in the closed starting compartment for 15 min. After this acclimatization period, the starting compartment was opened and fish could swim volitionally in the experimental setup. Test duration was limited to a maximum of 45 min. Fish behaviour was recorded by visual observation and video cameras installed up- and downstream of the bypass inlet gate. Fish swimming behavior and movement was assessed qualitatively by visual observation through the glass wall of the flume and video cameras installed up- and downstream of the bypass inlet gate.

Data analysis of live-fish tests

As the CBR was covered with a net to avoid fish rack passage, there are two possible outcome scenarios for the live-fish tests: (1) Swimming through the opening of the bypass gate (“bypassed”, subscript *by*); (2) Refusal to pass through the bypass gate opening within 45 min (“refusal”, subscript *ref*). Hence, the bypass passage efficiency (BPE) was defined as:

$$\mathrm{BPE} = \frac{N_{\mathrm{by}}}{N_{\mathrm{by}} + N_{\mathrm{ref}}} \tag{1}$$

with N_{by} as the number of fishes successfully bypassed and N_{ref} as the number of fish, which refused the bypass opening. Fish that did not interact with the FGR-BS within the test duration, i.e., stayed in the starting compartment or swam solely upstream, were excluded from data analysis. For statistical analyses, the software environment *R* was used. Different analyses were used to address different research questions.

Two-sided chi-square (χ^2) tests were conducted to test for statistically significant differences of BPE between fish species and configurations. The null hypothesis H_0 was formulated that no significant difference is present between two tested configurations, whereas the alternative hypothesis H_A stated a significant difference. To calculate the test quantity χ^2, the expected and occurring frequencies of bypass passage and refusal were used. Under H_0 it was assumed that $\chi^2 = 0$, whereas for H_A $\chi^2 > 0$ was implied. Type I error probability (rejection of H_0 although it is true) was defined as α = 5% to calculate the critical

χ^2 value. Additionally, Cramér's V was used to quantify the association between two tested configurations and BPE. Cramér's V varies from 0 (no association) to 1 (complete association). A drawback of the chi-square test is that the calculated significance of the deviation from H_0 is only exact for an infinite sample size. For small sample sizes and low observed frequencies, the resulting test statistic should be considered with caution. Hence, additionally one-sided Fisher's exact tests with the same significance level α = 5% were used as robustness check to confirm the results of the chi-square tests.

To determine which of the investigated parameters significantly affected the probability of bypass passage, multivariate regression was used. The response variable "bypass passage" is of binary form (0 – "no", 1 – "yes") and hence follows a binomial distribution. Tests were conducted with groups of three fish, but fish response was accounted for individually. As it is likely that individual fish behavior was influenced by the other fish in each test, pseudoreplicates are present and independence of data is violated. To take this into account, generalized linear mixed models (GLMM) were used. These models are an extension of generalized linear models (GLM) and allow for correlation between observations and nested data structures (Zuur *et al*. 2009). In addition to a set of explanatory variables (fixed effect) a random effect term is included. The statistical model becomes:

$$Y_{\mathrm{by}} \sim \mathrm{Bin}\left(1, p_{\mathrm{by}}\right) \tag{2}$$

$$\mathrm{logit}\left(p_{\mathrm{by}}\right) = \ln\frac{p_{\mathrm{by}}}{1-p_{\mathrm{by}}} = \alpha + \sum_i \beta_i \cdot X_i + r \tag{3}$$

$$r \sim N\left(0, \sigma_r^2\right) \tag{4}$$

Y_{by} is 1 if a fish passes the bypass gate and 0 otherwise. It is described by a binomial distribution with p_{by} as the probability of bypass passage. The logit (logistic link) of p_{by} is described as the sum of the fixed intercept α, a linear combination of explanatory variables X_i and corresponding regression parameters β_i, and a random intercept r. The latter is assumed to be normally distributed with mean 0 and variance σ_r^2. The parameters fish species, location of bypass opening, approach flow velocity U_{o}, velocity ratio $U_{\mathrm{by,in}}/U_{\mathrm{o}}$, total fish length c$TL$ (centered by the mean total length of each species), water temperature T_{w}, daytime (morning/afternoon), and the number of times a fish was used for a test (1 to 3) were identified as potential explanatory variables (fixed effect). However, high collinearity between location of bypass opening and $U_{\mathrm{by,in}}/U_{\mathrm{o}}$ (point biserial correlation coefficient r_{pb} = 0.76) and between fish species and T_{w} (r_{pb} = 0.96) are present. Hence, $U_{\mathrm{by,in}}/U_{\mathrm{o}}$ and T_{w} were removed from the set of explanatory variables. Verification of the Variance Inflation Factors (VIFs) confirmed that, after removal of $U_{\mathrm{by,in}}/U_{\mathrm{o}}$ and T_{w}, VIFs of all remaining explanatory variables are distinctly below 3, indicating there is no collinearity in these variables (Zuur *et al*. 2007). Random intercept models are implicitly introducing the compound symmetrical correlation structure (Zuur *et al*. 2009). Hence, the test ID was used as random effect to consider that the probability of a fish passing the bypass gate is correlated to other fish in the same test. The GLMMs were fitted using the function *lmer* from the *R* package *glmmML*. No statistically significant interaction terms between fixed effect parameters were found and hence models with different linear combinations of explanatory variables were investigated. Model selection was conducted based on Akaike Information Criterion (AIC) and Akaike weights. Additionally, *p*-values were used to check for (non-)significant explanatory variables. Finally, time-to-event (or survival) analysis of the elapsed times between each test start and bypass passage was conducted to also consider the temporal course of the tests (Castro-Santos & Perry 2012). Cumulative incidences of bypass passage were determined using the *R* package *survival*.

Flow fields

Figure 113 shows top view contour plots of the mean longitudinal flow velocity component u with streamlines and velocity vectors exemplarily for the medium load case U_{o} = 0.4 m/s and the bypass inlet gate with (top) bottom and (bottom) top opening. The horizontal planes are cut at two different elevations $Z = z/h_{\mathrm{o}}$ above the flume bottom. In both cases, the curvature of the streamlines and hence the velocity component normal to the rack plane increases towards the downstream end of the CBR. The velocity

vectors indicate the separation of flow through the rack and bypass opening. Close to the bypass opening the flow velocity increases sharply (high velocity gradient) and the maximum value occurs within the opening. In Figure 114 the flow fields are shown in a longitudinal section through the axis of the bypass opening at $Y = y/b = 0.67$ from the right flume wall. For the bottom opening (Figure 114a), all streamlines curve towards the flume bottom close to the bypass inlet gate. For the top opening (Figure 114b), streamlines within the upper third of the water column remain straight while in the middle third curvature towards the water surface is present. In the lower part of the water column a recirculation zone is formed close to the bypass inlet gate. As in Figure 113, the absolute flow velocity and velocity gradient are highest at the bypass opening. While for the bottom opening the flow velocity is about the same $U_{by,in} \approx 2.0$ m/s within the whole opening, $U_{by,in}$ increases from the water surface to the lower edge of the top opening. Flow fields for the other load cases are similar and hence the conclusions above do also apply for the configurations with low and high discharge.

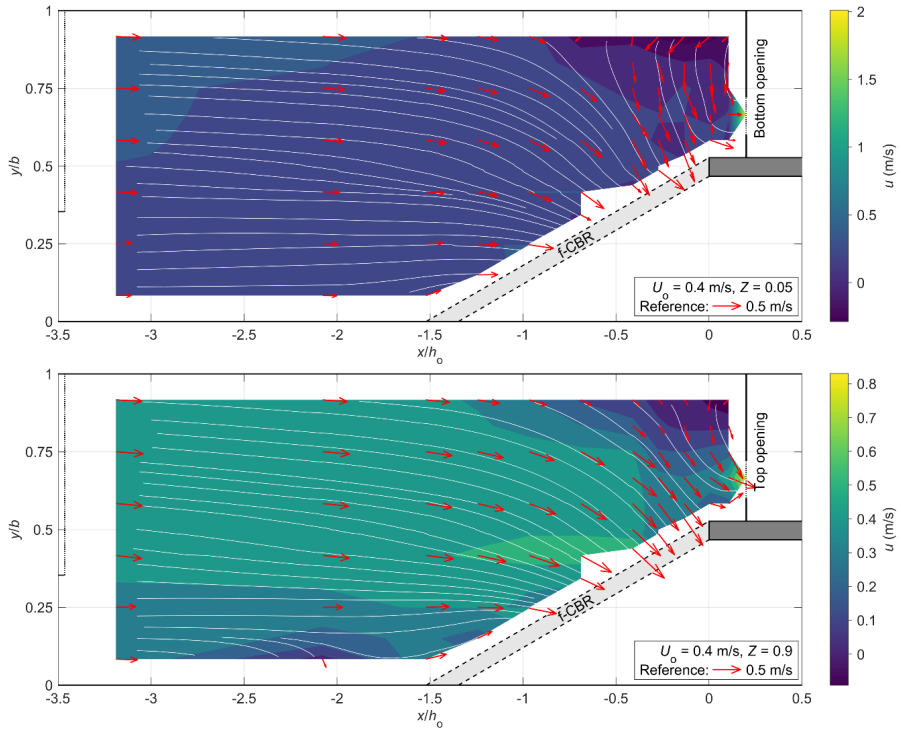

Figure 113: Contour plots of mean longitudinal flow velocity u, velocity vectors and streamlines for U_o = 0.4 m/s in the horizontal plane (top) above the flume bottom for the bypass gate with bottom opening and (bottom) below the water surface for the bypass gate with top opening.

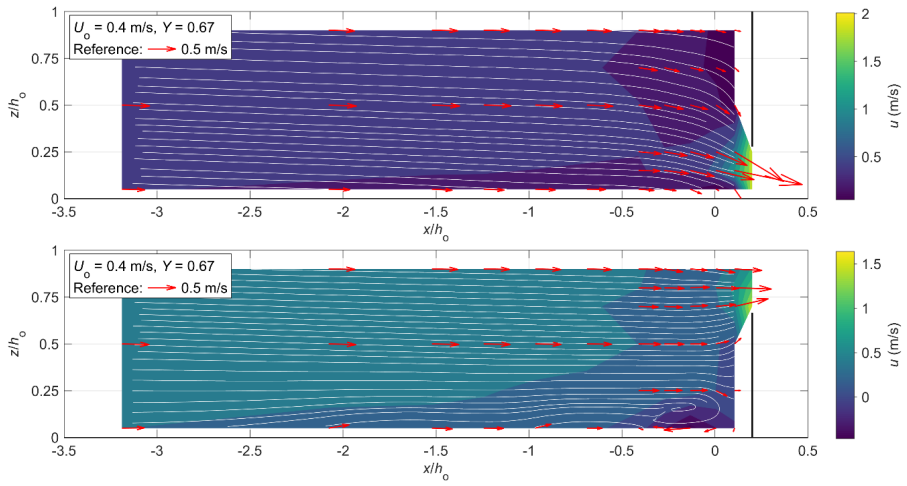

Figure 114: Contour plots of mean longitudinal flow velocity u, velocity vectors and streamlines for U_o = 0.4 m/s in the vertical plane for the bypass gate with (top) bottom and (bottom) top opening.

Fish swimming behavior

Both fish species usually approached the bypass inlet actively with positive rheotaxis, i.e., head oriented against the flow direction. Fish were either guided along the CBR towards the bypass gate or approached directly without rack interaction. Barbel often swam together in groups and touched the rack and bypass gate with their caudal fin (thigmotactic behavior). Trout showed a more individual swimming behavior and sometimes chased away other individuals, followed by short burst swimming events. Figure 115 shows frames from the video recording of the live-fish tests at the time when one or more fish passed the bypass inlet gate opening. When approaching the bypass opening, both species frequently exhibited avoidance responses to the high velocity gradients and absolute flow velocities in the vicinity of the opening. These included a sudden increase in caudal fin flapping frequency and a subsequent escape to zones with lower flow velocities. Passage of the bypass opening generally occurred with positive rheotaxis. Especially for smaller individuals, swimming through the bypass opening was often uncontrolled once the fish entered the zone of high flow velocities.

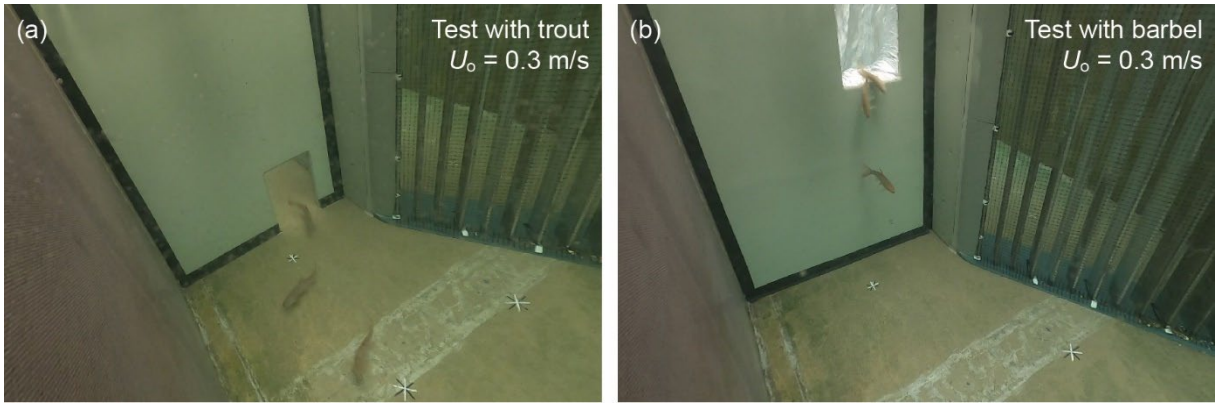

Figure 115: Video excerpts of ethohydraulic tests when fish passed the bypass inlet gate with a (a) bottom and (b) top opening.

Bypass passage efficiency

The proportions of bypass passage and refusal for each fish species and configuration are shown in Figure 116. The bypass passage efficiency (BPE) for the bottom opening is significantly higher than for the top opening for both species. For the top opening, values of BPE range between 8% and 21%, which is considered as very low. No significant differences in BPE between fish species or approach flow velocity are present. One-sided Fisher's exact tests were used to confirm the results of the chi-square

tests (robustness check). Besides small deviations of the *p*-values, both tests lead to the same conclusions when it comes to confirming or rejecting the hypotheses.

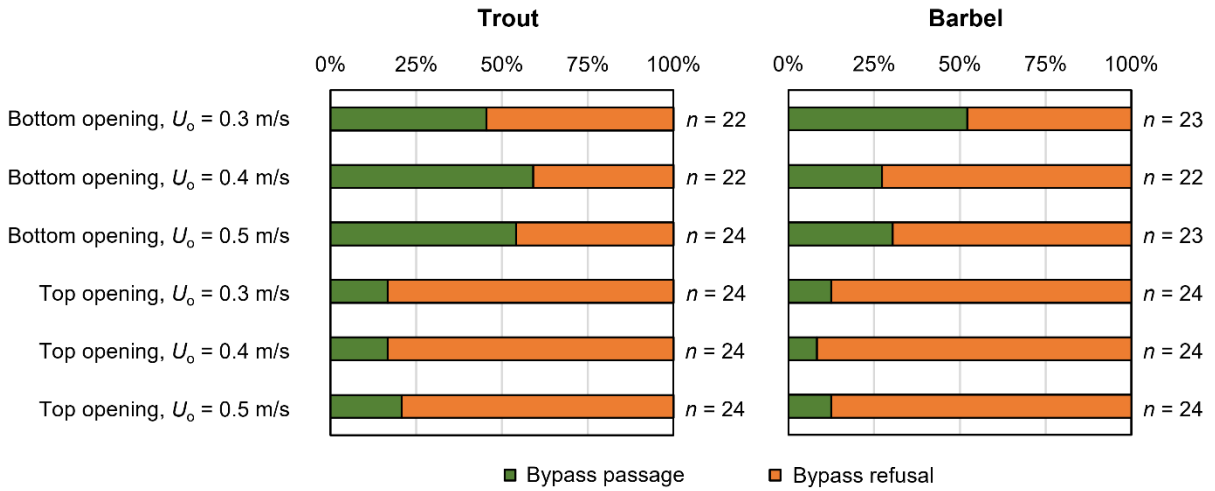

Figure 116: Proportions of bypass passages and refusals of live-fish tests with trout and barbel for each configuration.

In total, 64 GLMMs with different linear combinations of explanatory variables were investigated. Based on the model parameters, the probability of bypass passage p_{by} (predicted BPE) for a given fish species and opening location can be determined including a range of uncertainty due to the random effects. The latter was included with $r = \pm 1.96 \cdot \sigma_r$ in Eq. (3), i.e., considering 95% of the possible values of the random intercept *r*. For the bottom opening, the expected BPE is 52.5% (34.0%−70.3%) for trout and 36.8% (21.3%−55.5%) for barbel. For the top opening, the expected BPE is 17.7% (9.1%−31.6%) for trout and 10.2% (5.0%−19.6%) for barbel. These values are in good agreement with the actual BPEs determined from the ethohydraulic tests.

Time of bypass passage

Also considering the time of each passage through the bypass inlet opening, Figure 117 shows the distributions of the cumulative BPE over the test duration of 45 min for both fish species and each configuration.. With the bottom opening, fish generally found and used the bypass more quickly, and their passage behavior was more responsive to changes in approach flow velocity. Barbel tended to pass almost immediately under favorable flow conditions, while trout showed faster and more frequent passage as flow velocity increased. With the top opening, both species took considerably longer to begin using the bypass, and their passage patterns were less sensitive to flow velocity. Trout showed a delayed but fairly consistent passage pattern across velocities, while barbel exhibited even more delayed and sporadic passage events. Overall, the bottom opening encouraged earlier and more frequent bypass use, whereas the top opening resulted in slower and more hesitant fish behavior.

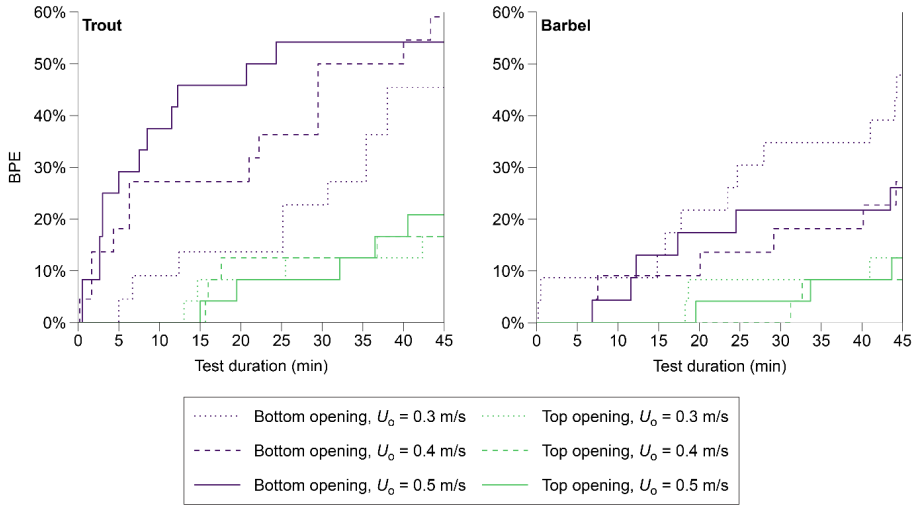

Figure 117: Cumulative bypass passage efficiency over the live-fish test duration with trout and barbel for each configuration.

Discussion

The study shows clear avoidance behaviors of barbel and trout toward high flow velocities and velocity gradients at bypass inlet gates, with fish species and bypass opening location strongly affecting BPE. Overall, the bottom opening achieved higher BPE than the top opening, and approach flow velocity had no significant effect on either opening, although species-specific patterns occurred. Trout maintained similar BPE across all velocities, while barbel avoided the bottom opening more frequently at higher velocities and used it earlier at lower velocity; in contrast, trout passed earlier at higher velocities, reflecting interspecies differences in response to high-velocity zones, barbel reacting quickly and avoiding them, trout having less control and thus passing more readily under such conditions. The top opening was rarely used by either species, showed no consistent timing trends, and was approached later than the bottom opening due to limited model water depth and light reflections, indicating possible model effects. Because BPEs were measured with rack passage prevented, actual efficiencies during regular operation would likely be lower. These results underline that bypass inlet design, especially when using a gate to regulate flow, is critical to achieving efficient and sustainable FGR-BS operation, as high flow velocities and velocity gradients can cause avoidance that reduces overall guidance efficiency. Consequently, the current HPP MBR bypass inlet design with a gated bottom and top opening is not recommended, as it would likely delay or prevent downstream migration and increase the risk of rack and turbine passage. For future planning, a redesign that reduces sharp velocity gradients and high absolute velocities, ideally through more continuous constriction and a full-depth opening, is advised. However, due to limited available research, no optimized design can yet be proposed, and additional ethohydraulic tests and field validations are needed. Further laboratory and field studies underway at VAW are expected to provide improved bypass design recommendations applicable to HPP MBR.

4.3.3 Study of suspended sediment and turbine erosion for sustainable operation

The study focuses on the suspended sediment load because it makes up most of the total sediment load. At HPP Lavey, just 6 km upstream of MBR, turbine erosion was severe until a hard coating was applied. At MBR, less turbine erosion is expected due to the lower head. However, the application of hard or soft coatings for turbine parts may be beneficial even at low-head HPPs (e.g. Rai & Kumar, 2016). Moreover, a variety of instrumentation for real-time measurements of suspended sediment is nowadays available (Felix *et al.*, 2018) and is expected to be useful for operational optimizations of the planned HPP.

The results allow for:

- Quantification of the *SSC* and sediment load in the Rhone River at the MBR site by evaluation of historical data from a federal hydrometric station and complementary field measurements,Characterization of the suspended sediment particles (particle size, shape, and hardness) by laboratory analyses of selected sediment samples,Estimation of the expected erosion rates in the turbines,Study of mitigation measures such as coatings of the turbine parts and temporary shutdowns of the HPP in periods of elevated sediment loads,Recommendations on instrumentation for real-time *SSC* measurements to allow for operation optimization of the HPP with respect to the turbine erosion and its consequences.**Evaluation of historic discharge and sediment data**

Firstly, hydrometric stations were identified to study the water and fine sediment transport in the Rhone River up- and downstream of the MBR project site. From one station, gravimetrical suspended sediment concentration *SSC* from bottle samples and measured turbidity was available in addition to discharge data. The measured turbidity was converted to *SSC* and the discharge data were scaled to the MBR site. The discharge and *SSC* time series were analyzed with respect to their dynamics. From monthly and annual water volumes and sediment loads, the average *SSC* in the river water was calculated. Then, the average *SSC* of the turbine water was calculated considering the planned HPP shutdowns if the discharge exceeds 400 m^3/s. Furthermore, flood and sediment transport events were statistically evaluated to capture how often and for how long unfavorable conditions occur. This served as a basis for the planning of mitigation measures. Lastly, the flow time of flood peaks from hydrological stations upstream of MBR was analyzed to estimate the prewarning time for HPP shutdowns. For the analysis of discharge and suspended sediment in the Rhone River with respect to MBR, the hydrometric station of Porte du Scex (station no. 2009) was selected. The following data are available:

- Discharge timeseries (available for more than 60 years)Turbidity timeseries (10 minutes averages) since 2003Suspended sediment mass concentrations determined in the laboratory by the gravimetric method from bottled water samples (SSC_G) since 1964In December 2018, the turbidimeter was replaced by a new model. The old turbidimeter model measured turbidity in *Nephelometic Turbidity Units* (NTU), whereas the new model measures in *BackScatter Turbidity Units* (BSTU, Grasso *et al.*, 2021). In the turbidity timeseries, values >350 NTU were not recorded before 2013. In the present study, however, peak values are most relevant and therefore, only the data since 2013 are further analysed. The following figures hence refer to the evaluated period of nine years from 2013 to 2021. Moreover, discharge data of these nine years from two hydrometric stations, Rhone-Branson (FOEN station 2024), the next federal hydrometric station upstream of MBR, and Drance-Martigny, Pont de Rossettan (FOEN station 2053), a major tributary upstream of MBR, were considered for comparison and to study the travel times of flood peaks. However, the MBR project site is located 17.4 km upstream of the hydrometric station of Porte du Scex. Within this distance, additional water flows into the Rhone River leading to different discharges at the two locations. The discharge timeseries of Porte du Scex is therefore scaled down with the fraction of the catchment area at the MBR project site. The discharge at the MBR project site was used for all remaining evaluations unless indicated otherwise. The distance between the MBR site and Porte du Scex further leads to a time shift of the water and sediments flows. This time shift is highly dependent on the momentary flow velocity and hence discharge. It is therefore estimated using average conditions. The *SSC* values measured at Porte du Scex were assumed to be valid for the MBR project site, as the *SSC* is not expected to change substantially between MBR and Porte du Scex. The *SSC*s are compared to the river discharge *Q* measured at the same times Due to a weak correlation between *SSC* and *Q*, real-time *SSC* measurements are an important basis for operational optimizations of HPPs with respect to fine sediment management. The suspended sediment loads *SSL* were obtained by integration of the sediment flux (i.e., the product of discharge and *SSC*) over time. For each year 2013-2021, the *SSL* were cumulated from the beginning to the end of the corresponding year From the steep sections of the cumulated timeseries, sediment transport events can be identified, during which high quantities of suspended sediment were transported within a few days. Almost all these events occurred from May to October. This

period, during which there is no snow cover in most of the catchment area, is referred to as the sediment transport season. The full analysis of sediments suspension is provided in Albayrak et al. (2025).

To quantify the water volumes passing through the powerhouse and the *SSL* of the turbines, shown in Figure 118 and Figure 119, the following two conditions were considered:

- If the river discharge exceeds the sum of the design discharge of the HPP of 220 m³/s and the design discharge of the fishways, the excess water flows through the weir gates.
- For river discharges above 400 m³/s, the HPP is shut down and the weir gates are fully opened

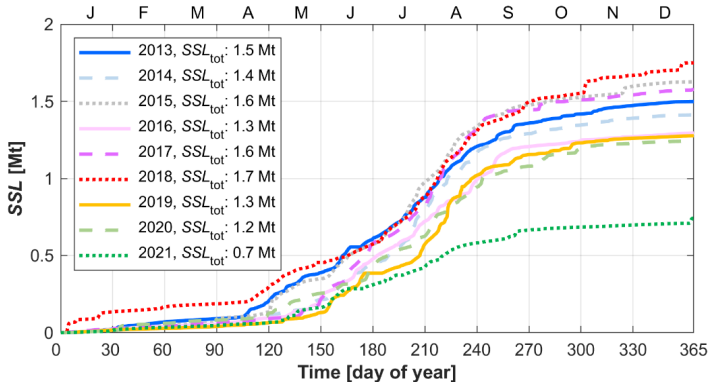

Figure 118: Cumulated suspended sediment load *SSL* of the years 2013 to 2021 through the turbines at MBR (Data source: FOEN).

The water volumes and mainly the *SSL* in Figure 119 (for both turbines) are smaller than in the whole river. In the year 2019, the *SSL* of the turbines was not outstanding whereas the *SSL* in the river was the highest in that year (Figure 119). This means that a great share of the annual *SSL* was transported in the river while the turbines were not operated. Therefore, rather small floods (below 400 m³/s) with high *SSC* cause most turbine erosion at MBR. The average *SSC* of the turbine water is only 0.3 g/l. This is 31% lower than the average *SSC* in the river water (0.43 g/l). The condition to stop the turbine operation for river discharges > 400 m³/s, contributes hence significantly to reduce turbine erosion.

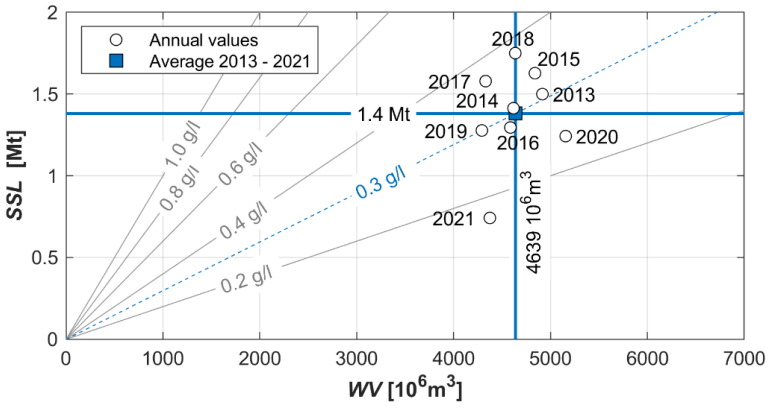

Figure 119: Annual turbined suspended sediment loads and water volumes of the years 2013 to 2021 at MBR (Data source: FOEN).

Water volumes *WV* and *SSL* vary not only among the years but also within each year. In summer, the monthly *WV* and *SSL* are much higher than in winter due to snow and glacier melt as well as intense rains due to thunderstorms (Figure 120). Overflow at the weir or flushing occurs usually from May to September (orange parts of the bars in Figure 120a). The monthly *SSL* vary more than the monthly *WV* because the *SSC* is low in winter in addition to the discharge. In June and July, less than half of the *SSL*

of the river passes the turbines (Figure 120b). The highest *SSL* for the turbines and hence erosion is expected in August, when the *SSC* is high due to mainly glacier melt.

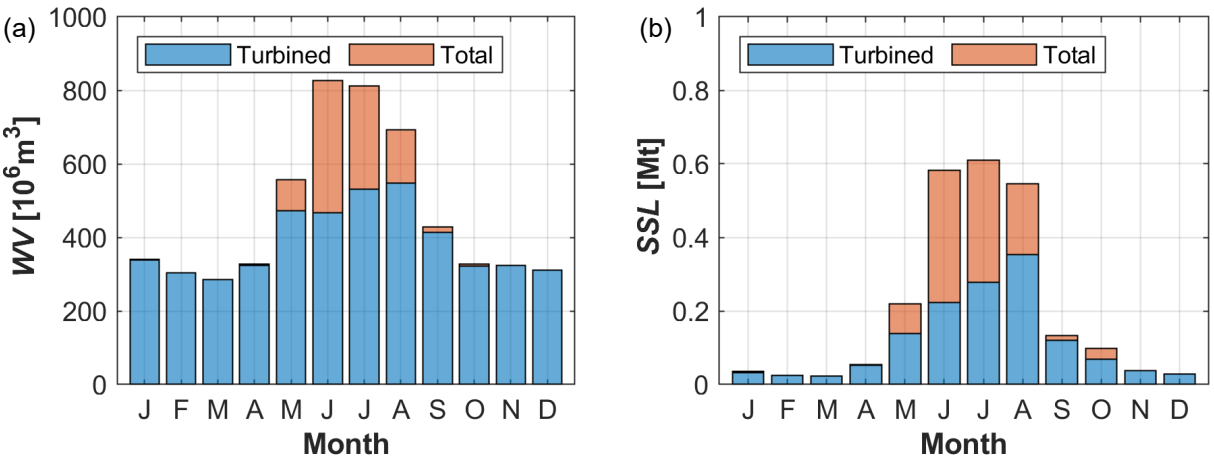

Figure 120: Monthly averages of (a) water volumes and (b) suspended sediment loads in the Rhone River and through the turbines of MBR (Data source: FOEN).

Furthermore, duration curves for *Q* and *SSC* in the Rhone River at the MBR site are analysed, in particular, for how long a certain *Q* or *SSC* value is exceeded on average for one year. The exceedance duration is of almost 10 days for $Q = 400$ m³/s. Regarding turbine erosion, it is advantageous that high *SSC*-values above 5 g/l only occur between 18 and 21 h per year and often coincide with high *Q* at which the HPP is not operated. High SSC_T, i.e. above 5 or 10 g/l, shall be interpreted with care because *SSC* from turbidimeters is likely to be underestimated due to multiple scattering and/or turbidity values above the working range of the sensors.

The amount of downtime is important for the profitability of a HPP. In the following, the discharge and *SSC* timeseries of the nine years are analysed to characterize how often and how long the planned HPP MBR would have had to shut down in the past because of flood events or possibly due to high *SSC*. Various thresholds for *Q* and *SSC* were defined above which a period is counted as a flood or sediment transport event, respectively. In a first step, event statistics (e.g., average number of events per year) were calculated for each type of threshold separately. In a second step, both types of thresholds, Q_{th} and SSC_{th}, were considered together. In that analysis, the focus was on events with high *SSC* and $Q \leq 400$ m³/s, because such events are relevant for turbine erosion at MBR. In Table 7, the average number of events per year, average total duration per year and the average event duration are listed for three event conditions, for which either one or both thresholds, Q_{th} and SSC_{th}, were exceeded. The crucial case for hydro-abrasive erosion, where *Q* is lower than 400 m³/s and *SSC* higher than 5 g/l, occurred less than 4 times per year with an average duration of 1.8 h resulting in 6.6 h per year.

Table 7: Average number, total duration per year and average duration per event of events fulfilling the indicated conditions for $Q_{th} = 400$ m³/s and $SSC_{th} = 5$ g/l.

Event Condition	Number of events [1/year]	Total duration per year [h/year]	Event duration [h]
$Q \leq Q_{th}$ & $SSC \geq SSC_{th}$	3.7	6.6	1.8
$Q > Q_{th}$ & $SSC \geq SSC_{th}$	3.9	1.5	0.4
$Q > Q_{th}$ & $SSC < SSC_{th}$	19.1	212.2	11.1

with $Q_{th} = 400$ m³/s and $SSC_{th} = 5$ g/l

To stop the turbines and to draw down the headwater level of MBR if the discharge exceeds 400 m^3/s, a certain prewarning time is an advantage. Therefore, the distances and flow times between existing federal hydrometric stations and MBR were investigated.

In Table 8 the flow times between different locations were calculated for two assumed flow velocities at normal conditions ($v \approx 2$ m/s) and during flood events ($v \approx 4$ m/s). The two timeseries of the hydrometric station on the Rhone at Branson and at the MBR project site were compared regarding the time shifts in discharge peaks. The time shift between corresponding peaks was identified and the histogram of all events shows that most of the discharge peak time shifts lie in the group between 1 and 1.5 h, which corresponds roughly to a velocity of 4 m/s (Table 8). For a longer prewarning time it can be investigated to use data from the intake of HPP Chippis (operated by FMV) further upstream.

Table 8: Distances and estimated flow time for normal conditions ($v \approx 2$ m/s) and flood events ($v \approx 4$ m/s) between relevant locations along the Rhone River.

River reach	Distance [km]	Flow time [h]	
		$v \approx 2$ m/s	$v \approx 4$ m/s
HPP Chippis intake – MBR	67.7	9.4	4.7
Drance – MBR	17.6	2.4	1.2
Branson – MBR	16.6	2.3	1.2
Dorénaz – MBR	11.0	1.5	0.8
HPP Lavey intake – MBR	6.3	0.9	0.4
MBR – Porte du Scex	17.4	2.4	1.2

Field study on suspended sediment and discharge in the Rhone

During a field study in July 2021, state-of-the-art measurement techniques were tested on the Rhone River for discharge and *SSC*. The objectives were to measure discharge, turbidity, *SSC* and to take suspended sediment samples close to the MBR project site at elevated *SSC*. Three sites were chosen for the measurements (in flow direction): the tailwater channel of HPP Lavey, the Rhone at the pedestrian bridge between the villages of Massongex and Bex as well as at the hydrometric station of FOEN in Porte du Scex. Discharge was measured at the first and the second site only. At the second site, the main measurements were conducted on the first and third day of the campaign.

During the campaign, discharge was high due to abundant rainfall (deep pressure zone Bernd), which lead to major floods in parts of Switzerland, Germany, and Belgium. At the Rhone River in the MBR region, a moderate flood led to challenging conditions which allowed to gather rare field data at elevated discharge, which is valuable to validate stage-discharge relations of hydrometric stations and conversions from turbidity to *SSC*. According to the peak discharge at Porte du Scex, the flood event had a return period of 8 years (FOEN, 2021).

For the measurements of flow depth, velocity and hence discharge, an Acoustic Doppler Current Profiler (ADCP) with four slightly inclined beams (1200 Hz) and one vertical (600 Hz) beam, integrated in a remotely controlled boat with a Real-Time Kinematic (RTK) GPS was used. During the flood, the flow velocity at the surface in the middle of the river was so high (about 5 m/s) that it was not possible to hold the ADCP boat in position by its propulsion engines only (max. boat speed 4 m/s). Therefore, a rope was attached to the boat and held from the pedestrian bridge in Massongex-Bex upstream of the measurement cross-section (Figure 121). At the tailwater channel of HPP Lavey, the flow conditions were more favourable with lower velocities up to 1.5 m/s. Generally, due to high turbulence and secondary flows, the ADCP measurements within a cross-section should be repeated several times to obtain sufficiently accurate average values (Maddahi *et al.*, 2021).

Moreover, the two sensors for indirect SSC measurements shown in Figure 121 were used to continuously record turbidity and uncalibrated *SSC*, respectively. These sensors were installed 0.7 m below the water surface close to the riverbanks where the flow velocities were moderate, and their output data were logged during a few hours. Simultaneously, several water samples were taken to investigate

the *SSC*-distribution over the river width and to convert the outputs of the two sensors to *SSC*. Selected water-sediment samples were prepared for the following analyses in the laboratory:

- *SSC* by the gravimetric method (*n* = 49 samples)Particle size distributions by wet sieving (≥125 µm) and laser diffraction (*n* = 13)Mineralogical composition for particle hardness by X-ray diffraction (*n* = 5)Microscope images for qualitative particle shapes (*n* = 6)

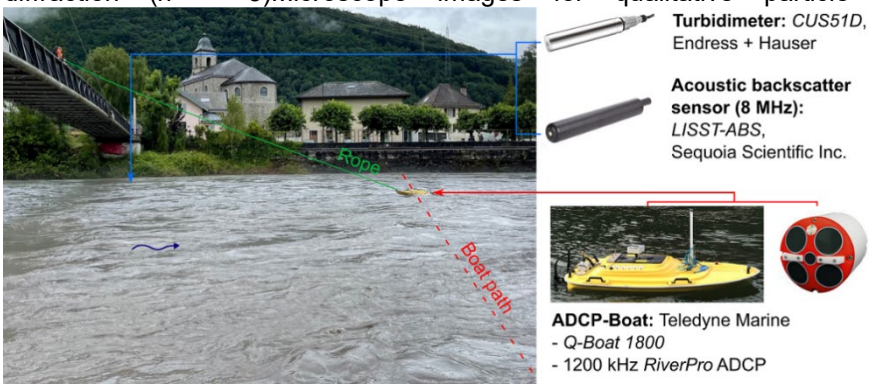

Figure 121: Rhone River between Massongex and Bex during the flood of July 2021 with the ADCP boat and the sensors for turbidity and indirect *SSC* measurements used during the campaign (Pictures: VAW and instrumentation suppliers).

Figure 122 shows the depth-averaged velocities normal to the cross-section measured on the three days in chronological order. In the Rhone at Massongex-Bex (Figure 122a and c) the depth-averaged flow velocity reached up to 4.0 m/s while in the tailwater channel of HPP Lavey, where the discharge is limited by the capacity of the HPP, the depth-averaged velocity did not exceed 1.3 m/s.

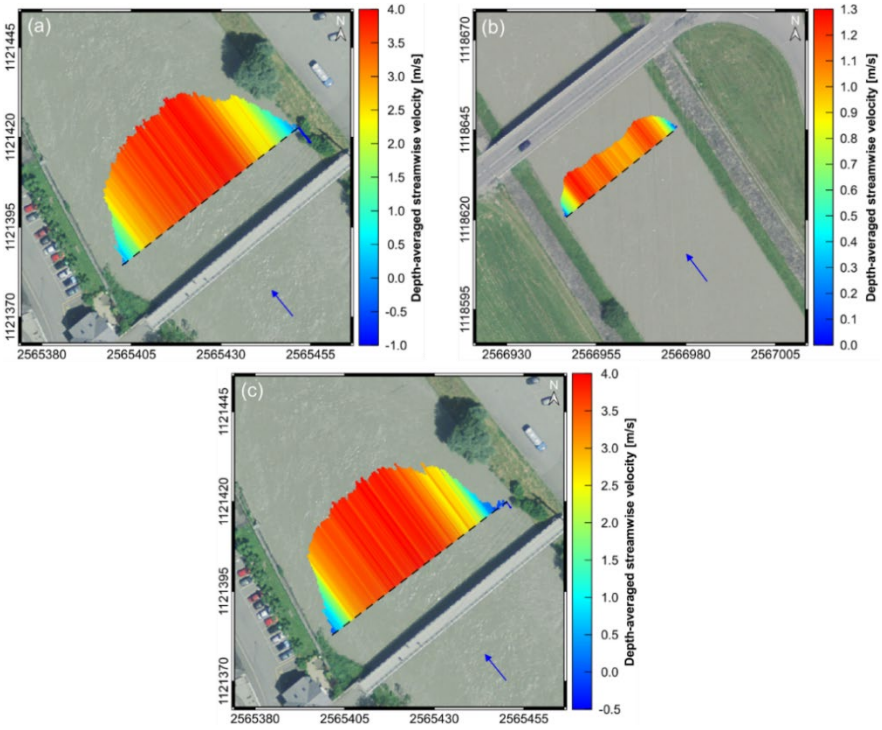

Figure 122: Depth-averaged streamwise velocity profiles: (a) 13th of July 2021 at Massongex-Bex, (b) 14th of July 2021 in the tailwater channel of HPP Lavey, and (c) 15th of July 2021 at Massongex-Bex. (aerial images: Swiss Federal Office of Topography, Coordinate system: CH1903+/LV95).

The rough flow conditions in the Rhone during the flood lead to strong turbulence, varying secondary flow structures, and surface waves, which made it hard to maneuver the boat. While pulling the boat across the river, it got pushed to the side and slightly tilted, and sometimes even jumped on waves, leading to erroneous measurements or data gaps. Additionally, the inflow of the creek Avançon into Rhone River directly upstream of the pedestrian bridge at the right bank disturbed the flow at the measurement cross-section. Hence, at least eighteen transects were done per cross-section. Streamwise velocities at Massongex-Bex partially exceeded 4 m/s in the river centre and decreases towards the banks and the bed. The negative flow velocities at the right bank resulted from a recirculation created by the perpendicular inflow of the Avançon creek which pushed the water of the Rhone towards the channel centre. While the water depth between the 13th and 15th of July decreased by only roughly three quarters of a meter, the change in riverbed was substantial. Sediments carried by the Rhone and additional sediments from the turbid Avançon were deposited on the right side due to the lower flow velocity in this part, which formed a sediment bank. From the velocity profile and the cross-sectional area at each measurement cross-section, the discharge was calculated for comparison with the data of the federal hydrometrical stations. The discharge at MBR was calculated based on the discharge at Porte du Scex and the downscaling factor for MBR. The discharges measured with the ADCP on the first and the third day of the measuring campaign in Massongex-Bex lie as expected between the discharges measured at the upstream and downstream hydrometric stations. Differences are attributed to mainly the discharges of further tributaries between these stations From the discharge measured by ADCP it is concluded that the discharges given by the federal hydrometric stations data are plausible also during such a flood event. As previously mentioned, the turbidity timeseries is not well correlated with the discharge, indicating that the *SSC* is not only related to discharge (transport capacity) but also to other factors such as sediment availability.

The calibration and verification of the *LISST-ABS* and *CUS51D* devices, was done with SSC_G from water samples taken during the measurement campaign. Figure 123a shows a chronological overview of all water samples collected. In Figure 123b, the focus is on Massongex-Bex, for which multiple transversal SSC_G profiles were measured. In Figure 123, no systematic variation of the SSC_G over the river width in Massongex-Bex was identified, as the *SSC* distribution may depend on the discharges and *SSC* of the Rhone and the Avançon. The elevated values at the right bank (blue and red points in Figure 123b) are probably caused by the Avançon tributary which discharged particularly turbid water into the Rhone River with different particle characteristics.

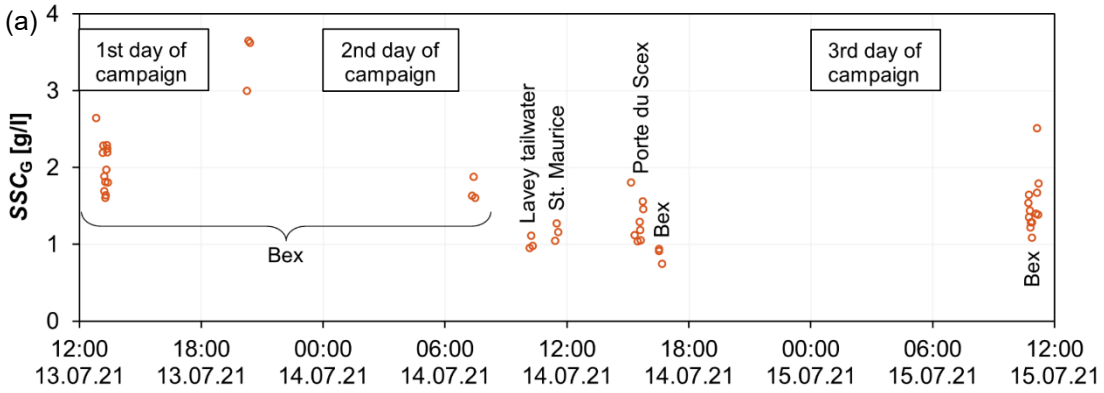

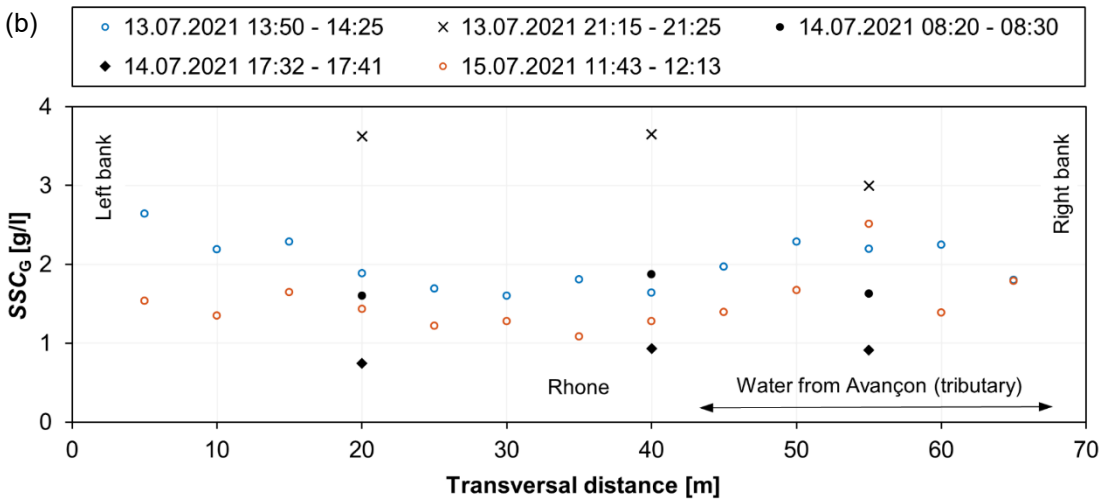

Figure 123: (a) SSC_G timeseries of water samples taken during the measurement campaign and (b) SSC_G profiles across of Rhone River at Massongex-Bex.

The water samples which were taken the closest in space and time to the turbidimeter and LISST-ABS measurements (SSC_L) were used to convert the data of the two devices to *SSC* (site-specific field calibration). Linear fits through the origin were determined for each of the two devices and are shown in Figure 124.

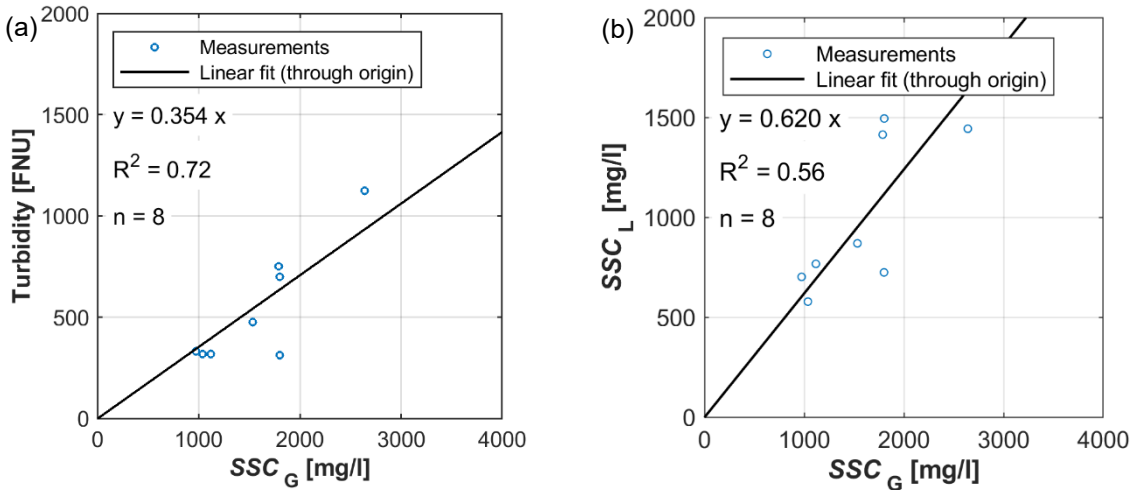

Figure 124: (a) Turbidity measured with the turbidimeter *CUS51D* and (b) *SSC* measured with the *LISST-ABS* device as a function of the gravimetrical suspended sediment concentration SSC_G from water samples of the Rhone River, 13th to 15th of July 2021.

The slope of these linear functions, which determine a conversion factor, depends on the particle size distributions of the suspended sediments (Felix *et al.*, 2018). For example, turbidimeters underestimate the *SSC* when the particles are temporarily coarser. The data are investigated with respect to this effect by comparing the conversion factor calculated as specific turbidity (Turbidity/SSC_G) for the turbidimeter and as ratio SSC_L/SSC_G for the *LISST-ABS* for each point as a function of two characteristic diameters d_{50} and d_m. For the data set during the flood in July 2021, however, the characteristic diameters lie all within the size range of medium and coarse silt and therefore, the particle size effect is probably smaller than the measurement uncertainty and other random influences.

As a last step, the *SSC* data from the various locations along the Rhone River were temporally shifted considering a flow velocity of 4 m/s (Table 9) to make them comparable with the *SSC* data from Porte

du Scex. The result is summarized in Figure 125, which shows that the *SSC* data of the measurement campaign correlate well with the *SSC* from Porte du Scex. For sediment studies, uncertainties in the range of ±20% are common. It is concluded that *SSC* data from Porte du Scex can be reasonably used to quantify the *SSC* at the MBR project site.

Table 9: Flow time for normal condition ($v \approx 2$ m/s) and flood event ($v \approx 4$ m/s) between the measurement locations along the Rhone River.

River reach	Distance [km]	Flow time [h]	
		$v = 2$ m/s	$v = 4$ m/s
HPP Lavey Tailwater – Pedestrian bridge Massongex-Bex	3.3	0.50	0.25
Pedestrian bridge Massongex-Bex – Porte du Scex	15.7	2.20	1.10

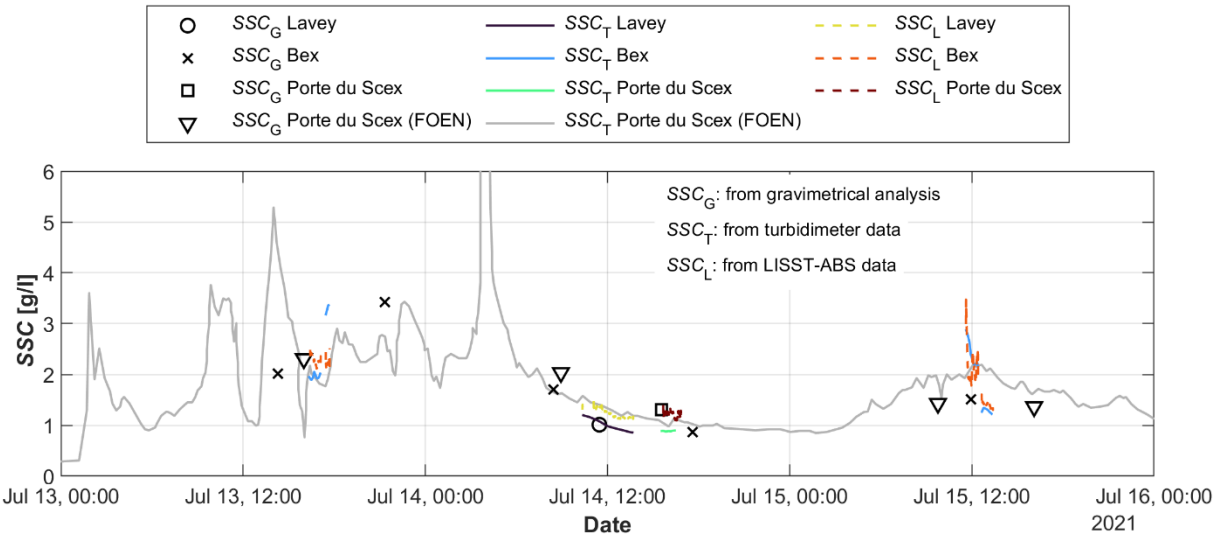

Figure 125: Timeseries of suspended sediment concentration *SSC* measured at three locations and with three techniques during the measurement campaign from 13th to 15th of July 2021. All data points were temporally shifted with the flow duration (see Table 9) between the respective measurement site and Porte du Scex.

The particle size distributions (PSDs) of 13 samples were determined by gravimetric analysis (wet sieving) for larger particles ($d \geq 125$ µm) and laser diffractometry on diluted samples for smaller particles ($d < 125$ µm) in the *ClayLab* of the Institute for Geotechnical Engineering (IGT) of ETH Zurich. Figure 126 shows the results of the analysis with a logarithmic scaling of the *d*-axis. Except for sample P09, all samples show a similar PSD with mostly silt and fine sand fractions. Sample P09 features a much coarser PSD with significant fine and medium sand fractions. In contrast to the other samples, which were collected at 0.1 m below the water surface, P09 was taken from a sediment deposit at the stairs of the hydrometric station Porte du Scex. Because the finer particles did not settle there, it is not representative for the sediment particles transported in the Rhone River and was hence excluded from further analysis. An averaged PSD without P09 is shown in Figure 126 (red line).

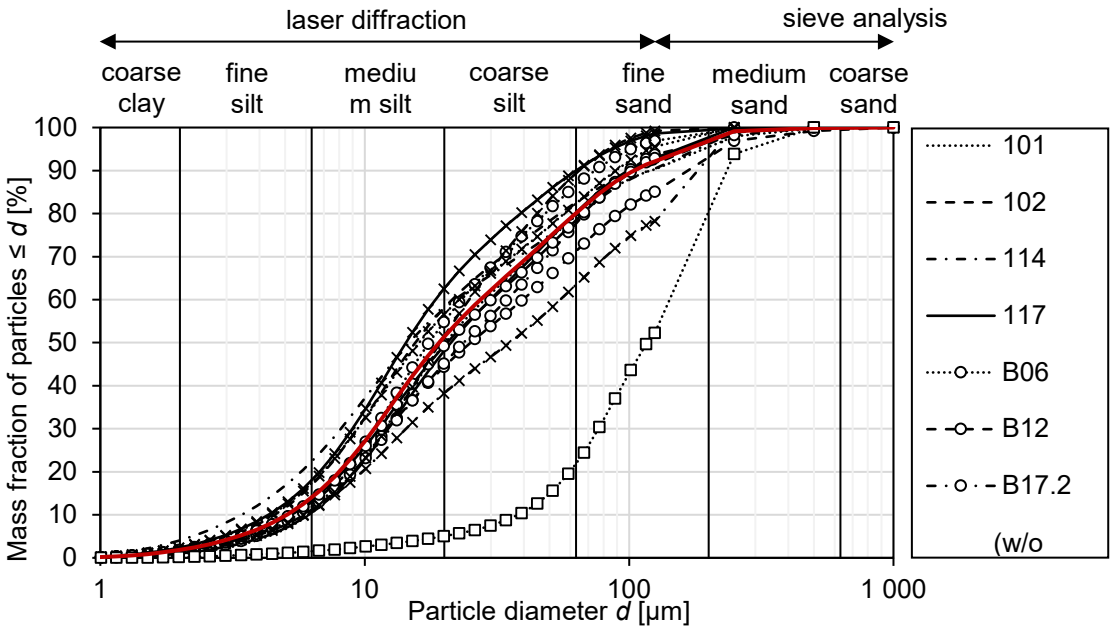

Figure 126: Particle size distributions (PSDs) of 13 samples and averages PSD (without P09) with logarithmic *d*-axis.

From the PSD, various characteristic particle diameters d_x are defined. Here, d_x denotes the diameter below which x% of the particle mass fall. For example, d_{50} (median particle diameter) corresponds to the diameter for which 50% of the sample mass is coarser or finer. The values of the different d_x were determined by linear interpolation of the PSDs in Figure 126.

From these characteristic diameters, further parameters for the characterization of a PSD can be derived. The values d_{84} and d_{16} are used to calculate the spreading (geometric standard deviation) σ_g as a measure of the width of a PSD:

$$\sigma_g = \sqrt{\frac{d_{84}}{d_{16}}} \tag{5}$$

PSDs with σ_g values of 2 to 3.2 are considered broad, >3.2 very broad (Merkus 2009).

A characteristic particle size that is often used in river engineering and in bedload transport calculations is the decisive particle diameter d_m (according to Meyer-Peter and Müller 1948). In contrast to d_{50}, this parameter has the advantage that the entire PSD is considered. To determine d_m, the PSD is divided into several grain size classes. For each size class *i*, the mean diameter $d_{m,i}$ is multiplied by the mass fraction of the size class Δp_i and this product $d_{m,i} \cdot \Delta p_i$ is summed up over all size classes(Bezzola 2020):

$$d_m = \sum d_{m,i} \cdot \Delta p_i \tag{6}$$

The mineralogical composition of five sediment samples was determined by X-ray diffractometry (XRD) at the Institute for Geotechnical Engineering (IGT) of ETH Zurich. Figure 127 shows the results of the analysis. The minerals are sorted according to their hardness on the Mohs scale. All samples have similar mineralogical composition, which is in line with expectations as they were collected very close to each other with respect to the Rhone River length and in each case in the middle of the flow cross section.

According to Uetz (1986, in Ortmanns 2006), particles cause significant hydro-abrasive erosion if they are harder than the target material exposed to their grinding and impact effects. Common turbine materials are usually assigned the following hardness:

- Martensitic stainless steel (13Cr-4Ni): Mohs hardness ≈ 4.5Hard coatings (tungsten carbide in cobalt-chromium matrix): Mohs hardness ≈ 6.5In Figure 127, the corresponding mass fractions of the abrasive minerals are indicated by grey (Mohs hardness > 4.5) and black (Mohs hardness > 6.5) fill areas. The mass fraction with Mohs hardness > 4.5 (hornblende, rutile, feldspar, and quartz) is 63% on average over the five samples, while it is 39% for Mohs hardness > 6.5 (quartz).

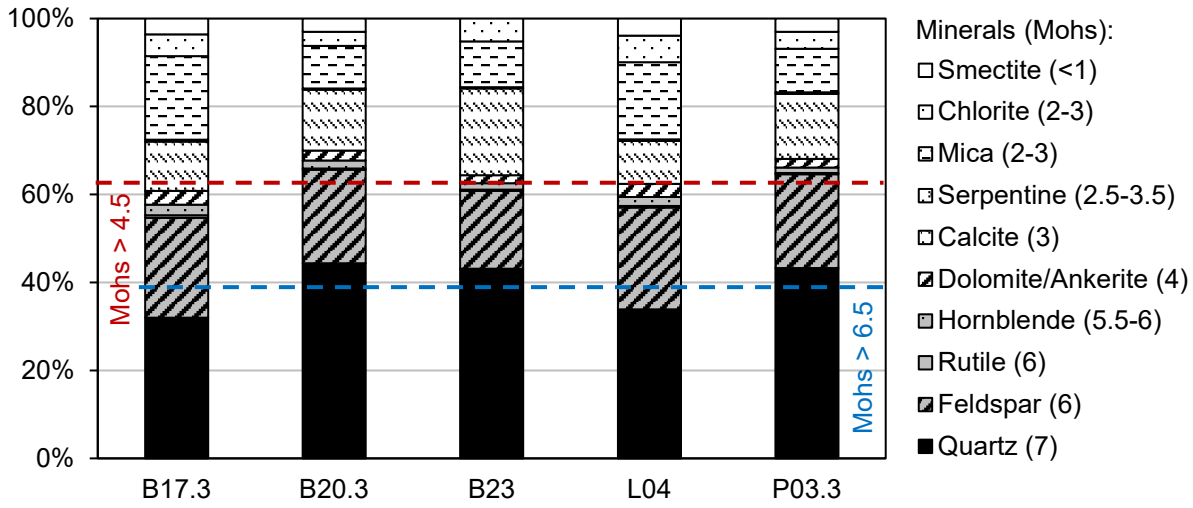

Figure 127: Mineralogical composition of five suspended sediment samples from the Rhone River during the flood in July 2021. The grey and black fill areas indicate minerals with Mohs hardness > 4.5 and 6.5, which are abrasive for uncoated and hard- coated turbine components, respectively.

A mass fraction of 63% with Mohs hardness > 4.5 for uncoated turbine components is in the lower range compared to other HPPs in Valais, i.e., the Central Alps of Switzerland. This means that the sediment particles in the catchment area of the HPP MBR are not particularly hard compared to other HPPs in Valais. However, the hardness is considerably higher than in pre-alpine catchments dominated by e.g., limestone or schists.

For the qualitative determination of the particle shape, electron microscope images were obtained of six selected sediment samples at the Institute for Building Materials (IfB) of ETH Zurich. A *FEI QUANTA 200 3D* (scanning electron microscope combined with focused ion-beam microscope) was used. Depending on the particle sizes, images were taken at 100x, 200x, 500x, 1000x and 2000x magnification. Plate-like particles are typically mica (layered silicates), which are non-abrasive due to their low hardness (Mohs scale < 3) and therefore not decisive. By visual comparison of the shapes of the non-platy particles in the present case, the particles are classified as angular. Non-rounded particles are typical for mountainous regions, as the sediment particles have only been transported over relatively short distances since their erosion.

Estimation of turbine erosion at MBR

Based on the previous findings, the extent of the expected hydro-abrasive erosion at the two turbines of MBR and potential mitigation measures are investigated. For that, the erosion model according to IEC 62364 (2019) with adaptions for Kaplan turbines is used. As mitigation measures, (i) turbine coating and (ii) temporary shutdowns of the HPP during periods with high *SSC* are considered. Furthermore, the uncertainties and potential systematic deviations of the estimated erosion depths are discussed.

In the present study, such a WC-Co-Cr coating (hard coating made of tungsten carbide = WC), similar to the one applied in HPP Lavey, was considered as an option to slow down the erosion on the turbine components.

According to the guideline IEC 62364 (2019), the absolute erosion rate due to hydro-abrasive wear on hydraulic turbines can be estimated as the integral of the erosion depth variation over time of operation. With measured values at specific times, this leads to a summation of the "weighted concentration hours". The IEC guideline contains numerical values for the parameters for Francis turbines, but not for Kaplan turbines which are relevant for the present case. The literature on the application of the IEC erosion model for Kaplan turbines is sparse. Only one published study was found. Rai and Kumar (2016) analyzed the hydro-abrasive erosion in uncoated Kaplan turbines with vertical shafts of a run-of-river HPP in India. With the available data, not all influencing variables could be quantified separately. Therefore, a combined factor *CF* was introduced, which served as a calibration constant of the model (all variables defined in the table below):

$$CF = \frac{K_f}{RS^p} \tag{7}$$

The *CF*-values from the model calibration and the corresponding uncertainties of the erosion depths d_e for four erosion zones are take as reference from the case study of Rai and Kumar (2016) with reference size *RS*, i.e., runner chamber diameter *D* was 4 m, which is similar to the 3.86 m at MBR. Hence, the transferability of the calibrated literature values of *CF* to the present study was assumed. IEC 62364 (2019) does not contain any numerical values for the parameter K_m for coated turbine components. Rai *et al*. (2020) determined values for K_m based on physical model tests for runner buckets of a Pelton turbine for six different base and coating materials. Since K_m is a material constant that describes the abrasion resistance in comparison to martensitic stainless steel (13Cr-4Ni), it is assumed that these literature values of K_m are also applicable to other turbine types. For the present estimations, K_m = 1 is used for uncoated surfaces (13Cr-4Ni) and K_m = 0.12 for hard-coated components (WC-Co-Cr).The coefficient for the particle hardness $k_{hardness}$ is also differentiated for non-coated or coated surfaces. The *SSC* and PSD of the individual turbines may differ from those of the Rhone River. However, since no more detailed information is available, it was assumed that the conditions for both turbines are identical, and particularly that the particle load is the same. The expected erosion depths were estimated using the IEC erosion model. The basic case of uncoated turbine parts as well as the option of hard coating were considered. Table 10 summarizes the underlying values of the input parameters for the erosion model.

Table 10: Summary of the input parameter values for the IEC erosion model.

Parameter	Value
Turbine design discharge *Q*	110 m^3/s
Runner chamber diameter *D*	3.86 m
Runner hub diameter D_h	1.55 m
Turbine rotational speed *n*	125 min^{-1}
Operation hours per turbine Δt	7'200 h/year
Suspended sediment mass concentration *SSC*	0.30 g/l
Coefficient for particle size k_{size} = d_{50} / 1000 µm	0.02
Coefficient for particle hardness $k_{hardness}$ - Uncoated (13Cr-4Ni steel) - Coated (WC-Co-Cr)	 0.63 0.39
Coefficient for particle shape k_{shape}	2.0
Coefficient for turbine material properties K_m	

- Uncoated (13Cr-4Ni steel) - Coated (WC-Co-Cr)	1.0 0.12
Characteristic velocity *w* - Turbine runner - Runner chamber	 27.6 m/s 11.2 m/s

The annual particle loads *PL* and erosion depths d_e per year, i.e., erosion rates, were estimated. For the coating a nominal initial coating thickness of 400 μm was assumed (usually 300 to 500 μm).

The results are presented in Table 11 for the four erosion zones within the turbine. The particle load *PL* reduces from 53.7 h·g/l to 33.7 h·g/l (i.e., by 37%) due to hard coating because only a smaller fraction of the suspended sediments is abrasive for the harder surface. The annual erosion depths d_e for uncoated turbine components vary between 82 and 166 μm/year for different erosion zones. The highest erosion is estimated for the turbine blade outlet or trailing edge. This corresponds to literature findings by Arora *et al*. (2022). Depending on the acceptable erosion depth, refurbishment works will be required when this threshold will be exceeded. If for example an erosion depth of 3 mm is accepted, refurbishment of the uncoated blades is required after 18 years. It is expected that the coating reduces the erosion depths d_e by a factor of about 12. For the decisive erosion on the blades, the coating is expected to be eroded over its full thickness of 400 μm after a duration Δt_c of about 30 years of operation.

Table 11: Particle loads and erosion rates for uncoated and hard-coated turbine components according to the IEC erosion model.

	Uncoated (13Cr-4Ni)	Hard-coated (WC-Co-Cr)
Annual Particle load *PL* [h·g/l per year]	53.7	33.7
Erosion rates [μm/year] - Turbine blade outlet - Turbine blade tip - Runner chamber upper cone - Runner chamber middle cone	 166 88 82 137	 12 7 6 10
Duration until coating is eroded over its full thickness Δt_c [years] - Turbine blade outlet - Turbine blade tip - Runner chamber upper cone - Runner chamber middle cone	 – – – –	 32 60 65 39

IEC 62364 (2019) does not specify which erosion depths are acceptable for the individual turbine components. It is recommended to discuss this with turbine specialists.The calculated particle loads and erosion depths are subject to the following uncertainties and systematic deviations:

- The parameter *CF* of the IEC erosion model was calibrated for Kaplan turbines based on a single case study from India by Rai and Kumar (2016). The underlying data set features erosion depth measurements from two years. This results in uncertainties for the estimation of the erosion depth d_e between 14 and 55%. For forecasts at the usual 95% confidence level (assuming normally distributed deviations) even twice the standard deviation must be

considered as an error band. Moreover, erosion depths may be locally higher than on average and it is assumed that the erosion depths reported in the calibration data and obtained from the IEC model refer to average values in certain areas.Beyond that, the parameter *CF* was determined using approximate values of d_{50}, which do not consider the whole shape of the PSD. Instead, the decisive particle diameter d_m would be a better measure to consider the effect of coarser particles. However, using d_m instead of d_{50} for the IEC erosion model would also require a recalibration of *CF*.Rai and Kumar (2016) present calibration factors *CF* for four different erosion zones. However, no further information on the exact location of the estimated erosion depths is given. For example, the erosion depth is expected to vary along the trailing edge of the turbine blade.The erosion rate generally increases with particle size. The applied guideline IEC 62364 (2019) assumes a linear increase for simplicity and lack or more specific information. Other, non-linear functions can also be found in the literature to describe the influence of particle size on the erosion rate (Felix 2017). These functions depend not only on the type of turbine, but also on the location considered within the turbine and the materials. Moreover, these literature findings refer to mainly Francis and Pelton turbines.When estimating the erosion, it was assumed that the *SSC* and PSD are identical for both turbines. However, due to secondary flows in the approach flow and inertia effects, the coarser suspended particles can be distributed unevenly among the two turbines. If an uneven erosion of the individual turbines should occur in the future, a balancing of the erosion depths can be aimed for by adjusting the operating hours of the individual machines accordingly.The erosion of the coating material was modelled linearly to zero with a resistance coefficient K_m according to Rai et al. (2020), which was determined for buckets of Pelton turbines. It has not yet been proven that the K_m value can also be transferred to other turbine components or types. In reality, the coating cannot be worn down to zero, but only down to a minimum thickness, below which the remaining layer of coating may be suddenly removed. This minimum thickness is due to the size of the ceramic particles and their embedding in the metal matrix. Spalling and splintering of the coating may also occur instead of continuous coating erosion. For example, splintering may be caused due to occasional impacts of stones passing the turbines despite the planned protection measures against bed load, leading to a faster loss of coating over its full thickness than the estimated Δt_c in Table 11.As a result of turbine erosion, cavitation may occur (secondary damage). Cavitation and combined effects of erosion and cavitation are not formally included in the estimates according to IEC 62364 (2019) or Rai and Kumar (2016). However, with a suitable hydraulic design of the turbine components, cavitation should only play a minor role, at least as long as the wear is not pronounced.Despite its limitations, the procedure according to IEC 62364 (2019) allows usually to estimate erosion rates in a realistic order of magnitude and to study the influences of individual parameters with a manageable effort compared to numerical simulations.

Measures to better cope with the fine sediment load and its consequences at MBR

While the hard coating proved to be a convincing solution for the upstream HPP Lavey with a gross head of 44 m, it is not yet clear if a coating can be economically justified for a low head HPP such as MBR.Based on the present information, coating of the two Kaplan turbines seems to be an interesting option for MBR, mainly because of the expected longer times between overhauls and the associated savings due to less frequent refurbishment works (installation of stoplogs for dewatering etc.). It is recommended to consider the operation experience in HPP Lavey and to collect information from operators of other low-head run-of-river HPPs at sediment-laden rivers, e.g., in Austria and France, and their turbine suppliers. In the tendering phase of the project, it is recommended to request offers for both uncoated and coated turbines. To do so, the numerical values of the input parameters in Table 10 may be provided to the turbine suppliers. For the economical evaluation of the offers, the costs of coating can be compared to the savings due to lower annual refurbishment costs and due to lower production losses because of a slower reduction of turbine efficiency.

Temporary shutdowns of the HPP in periods of high *SSC*, i.e., typically during floods, are generally an important measure to economically improve the operation of run-of-river HPPs at sediment laden rivers

(Felix *et al.*, 2022). During major floods, the sediment load and the resulting erosion may be so high that the turbines cannot be operated as planned until the next scheduled maintenance, leading to high additional costs and production losses. A shutdown is economically beneficial if the direct and consequential savings due to the avoided turbine erosion are higher than the lost revenue during the standstill. Prerequisites for such shutdowns are information on the actual *SSC* in the river, the knowledge of a threshold concentration ($SSC_{shutdown}$) and the possibility to not comply with the scheduled production plan on short notice, i.e., thanks to compensation of the production with other HPPs in the region of the same operator.

Numerical values of $SSC_{shutdown}$ reported in literature range between 1.1 and 15 g/l for uncoated and coated Pelton and Francis turbines (Felix *et al.*, 2022). In those studies, moderate electricity prices around 50 EUR/MWh were assumed, which were common before the year 2022. The $SSC_{shutdown}$ is specific for each HPP, depending on the properties of the sediments, the turbines, the operation pattern, the costs, and revenues.

Based on the available discharge and sediment data of the period 2013-2021, the operation of MBR was simulated to investigate the effect of $SSC_{shutdown}$ on the turbined sediment load and production loss. Besides the planned shutdowns when the river discharge exceeds 400 m^3/s, it was assumed that an alarm is released when the threshold value $SSC_{shutdown}$ in the river water is exceeded for 10 min. The HPP is shut down after a reaction time t_{react}, which is varied between 0 and 110 min. The suspended sediment event is considered as terminated when the *SSC* has fallen below half of the $SSC_{shutdown}$ for at least 10 min. Subsequently, the HPP operation is resumed after a reaction time which was assumed to be the same as for the shutdown.

The influence of $SSC_{shutdown}$ on the average suspended sediment mass concentration SSC_{avg} of the turbines for different reaction times t_{react}. Shows that there is almost no effect for $SSC_{shutdown} > 8$ g/l, whereas SSC_{avg} reduces significantly for $SSC_{shutdown} < 2$ g/l. The effect of the reaction time t_{react} is negligible for the Rhone River in the region of MBR. In Figure 128 the mean annual production loss due to HPP shutdowns and the mean annual suspended sediment load *SSL* of the turbines is plotted as a function of $SSC_{shutdown}$, again for different reaction times t_{react}. The annual production loss is an indicator of the lost revenue. The *SSL* of the turbines is an indicator for their erosion and the associated sediment-induced costs.

Hardly any production loss due to standstills is expected for $SSC_{shutdown} > 10$ g/l. On the other hand, for $SSC_{shutdown}$ below 2 g/l, the production losses would make up more than 2% percent of the annual production, which is estimated to be not acceptable. Similarly, the mean annual *SSL* starts to reduce notably for $SSC_{shutdown} < 10$ g/l. The limit of 10 g/l should be interpreted with care because the analysed *SSC* time series stems from a turbidimeter. *SSC* in rivers may exceed the measuring range of such instruments and hence it is likely that high *SSC* were not recorded. The comments on Figure 128 (*SSL*) apply also to the mean annual particle load *PL* of the turbines. This is the case because with mainly full load operation during the sediment transport season, the *PL* and the erosion depths are almost proportional to the *SSL*. The reaction time t_{react} up to 2 h has no major effect. With a river the size of the Rhone at MBR, and the first shutdown criterion regarding discharge, a reaction time from the alarm to the shutdown of 0.5 to 1 h is considered as sufficient and feasible.

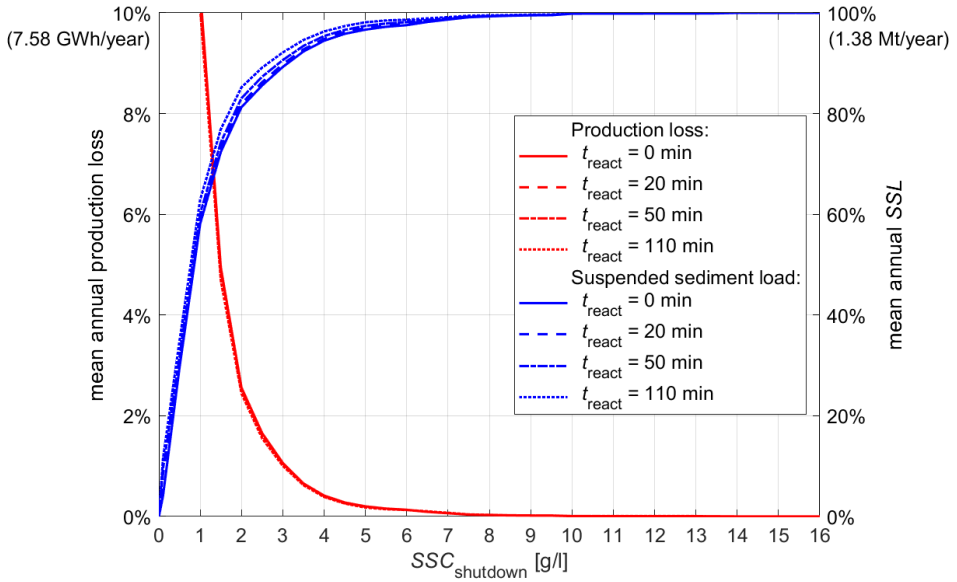

Figure 128: Mean annual production loss and *SSL* as a function of $SSC_{shutdown}$ for different reaction times t_{react} until HPP shutdown.

To determine the HPP-specific $SSC_{shutdown}$ based on economic optimization, knowledge on the sediment-induced costs (refurbishment and replacement of turbine parts, loss of efficiency) is required. To do so, it is important to document all sediment related costs over the years. Until such data will become available after e.g., 10 to 20 years of operation, an initial value of e.g., 10 g/l can be adopted to prevent the turbines from excessive damages due to exceptionally high *SSC*. The installation of a real-time sediment monitoring system at MBR or upstream on the Rhone River is recommended for the following reasons:

- Optimization of HPP operation by temporary shutdowns if *SSC*-threshold value is exceeded, in addition to the already planned shutdowns due to discharges > 400 m³/s.Quantification of the sediment/particle load for checking of the turbine performance guaranteed by the turbine supplier.Establishment of correlations with turbine erosion and efficiency for predictive maintenance and replacement of turbine parts.In view of the rather short distance between MBR and Lavey, the same operator companies, and the more pronounced turbine erosion in Lavey, it is recommended to install instruments for real-time suspended sediment monitoring mainly at the intake of HPP Lavey. Like this, the sediment monitoring system will be useful for two HPPs and offers some pre-warning time for MBR. A significant part of the *SSL* is already prevented from turbine passage by the discharge shutdown criterion. Hence, a system for real-time sediment monitoring at MBR alone is not so important as for a HPP with no discharge shutdown criterion.

The instrumentation for such a system may include

- A turbidimeter (e.g., *CUS51* from Endress+Hauser) with automatic cleaning by pressurized air. The measuring range of most commercially available turbidimeters is limited to a few g/l (depending on the model and the particle sizes).An acoustic sensor (e.g., *LISST-ABS* from Sequoia Scientific) with a higher sensitivity to more abrasive sand rather than silt particles or a more recent multi-frequency instrument (*NivuParQ850* from Nivus) for *SSC* measurements in five size classes, but limited to about 6 g/l.A Coriolis Flow and Density Meter (CFDM, e.g., *Promass 500* DN 25, from Endress+Hauser) suitable to measure medium and high *SSC* to complement the other instruments.If the river discharge upstream of MBR exceeds 400 m³/s, it is planned to stop the turbine operation and to open the weir gates for flood discharge and sediment passage. As the drawdown of the headwater level requires a certain time to avoid an additional discharge peak downstream and some preparations, the flow time of flood peaks from

two federal hydrometric stations upstream of MBR (Rhone at Branson and Drance at Martigny) was investigated.

As the time shift between flood peaks at these hydrometric stations to MBR is around 1.2 h, discharge data from these stations may be useful to issue warnings to prepare for HPP shutdowns with reservoir drawdowns and flushing. Nowadays it is possible to receive data from federal hydrometric stations in real-time upon request and to integrate them into the HPP operator's control system.

To increase the prewarning time, it may be checked if real-time data of the Rhone discharge at the intake of HPP Chippis, about 70 km upstream of MBR and operated by FMV, can be additionally made available. With a flow time of about 4.7 h, the prewarning time would considerably increase. However, due to several major tributaries between Chippis and Branson, it is expected that the reliability of the warning is lower than the one based on the hydrometric stations in Branson and Martigny.

Turbine erosion may affect turbine efficiency in the range of up to a few percent, often particularly at partial load. There are many ways to monitor changes in turbine efficiency over time from classical index tests to continuous efficiency monitoring. The latter has the advantage that also other effects which lead to efficiency reductions, such as debris (grass and fine driftwood) on the leading blade edges can be detected in real-time. In addition to efficiency, vibration monitoring may contribute to detect suboptimal performance of the turbines as early as possible to take counteractions.

It is recommended to measure the extent of erosion if there is an opportunity to access the turbines after some years of operation. Based on such measurements, the IEC erosion model can be site-specifically calibrated to reduce the uncertainty of the predictions. This is valuable to better estimate the remaining lifetime of the turbine components and to anticipate the need for refurbishment works and replacement of turbine parts (including procurement of spare parts on time) in the future.

5 Conclusion and Outlook

The HydroLEAP project has established a comprehensive and forward-looking framework for the modernization, digitalization, and ecological improvements of hydropower systems, addressing both technological and environmental challenges under the ongoing energy transition. By combining advanced simulations, experimental validation, digital monitoring, and infrastructure upgrades, the project has provided practical tools and scientific insights that will shape the next generation of flexible and sustainable hydropower plants.

At the FMHL pumped-storage facility, the exploration of HSC operation demonstrated new pathways for enhancing flexibility and grid support. The successful validation of intra-unit, inter-unit, and inter-plant configurations through extensive CFD and 1D transient simulations, coupled with on-site testing, proved the feasibility and safety of dynamic operation even during pumping mode. The integration of the Hydro-Clone digital twin enabled real-time monitoring and predictive analytics, significantly improving situational awareness and operational resilience. Reduced scale model testing and full-scale experiments further advanced understanding of transient-induced fatigue mechanisms in both Pelton turbines and multistage pumps, revealing that optimized acceleration strategies and dynamic monitoring approaches can mitigate mechanical degradation and extend component lifespan.

At KW Ernen, the hybridization of hydropower with Battery Energy Storage Systems demonstrated its effectiveness in improving operational flexibility, reducing mechanical stress, and enhancing energy market participation. The use of advanced control strategies and MPC algorithms reduced guide vane movements and pressure fluctuations, while machine learning–based virtual sensors and the Vibration Content Index supported predictive maintenance and reduced operational costs. The hydropeaking analyses confirmed that hybrid operation can increase energy revenues while maintaining limited ecological impact—validating hybridization as a key enabler for future flexible hydropower systems.

At the MBR hydropower site, the project achieved major innovations in fish protection and sediment management. The Curved-Bar Rack and foiled-bar configurations optimized fish guidance while reducing hydraulic losses. Bypass system experiments led to design refinements for improved fish passage, and real-time suspended sediment concentration monitoring was proposed to mitigate erosion risks and inform operational decisions. These results directly contribute to the ecological modernization of hydropower operations.

A key enabler of these achievements was the modernization of the EPFL Technology Platform for Hydraulic Machines, a world-class facility supporting reduced-scale testing and validation of advanced hydropower technologies. The upgrades to Test Rigs 1, 2, and 3 have expanded PTMH's experimental capabilities: from high-head Pelton turbine transient studies and hybrid battery-hydraulic experiments to variable-speed operation and grid emulation. This modernization ensures the facility's long-term role as a global hub for cutting-edge hydropower research, training, and technology transfer. It reinforces Switzerland's leadership in addressing challenges related to grid flexibility, climate-resilient operation, and digitalization of hydropower assets.

The project results offer numerous opportunities for further exploitation, industrial application, and scientific advancement, shaping the evolution of sustainable hydropower in the coming decades:

- Wider deployment of flexible operation concepts: The validated HSC configurations and hybrid operation schemes can be implemented across other pumped-storage and conventional plants to enhance system flexibility, grid balancing, and ancillary service provision. Their integration into operational standards and energy market frameworks could redefine hydropower's role in renewable integration.
- Expansion of digital twin ecosystems: The Hydro-Clone platform demonstrated the power of combining real-time plant data with high-fidelity simulations. Future work will focus on scaling this approach to fleet-level digital twins, enabling predictive control, life-cycle asset management, and continuous optimization under variable environmental and grid conditions.

- Advancement of AI-driven predictive maintenance: The convergence of vibration-based monitoring, modal analysis, and machine learning provides a foundation for next-generation diagnostic systems. Expanding datasets across facilities will enhance model generalization, leading to standardized health indices and early-warning systems applicable industry-wide.
- Field implementation of eco-hydraulic solutions: The CBR–Bypass System and redesigned bypass geometries will undergo full-scale field validation to quantify biological performance and hydraulic efficiency. These results will inform future design guidelines and regulatory standards for fish-friendly hydropower.
- Development of predictive sediment management systems: The proposed multi-sensor SSC monitoring concept can evolve into digital twins for sediment dynamics, integrating hydrological forecasting and operational optimization to reduce erosion, improve turbine longevity, and enhance sustainability.
- Strategic upgrades and uses of PTMH facilities: The modernization of PTMH establishes a unique research infrastructure for exploring future hydropower challenges—such as variable-speed operation, hybrid energy systems, hydraulic transients, and climate adaptation. This facility will be instrumental in performing fundamental research on hydraulic machinery and supporting collaborative R&D initiatives, pilot testing, and workforce training for the next generation of hydropower engineers.
- New research avenues in resilience and climate adaptation: Building on the upgraded experimental platforms and digital tools, future research can address hydropower resilience under changing hydrological regimes, system dynamics under renewable variability, and integration with emerging energy storage technologies.

In conclusion, HydroLEAP has delivered a comprehensive portfolio of technological, methodological, and infrastructural innovations that will directly support the sustainable modernization of hydropower. By uniting hybrid operation, digital monitoring, eco-design, and advanced experimentation, the project not only reinforces hydropower's position as a cornerstone of Switzerland's Energy Strategy 2050, but also opens new frontiers for research, innovation, and global collaboration in achieving a resilient, flexible, and environmentally responsible energy future. Collectively, these outcomes confirm that HydroLEAP has successfully bridged fundamental research and applied innovation, delivering tools and methodologies that strengthen the resilience, efficiency, and environmental compatibility of hydropower.

6 National and International Cooperation

The project benefited from national and international collaborations that significantly enhanced both its scientific depth, impact, and its industrial relevance. At the national level, a close partnership was established with Andritz Hydro (Vevey, Switzerland), the hydraulic turbine manufacturer for the FMHL and KW-Ernen power plants. This collaboration took place within the activities of WP2 and WP3, which focused on advanced demonstrations and validation under real operating conditions. The direct involvement of Andritz Hydro ensured a continuous and productive exchange between the research team and industrial practitioners. Scientific results were regularly discussed, validated, and progressively integrated into industrial workflows, contributing to the modernization of turbine components and operational strategies. This cooperation proved instrumental in improving machine flexibility, informing updated guidelines, and accelerating the transfer of innovative methodologies from research to practice.

Beyond the national dimension, the project was strongly embedded in the broader European hydropower research community. Key results, methodological insights, and future research needs were discussed extensively within a series of dedicated workshops organized under the umbrella of the EERA Joint Programme Hydropower (EERA JP Hydropower) and ETIP Hydropower. These workshops

gathered experts from academia, industry, and institutions, fostering a shared understanding of emerging challenges and co-developing strategic directions for future innovation. The outcomes of these discussions have contributed directly to the preparation of a forthcoming white paper, aimed at shaping research and innovation priorities and influencing future Horizon Europe funding pathways.

Through these combined national and international efforts, the project has strengthened collaboration across sectors, promoted knowledge exchange, and helped align scientific advances with industrial and policy needs. This cooperative framework has laid the foundation for sustained progress in hydropower flexibility and sustainability, and the development of next-generation guidelines supporting the energy transition.

7 Publications

[1] A. Alerci, E. Vagnoni, C. Nicolet, N. Hugo, and M. Paolone, “1D numerical study of a multistage centrifugal pump during transient operation,” *IOP Conf. Ser.: Earth Environ. Sci.*, vol. 1079, p. 012103, 2022, doi: 10.1088/1755-1315/1079/1/012103.

[2] M. Chiarelli, V. C. Hasmatuchi, D. F. Vetsch, R. M. Boes, and C. Münch-Alligné, “On-site measurements of the dynamic behaviour of Pelton turbines in the context of predictive maintenance,” *IOP Conf. Ser.: Earth Environ. Sci.*, vol. 1079, p. 012096, 2022, doi: 10.1088/1755-1315/1079/1/012096.

[3] J. Decaix, M. Mettille, N. Hugo, B. Valluy, and C. Münch-Alligné, “CFD Investigation of the hydraulic short-circuit mode in the FMHL+ pumped storage power plant,” presented at *ViennaHydro Conf.*, 2022.

[4] J. Decaix, M. Mettille, J.-L. Drommi, N. Hugo, and C. Münch-Alligné, “Computation fluid dynamics investigation of the flow in junctions: application to hydraulic short circuit operating mode,” *LHB*, vol. 109, no. 1, 2023, doi: 10.1080/27678490.2023.22900250.

[5] A. L. Alerci, E. Vagnoni, and M. Paolone, “Structural impact of the start-up sequence on Pelton turbines lifetime: Analytical prediction and polynomial optimization,” *Renew. Energy*, vol. 218, 2023, doi: 10.1016/j.renene.2023.119341.

[6] M. Kastinger, I. Albayrak, L. G. M. Silva, and R. Boes, “Passage stromabwärts schwimmender Fische an einem Bypass-Einlauf mit bodennaher Öffnung,” in *Proc. 21. Wasserbau-Symposium*, Wallgau, Germany, Jun. 2023, vol. 2, pp. 21–28, doi: 10.3929/ethz-b-000623631.

[7] M. Kastinger, I. Albayrak, L. G. M. Silva, and R. M. Boes, “Passage of downstream moving fish at a bypass gate with bottom opening,” in *Proc. 40th IAHR World Congress*, Vienna, Austria, Aug. 2023, doi: 10.3850/978-90-833476-1-5_iahr40wc-p0082-cd.

[8] M. Chiarelli, C. Münch-Alligné, D. F. Vetsch, and R. M. Boes, “Characterisation of dominant frequencies during transient operations of Pelton turbines at the FMHL PSP,” in *Proc. HYDRO 2023 Conference*, Edinburgh, 2023.

[9] A. L. Alerci, E. Vagnoni, and M. Paolone, “Evaluation of the fatigue-related influence of start-ups on Pelton turbines based on reduced scale model stress measurements,” *IOP Conf. Ser.: Earth Environ. Sci.*, vol. 1411, p. 012040, 2024, doi: 10.1088/1755-1315/1411/1/012040.

[10] I. Albayrak, Y. Marshall, C. Leuch, D. Vetsch, and R. M. Boes, “Fish protection and guidance at hydropower intakes with novel f-curved bar rack-bypass systems: lessons learnt from two Swiss case studies,” in *Proc. HYDRO 2024 International Conference and Exhibition*, Graz, Austria, Nov. 2024.

[11] J. Decaix, M. Mettille, N. Hugo, B. Valluy, and C. Münch-Alligné, “CFD Investigation of the Hydraulic Short-Circuit Mode in the FMHL/FMHL+ Pumped Storage Power Plant,” *Energies*, vol. 17, no. 2, p. 473, 2024, doi: 10.3390/en17020473.

[12] A. Amini, S. Rey-Mermet, S. Crettenand, and C. Münch-Alligné, “A hybrid methodology for assessing hydropower plants under flexible operations: Leveraging experimental data and machine learning techniques,” *Appl. Energy*, vol. 383, p. 125402, 2025.

[13] M. Chiarelli, D. F. Vetsch, R. M. Boes, and C. Münch-Alligné, “Investigation of the natural modes of a Pelton runner prototype,” *IOP Conf. Ser.: Earth Environ. Sci.*, vol. 1483, p. 012015, 2025, doi: 10.1088/1755-1315/1483/1/012015.

[14] J. Decaix, D. Fischer, C. Münch-Alligné, and M. Boden, “Suppression des tourbillons en entrée de la pompe de mise en charge de Veytaux 1,” *Wasser Energie Luft*, vol. 117, no. 2, pp. 49–54, 2025.

[15] M. Chiarelli, D. F. Vetsch, R. M. Boes, L. Andolfatto, and C. Münch-Alligné, “On the influence of geometrical parameters and erosive wear on the dynamic behaviour of Pelton turbine runners,” *Results Eng.*, 2025, doi: 10.1016/j.rineng.2025.105638.

[16] M. Kastinger, I. Albayrak, L. G. M. Silva, and R. M. Boes, “Downstream fish passage and swimming behaviour at a bypass gate with bottom and top opening,” *J. Ecohydraulics*, accepted with revision, 2025.

[17] I. Albayrak, D. Felix, N. Cracknell, M. Kastinger, and R. M. Boes, “Investigation of suspended sediment and turbine erosion for the sustainable operation of a planned low-head hydropower plant,” in *Proc. 41st IAHR World Congress*, Singapore, Jun. 2025.

[18] A. L. Alerci, M. Paolone, and E. Vagnoni, “Optimization of Pelton turbines start-up considering fatigue damage via a fracture mechanics model,” *Int. J. Fatigue*, accepted with revision, 2025.

[19] A. L. Alerci and E. Vagnoni, “Fracture mechanics-based study of structural damage in multistage pumps during start-up,” under review, 2025.

[20] A. L. Alerci, E. Vagnoni, and M. Paolone, “Monitoring of the stress-induced crack propagation in Pelton turbines by reduced scale model testing,” accepted at *Colloque HydroES 2025: Hydroélectricité, Innovation & Résilience*, Grenoble, Sep. 2025.

[21] J. Schmid, C. Bussard, C. Nicolet, S. Forest, S. Stojanovic-Roth, and J. N. Saugy, “Investigation of Pressure Relief Valve Performance from 1D Hydraulic Transient Model Calibration to Advanced CFD Analysis,” accepted for *10th IAHR International Meeting of the Workgroup on Cavitation and Dynamic Problems in Hydraulic Machinery and Systems*, Brno, Czech Republic, Oct. 2025.

[22] J. Decaix, M. Mettille, and C. Münch-Alligné, “Cavitation simulation of a prototype double Francis turbine at off design operating points,” accepted at *10th IAHR Meeting of the WorkGroup on Cavitation and Dynamic Problems in Hydraulic Machinery and Systems*, Brno, Czech Republic, 2025.

-

8 References

Abdi Ali. Start and stop costs for secondary regulation of fortum hydropower plants. test, 2015.

Arora, N., Kumar, A., Sunil, K. S. (2022). Technological advancement in measurements of suspended sediment and hydraulic turbine erosion. *Measurement* 190: 110700, https://doi.org/10.1016/j.measurement.2022.110700.

Beck, C. (2020). Fish protection and fish guidance at water intakes using innovative curved-bar rack bypass systems. VAW-Mitteilung 257 (R. Boes, ed.), VAW, ETH Zürich.

Beck, C., Albayrak, I., Meister, J., Boes R.M. (2020a). Hydraulic performance of fish guidance structures with curved bars: Part 1: Head loss assessment. Journal of Hydraulic Research, 58(5), 807-818, https://doi.org/10.1080/00221686.2019.1671515.

Beck, C., Albayrak, I., Meister, J., Boes R.M. (2020b). Hydraulic performance of fish guidance structures with curved bars: Part 2: Flow fields. Journal of Hydraulic Research, 58(5): 819-830, https://doi.org/10.1080/00221686.2019.1671516.

Beck, C., Albayrak, I., Meister, J., Peter, A., Selz, O.M., Leuch, C.; Vetsch, D.F., Boes, R.M. (2020c). Swimming behavior of downstream moving fish at innovative curved-bar rack bypass systems for fish protection at water intakes. Water 12 (11), 3244, https://doi.org/10.3390/w12113244.

Beck, C., Albayrak, I., Meister, J., Leuch, C., Vetsch, D., Peter, A., Boes, R. (2021). Curved-Bar-Rack-Bypass-Bypass-Systeme für den Fischschutz an Wasserkraftanlagen und Wasserfassungen. WasserWirtschaft 111(9-10): 54-61 (in German).

Felix D., Albayrak I., Abgottspon A., Boes R.M. (2016). Hydro-abrasive erosion of hydraulic turbines caused by sediment – a century of research and development. Proc. 28th IAHR-Symposium on Hydraulic Machinery and Systems, Grenoble, France: 907-916 and IOP Conf. Series: Earth Environ. Sci. 49, 122001.

Felix D., Albayrak I., Boes R. (2018). In-situ investigation on real-time suspended sediment measurement techniques: Turbidimetry, acoustic attenuation, laser diffraction (LISST) and vibrating tube densimetry. International Journal of Sediment Research, 33: 3-17.

Felix, D., Abgottspon, A., von Burg, M., Albayrak, I., Staubli, T., Boes, R. M. (2022). Hydro-abrasive erosion on coated Pelton turbines: Nine years of measurements and temporary shutdowns of HPP Fieschertal. *13th International Conference on Hydraulic Efficiency Measurement*, Grenoble, France.

Florjancic D., Bachler J., Wernli, HP48, 4-stufig – HONGRIN, 1967, Sulzer report

FOEN (2021). Hydrological data of Rhone at Porte du Scex, Station 2009. Hydrological data and forecasts, Federal Office for the Environment. https://www.hydrodaten.admin.ch/en/2009.html

Gerini F., Vagnoni E., Seydoux M., Cherkaoui R., Paolone M., (2024), Enhanced frequency containment reserve provision from battery hybridized hydropower plants: Theory and experimental validation, *Electric Power Systems Research*, https://doi.org/10.1016/j.epsr.2024.110765

Goring, D.G. & Nikora, V.I. (2002). Despiking Acoustic Doppler Velocimeter Data. Journal of Hydraulic Engineering, 128 (1): 117–126. https://doi.org/10.1061/(ASCE)0733-9429(2002)128:1(117).

Grasso A., Scapozza C., Storck F. (2021). Betrieb des Bundes-Messnetzes für den Transport suspendierter Sedimente in Fliessgewässern. Wasser Energie Luft, 1, 23-28 (in German).

Godde, D. (1994). Experimentelle Untersuchungen zur Abströmung von Rohrturbinen. Ein Beitrag zur Optimierung des Turbineneinlaufes. Dissertation, Technische Universität München, Oskar v. Miller-Institut, Heft Nr. 75 (in German).

Grein H., Angehrn R., Lorenz M. and Bezinge A., “Inspection periods of Pelton runners”. In: The 12th IAHR Symposium, Stirling (1984).

Habersack H., Wagner B., Schoder A., Hauer C. (2013). Die Bedeutung von Feststoffhaushalt und Sedimentdurchgängigkeit für eine nachhaltige Nutzung der Wasserkraft. Österreichische Wasser- und Abfallwirtschaft 65, 354–361. https://doi.org/10.1007/s00506-013-0108-0 (in German).

IEC 62364 (2019). Guide for dealing with hydro-abrasive erosion in Kaplan, Francis, and Pelton turbines. 2nd Edition.

International Electrotechnical Commission, Geneva.

Kriewitz, C. R. (2015). Leitrechen an Fischabstiegsanlagen: Hydraulik und fischbiologische Effizienz. VAW-Mitteilung 230 (R. Boes, ed.), VAW, ETH Zürich (in German).

Larinier, M., & Couret, D. (2008). Guide pour la conception de prises d'eau «ichtyocompatibles» pour les petites centrales hydroélectriques. RAPPORT GHAAPPE RA08, 4 (in French).

Maddahi M. R., Rahimpour M., Boes R., Albayrak I. (2021). Determining minimum numbers of transects for accurate flow measurements using moving-vessel ADCPs. Proc. 13th Symposium on Ultrasonic Doppler Methods for Fluid Mechanics and Fluid Engineering (pp. 48-51). ETH Zurich, Laboratory of Food Process Engineering.

Meister, J. (2020). Fish protection and guidance at water intakes with horizontal bar rack bypass systems. VAW-Mitteilung 258 (R. Boes, ed.), VAW, ETH Zürich.

Meister, J., Fuchs, H., Beck, C., Albayrak, I., Boes, R.M. (2020). Velocity fields at horizontal bar racks as fish guidance structures. Water 12(1): 280, doi:10.3390/w12010280

Meister, J., Beck, C., Albayrak, I., Boes, R. (2021a). Hydraulik und betriebliche Aspekte von Horizontalrechen-Bypass-Systemen. WasserWirtschaft 111(9-10): 20-27 (in German).

Meister, J., Beck, C., Selz, O.M., Peter, A., Albayrak, I., Boes, R. (2021b). Bemessungsempfehlungen für den Fischschutz mit Horizontalrechen-Bypass-Systemen. WasserWirtschaft 111(9-10): 28-33 (in German).

Nicolet, C., Hydroacoustic modelling and numerical simulation of unsteady operation of hydroelectric systems, AEPFL-Thesis, 2007

Nicolet, C, Braun O, Ruchonnet N, Beguin A, Hell J and Avellan F, 2016, Hydroacoustic modelling and numerical simulation of unsteady operation of hydroelectric systems, Proc. of HYDROVISION International 2016, July 26–29, 2016, in Minneapolis, USA

Ortmanns, C. (2006). Entsander von Wasserkraftanlagen (Sand traps of hydropower plants). [In German.] *VAW-Mitteilungen* 139 (H.-E. Minor, Ed.), VAW, ETH Zurich.

Rai A. K., Kumar A. (2016). Analyzing hydro abrasive erosion in Kaplan turbine: A case study from India. Journal of Hydrodynamics, Ser. B, 28(5), 863-872.

Silva, A.T., Lucas, M.C., Castro-Santos, T., Katopodis, C., Baumgartner, L.J., Thiem, J.D., Aarestrup, K., Pompeu, P.S., O'Brien, G.C., Braun, D.C., Burnett, N.J., Zhu, D.Z., Fjeldstad, H-P., Forseth, T., Rajaratman, N., Williams, J.G. and Cooke, S.J. (2018). The future of fish passage science, engineering, and practice. Fish and Fisheries 19, 340-362.

Suresh S. (1998). Fatigue of materials. Second edition. Cambridge University Press, ISBN:9780511806575.

Uetz, H. (1986). Abrasion und Erosion (Abrasion and erosion). [In German], Carl Hanser Publisher, Munich.

Wahl, T.L. (2003). Discussion of "Despiking acoustic doppler velocimeter data" by Derek G. Goring and Vladimir I. Nikora. Journal of Hydraulic Engineering, 129 (6): 484–487. https://doi.org/10.1061/(ASCE)0733-9429(2003)129:6(484).

Walker, K. "The Effect of Stress Ratio During Crack Propagation and Fatigue for 2024-T3 and 7075-T6 Aluminum". In: Effects of Environment and Complex Load History on Fatigue Life, ASTM STP 462 (1970). DOI: 10.1520/STP32032S.